

Photo-Induced Formation of Fluorescent Single Chain Polymer Nanoparticles as Imaging Agents in Biology

Zur Erlangung des akademischen Grades einer

DOKTORIN DER NATURWISSENSCHAFTEN

(Dr. rer. nat)

von der KIT-Fakultät für Chemie und Biowissenschaften

des Karlsruher Instituts für Technologie (KIT)

genehmigte

DISSERTATION

von

M. Sc. Carolin Heiler

1. Referent: Prof. Dr. Christopher Barner-Kowollik

2. Referent: Prof. Dr. Hans-Achim Wagenknecht

Tag der mündlichen Prüfung: 16.07.2018

Die vorliegende Arbeit wurde von April 2015 bis Juni 2018 unter Anleitung von Prof. Dr. Christopher Barner-Kowollik am Karlsruher Institut für Technologie (KIT) angefertigt.

*"Glück und Erfolg werden einem nur vergeben,
wenn man großmütig einwilligt, beides zu teilen"*

Albert Camus

Abstract

In the present thesis, the formation of fluorescent single chain polymer nanoparticles (SCNPs) and their potential application as imaging agent in biological environments is investigated, exploiting tetrazole based photochemistry. The so-called nitrile imine-mediated tetrazole-ene cycloaddition (NITEC) is hereby the reaction of choice, capable to form highly fluorescent pyrazoline adducts. The NITEC reaction is utilized to induce single chain collapse to generate inherently fluorescent SCNPs, which should be suitable as imaging agents *in vivo*. The light activation of the tetrazole forms a highly reactive nitrile imine under the release of nitrogen, undergoing rapid conversion with electron deficient and nucleophilic compounds. Moreover, several small molecule studies with an UV- and visible light active tetrazole were carried out to investigate the suitability of the photochemistry for the SCNPs collapse.

Initially, monomers equipped with the photoreactive moieties were synthesized, *i.e.* acrylate based tetrazole and maleimide containing monomers. Water solubility of the prepolymers was achieved *via* commercially available monomers such as *N,N*-dimethylacrylamide (DMAA) and poly(ethylene glycol acrylate) (PEGA), which were polymerized with the acrylate-based functional monomers. While these terpolymerizations were carried out, a paper was published, reinvestigating the reactions of nitrile imines with carboxylic acids in a so-called nitrile imine carboxylic acid ligation (NICAL).¹ As a result, the synthetic route was adapted by using acrylic acid as water-soluble monomer featuring both the water-soluble moieties as well as the potential reactive partner for the UV-induced polymer collapse. Subsequently, poly(acrylic acid) was synthesized *via* Reversible Addition Fragmentation Chain Transfer (RAFT) polymerization. To incorporate the photoreactive compounds, statistical Steglich esterifications were conducted along the polymer backbone with the UV-active tetrazole and the furan protected maleimide. The functionalization of poly(acrylic acid) resulted in water-soluble UV-light active polymer precursors. Due to a non-quantitative functionalization of the poly(acrylic acid), the single chain collapse is capable to proceed *via* a dual folding mechanism, exploiting NITEC and NICAL reactions.

The photoreaction was carried out in pure water, affording highly fluorescent SCNPs, which showed, due to their small sizes, good cellular uptake in first biological tests *in vivo*, which were carried out in a collaborative effort (team of Prof. Dr. Ute Schepers, KIT).

The second aspect of the current thesis features the application of a visible light active pyrene-aryl tetrazole (PAT), which opens a variety of reactions employing light in the visible range. The reactivity of PAT was investigated in several small molecule studies, resulting in fluorescent adducts, which have the potential to act as imaging agents in cells. Consequently, the synthesis of water-soluble, visible light active polymers was targeted, providing a mild access route to fluorescent SCNPs. In a collaborative work (team of Prof. Dr. Stefan Bräse, KIT), a peptidomimetic, *i.e.* peptoid, which is known for its ability to act as a molecular transporter in cells, was synthesized, affording a visible light active polymer precursor including a specific cell recognition site. Since RAFT polymerization was used, the peptoid was introduced within the R-group of the RAFT agent. The polymerization of acrylic acid resulted in a linear PAA, which was subsequently functionalized in a statistical esterification with PAT, maleimide units and (triethylene glycol monomethylether) segments. Based on the previous investigations employing the UV-light active tetrazoles in PAA polymers, a dual folding mechanism with NICAL and NITEC was expected. However, only the weakly fluorescent NICAL reaction was triggered after irradiation with visible-light, generating non-suitable SCNPs for the application as imaging agent. Therefore, a bismaleimide linker was utilized to induce a NITEC reaction, yielding highly fluorescent water-soluble SCNPs. Unfortunately the reaction could not be reproduced due to an unstable functionalized PAA precursor over time. As a result, the polymeric backbone was changed to a poly(styrene) (PS) chain.

Consequently, PS based polymers were synthesized *via* nitroxide mediated polymerization (NMP) for the visible light approach. Here, the results stemming from the small molecule studies of the visible light tetrazole were utilized, resulting in PS based photoreactive polymer precursors. The mild light trigger in combination with the inert polymers accomplished the SCNP formation with the incorporated photochemical reactants in a swift and reliable fashion.

Zusammenfassung

Die vorliegende Arbeit beschäftigt sich mit der Herstellung von Einzelkettenpolymernanopartikeln und deren potenzieller Anwendung als Fluoreszenzmarker in biologischen Organismen, mittels der photochemisch induzierten Tetrazolchemie. Die sogenannte Nitril-imin vermittelte Cycloaddition (NITEC) steht hierbei im Fokus, da sie die Bildung von fluoreszenten Pyrazolinderivaten ermöglicht. Die NITEC Reaktion soll hierbei genutzt werden, um die fluoreszenten Einzelkettenpolymernanopartikel herzustellen. Das hochreaktive 1,3-Dipol-Intermediat, welches nach der Bestrahlung von Tetrazolen gebildet wird, kann mit unterschiedlichen Nucleophilen sowie elektronenarmen Doppelbindungen reagieren. In dieser Arbeit wurde zunächst die Reaktivität von zwei unterschiedlichen mit Licht aktivierbaren Tetrazolen untersucht, um sie anschließend separat in verschiedenen Polymeren als Auslöser für die Einzelkettenpolymernanopartikelbildung zu verwenden.

Zu Beginn dieser Arbeit wurden funktionelle acrylatbasierte Tetrazol und Furan geschützte Maleimid Monomere hergestellt, welche mit Licht aktivierbare Eigenschaften beinhalten sollten. Die Wasserlöslichkeit wurde durch die kommerziell erhältlichen Monomere *N,N*-Dimethylacrylamid (DMAA) und Polyethylenglycolacrylat (PEGA) erhalten, die mit den funktionellen Monomeren polymerisiert werden sollen. Während verschiedene Terpolymerisationen durchgeführt wurden, ist eine wissenschaftliche Publikation veröffentlicht worden, die die Reaktion von Tetrazolen mit Carbonsäuren in einer so genannten Nitril-imin vermittelten Carbonsäure Ligation (NICAL) beschreibt. Aufgrund der neuen Erkenntnisse über die Reaktivität von Tetrazolen wurde die Synthesestrategie angepasst. Anstatt der funktionalen Monomere wurde nun die wasserlösliche Acrylsäure als Monomer verwendet, die zum einen als potentieller Reaktionspartner des Nitril-imins dient und zum anderen die benötigte Wasserlöslichkeit mit sich bringt.

Der nächste Schritt beinhaltet die Polymerisation der Acrylsäure über die Reversible Additions-Fragmentierungs-Ketten-Transfer Polymerisation (RAFT).

Um die photoreaktiven Moleküle an das Polymer anzubinden, wurden die Hydroxylderivate der photoreaktiven Moleküle mittels einer statistischen Steglich Veresterung verknüpft. Die nicht-quantitativen Veresterungen am Polymer resultierten in zwei möglichen Faltungsmechanismen (NITEC und NICAL) während der Bestrahlung mit UV-Licht. Die Photoreaktion wurde in reinem Wasser durchgeführt und resultierte in fluoreszenten und wasserlöslichen Nanopartikeln, die durch ihre kleinen Durchmesser eine gute zelluläre Aufnahme in ersten biologischen Zellexperimenten zeigten. Die Zellexperimente wurden in einer kooperativen Arbeit mit der Gruppe von Prof. Dr. Ute Schepers (KIT) durchgeführt.

Ein weiterer Aspekt der vorliegenden Arbeit beschäftigt sich mit der Anwendung eines Pyren-aryl-tetrazols (PAT), welches mit Licht im sichtbaren Wellenlängenbereich aktiviert wird und dadurch eine breite Anwendung in biologischen Bereichen aufgrund der milden Photoreaktionsbedingungen ermöglicht. Die Reaktivität von PAT wurde in mehreren Kleinmolekülstudien untersucht, woraus fluoreszente Produkte resultierten, die als potentielle Fluoreszenzmarker in Zellen eingesetzt werden können. Anschließend wurde die Synthese eines wasserbasierten, mit sichtbarem Licht aktivierbaren und biokompatiblen Polymers umgesetzt.

Desweiteren wurde ein Peptid imitierendes Molekül ein sogenanntes Peptoid in Kooperation mit der Gruppe von Prof. Dr. Stefan Bräse (KIT) hergestellt, welches als molekularer Transporter in Zellen verwendet werden kann. Zunächst wurde das Peptoid mit der Kettenübertragungsreagenz, welches in der RAFT Polymerisation verwendet wird, umgesetzt und anschließend in einer Acrylsäurepolymerisation verwendet. Die Polymerisation der Acrylsäure resultierte in linearen Polyacrylsäurepolymeren, die anschließend durch eine statistische Veresterung mit den funktionalen Gruppen, Pyren-aryl-tetrazol, Furan geschütztes Maleimid und Triethylenmonomethylether am Polymer verankert wurden. Leider konnten in den ersten Faltungsexperimenten nur Hinweise auf eine säurebasierte Kupplung gefunden werden, die aufgrund ihrer geringfügigen Fluoreszenzeigenschaften für die anschließende Anwendung als Fluoreszenzmarker nicht geeignet ist.

Aus diesem Grund wurde die NITEC Reaktion mit einem Bismaleimid-Linker induziert, was in fluoreszenten und wasserlöslichen Nanopartikeln resultierte. Allerdings zeigte sich, dass die funktionalisierte Polyacrylsäure über einen längeren Zeitraum instabil war. Aus diesem Grund wurde die reaktive Polyacrylsäure durch das inerte Polystyrol ersetzt. Für die Synthese des Polystyrolpolymers wurde die Nitroxid vermittelte Polymerisation (NMP) verwendet. Die erworbenen Erkenntnisse aus der Kleinmolekülstudie konnten in den polystyrolbasierten Polymeren umgesetzt werden. Die anschließende milde Bestrahlung mit sichtbarem Licht in hoher Verdünnung führte zu den gewünschten fluoreszenten Einzelkettenpolymernanopartikeln.

Publications arising from the Thesis

Photochemically Induced Folding of Single Chain Polymer Nanoparticles in Water

Heiler, C.; Offenloch, J.; Blasco, E.; Barner-Kowollik, C. *ACS Macro Lett.* **2017**, *6*, 56-61.

Folding Polymers with Visible Light

Heiler, C.; Bastian, S.; Lederhose, P.; Blinco P. J.; Blasco, E.; Barner-Kowollik, C. *Chem. Commun.* **2018**, *54*, 3476-3479.

Additional publications

Degradable Fluorescent Single-Chain Nanoparticles Based on Metathesis Polymers

Offenloch, J. T.; Willenbacher, J.; Tzvetkova, P.; Heiler, C.; Mutlu, H.; Barner-Kowollik, C. *Chem. Commun.* **2017**, *53*, 775-778.

Table of Contents

Abstract.....	VII
Zusammenfassung.....	IX
Publications arising from the Thesis	XIII
1. Introduction and Motivation	1
2. Theoretical Background and Literature Overview	5
2.1 Radical Polymerization Techniques	5
2.1.1 Conventional Free Radical Polymerization.....	6
2.1.2 Atom Transfer Radical Polymerization (ATRP)	10
2.1.3 Nitroxide mediated Polymerization (NMP).....	11
2.1.4 Reversible Addition-Fragmentation Chain Transfer (RAFT) Polymerization ..	13
2.2 Photochemistry.....	18
2.2.1 Principles of Photochemistry.....	18
2.2.2 Light-induced Reactions in Polymer Chemistry	24
2.3 Single Chain Polymer Nanoparticles (SCNPs).....	39
2.3.1 Photoinduced SCNP Formation	42
2.3.2 Fluorescent SCNPs for <i>in vivo</i> Applications	48
2.4 Analytical Tools for SCNPs.....	55
2.4.1 Size Exclusion Chromatography (SEC)	55
2.4.2 Dynamic Light Scattering (DLS).....	58
2.4.3 Diffusion Ordered Spectroscopy (DOSY).....	61
3. Fluorescent Single Chain Polymer Nanoparticles <i>via</i> Tetrazole Photochemistry	67
3.1 UV-Light Induced Folding of Polymers into SCNPs	69
3.1.1 Photoreactive Monomer and RAFT Agent Synthesis	69
3.1.2 Small Molecule Study of the UV-Tetrazole.....	74
3.1.3 Preparation of PAA Polymers Containing the UV-Light Active Tetrazole.....	81
3.1.4 UV-light Induced Folding of PAA Polymers and their Characterization.....	89
3.1.5 Application as Imaging Agents.....	97

3.2 Visible Light Induced Folding of Polymers into SCNPs	99
3.2.1 Small Molecule Study of the Visible Light Tetrazole.....	100
3.2.2 Preparation of PAA Polymers Containing the Visible Light Active Tetrazole	111
3.2.3 Visible Light Induced Folding of PAA Polymers and their Characterization .	116
3.2.4 Polymerization of Polystyrene <i>via</i> NMP	126
3.2.5 Visible Light Induced Folding of PS Polymers and their Characterization ...	135
4. Concluding Remarks and Outlook.....	147
5. Experimental Part.....	153
5.1 Materials and Methods	153
5.2 Small Molecule Synthesis.....	159
5.2.1 RAFT Agent Synthesis	159
5.2.2 Synthesis of the Photoreactive Compounds	161
5.3 Small Molecule Studies	168
5.3.1 UV-Tetrazole	168
5.3.2 Visible Light active Tetrazole	169
5.3.3 Competitive Irradiation Studies (PAT).....	169
5.4 Peptoid Synthesis.....	170
5.5 Polymerizations	172
5.5.1 RAFT Polymerizations	172
5.5.2 Post Functionalization of PAA based Polymers	174
5.5.3 NMP Polymerizations	176
5.6 General Procedure for the Photo-induced SCNP Formation.....	177
6. Appendix.....	178



Introduction and Motivation

"Nature alone is infinitely rich, and it alone forms the great artist" was already stated in 1774 by Johann Wolfgang von Goethe.² This "great artist" – Nature – has been a main source of inspiration in science. Biomimetic technologies encounter almost every field in our everyday life from the non-adhesive effect inspired by lotus leaf to adhesive materials inspired by gecko feet.³

Mimicking nature has been and continues to be of great importance in the field of macromolecular chemistry, too. One example is the mimicry of precise and complex biomacromolecules such as proteins. Proteins are sequence-defined linear monodisperse macromolecules, which can undergo rapid formation into a functional three dimensional structure and act as catalysts in cells. These structures are known as enzymes and assume multiple tasks in cells. Initially, a linear – primary – structure by the consecutive substitution of amino acids is generated followed by the formation of a so-called secondary structure taking the shape of e.g. α -helices and β -sheets.

The linkage of the linear structure is realized *via* covalent bonds – mainly peptide bonds – while the secondary structure is accomplished with the formation of hydrogen bonds of the amino acid residues.

The folding into a three dimensional structure entails dynamic-covalent (disulfide bonds) and non-covalent interactions (Van-der Waals or hydrophobic stacking). Overall, the three dimensional structure is achieved by utilizing different types of chemical interactions such as covalent, dynamic and dynamic-covalent. The largest polypeptide found in humans was titin⁴ where approx. 30.000 amino acids form its structure, indicating the highly precise and effective biosynthesis of proteins. A synthetic approach for polypeptides is represented by the Nobel price endowed Merrifield synthesis, initially reported in 1963.⁵ Here, exploitation of a solid phase and liquid phase synthetic process lead to an efficient synthesis of polypeptides. Although this solid phase procedure is highly efficient, the synthesis of polypeptides comprising thousands of amino acids is still unattainable.

One approach employed by polymer chemists to mimic the precise folding of proteins, consists of the controlled intramolecular collapse of tailor-made linear precursor polymers to form the so-called single chain polymer nanoparticles (SCNPs). This collapse to a folded SCNP that entails some of the characteristics of a biomolecule, however is still a very simple mimicry of the complex and precise folding processes seen in proteins. The advantage of using SCNPs is their less demanding synthesis as well as the possibility of employing varied stimuli such as temperature, light or chemical cues, inducing the single chain collapse. Especially the use of light constitutes a powerful way to generate SCNPs without the need of a catalyst or an additive to fold polymers in a spatial and temporal controlled manner. In recent years, different types of SCNPs were generated with a multitude of applications in the fields of imaging agents,^{6,7} drug delivery,⁸ enzym-mimetics,⁹⁻¹¹ catalysis^{12,13} and tumor targeting⁷ among others.

The current thesis aims at providing a novel platform for the synthesis of fluorescent SCNPs, which can be applied as imaging agents in biology. A well-established reaction is the tetrazole chemistry, which was initially employed as explosives or for bioconjugation reactions.^{14,15}

Tetrazole chemistry has been selected as a suitable light-induced reaction for the generation of the targeted SCNPs. Many tetrazoles are known to undergo a rapid conversion into nitrile imines when irradiated with light, which undergo 1,3-dipolar reactions with a range of double bonds or nucleophiles (refer to Section 2.2.6).

Depending on the double bonds employed, highly fluorescent compounds can be observed after reaction with the formed nitrile imine. This reaction often involves the cycloaddition with the double bonds in a so-called nitrile imine-mediated tetrazole-ene cycloaddition (NITEC). Thus, the generation of a fluorescent adduct makes this a chemistry highly promising for the envisioned application, *i.e.* as fluorescence marker. The NITEC process is ideally suited for bioapplications due to typical excitation wavelengths of the cycloadduct in the visible range at approx. 400 nm with subsequent emission above 500 nm. Furthermore, the targeted fluorescent SCNPs provide avenues for the preparation of biofunctional intracellular transport imaging. The application as molecular transporter can be realized when a functional biomolecule *e.g.* peptide is additionally coupled to the fluorescent SCNPs, providing the ability to monitor the molecular transport across cell membranes. Initially, the synthesis of water-soluble and fluorescent SCNPs was targeted. Hence, in the first part of the current thesis, the photochemistry of tetrazoles using UV-light is exploited directly in water for the formation of fluorescent and water-soluble SCNPs (refer to Chapter 3.1). Furthermore, the tetrazoles can be structurally varied to change the wavelength for triggering the 1,3-dipolar reaction. Especially bathochromic wavelength shifts are of major interest in biology allowing for the generation of fluorescent SCNPs under very mild and biocompatible conditions. Thus, in the second part of the present thesis, a pyrene-functionalized tetrazole was incorporated into different polymers and their photochemistry with different reactive groups as well as the SCNP collapse was carefully investigated (refer to Chapter 3.2).

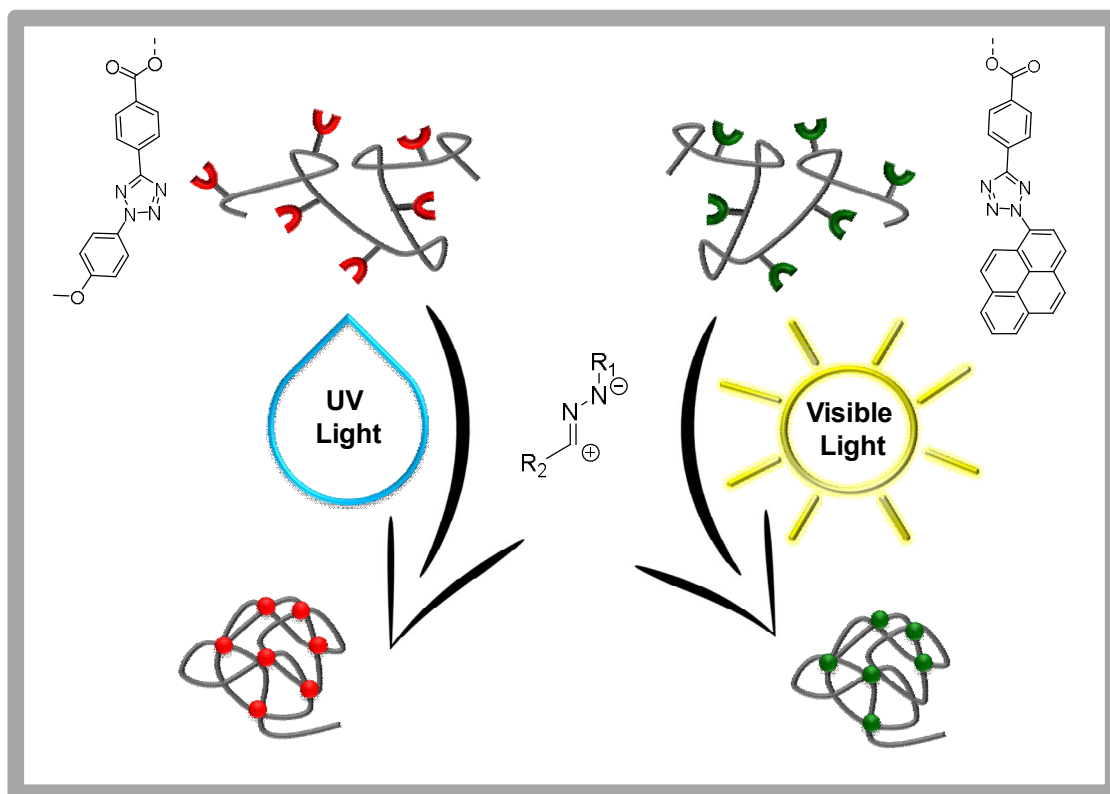


Figure 1: Schematic representation of the SCNP approaches employing the photo-induced nitrile imines arising from tetrazole with UV- and visible light.



Theoretical Background and Literature Overview

The following section of the current thesis provides the information of the theoretical overview and background information of the subjects applied. In the first section (Section 2.1), radical polymerization techniques are introduced, giving an insight in the relevant and modern polymerization techniques. In the next section (Section 2.2) the photochemical processes together with some examples of photochemical reactions employed in polymer chemistry are described. An overview of the formation of single chain polymer nanoparticle (SCNP) and the common characterization methods is given in the last theoretical sections (Section 2.3 and Section 2.4).

2.1 Radical Polymerization Techniques

In this section, key radical polymerization techniques are described. Initially, conventional free radical polymerization is explained followed by reversible deactivation radical polymerization (RDRP) protocols such as atom transfer radical polymerization (ATRP), nitroxide-mediated polymerization (NMP) and reversible addition-fragmentation chain transfer polymerization (RAFT).

The radicals, arising from the cleavage of the initiator are able to add to C-C double bonds ($I^{\cdot} + M$) and create a propagating monomer unit (R_1^{\cdot}). In summary, a two-step mechanism is responsible for initiating the polymerization reaction.

The efficiency of the initiator as well as the chemical constitution of the double bond affect the propagation rate during polymerization. The propagation rate coefficient of the growing polymer chain (k_p) is dependent on the chemical constitution of the monomers.¹⁷ The growth of the chain is achieved by the consecutive addition of monomers, leading to a growing polymer chain (R_{n+1}^{\cdot}). Additional key reactions in conventional FRP lead to "dead" chain ends and are occurring due to the reactivity of the generated radicals.¹⁸ Two key reactions are discussed here, *i.e.* the termination and chain transfer reaction. The termination reaction is diffusion controlled, and thus dependent on the viscosity of the solvent, the intrinsically changing viscosity of the reaction mixture with increasing conversion and the chain length of the radical species.¹⁷ The chain transfer reaction leads to a dead end of a growing polymer chain and an activated transfer agent, which is able to reinitiate the polymerization. The kinetic investigation of FRP is discussed below.

The kinetics of FRP are dependent on the initiation mechanism, since the dissociation of the initiator proceeds much slower than the reaction of the initiator radical with a monomer unit and is therefore the rate determining step in FRP. Here, the thermal and photoinduced initiation is taken into account with the measureable decrease of the initiator concentration during its decomposition. The change of the initiator concentration over time proceeds according to first order kinetics and is described in Eq.(1) with k_d being the initiator dissociation coefficient.

$$-\frac{d[I]}{dt} = k_d[I] \quad \text{Eq. (1)}$$

It has to be noted that depending on the molecular constitution of the initiator and the molecular surroundings not every generated radical initiates the polymerization, which leads to a decreased initiator efficiency, f , with typical values between 0.5 and 0.8.¹⁷ As the initiation is a two step mechanism, the reaction of the monomer with the initiating radical is described in Eq.(2) with the initiator efficiency f .

$$\frac{d[R_1\bullet]}{dt} = 2 f k_d [I] \quad \text{Eq. (2)}$$

In Eq.(2), a factor of two is involved due to the dissociation of the initiator into two radical species. As next step, the propagation reaction can be described with Eq.(3).

$$-\frac{d[M]}{dt} = \sum_i k_p^i [R_i\bullet][M] \quad \text{Eq. (3)}$$

Here, the monomer conversion is depicted, revealing that the monomer conversion is the sum of the (in theory chain length dependent) propagation rate coefficients k_p multiplied by the macro-radicals $R_i\bullet$ and monomer M concentration. The index i implies the change of the propagation rate over time due to different monomer propagation rates during polymerization, which potentially makes k_p to a chain-length dependent coefficient.¹⁷ Fast propagation rates are observed for e.g. acrylate based monomers with $10^4 \text{ L mol}^{-1} \text{ s}^{-1}$ and slow polymerization rates for monomers such as styrene or methyl methacrylate with $10^2 \text{ L mol}^{-1} \text{ s}^{-1}$.^{19,20}

As described above, termination reactions lead to – in principle – undesired side products, affecting the end-group fidelity in FRP and molecular weight distribution negatively. Termination reactions can occur when two propagating species are reacting with each other for example *via* a recombination or disproportionation pathway. In a recombination reaction, a macromolecule, unable to grow further, is formed by the reaction of two propagating chains. The disproportionation reaction involves a H-abstraction at one propagating chain end leading to a macromolecular monomer, containing a double bond as end group and a macromolecule that is unable to grow further.

Such a macro-monomer is – in principle – able to participate in the polymerization when it is reactivated again with an initiator, resulting in branched polymers, however, the bulky nature of these macromonomers prevents their large scale incorporation.²¹ The termination reactions are also dependent on the monomer constitution. For instance, the recombination pathway is preferred for monomers that are not sterically hindered as is the case for polystyrene based polymers.²² The kinetics of the termination are second order, since always two propagating chains participate in a termination event and can be described with Eq. (4).

$$-\frac{d[R_n\bullet]}{dt} = 2 k_t [R_n\bullet]^2 \quad \text{Eq. (4)}$$

The second reaction leading to chain stoppage is the chain transfer reaction. Chain transfer reactions (Scheme 2.1.1) lead to termination of the growing polymer chains by reaction with transfer agents (T). Radical transfer can occur to solvent molecules or in general to any impurity present in the polymerization or added transfer agents. The kinetics of the chain transfer reaction can be expressed with Eq. (5).

$$-\frac{d[T]}{dt} = k_{ct} [R_1\bullet][T] \quad \text{Eq. (5)}$$

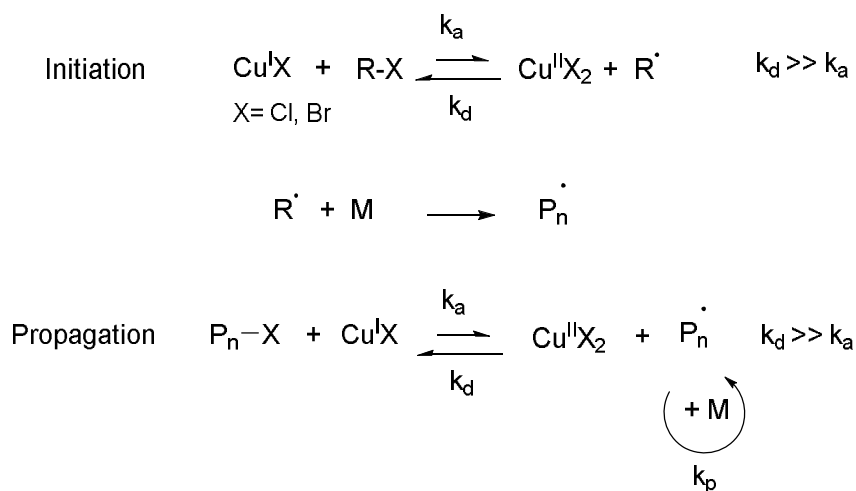
If a propagating chain is transferred to the transfer agent, reinitiation with monomer units can take place – depending on the reactivity of the generated radical – reducing the overall molecular weight resulting from the polymerization.²³

In summary, conventional FRP entails advantages and drawbacks, which have to be considered when choosing a polymerization technique employing free radicals. The radical concentration during a FRP plays a major role, since the kinetics of the termination reaction is second order and diffusion controlled, leading to a possible isothermal self-accelerating phenomenon termed the Norrish-Trommsdorff effect.²⁴ One approach to decrease termination reactions in a polymerization is to decrease the radical concentration by the addition of controlling agents to the polymerization.

In comparison to conventional FRP, RDRPs offer many advantages such as low polydispersities, high end group fidelity, exact tuning of polymer constitution and control of the molecular weight. Therefore, RDRPs are well established, due to the easy accessibility of tunable soft matter materials leading to well-defined structures and controlled polymer architectures.²⁵ RDRP techniques such as ATRP,²⁶ NMP²⁷ and RAFT²⁸ have been invented in the 90's. In the following, the RDRP techniques for controlling radicals using either persistent radical effects²⁶ or reversible transfer agents are described.

2.1.2 Atom Transfer Radical Polymerization (ATRP)

ATRP was first described by Matyjaszewski²⁹ and Sawamoto³⁰ in 1995, in which the controlling properties are achieved by the usage of a reversible redox process, employing a transition metal catalyst. In Scheme 2.1.2, the ATRP mechanism is illustrated, using a copper-based controlling agent, which is commonly used for catalyzing ATRP. To increase the solubility of the transition metal complex, an efficient ligand, for example 2,2-bipyridine (bipy), is added which is coordinating to the metal complex.



Scheme 2.1.2: ATRP mechanism illustrated exemplarily using a copper(I) halide ($\text{Cu}^{\text{I}}\text{X}$). The initiation involves the oxidation of the copper complex, where a radical is generated, initiating the polymerization (R^{\cdot}). The propagation of the polymer involves a similar equilibrium, employing the metal transition complex. The controlled consecutive feed of monomer to achieve linear polymer growth is achieved due to the different rate coefficients ($k_{\text{d}} \gg k_{\text{a}}$).

In the initiation step of ATRP, the transition metal complex abstracts a halide from the organic halide initiator (R-X), causing an oxidation of the metal complex ($\text{Cu}^{\text{II}}\text{X}_2$). The abstraction of the halide generates a radical (R^{\cdot}), which initiates the polymerization in the next step. The rate coefficients of the redox reaction in the initiation equilibrium are the key feature of the polymerization method.²⁹ The reaction rate coefficient (k_{d}) of the deactivation in the initiating step has to be significantly higher than the activation coefficient (k_{a}), as otherwise the radical concentration is too high and termination reactions will proceed during polymerization.

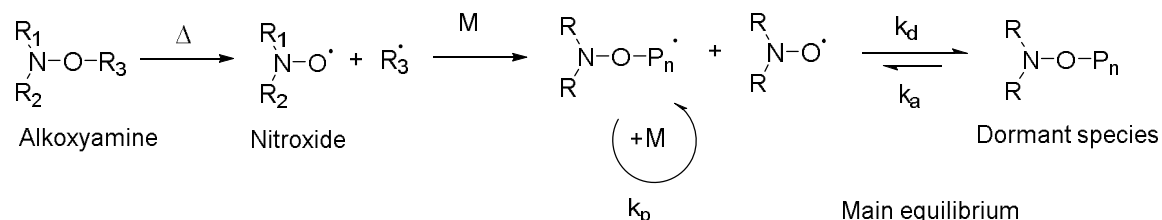
The propagation of the polymerization is controlled by similar equilibrium conditions as mentioned before ($k_d \gg k_a$), effectively reducing the active radical concentration and effecting linear macromolecular growth. Here, the redox activation-deactivation equilibrium is established between a propagating chain ($P_n\cdot$) and the transition metal complex in its oxidized state ($Cu^{II}X_2$) and a dormant chain (P_n-X) as well as the transition metal complex in its initial state (Cu^IX). The halide is continuously transferred between the polymer chain and the transition metal complex during the polymerization. The key feature of controlling the radical concentration in ATRP lies in the equilibrium, where the dormant species (P_n-X) is much more preferred than the active species ($P_n\cdot$). The control of the radical concentration in ATRP leads to narrow MWDs and reduced termination reactions. The termination reactions are strongly reduced due to the quadratic dependency of the radical concentration (Eq. 4), which is kept low based on the redox properties of the metal transition complex.²⁹ However, the reaction rate of the propagation is reduced at the same time, since the polymerization rate is dependent on the radical concentration as well, as described in Eq.(3).

In summary, the ATRP polymerization technique represents a versatile controlled radical polymerization method, allowing access to narrow MWDs with limited side reactions. Besides the advantages of employing ATRP, one drawback is noteworthy. One of the main disadvantages of ATRP is the removal of the transition metal catalyst after polymerization for subsequent polymer processing. Regarding this issue, one excellent method to remove the residual metal transition complex is *via* an electrochemical approach.³¹ To circumvent the usage of a metal transition complex in the polymerization, an alternative RDRP polymerization technique is introduced below, employing nitroxides as controlling agents.

2.1.3 Nitroxide Mediated Polymerization (NMP)

NMP is a commonly employed RDRP technique, utilizing alkoxyamines as controlling agents. Alkoxyamines feature a labile C-O bond, which form upon thermolysis at elevated temperatures a nitroxide radical ($N-O\cdot$) and an initiating radical ($R\cdot$) (Scheme 2.1.3). The generated nitroxide radical is able to trap carbon-centered free radicals during the polymerization.³²

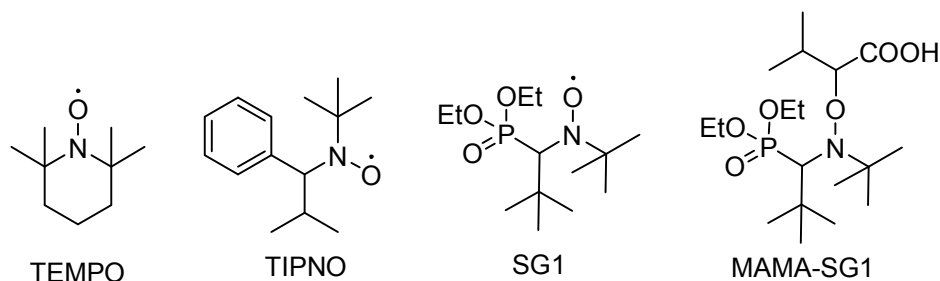
In particular, the control of the polymerization is achieved by the reversible trapping of the propagation chains with the generated nitroxide radicals in the main equilibrium. Analogue to ATRP, the main equilibrium is controlled based on different activation (k_a) and deactivation (k_d) rate coefficients. To afford a low radical concentration, k_d must be several magnitudes larger than k_a .



Scheme 2.1.3: Schematic overview of the NMP induced polymerization employing alkoxyamines at elevated temperatures producing nitroxide radicals ($N-O\cdot$), enabling the formation of dormant species during polymerization. A controlled addition of monomers to the propagating chain is feasible due to the fact that the equilibrium lies on the dormant side ($k_d \gg k_a$).

Maintaining a low radical concentration during polymerization causes a reduction of recombination and disproportionation events, thus imparting living characteristic onto the polymerization process.³³

In early attempts for controlling the radical polymerizations with nitroxides, two component systems dominated. Typically, common initiators such AIBN and BPO were employed as radical sources together with *i.e.* the stable nitroxide 2,2,6,6-tetramethyl-1-piperidinyloxy (TEMPO) species (Scheme 2.1.4). However, the two component initiating system is more challenging due to the complicated adjustment of the initiator to nitroxide ratio leading to non-ideal polymerization kinetics.³⁴



Scheme 2.1.4: Nitroxide species for the NMP polymerization with 2,2,6,6-tetramethyl-1-piperidinyloxy (TEMPO), 2,2,5-trimethyl-4-phenyl-3-azahexane-N-oxyl (TIPNO) and 4-(diethoxyphosphinyl)-2,2,5,5-tetramethyl-3-azahexane-N-oxyl (SG1). A second generation alkoxyamine is illustrated on the example of MAMA-SG1.

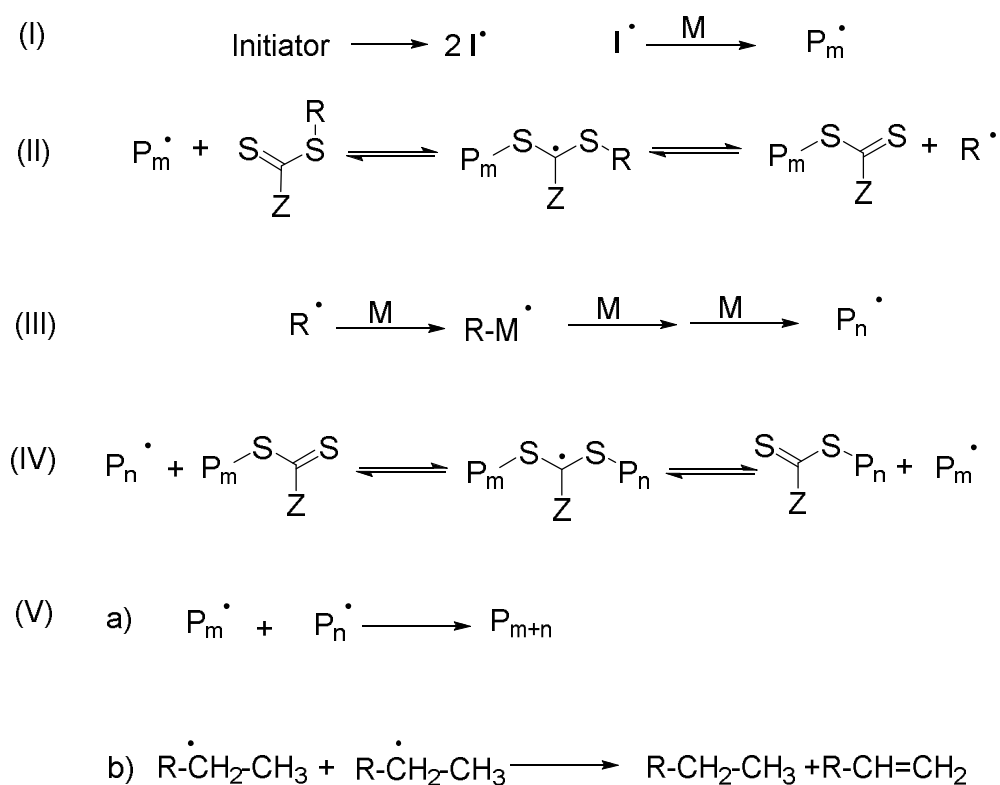
The nitroxide TEMPO was mainly used for the polymerization of styrene derivatives, due to lower equilibrium constants, which were suitable for the synthesis of polystyrenes.¹⁷ It has to be noted that the high temperatures usually employed for NMP (approx. 125°C), which are necessary to cleave the C-O bond, are one of the drawbacks employing NMP. A solution was found for reducing the high temperatures typically required, when the sterically hindered 2,2,5-trimethyl-4-phenyl-3-azahexane-*N*-oxyl (TIPNO) and 4-(diethoxyphosphinyl)-2,2,5,5-tetra-methyl-3-azahexane-*N*-oxyl (SG1) species were synthesized. Their bulky groups increase the labile character of the C-O bond in the alkoxyamines, allowing to cleave the C-O bond at lower temperatures.¹⁷ With the development of the second generation nitroxides (TIPNO and SG1), the one component system for NMP polymerization employing alkoxyamines was introduced. The MAMA-SG1 (BlocBuilder®) alkoxyamine combines the advantages of being a one component system, while featuring a more labile C-O bond, which allows for to polymerize *i.e.* methyl methacrylate.³⁴

In summary, the NMP polymerization technique provides access to well-defined polymers employing nitroxides or alkoxyamines as controlling agents. The main advantage of NMP in contrast to ATRP lies in the absence of a metal transition catalyst. However, it has to be noted that many nitroxides and alkoxyamines are not commercially available representing a drawback using NMP.

2.1.4 Reversible Addition-Fragmentation Chain Transfer (RAFT) Polymerization

RAFT was introduced in 1988³⁵ by the Commonwealth Scientific and Industrial Research Organization (CSIRO) in Melbourne, Australia. Almost simultaneously, Zard and colleagues submitted a patent investigating Macromolecular Design *via* the Interchange of Xanthates (MADIX).³⁶ Identical mechanisms have been reported, employing different chain transfer agents (CTAs). Therefore, a shared discovery of the polymerization method describes the situation best. Since RAFT polymerization was reported in literature for the first time, it has become a widely employed polymerization method to synthesize polymers in a controlled fashion, avoiding heavy metal catalysts and high temperatures.

In addition, the RAFT polymerization offers many advantages such as variety in monomers, high end-group fidelity and simple preparation of polymers. The accepted mechanism is illustrated in Scheme 2.1.5.²⁸ RAFT polymerization is typically initiated using conventional radical initiators such as AIBN or BPO. Control over the polymerization is achieved by the addition of CTAs, bearing a leaving group (R) and a stabilizing group (Z), which enables to control the radical polymerization. After the initiation step (I), a pre-equilibrium (II) is established between the propagating chain (P_m^\bullet) and the employed CTA. The leaving group (R^\bullet) in step III is able to reinitiate the monomers and create, after the addition of monomer, a new propagating radical (P_n^\bullet).



Scheme 2.1.5 RAFT mechanism showing the important pre-equilibrium (II) and main equilibrium (IV) employing a chain transfer agent carrying a leaving group (R) and a stabilizing group (Z). Termination reactions (V) with the active polymer chains are illustrated with the recombination (a) and disproportionation (b). Adapted from reference [28].²⁸

The main equilibrium (IV) is reached when all polymer chains carry a controlling terminus generating macro-CTAs.³⁷ In the main equilibrium (IV), a propagating polymer chain is coupled to a macro-CTA resulting in a radical intermediate state.

Subsequently, a polymer chain is cleaved off from the macro-CTA that propagates further.

In the main-equilibrium, an equal growth probability is ensured for all polymer chains leading to polymers with a narrow MWD. However, the stabilizing effect of the CTA can lead to radicals being trapped in the intermediate state resulting in a loss of control. Termination (V) of the polymerization can occur *via* recombination or disproportionation as previously described for conventional FRP (Section 2.1.1).

A suitable CTA has to be selected for the respective RAFT polymerization (Figure 2.1.1).³⁸ The CTA of the RAFT polymerization should be carefully chosen with respect to electronic factors and steric considerations of the monomer being polymerized.³⁹ Therefore, the in the pre-equilibrium generated radical from the leaving group R^\cdot needs to be sufficiently reactive for reinitiating a polymerization.⁴⁰ The stabilizing group Z of a CTA is dependent as well on the aforementioned factors and should stabilize the radical intermediate state of the macro-CTA, yet also ensure an adequate reactivity for the addition of the next incoming radical.⁴¹

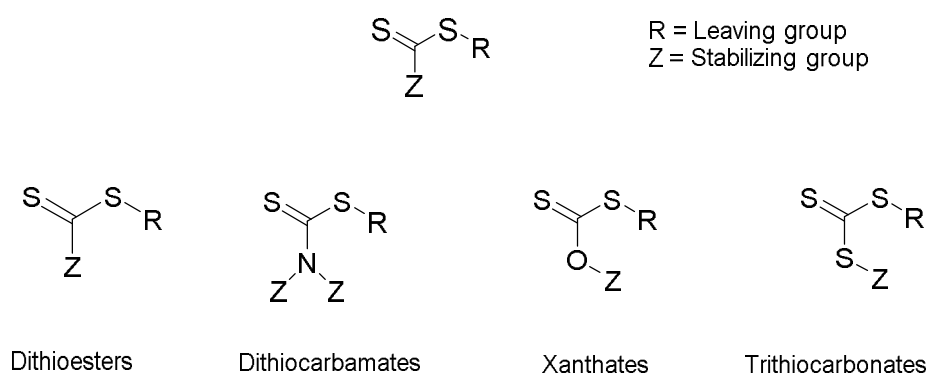


Figure 2.1.1: Chemical structure of different CTAs including R-and Z-group as leaving and stabilizing groups.

Employing the appropriate CTA, a wide range of monomers can be polymerized employing RAFT polymerization.⁴² Examples for the corresponding R groups are illustrated in Figure 2.1.2. Here, the different leaving groups in order of their leaving ability are illustrated. Furthermore, the suitable monomers are depicted below. The continuous line represents a good control during polymerization, whereas the dashed line represents partial control. As aforementioned, the

selection of a suitable RAFT agent plays a major role for the polymerization of various monomers.

The ideal R-group in the RAFT agent entails a good homolytic leaving group, which can also efficiently reinitiate the polymerization after cleavage. The stability of the generated radical plays therefore a major role.

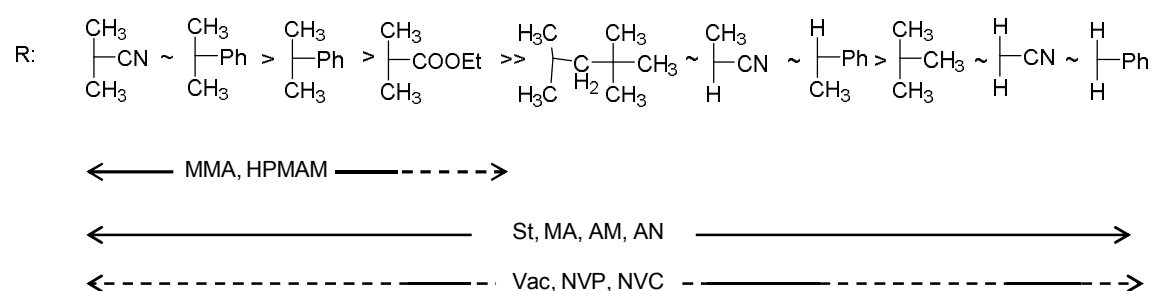


Figure 2.1.2: Schematic overview of a selection of different R-groups in a RAFT agent (ZC=S)SR for the polymerization of various monomers. methyl methacrylate, (MMA), N-(2hydroxypropyl)methacrylamide, vinyl acetate (Vac), N-vinylpyrrolidone (NVP), styrene (St), methyl acrylate (MA), acrylamide (AM) and acrylonitrile (AN). The figure was adapted from reference [39]. Copyright (2012) American Chemical Society (ACS).³⁹

The Z-group of a RAFT agent plays as major role in stabilizing the growing polymer chain during polymerization. The propagation rate coefficient can be adjusted by choosing the suitable Z-group up to five orders of magnitude.³⁹ One of the most reactive RAFT agents are dithioesters or trithiocarbonates, which were compared to RAFT agents entailing a nitrogen or oxygen moiety adjacent to the thiocarbonyl group, more efficient for the radical addition.³⁹ The reduced activity of thiocarbonyl groups containing nitrogen or oxygen moieties is based on the lone pair, which is able to form mesomeric structures. Here, a selection of Z-groups is illustrated (Figure 2.1.3), showing increased fragmentation rates from left to right. As aforementioned the continuous line represent a good control during polymerization whereas the dashed line represents partial control.

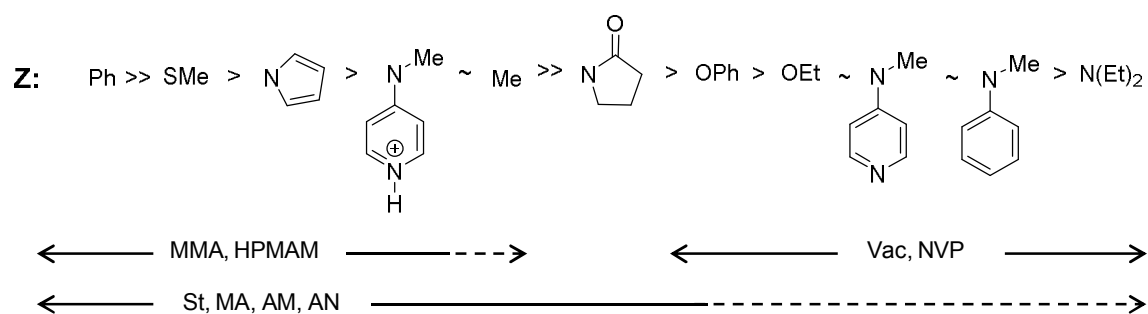


Figure 2.1.3: Schematic overview of a selection of different Z-groups in a RAFT agent (ZC=S)SR for the polymerization of numerous monomers with methyl methacrylate, (MMA), N-(2hydroxypropyl)methacrylamide (HPMAM), vinyl acetate (Vac), N-vinylpyrrolidone (NVP), styrene (St), methyl acrylate (MA), acrylamide (AM) and acrylonitrile (AN). The figure was adapted from reference [39]. Copyright (2012) American Chemical Society (ACS).³⁹

An advantage of the RAFT polymerization is the generation of endfunctionalized polymers *in situ* carrying a carboxylic acid,⁴³ hydroxy,⁴³ alkyne or azide group,⁴⁴ respectively, which are introduced *via* an endgroup variation of the CTA. The high tolerance of functional groups exploiting the RAFT methods allows for to polymerize a variety of monomers such as styrene, acrylate, acrylamides, methacrylates and methacrylamides and vinyl acetate among others.^{45,36} Furthermore, several macromolecular architectures applying the RAFT polymerization are feasible such as star, block and comb-like structures, brush polymer, palm tree, H-shaped B2AB2, dumbbell, ring diblock and coil-cycle-coil.^{42,46}

In summary, the RDRP polymerization techniques give the opportunity to polymerize monomers in a controlled fashion with the ease of the conventional FRP. The polymerization technique of choice is dependent on the application of the synthesized polymer. For example, ATRP may not be suitable for macromolecules, which are to be used in biological environments, due to the (toxic) metal transition catalyst.⁴⁷ In this thesis RAFT was mainly employed as polymerization technique due its high tolerance towards functional groups and high end-group fidelity.

2.2 Photochemistry

Photochemical reactions are essential in many natural as well as synthetic processes. For example, light is necessary for the formation of vitamin D, involving a photochemical ring opening reaction⁴⁸ or for visual perception, which relies on a *cis-trans* isomerization of organic molecules in the human retina.⁴⁹ Moreover, the energy of light is employed in the photosynthesis process in plants, where the energy of light is converted into chemical energy, leading to the synthesis of glucose molecules.⁵⁰ In addition, photochemistry allows for molecular excited states, thus being able to undergo chemical reactions that are otherwise forbidden, opening new avenues in organic synthesis. Furthermore, light triggered reactions possess many advantages, including spatiotemporal control.⁵¹

In the first part of the following section, the principles of photochemistry, including a detailed description of absorption, fluorescence and phosphorescence processes, will be presented (Section 2.2.1). The second part addresses the most recent light-induced reactions relevant for the current thesis and their usage in polymer chemistry, highlighted with selected examples (Section 2.2.2).

2.2.1 Principles of Photochemistry

Absorption: The absorption of light can be described with the uptake of energy in form of photons leading to excited states of a molecule, capable to trigger chemical reactions. In this context, several energy transfer transitions can be described.

The light absorption of a molecule was described by Pierre Bouguer and Johann Heinrich Lambert and August Beer and is known as the Beer Lambert's law.⁵²⁻⁵⁴

The law can be expressed with

$$A = \epsilon_{\lambda} c d \quad \text{Eq. (6)}$$

where A is the absorbance, ϵ_{λ} is the molar extinction coefficient dependent on the wavelength, d is the path length and c is the concentration of the absorbing species.

Beer-Lambert's law states that the dimensionless absorbance of a certain molecule is dependent on its molar extinction coefficient ϵ_λ in $\text{L mol}^{-1} \text{cm}^{-1}$, its concentration (c in mol L^{-1}) and the path length (d in cm) of the medium. The validity of this law is limited to highly diluted solutions ($c \leq 10^{-2} \text{ mol L}^{-1}$) and to the application of monochromatic light.⁵³ The derivation of this law is based on the differential reduction of the radiation intensity by passing medium with a molecule, which absorbs light and is defined as follows:

$$-dI(x) = I(x) \epsilon' c dx \quad \text{Eq.(7)}$$

where dI is the differential reduction of the radiation intensity, $I(x)$ the radiation intensity, ϵ' the molar extinction coefficient, c the molar concentration and dx differential path length. After integration of Eq.(7) and insertion of the linear dependency of the decadic logarithm with the natural logarithm, the equation can be written as follows:

$$\log \left(\frac{I_0}{I_1} \right) = \epsilon c d \quad \text{Eq.(8)}$$

known as the Beer-Lambert's law.⁵³ Quantum mechanics state that transitions with a low ϵ (< 10) are mostly forbidden, whereas transitions with a high ϵ are allowed.⁵³ There are several pathways for a molecule after the absorption of light, which can be illustrated in a Jablonski diagram (Figure 2.2.1). The diagram depicts an overview of the different electronic states of a molecule, which can be achieved after the absorption of light.

A molecule at ambient temperature is usually located in its energetic and vibrational ground state S_0 , where the photochemical reaction starts with the absorption of light. Thus, the molecule absorbs light in form of energy, exciting the molecule to certain excited singlet states S_n , where one electron from the highest occupied molecule orbital (HOMO) is transferred to the lowest unoccupied molecule orbital (LUMO). After the excitation of the molecule, several relaxation pathways can lead to relaxation to its ground state S_0 , either *via* a radiative (fluorescence) or a non-radiative (vibrational) relaxation process. If an excited state is reached, as illustrated for S_2 internal conversion (IC) can occur, leading to S_1 .

Furthermore, inter system crossing (ISC) from S_1 to a vibrational state of T_1 , where a spin inversion of the electron takes place, can also occur. After relaxation to the vibrational ground state of T_1 , another relaxation process can proceed, named as phosphorescence, ending up in the ground state S_0 (Kasha's rule).⁵⁵

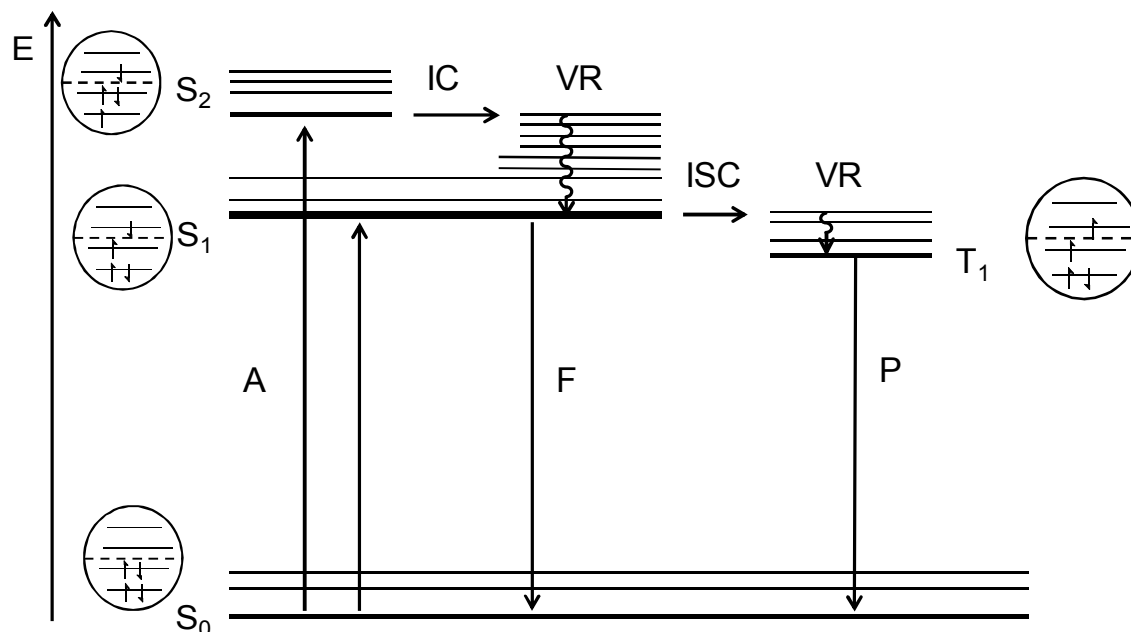


Figure 2.2.1: Schematic illustration of the Jablonski diagram. The absorption is denoted with **A** starting from the ground state S_0 to the first excited state S_1 . From here, radiative (Fluorescence (**F**) and Phosphorescence (**P**) after inter system crossing (**ISC**) and non-radiative (vibrational relaxation **VR**) processes can take place.

The rules for the different transition states of a molecule, which are quantum mechanically "allowed" or "forbidden" will be explained in the following. Two rules are considered: the spin selection and the symmetry selection rule.⁵³ The spin selection rule describes that transition states with the same spin multiplicity are allowed, implying that the multiplicity of the spins are maintained. The symmetry rule describes that only transitions between states with a change in parity are allowed (Laporte).⁵⁶ Here, the quantum numbers n , m , l and s have to differ in at least one number from each other. Both rules do not strictly apply, for instance, a transition of the singlet state S_1 via an ISC to the triplet state T_1 is in principle – with regard to the spin selection rule – a forbidden transition. However, due to several factors such as the heavy atom effect or the presence of photosensitizers, the transition becomes possible.⁵⁷

In the following the rules will be explained in detail with the possible relaxation processes of an excited molecule.

Fluorescence: The absorption of light leads to an excited state from $S_0 \rightarrow S_1$, where an electron will be promoted from the HOMO molecular orbital to the LUMO orbital without any spin inversion process and is therefore allowed. The subsequent radiative relaxation proceeds afterwards from $S_1 \rightarrow S_0$, which is a rather fast process (10^{-12} to 10^{-9} s) compared to phosphorescence.⁵⁸

Phosphorescence: Phosphorescence overall is a spin-forbidden process regarding the spin selection rule. Before the phosphorescence takes place from the triplet T_1 , a spin inversion – *i.e.* ISC – from $S_1 \rightarrow T_1$ takes place. The phosphorescence itself starts from a spin-forbidden triplet state T_1 , leading to the ground state S_0 . The longer lifetime (10^{-6} to 10^{-3} s) of the phosphorescence is based on the spin-forbidden relaxation process from the triplet to the singlet state.⁵⁸

IC and ISC: The non-radiative transitions including internal conversion as well as the intersystem crossing underlie the same selection rules as the radiative transitions. Energy transfers from higher to lower energy singlet states *i.e.* $S_n \rightarrow S_{n-1}$, where no spin inversion takes place, are allowed based on the compliance of the symmetry and selection rule. In contrast, the ISC transitions, where a spin inversion is involved are photochemically forbidden.⁵⁸

2.2.1.1 Electronic Transitions

A classification of some transitions involving the molecular orbitals are depicted in Figure 2.2.2. The symbols without the asterisk represent the bonding molecular orbitals (σ , π) and the ones with the asterisk represent the antibonding molecular orbitals (σ^* , π^*) (Figure 2.2.2). Furthermore, a non-bonding molecule orbital is illustrated and is highlighted with 'n'. Depending on the molecular constitution, different energy barriers can be reached, which will be explained in the following.

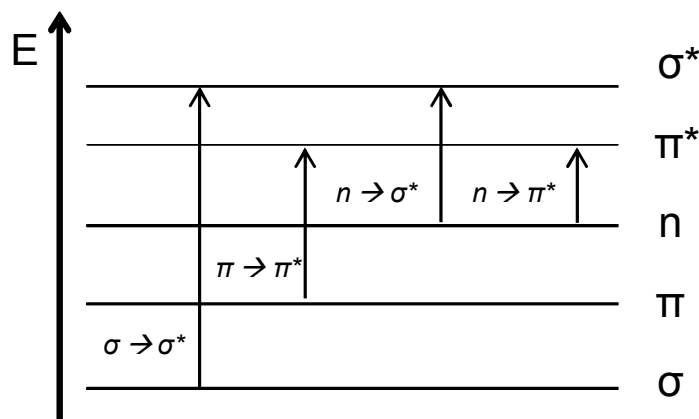


Figure 2.2.2: Molecular orbitals with the different transitions $\sigma \rightarrow \sigma^*$, $\pi \rightarrow \pi^*$, $n \rightarrow \sigma^*$ and $n \rightarrow \pi^*$, indicating the smallest energy barrier for the $n \rightarrow \pi^*$ transition.

The $\sigma \rightarrow \sigma^*$ transitions often display saturated hydrocarbons and require high energies ($\lambda < 200$ nm) to reach the excited states. A high molar decadic extinction coefficient is often observed ($\epsilon = \text{approx. } 10^5 \text{ L mol}^{-1} \text{ cm}^{-1}$) for these transitions.⁵³

The second transitions, illustrated in Figure 2.2.2, are $\pi \rightarrow \pi^*$ transitions representing mostly aromatic molecules or conjugated π -systems, where π -orbitals are involved. The excited states are accessible employing slightly lower energy as for the $\sigma \rightarrow \sigma^*$ transitions ($\lambda > 200$ nm). Here, the transition occurs with relatively high molar extinction coefficients ($\epsilon = 10^3\text{-}10^5 \text{ L mol}^{-1} \text{ cm}^{-1}$).⁵³

The $n \rightarrow \sigma^*$ transitions are often observed in saturated molecules including heteroatoms with free electron pairs. The wavelength necessary to trigger these transitions are often less than 250 nm. The molar extinction coefficient is slightly higher compared to the $n \rightarrow \pi^*$ transitions with $10^3\text{-}10^1 \text{ L mol}^{-1} \text{ cm}^{-1}$ and these transitions are therefore partially allowed.⁵³

The weak $n \rightarrow \pi^*$ transition counts as a forbidden transition, entailing rather low ϵ values ($10^1 \text{ L mol}^{-1} \text{ cm}^{-1}$).⁵³ A transition of $n \rightarrow \pi^*$ is only observed when free electron pairs are available. The energy barrier from $n \rightarrow \pi^*$ is the lowest of all transitions and can therefore be reached with light of higher wavelengths (>280 nm). Furthermore, the absorption band is highly influenced by the polarity of the utilized solvent.

2.2.1.2 Franck-Condon Principle

The probability of the transitions can be explained with the Frank-Condon principle, which is the link between spectroscopy and quantum mechanics. The principle states that an electronic transition is more likely when the vibrational wave functions show the highest overlap.⁵⁸ Furthermore, it states that the motion of the electrons is much faster (up to 10^2 - 10^3 times) than the motion of the nuclei, which are almost left unchanged.⁵³ An exemplary illustration of the Franck-Condon principle is given in Figure 2.2.3 for $n \rightarrow \pi^*$ transitions. The squared wave functions are illustrated by the wavy black lines, whose integrals represent the electron probability density. The wave functions of the different vibrational states are highlighted with v_n for the variable vibrational ground states and v'_n for the vibrational excited states. The absorption from the vibrational ground state S_0 ($v=0$) is depicted with an arrow. As already noted a transition to an excited state occurs most probably when the excited vibrational wave function overlap significantly. Here, a transition to the excited singlet vibrational ground state is shown, which is typical for $n \rightarrow \pi^*$ transitions. The most probable electronic transition shows the highest intensity in the absorption spectrum, which is demonstrated in Figure 2.2.3. Other transitions from the excited S_1 state are less likely and show smaller absorption intensity.

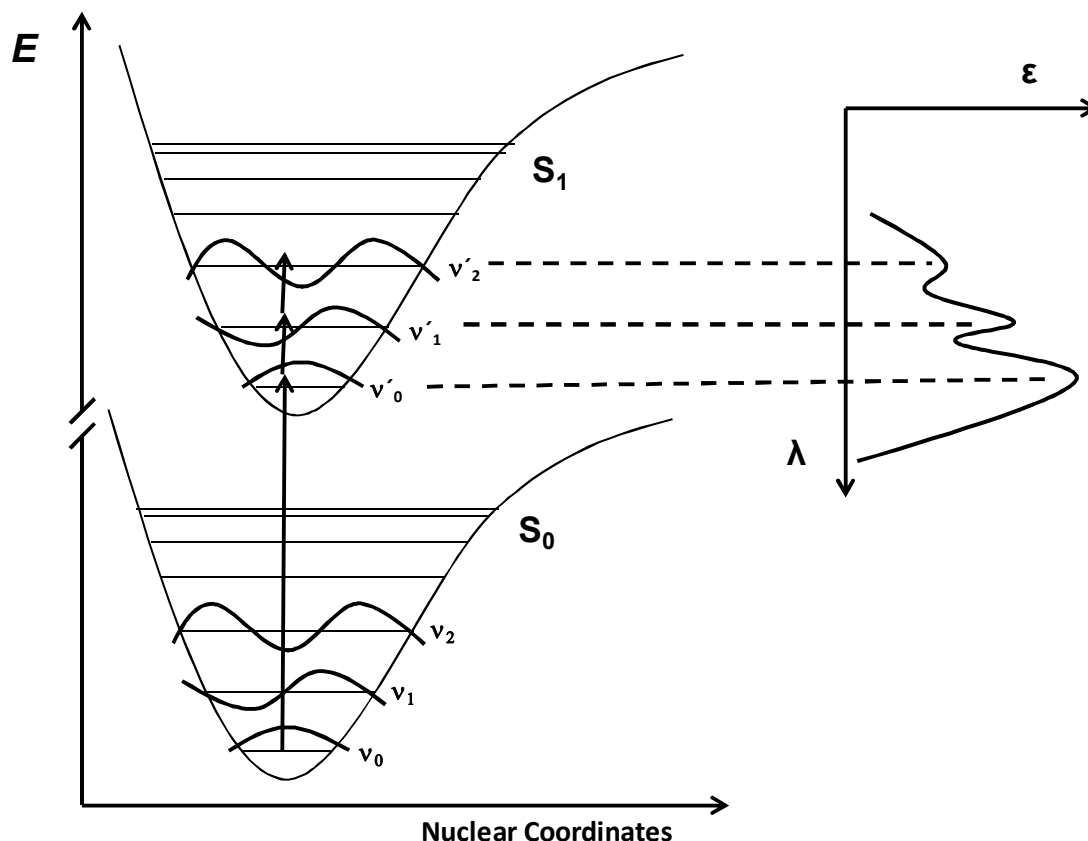


Figure 2.2.3: Schematic representation of the Franck-Condon principle. The most probable electronic transition takes place if the vibrational wave functions overlap significantly, shown here from the vibrational ground state S_0 to the excited singlet state ($S_1, v=0$).

2.2.2 Light-induced Reactions in Polymer Chemistry

In recent years, light induced reactions have been utilized not only for small molecule synthesis, but also for polymer synthesis. Among the strategies employing light induced processes, photoinitiated free-radical or cationic polymerizations have been extensively studied and exploited in several applications.^{51,59} However, in this part of the current thesis, specific attention will be paid to the most recent light induced reactions and their use in polymer formation and functionalization as well as in crosslinking reactions for the formation of defined macromolecular architectures, including single chain polymer nanoparticles (SCNPs). In particular, thiol-based reactions, photodimerizations as well as light induced Diels-Alder and 1,3-dipolar cycloadditions are discussed in detail.

2.2.2.1 Thiol-based Photoreactions

Thiol-ene Reaction

The reaction between thiols and enes was first reported by Posner in 1905.⁶⁰ Since then, radical thiol-ene reactions have been widely investigated and successfully applied in polymer science.^{61,62}

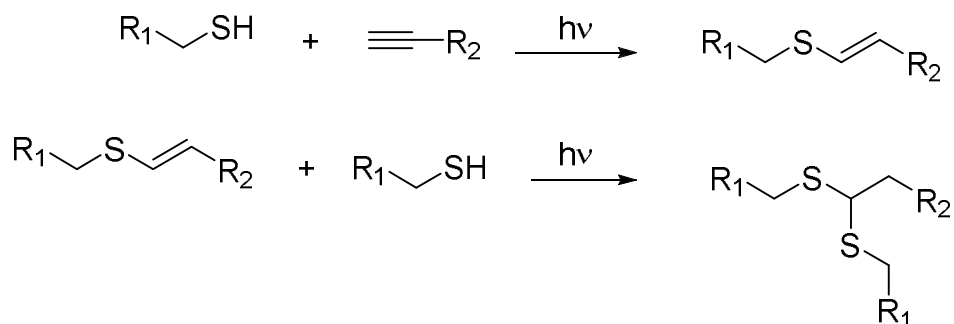
Briefly, radical thiol-ene reactions proceed *via* the generation of radicals upon irradiation with light, heat or radical initiators. Here, special attention is being paid to the photoinitiated pathway (Scheme 2.2.1). Initially, a thiyl radical is generated upon irradiation with light, which subsequently reacts with the alkene moiety. The formed radical can abstract a hydrogen from a thiol group, forming a thioether moiety and regenerating the thiyl radical.^{63–66}



Scheme 2.2.1: Light-induced thiol-ene reaction yielding the anti-Markovnikov product.

Thiol-yne Reaction

The reaction between a thiol and an alkyne is also a well-known light induced reaction (Scheme 2.2.2). The mechanism of thiol-yne reactions is analogue to the thiol-ene mechanism as described above, with the added advantage that each alkyne functional group is able to react consecutively with two thiol functional groups. Again, the formed thiyl radical after light irradiation reacts with the alkyne moiety forming a vinyl sulfide. A second photoinduced reaction – a thiol-ene reaction – can take place, forming a dithioether after the successful addition of the thiyl radical. In summary, two thiol moieties are capable to react with one alkyne molecule.



Scheme 2.2.2: Light-induced thiol-yne reaction generating initially an unsaturated vinyl thioether, which is capable of undergoing a thiol-ene reaction before forming a dithioether.

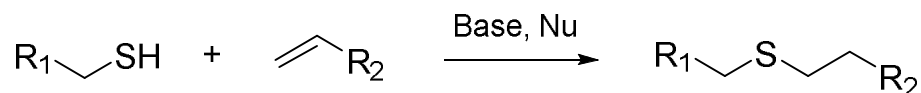
By employing difunctional monomers, thiol-ene/yne reactions can proceed *via* a radical-mediated step growth mechanism leading to polymers. In comparison to common radical induced polymerization methods, the thiol-ene induced polymerization entails advantages such as lower inhibition in the presence of oxygen,⁶⁷ the absence of photoinitiator molecules and high conversion rates.⁶⁸ When multifunctional monomers with an average functionality higher than two are used, cross-linked polymer networks are formed.⁶⁹

Furthermore, post-modifications of polymers utilizing thiol-ene/yne reactions are feasible. Especially poly(butadiene) based polymers were intensively modified with thiols comprising a variety of functional moieties such as amines,⁷⁰ amino acids,⁷¹ benzyl groups⁷⁰ and non-hydrophilic esters.⁷²

In addition, thiol ene/yne reactions have been successfully applied for surface modification,^{73,74} nano-imprinting,⁷⁵ microfluidic devices,^{76,77} functionalization of linear polymers and network formation.⁶⁹ The interested reader is referred to the main thiol-ene/yne based reviews, illustrating the broad field of applications for these reactions.^{65,78,69,79}

Thiol-Michael Reaction

In contrast to the radical-mediated thiol-ene/yne reactions, thiol-Michael addition is a base- or nucleophile-catalyzed reaction (Scheme 2.2.3).

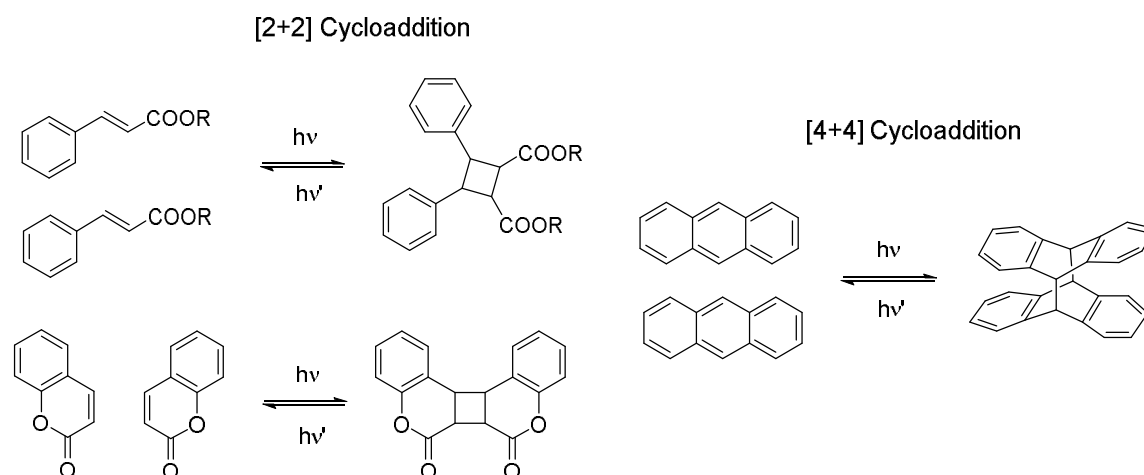


Scheme 2.2.3: Thiol-Michael addition reaction employing a base or a nucleophile to generate the thioether.

Therefore, the use of light to induce the reaction is in principle not possible. Nevertheless, the use of photo-caged bases or nucleophiles allows for the possibility of inducing thiol-Michael reactions with light. As an example, pioneering work of Bowman and coworkers demonstrated the capability of using photo-caged amines for photo-patterning in a spatially and temporally controlled fashion.⁸⁰

2.2.2.2 Photoinduced Cycloaddition Reactions/Photodimerization

Photodimerization reactions are another example of light induced reactions. The most widely employed photodimerization reactions are [2+2] cycloadditions of cinnamate and coumarin as well as [4+4] cycloaddition of anthracene.⁶⁹ Initially, the cycloaddition is induced by irradiation of light to form covalent C-C bonds. The cycloreversion is triggered by irradiation with a wavelength featuring higher levels of energy, usually deep UV, as used for the dimerization reaction. Thus, this approach allows both light induced formation and cleavage of covalent bonds. The reversible character of the photodimerization is very appealing, enabling a multitude of new applications, which will be discussed below.



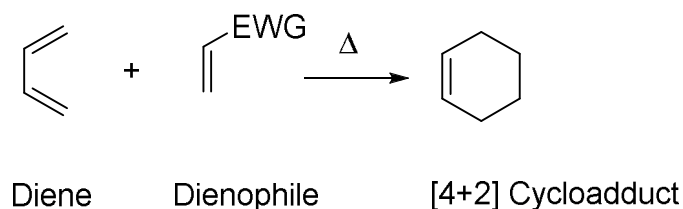
Scheme 2.2.4: Examples of photodimerization reactions commonly employed in polymer chemistry. Cinnamate and coumarin compounds undergo reversible [2+2] cycloaddition upon irradiation with UV-light, whereas anthracenes undergo upon irradiation with light [4+4] cycloadditions.

Cinnamates undergo photodimerization by irradiation with a wavelength of ~ 280 nm, whereas the cycloreversion can be introduced with a wavelength at 254 nm.⁸¹ The wavelength for inducing the coumarin photodimerization reaction is slightly higher with >310 nm. However, the photocleavage reaction requires harsh conditions (deep UV) *i.e.* wavelength of ~ 250 nm.⁸² One of the disadvantages of using these low wavelengths (high energy) is the possibility of cleaving other C-C bonds of the system, leading to irreversible degradation. In contrast, anthracene can be dimerized and cleaved using higher wavelengths, *i.e.* ~ 350 nm and 300 nm, respectively, making this system more promising for real life applications.

In the last years, all these systems have been successfully incorporated into polymeric systems, allowing the preparation of reversible networks,^{83,84} reversible surface patterning,^{85,86} nanoparticle formation,⁸² and hyperbranching of polymers.⁸² For example, the dimerization of anthracenes was employed for reversible surface patterning. In a first step, the anthracenes were successfully coated onto silicon wafers and subsequently dimerized with a wavelength in the visible light regime (410 nm) utilizing a second anthracene moiety. Afterwards a cycloreversion of the anthracene dimers was performed employing light with a wavelength of 360 nm.⁸⁵

2.2.2.3 Photoinduced Diels-Alder Reactions

In 1950, Otto Paul Hermann Diels and Kurt Alder were awarded with the Nobel Prize in Chemistry "for their discovery and development of the diene synthesis".⁸⁷ Diels-Alder (DA) reactions describe a [4+2] cycloaddition reaction between a conjugated diene and an alkene, commonly termed as dienophile, at elevated temperatures (Scheme 2.2.5).



Scheme 2.2.5: Diels-Alder reaction of a diene and an activated dienophile undergoing upon treatment with heat a [4+2] cycloaddition.

Some of the DA reactions can be considered as 'click' reactions, since they fulfill the criteria of efficiency, versatility and selectivity as stated by Sharpless.⁸⁸ Diels-Alder reactions can be reversible under certain conditions and the reverse reaction is called retro-Diels-Alder (rDA) reaction. In addition, in the presence of heteroatoms the reaction is termed hetero Diels-Alder reaction (HDA).

For simplicity, the classical thermally induced DA reaction is mechanistically explained using butadiene and ethylene as an example (Figure 2.2.4). The HOMO of the diene interacts with the LUMO of the dienophile, creating a new σ -bond.

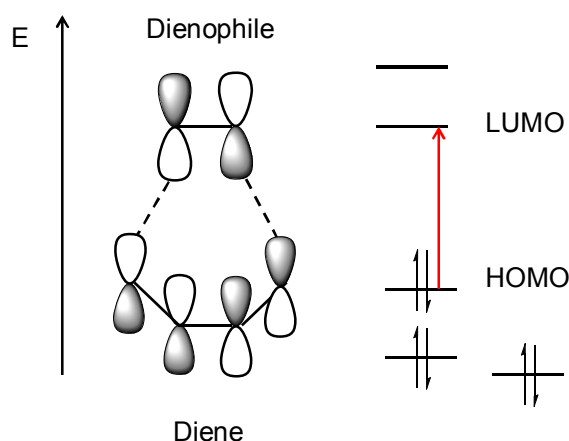


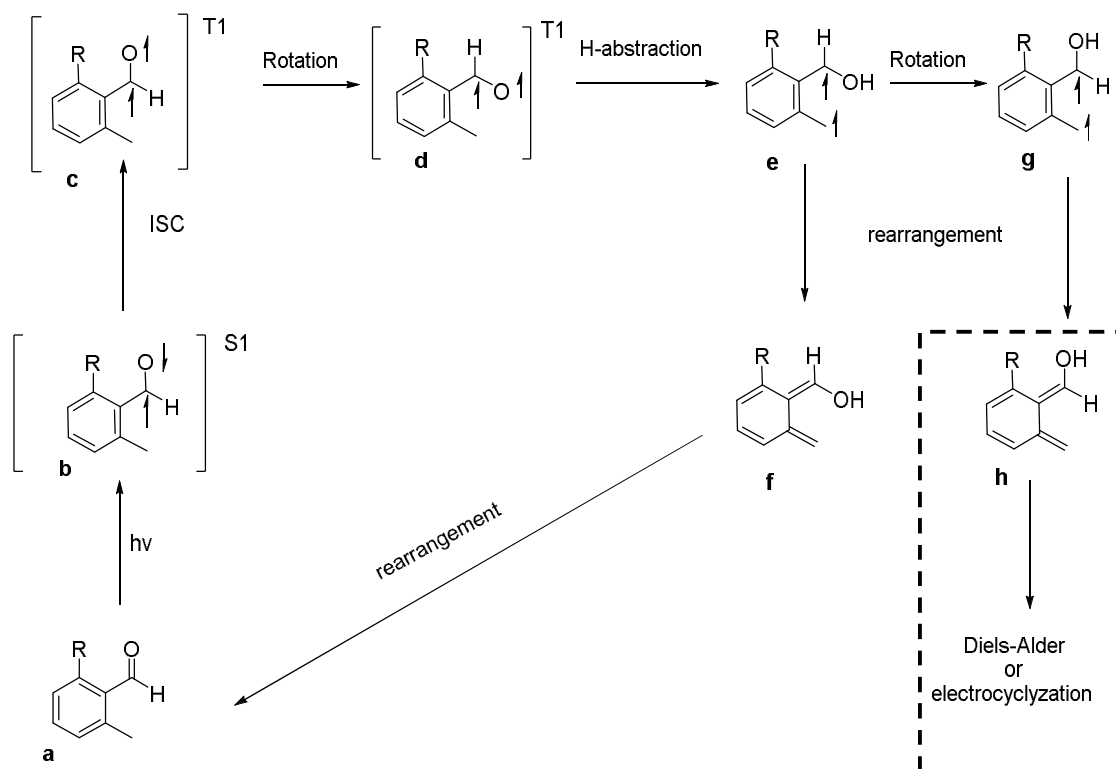
Figure 2.2.4: Classic Diels Alder reaction involving a diene and a dienophile including the orbital symmetry. The molecular orbital energies of the HOMO and the LUMO are close to each other and possess the same symmetry allowing the cycloaddition (Woodward-Hoffmann rules).

The rules of Woodward-Hoffman state that the orbital-symmetry has to be maintained in pericyclic and concerted reactions.⁸⁹ For [4+2] cycloadditions, terminal bonding interaction within ground-state molecules require an overlap of the molecular orbitals with the same symmetry. Thus, a Diels–Alder reaction cannot be light triggered. One strategy employed to overcome this issue is to generate materials of a Diels-Alder reaction photochemically. Once the starting materials were generated, they can undergo a thermal Diels-Alder reaction. Photoinduced DA reactions allow for the preparation of adducts exhibiting a stereochemical conformation, which were not readily available with a thermal processes, *i.e.* an *exo*- isomer upon irradiation with light in presence of maleic anhydride and furan.⁹⁰

In polymer science, photochemically induced HDA reactions are employed for functional surface pattern,^{91,92} polymer building blocks,^{93–96} 3D microstructures^{97,74} among others. In the following sections, the role of light in two examples of Diels-Alder reactions – *ortho*-quinodimethanes and triazolinedione (TAD) chemistries – will be highlighted.

***Ortho*-Quinodimethanes (Photoenol) Chemistry**

The photoinduced DA reaction of *ortho*-alkylbenzophenone with active enes was first reported in 1970.⁹⁸ The proposed reaction mechanism is depicted in Scheme 2.2.6. Initially, an *ortho*-alkylbenzophenone absorbs light (**a**), generating the excited singlet state (**b**) *via* a $n \rightarrow \pi^*$ transition. Subsequently, intersystem crossing (ISC) and a spin inversion of the carbonyl group to form the triplet state (**c**) occur. Next, a rotation with a subsequent H-abstraction takes place to yield the radical intermediate (**e**). Subsequently, two pathways are available: either the rotation with its rearrangement to the active diene (**h**) or the rearrangement to the starting material (**a**). Importantly, the active photogenerated *ortho*-alkylbenzophenone (**h**) – or so called photoenols – can rapidly undergo a thermal Diels-Alder cycloaddition with an electron deficient ene.



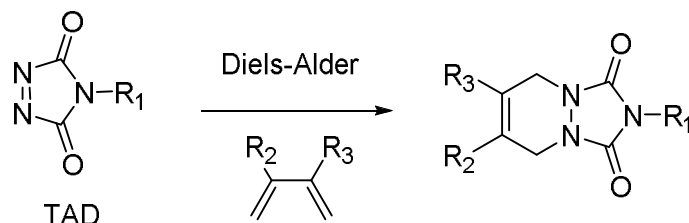
Scheme 2.2.6: First reaction mechanism proposed for the photogeneration of active dienes from of ortho-alkylbenzophenones by Tchir and Porter.⁹⁸

The photoinduced Diels-Alder reaction was successfully employed for polymer ligation,⁹⁹ generation of multiblock components,^{95,100} surface patterning,^{99,101,102} λ -orthogonal reactions¹⁰³ and SCNPs formation (refer to Section 2.3) or the preparation of polymeric microstructures *via* two photon irradiation.¹⁰³ For example, Fruk, Barner-Kowollik and coworkers reported the use of this photochemistry for spatially controlled DNA immobilization onto surfaces.⁹⁹ Recently, taking the advantage of the rearrangement process, the Wegener and Barner-Kowollik groups exploited the photoenol system for high resolution lithography beyond the diffraction limit.¹⁰¹

Triazolinedione (TAD) Chemistry

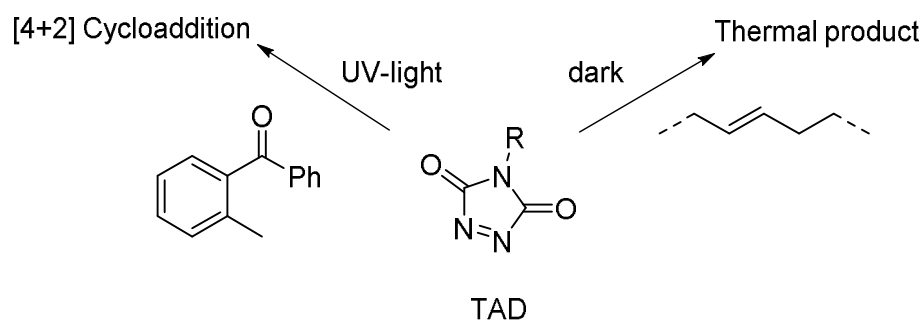
Du Prez and coworkers have recently revived highly efficient reactions based on triazolinediones (so-called TADs). TADs are able to act as reactants in numerous reactions such as Diels-Alder,¹⁰⁴ Alder-ene,¹⁰⁵ electrophilic aromatic substitution¹⁰⁶ and [2+2] cycloadditions.^{107,108} In the last years, particular attention has been paid to their reactivity *via* Diels-Alder [4+2] cycloadditions (Scheme 2.2.7).

Depending on the dienophile employed, the DA reaction proceeds almost instantaneously at low temperatures.¹⁰⁴ The development of variable synthetic routes employing TADs in polymer chemistry has been one of the main efforts of Du Prez's group in the last few years.¹⁰⁸



Scheme 2.2.7: DA [4+2] cycloaddition between a triazolinedione (TAD) and a diene.

Very recently, the Du Prez and Barner-Kowollik groups discovered that this reaction can be switched on and off with light.¹⁰⁹ The TAD moiety was activated with visible light, (544 nm) offering subsequently two reaction pathways in the presence of two potential reactants (ene and *ortho*-quinodimethane), when the light was switched on or off (Scheme 2.2.8). In the dark, the thermal reaction product with the ene was observed. By irradiation with UV-light, the [4+2] cycloaddition reaction was observed. Thus, it was demonstrated that the TAD chemistry is able to switch between a thermal and a photoinduced reaction channel, enabling to specifically trigger different chemical reactions.



Scheme 2.2.8: Basic mechanism of the TAD photoswitchable reaction. After deactivation of TAD with visible light the UV-induced DA or the thermally reaction pathway can be chosen. Adapted from reference [109] with permission from Nature Communications.¹⁰⁹

2.2.2.4 Photoinduced 1,3-Dipolar Reactions employing Tetrazole Chemistry

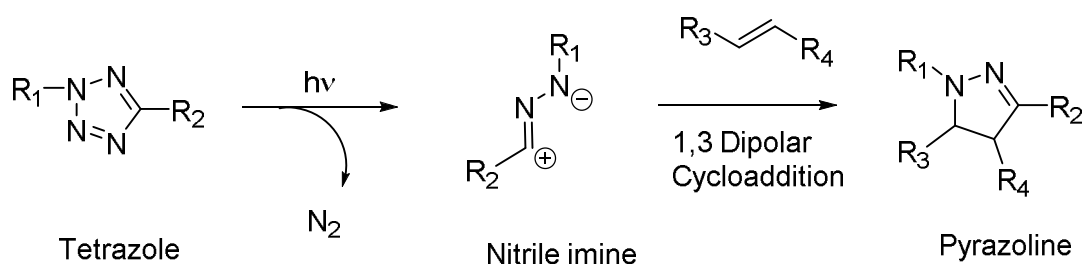
Tetrazoles are heterocycles containing four *N*-atoms in a five membered ring and were first prepared and characterized in 1885 by Bladin.¹¹⁰ Tetrazole derivatives have found applications in various chemical fields, including in organic synthesis as acidic activators for the coupling reaction in oligonucleotide synthesis, biomedicine as pharmaceutical agents or for their use in DNA assays and in explosives.^{15,111–113}

Herein, the focus placed on tetrazoles as starting materials for light induced reactions. In particular, two photoinduced reactions employing tetrazoles will be discussed, *i.e.*, nitrile imine-mediated tetrazole-ene cycloaddition (NITEC) and nitrile imine carboxylic acid ligation (NICAL).

Nitrile Imine-mediated Tetrazole-Ene Cycloaddition (NITEC)

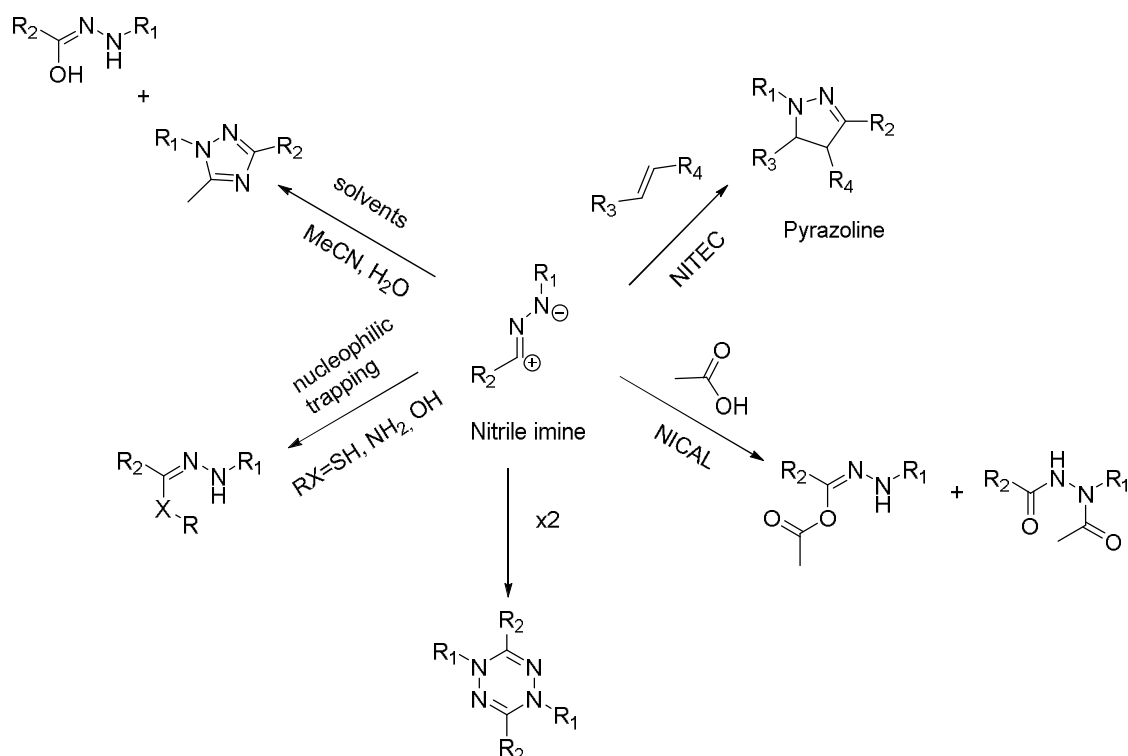
Tetrazoles are capable of forming a reactive 1,3-dipole intermediate – termed as nitrile imine – upon irradiation with light or the use of elevated temperatures, which allows for a variety of different reactions, including 1,3-dipolar cycloadditions. The nitrogen release is the driving force for nitrile imine formation, which is due to the nitrogen release an irreversible intermediate formation.¹¹⁴ In the case of the thermally induced formation of the nitrile imine, elevated temperatures are necessary to cleave the nitrogen from the *N*-heterocycles.¹¹⁵ The high thermal decomposition temperatures represents one of the drawbacks of the thermal reaction route. In contrast, light enables a rather mild route for the generation of the highly reactive nitrile imines. The activation of the tetrazoles with light has recently been investigated in detail.¹¹⁶

As already noted, nitrile imines generated from tetrazole moieties can undergo 1,3-dipolar cycloadditions, known as NITEC reactions first described by Huisgen *et al.* in 1967.¹¹⁴ Here, tetrazoles reacted thermally with methyl acrylate in the presence of triethylamine (Et₃N), yielding a pyrazoline. One of the most appealing features of this reaction is that the generated pyrazoline molecule shows dependent on the used ene, fluorescent properties, which is therefore often utilized in bioconjugation reactions (Scheme 2.2.9).¹¹⁷



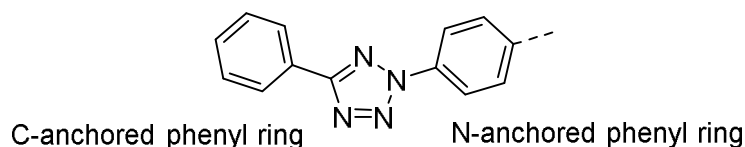
Scheme 2.2.9: Overview of the nitrile imine tetrazole-ene cycloaddition (NITEC), activated with light, affording after nitrogen release a nitrile imine intermediate, able to react with electron deficient enes.

The activation of tetrazoles and their reaction were long denoted as orthothogonal^{14,118} or even as "photoclick"¹¹⁸ reactions. However, recent investigations of the reaction indicated that the nitrile imine reacts with a variety of compounds. Besides the NITEC reaction, *i.e.* reaction with double bonds, several reaction pathways of the nitrile imine are documented in the literature, including the reaction with nucleophiles,¹¹⁹ solvents,^{120,121} amino acids¹²² and carboxylic acids¹²³ among others (Scheme 2.2.10). Even a NITEC reaction of furan protected maleimides, generating the highly fluorescent pyrazoline adduct was observed.⁶ Furthermore, an interesting phenomenon was observed when maleimides were converted with the nitrile imines forming the pyrazoline derivative. Here, a rearomatization of the formed pyrazoline adduct was observed.¹²⁴ The reaction of nitrile imines with carboxylic acids (NICAL) will be explained in detail in the following section.



Scheme 2.2.10: Reaction pathways for the nitrile imine with several reactants such as solvents, nucleophiles, carboxylic acids, self-dimerization and enes.

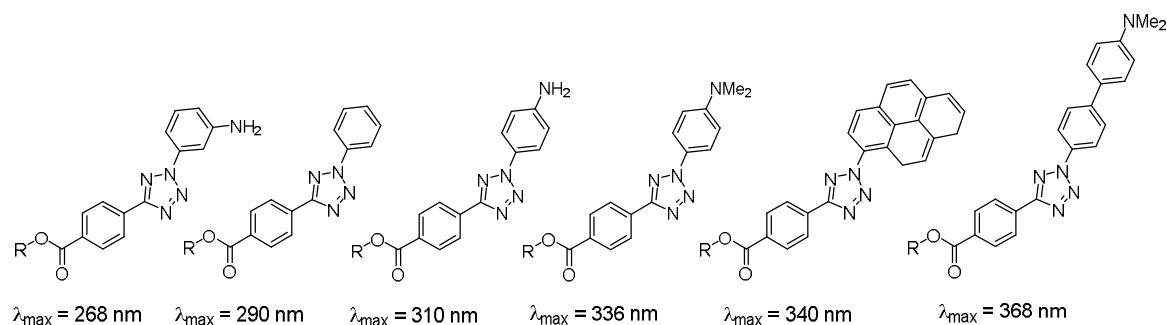
Furthermore, different irradiation wavelengths for the activation of tetrazoles can be employed, depending on their substituents. Tuning of the activation wavelength has been widely studied for diaryl tetrazole, entailing a C-anchored phenyl ring and a *N*-anchored phenyl ring (Scheme 2.2.11).



Scheme 2.2.11: Diaryl tetrazole with the C-anchored phenyl ring and the *N*-anchored phenyl ring of a diaryl tetrazole.

A brief overview of the modified tetrazoles known in literature is illustrated in Scheme 2.2.12, highlighting the influence of the substitution of the *N*-phenyl ring in the tetrazole on the activation wavelength. The wavelength given for each tetrazole corresponds to their absorbance maximum in UV/Vis spectroscopy, which often – but certainly not always¹¹⁶ – correlates with the activation wavelength of the tetrazole. As a reference, the non-substituted diaryl is included, having an absorbance maximum at 290 nm.¹¹⁶

Thus, the non-substituted diaryl tetrazole can be exploited to investigate the effect in the absorption wavelength, dependent on the substitution of the *N*-anchored phenyl ring.



Scheme 2.2.12: Examples of tetrazoles in literature giving an impression of the influence of the substituent in the *N*-phenyl ring on the activation wavelength. From left to right: Increasing absorption wavelengths dependent on the *N*-phenyl ring substitution.

By incorporating an amino group (NH_2) in the *meta*-position of the *N*-anchored phenyl ring, a hypsochromic shift of the absorption maximum at 268 nm was observed (Scheme 2.2.12).^{116,125} However, if the same substituent is introduced in the *para*-position of the *N*-phenyl ring a bathochromic shift was observed with a wavelength at 310 nm, revealing the importance of the position of the substituent in the *N*-phenyl group. Exchanging the primary amine with NMe_2 , which is an electron-donating group, even a shift to higher wavelengths (336 nm) was reached. A higher bathochromic shift was observed when an extension of the chromophore with an additional aryl group carrying a NMe_2 group was introduced, leading to a maximum absorption at 368 nm.¹¹⁶

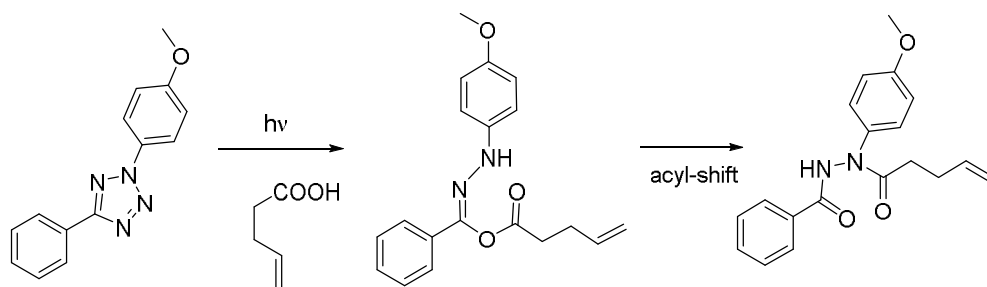
However, this tetrazole was not able to form the highly reactive 1,3-dipole intermediate, due to a more favorable non-radiative deactivation.¹¹⁶ Thus, although a red shift can be achieved with the extension of the chromophore, the photochemical triplet states necessary for the generation of the nitrile-imine need to be accessible. For the tetrazole featuring a pyrene moiety, a maximum absorption at 340 nm was observed. The pyrene containing tetrazole has been shown to form the nitrile imine employing visible light.¹²⁴

The light source for triggering the photoinduced reaction plays a major role, especially for applications in a biological environment. Wavelengths in the visible light regime are a mild trigger for photochemical reactions. In addition, the tissue penetration depth employing higher wavelengths is increased, which could in principle allow tetrazole *in vivo* reactions. Thus, establishing strongly red-shifted tetrazoles is of high interest.

In addition to applications in biology, polymer scientist have utilized the versatile tetrazole chemistry. The group of Barner-Kowollik showed that even photoinduced step-growth polymers can be prepared by utilizing a tetrazole based monomer.¹²⁶ An acrylate based monomer, containing tetrazole moieties, was employed, inducing upon irradiation with UV-light a step-growth polymerization based on the NITEC reaction. Furthermore, tetrazole-ene chemistry was utilized for spatially resolved surface coatings,^{127,91,73,128,129} network formation^{69,130,131} and single chain polymer nanoparticle formation^{6,132} (refer to Section 2.3). In addition, the λ -orthogonal generation of star-polymers was feasible using the UV-light tetrazole and photoenol chemistry.¹³³ Therefore, tetrazole chemistry offers a wide field of application. Furthermore, this light triggered reaction can be employed without any additional catalyst, enabling mild and versatile access to highly reactive nitrile imines intermediates.

Nitrile Imine Carboxylic Acid Ligation (NICAL)

As already mentioned, the application of the tetrazole chemistry was often utilized in bioconjugation reactions. Although a screening of the reactivity towards amino acids was performed in 2013,¹²² including a primary amine and a carboxylic acid, the reaction with carboxylic acid was not reported until very recently. The carboxylic acid ligation was found in 2017 by Li and coworkers, when a competitive reaction employing an ene and a carboxylic was carried out.¹²³ The expected NITEC reaction was not taking place when the diaryl tetrazole was irradiated with light. The reaction with the carboxyl moiety proceeded instead with a subsequent 1,4 acyl shift of the hydrazone reaction product, generating a hydrazine adduct (Scheme 2.2.13).



Scheme 2.2.13: Competitive NITEC and NICAL reaction. The NICAL reaction was preferred when the tetrazole was irradiated, including a 1,4 acyl shift.¹²³ Adapted with permission from reference [123]. Copyright (2015) John Wiley and sons.

2.3 Single Chain Polymer Nanoparticles (SCNPs)

The polymerization of monomers *via* various different controlled radical polymerization techniques was described in Section 2.1, demonstrating the variety of complex macromolecular architectures accessible by employing these methods. In the current chapter, only one macromolecular structure will be highlighted based on a rich literature background, *i.e.* single chain polymer nanoparticles (SCNPs). For the preparation of SCNPs, initially a linear prepolymer is prepared, followed by an external stimuli, which induces an intramolecular single chain collapse. During the collapse, the concentration of the solution entailing the linear polymer structure should be highly diluted ($< 1 \text{ mg mL}^{-1}$), otherwise intermolecular cross-linking reactions can take place resulting in insoluble networks.¹³⁴ The possibilities to induce single chain collapse are almost unlimited, because every chemical reaction that leads to bond formation can be employed. The chemical character of the functional groups, responsible for the compaction, can be divided into three types of linkages such as dynamic,^{135,136} covalent^{137,138} and dynamic-covalent^{139–141} (Figure 2.3.1.).

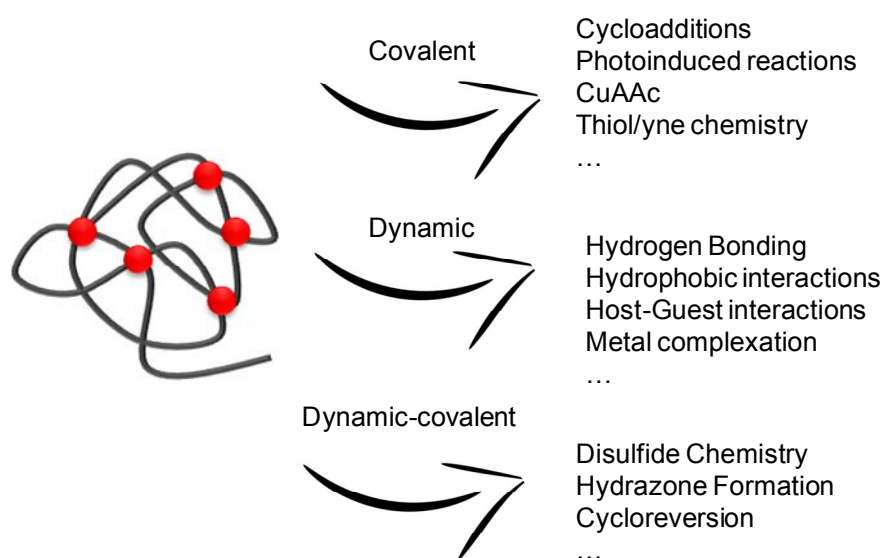


Figure 2.3.1: Overview of the reactions used for SCNP compactions, constituted of covalent, dynamic and dynamic-covalent interactions.

There are, especially for SCNP formation *via* covalent linkage, many examples in the literature such as cycloadditions,^{142,143} dimerization reactions,¹⁴⁴ click chemistry,^{145–149} metathesis¹⁵⁰ and several more. The reader is referred to an excellent review for the interactions employed to induce single chain formation.^{151–153} Among all those examples, the synthesis of photoinduced, water-soluble and fluorescent SCNP formation is described in more detail in the next section, since it is the type of chemistry applied in the current thesis. (Section 2.3.1). An advantage of covalently linked SCNP is the stability of the formed linkages that are sufficiently stable to withstand high temperatures or changes in pH. On the other hand, many covalent bonds cannot be re-opened again leading to irreversible formed bonds.

A reversible interaction is established by the dynamic and dynamic-covalent bonds allowing for to trigger a folding and unfolding reaction. Dynamic bonds employed in SCNP synthesis are, among others, hydrogen bonding,^{154–159} host guest interactions,^{160–162} hydrophobic interactions,^{163–165} π -stacking^{166,167} and metal complexation.^{168–170,11} The reversible collapse can be induced by changing pH, polarity of the solvent concentration or temperature changes. The fine tuning of the reversible bonds allows to align the SCNPs to a certain environment, which can be used for drug delivery, self healing and sensors.^{171,172}

Dynamic-covalent interactions combine the advantage of the fine tuning ability together with increased stability compared to dynamic interactions only.¹³⁹ The formation of SCNPs based on dynamic covalent chemistry are often driven by disulfide,^{144,173–176} hydrazone,^{139,140} enamine^{177,141} and reversible cycloadditions. The labile nature of dynamic-covalent bonds enables even to release a compound if an external stimulus is applied.¹⁵³ Apart from the chemistry employed for single chain technology, the folding nature can be divided in two main fields: selective point or repeating unit folding (Figure 2.3.2).

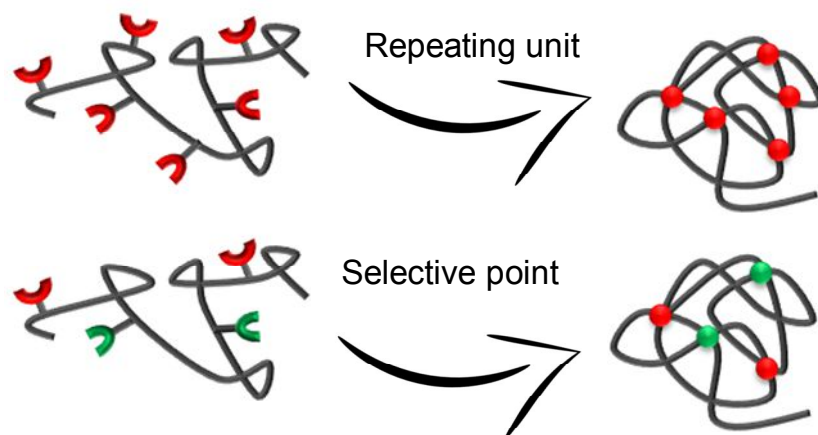


Figure 2.3.2: General overview of SCNP synthesis employing different methods. The repeating unit approach leads to the unspecific collapse of the polymer precursor after triggering the reaction whereas the selective point folding enables a specific folding of a polymer chain at precision placed linkage points within the prepolymer chain.

The repeating unit approach is a versatile folding method, where functional groups, are statistically introduced in a polymer chain. The introduction of the functional groups in the repeating unit approach can be introduced *via* functional monomers or in a post-modification of the polymers, leading to their statistical introduction into the polymer chain. The subsequent collapse upon an external stimulus takes place by non-directed folding of the polymer, due to the statistically placed functional groups.

In contrast, the selective point folding unit within a polymer chain can be described as an orthogonal recognition unit, which functions independently of other incorporated folding points. Furthermore, the selective-point folding method is more precise, due to the control over the location of the incorporated groups within the polymer chain. Applying the selective repeating unit approach, the precision step-wise folding of a polymer chain unit into a precise geometry is possible.

Comparing both approaches, the repeating unit approach represents only a very simple mimicry of the precise folding of biomacromolecules. Both methods entail specific advantages and disadvantages and the selected approach should match with the application of the generated SCNPs. In the present thesis the repeating unit approach was utilized to introduce the photo-responsive groups. As mentioned above, the photoinduced chemistries thus far employed for the single chain nanoparticle formation are discussed in detail in the next section.

2.3.1 Photoinduced SCNP Formation

Photoinduced reactions employed for SCNP formation are often cycloadditions. In the current section, a literature overview of the photoinduced reactions employed for SCNP formation is provided. In particular, examples using photoinduced [2+2] cycloaddition of cinnamate and coumarin, [4+4] cycloadditions of anthracene, [4+2] cycloadditions where one of the precursors is photochemically generated and 1,3 dipolar cycloadditions employing tetrazole chemistry, will be described.

2.3.1.1 SCNP Formation utilizing Cinnamoyl Dimerization

One of the most employed photoinduced reaction for SCNP formation is cinnamoyl photochemistry (for the detailed photochemical reaction description refer to Section 2.2), where upon irradiation with UV-light a [2+2] cycloaddition occurs.¹⁵³ As an example, Liu and coworkers reported the synthesis of the so-called 'tadpole' (Figure 2.3.3) molecules utilizing block copolymers, where one block was functionalized with cinnamoyl moieties.¹⁷⁸ Initially, poly(styrene)-block-poly(2-cinnamoyloxyethyl methacrylate) was utilized to generate spherical polymeric nanoparticles. The same team utilized blockcopolymers of poly(tert-butyl acrylate)-block-poly(2-cinnamoyloxyethyl methacrylate) to synthesize water-soluble cross-linked micelles, which were able to absorb organic molecules from aqueous solutions.¹⁷⁹

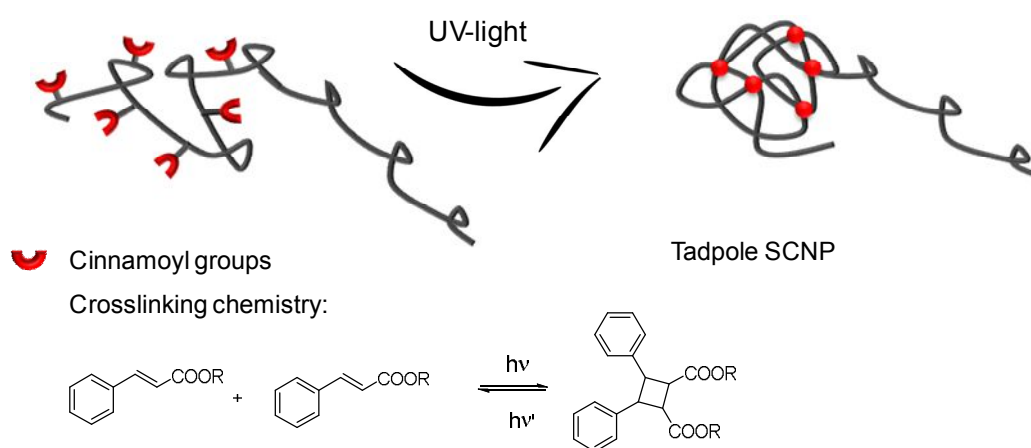


Figure 2.3.3: Schematic representation of the photoinduced formation of tadpole SCNPs employing cinnamoyl functional groups in coblock polymers. The polymer was partially collapsed upon irradiation with UV-light, generating dimerized cinnamoyl groups.

Another example for achieving such tadpole SCNP structures *via* cinnamoyl groups was presented by the group of Chen.¹⁸⁰ They grafted poly(ethylene oxide)-*b*-poly(2-cinnamoyloxyethyl methacrylate) onto silica spheres and irradiated the polymer with UV-light with a wavelength of 254 nm. After HF etching of the silica sphere the tadpole nanoparticles were isolated.

Zhou *et al.* introduced the formation of tadpole-like Janus SCNPs using poly(ethylene oxide)-*block*-poly(2-cinnamoyloxyethyl methacrylate), where only the 'head' of the polymer was collapsed.¹⁸¹ The degree of collapse was controlled by varying the distance of the light source, which is directly dependent on the emission intensity.

Besides the tadpole structures, another interesting macromolecular SCNP architecture was demonstrated by the group of Hecht.¹⁸² Here, organic nanotubes were formed upon irradiation of helical assembled amphiphilic poly(*m*-phenylenethynylene) polymers bearing cinnamoyl moieties (Figure 2.3.4). The helical assembly was achieved through π - π stacking properties of the poly(*m*-phenylenethynylene) and subsequent irradiation formed covalent bonds that stabilized the nanotube. The intramolecular collapse into SCNPs was observed when short irradiation times were chosen, whereas longer irradiation times lead to intermolecular crosslinking of the cinnamates in the block.

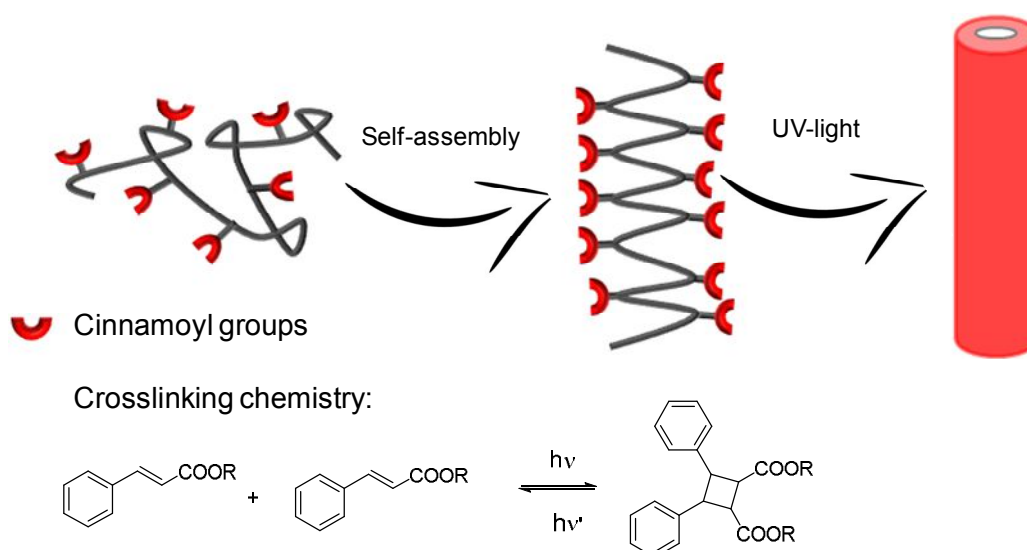


Figure 2.3.4: Schematic representation of the helical-assembled nanotubes with intramolecularly formed cinnamoyl dimers upon irradiation with UV-light. Adapted with permission from *Angewandte Chemie International Edition* reference [182].¹⁸²

In summary, the photoinduced dimerization reaction of cinnamates was mostly employed to generate tadpole structures, which originate from diblock polymers. It must be noted that for the dimerization of cinnamates, high level of energies (deep UV) were employed to induce the photoreaction. However, as discussed in Section 2.2. lower energy levels can be applied for the photoinduced reactions of coumarines, where the [2+2] cycloaddition is performed at somewhat longer wavelength (at approx. 310 nm).

2.3.1.2 SCNP Formation utilizing Coumarin Dimerization

The use of [2+2] cycloaddition of coumarines for SCNP formation was demonstrated by Zhao and coworkers.⁸² They employed *N,N*-dimethylaminoethyl methacrylate and 4-methyl-[7-(methacryloyl)oxy-ethyl-oxy]coumarin based copolymers. The copolymer was irradiated at a wavelength of > 310 nm under high dilution (< 1 mg mL⁻¹) to prepare SCNPs induced by coumarin dimerization. Furthermore, a partial cycloreversion of the coumarin dimers was observed, when the SCNPs were irradiated with higher energetic wavelength (254 nm). A further example exploiting the photoinduced dimerization of coumarin moieties was shown by the same team.¹⁸³ Here, poly(propylene glycol) was functionalized with coumarin moieties and irradiated with a wavelength of > 320 nm (Figure 2.3.5). The reversible nature of the coumarin dimerization reaction was additionally exploited to induce cycloreversion and photodegradation of the generated SCNP upon irradiation with UV-light (254 nm).

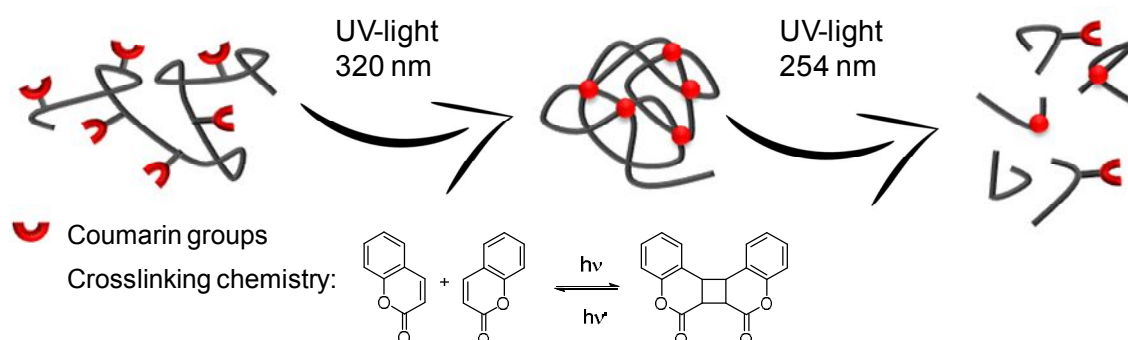


Figure 2.3.5: Photoinduced collapse of coumarin functionalized polymers with UV-light at (320 nm) and the subsequent partial cycloreversion of the dimerized coumarin groups and photodegradation (254 nm). Adapted with permission from reference [82] with permission of the Royal Society of Chemistry (RSC).⁸²

Although the coumarin photodimerization reaction requires lower energies than the cinnamate photoreaction, the cycloreversion of the coumarines were observed by employing a wavelength of 254 nm, which can lead to photodegradation, too. The advantage of the reversible nature of these cycloaddition reaction can therefore only be exploited using deep UV.

2.3.1.3 SCNP Formation Utilizing [4+4] and [4+2] Cycloaddition Reactions

Alternative cycloaddition reactions employing 4π electrons were used for the SCNP formation: Specifically, [4+4] cycloadditions and photo-induced Diels-Alder [4+2] reactions. The dimerization of anthracenes undergoing a [4+4] cycloaddition for SCNP formation was demonstrated by the Berda group.¹⁸⁴ For the dimerization of anthracene, a higher irradiation wavelength was used with approx. 350 nm compared to the dimerization reaction of cinnamates, where a wavelength of 254 nm was employed. Berda and colleagues demonstrated the photodimerization reaction of anthracene to compact methacrylate based polymers into sub-20 nm SCNPs.

Another photoinduced reaction, which was utilized for the formation of intramolecular crosslinked SCNPs, is a variant of a photo-induced Diels-Alder [4+2] reaction. Specifically, Barner-Kowollik and coworkers showed an efficient route to generate photo-induced SCNPs exploiting DA chemistry.¹⁴³ Here, 4-hydroxy-2,5-dimethylbenzophenones and maleimide functional poly(styrene-co-chloromethylstyrene) polymers were irradiated with UV-light at 320 nm (λ_{\max}) in dilute solution to effect SCNP formation. In the same research group, even the stepwise folding *via* UV-light was demonstrated using photoreactive phenacyl sulfides and α -methylbenzaldehyde units, which were linked to a methylmethacrylate based polymer.¹⁸⁵ The first compaction of the poly(methylmethacrylate) based triblock copolymer was induced by UV-irradiation with a wavelength of 355 nm in the presence of a dithiol reacting with the polymer anchored phenacylsulfide. The second compaction was triggered when the copolymer was irradiated with 320 nm (λ_{\max}). The incorporated photoenol reacted with an acrylate dilinker in a [4+2] Diels-Alder cycloaddition. This stepwise folding into compact SCNPs employing different wavelength represents an enhanced control over SCNP folding with UV-light.

In summary, the [4+4] cycloaddition reaction bears the advantage of a relatively mild trigger with 350 nm and the ability to induce a cycloreversion employing lower wavelength (for the detailed photochemistry refer to Section 2.2). The second approach, exploiting DA chemistry, can entail the advantage of a relatively mild trigger wavelength, however the photoinduced cycloreversion is not possible.

2.3.1.4 SCNP Formation Utilizing 1,3-Dipolar Cycloaddition and Radical Reactions

In addition to [4+2] cycloadditions, also 1,3-dipolar cycloaddition reactions were employed to form SCNPs, for instance *via* tetrazoles, which are able to form reactive nitrile imines intermediates upon UV irradiation (refer to section 2.2). In a very first report in the field using this approach, Barner-Kowollik and coworkers demonstrated the tetrazole driven chain compaction of poly(styrene) based polymers.⁶ The post-modifications of poly(styrene-co-chloromethylstyrene) with tetrazoles and furan protected maleimides or tetrazoles only led to photoreactive polymer precursors. After irradiation with UV-light ($\lambda_{\text{max}} = 320 \text{ nm}$) under diluted conditions, intramolecular cross-linking occurred. In particular, fluorescent SCNPs were generated *via* the noted reaction of furan protected maleimides with the tetrazoles to generate fluorescent pyrazoline derivatives (Figure 2.3 6). A recently published study from the same team also reported the reaction between enes and tetrazoles generating fluorescent SCNPs, which are degradable based on an azobenzene motif in the polymer backbone.¹³²

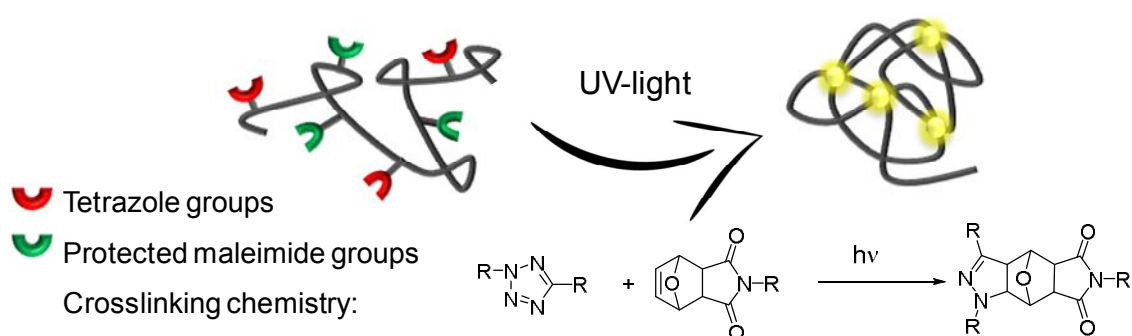


Figure 2.3 6: Schematic representation of the formation of fluorescent SCNPs upon irradiation with UV-light. Adapted with permission from reference [6]. Copyright (2015) American Chemical Society (ACS).⁶

Although the 1,3-dipolar reactions of tetrazole derived nitrile imines are not reversible, due to the release of nitrogen, one of the advantages using this chemistry is the generation of fluorescent products. In contrast, the [4+2] cycloaddition reaction neither entails a reversible photoreaction nor imparts fluorescent features to the formed linkage.

A very interesting radical based photochemical approach was recently published by the Barner-Kowollik team, exploiting the reaction of nitroxide radicals with a photo-active crosslinker (Figure 2.3.7).¹⁸⁶ This example combines both advantages, reversibility and fluorescent self-reporting properties. A nitroxide functionalized poly(styrene-co-chloromethylstyrene) copolymer was irradiated with UV-light ($\lambda_{\text{max}} = 320 \text{ nm}$) in the presence of a photo-active radical-generating dilinker. Based on the fluorescence quenching properties of nitroxides, the formed alkoxyamine upon irradiation, led to self-reporting SCNPs, which were only fluorescent in their collapsed state. The UV-light induced fluorescent SCNPs represent a powerful tool, due to the self-reporting nature of the SCNPs.

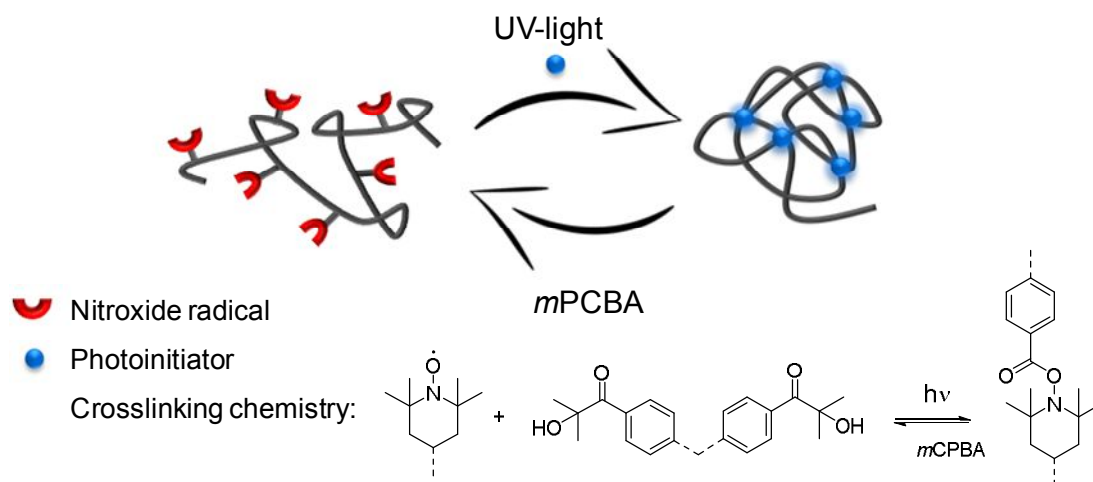


Figure 2.3.7: Schematic representation of the radical reaction of nitroxides (red) with a photoinitiator (blue), generating fluorescent and refoldable SCNPs. The fluorescence is only observed in the collapsed state of the polymer, which generates self-reporting properties of the SCNP. Adapted with permission from reference [186] with permission of the Royal Society of Chemistry (RSC).¹⁸⁶

In summary, mainly cycloaddition reactions were employed to successfully synthesize SCNPs *via* irradiation with UV-light. Importantly, only the minority of the presented examples show fluorescent properties after the photoinduced collapse, which is an important feature for their applications in biology, for example as imaging agents. Thus, a second literature overview is given in the next section, addressing specifically water-soluble and fluorescent SCNPs and their potential applications.

2.3.2 Fluorescent SCNPs for *in vivo* Applications

The current section will focus on fluorescent SCNPs, which have the potential to act as fluorescent molecules in a biological environment. In particular, the fluorescent features of SCNPs can be utilized as imaging agents to monitor cellular uptake or to image the accumulation of SCNPs in a specific cell compartment. Herein, various approaches for introducing fluorescent moieties into polymer chains such as incorporation in the polymer precursor, *in situ* generation, post-functionalization of SCNPs and generation of fluorescent moieties *via* SCNPs formation will be described.¹⁸⁷ In summary, four approaches are described in the following section.

2.3.2.1 Incorporation of the Fluorophore into Linear Polymers

One of the most common approach for the preparation of fluorescent SCNPs is the direct incorporation of a fluorophore into a polymer precursor followed by folding of the polymers. Thus, the polymers are functionalized with a fluorescent molecule in a post-modification step and were subsequently collapsed into compact SCNPs.

An example of fluorescent and water-soluble SCNPs prepared using this strategy was described by Wang *et al.*, who synthesized styrene based copolymers including functional and fluorescent anthracene and crosslinkable groups.¹⁸⁸ In particular, poly(styrene-co-methyl methacrylate) polymers were post-modified employing a 'click' reaction with anthracene and fluorescent benzoxazine (Figure 2.3.8). The functionalized polymer was subsequently thermally cross-linked *via* dimerization of the benzoxazine moieties at elevated temperatures (250°C), thereby generating the fluorescent SCNPs.

Although the initial polymer was based on poly(styrene), the water solubility was achieved by hydrolysis under acidic conditions to result in water-soluble and fluorescent SCNPs.

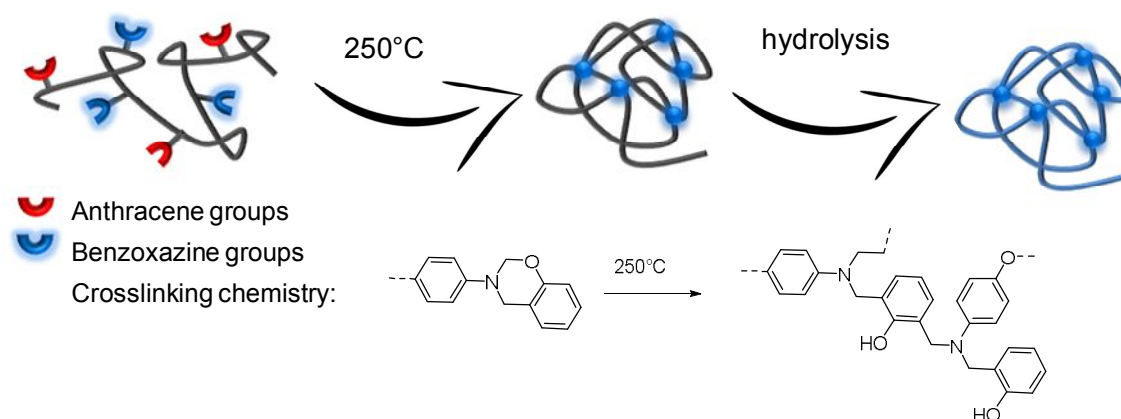


Figure 2.3.8: Schematic overview of the formation of fluorescent and water soluble SCNPs, originating from poly(styrene/methyl methacrylate) based on anthracene (red) and benzoxazine (blue) decorated polymers to generate fluorescent SCNPs employing elevated temperatures. The water-solubility was subsequently achieved with hydrolysis of the polymer. Adapted with permission from reference [188] with permission from Elsevier B.V, Copyright 2014.¹⁸⁸

Another example for the generation of fluorescent SCNPs *via* direct incorporation of the fluorophore in the polymer precursor was shown by Adkins *et al.*¹⁸⁹ Here, ABA triblock copolymers, entailing a poly(ethylene oxide) block B with fluorescent poly(fluorene) segments, were utilized. The non-fluorescent block A carried poly(acrylate) segments with benzocyclobutene functionalities, reacting with each other in a dimerization reaction at higher temperatures (150°C). The water-solubility was achieved in a subsequent pegylation reaction to afford biocompatible SCNPs.

Furthermore, the synthesis of fluorescent and water-soluble SCNPs using metathesis reactions for the polymerizations as well as for the SCNP collapse is demonstrated by Bai *et al.*¹⁵⁰ The precursor polymers were synthesized *via* ring-opening metathesis polymerization (ROMP) of two different functionalized norbornene monomers. One norbornene group carried an active ester, while the second one was coupled to the commercially available fluorophore fluorescein (refer to Figure 2.3.9). The active ester of the first norbornene monomer was subsequently converted into allylic groups, which were exploited for the reaction in a ring closing metathesis (RCM), inducing the SCNP collapse.

Thereby, alkene moieties were formed that allowed dihydroxylation to achieve the water-soluble properties in the SCNP. Finally, the water-soluble and fluorescent SCNPs were tested on HeLa cells showing an accumulation in the lysosomes of the cells.

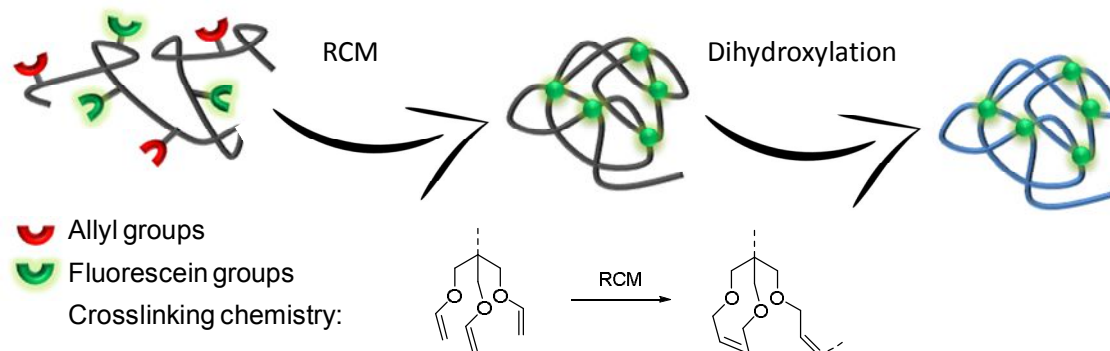


Figure 2.3.9: Schematic representation for the compaction of the polymer precursor was performed using a ring-closing metathesis (RCM) reaction to connect the allyl moieties (red) inducing the SCNP formation. The water-solubility was implied with a subsequent dihydroxylation reaction. Adapted with permission from reference [150] with permission of The Royal Society of Chemistry (RSC).¹⁵⁰

The described examples present different pathways to incorporate a fluorescent molecule before the SCNP is formed. An advantage of this method is the versatility of the fluorophore introduction, while one drawback is the possibility of fluorophore-fluorophore quenching interactions after folding.¹⁸⁷

2.3.2.2 Entrapment of Fluorophores and *in situ* Generation of Fluorophores inside SCNPs

Alternative strategies employed for the formation of fluorescent SCNPs rely on the entrapment of fluorophores or on the *in situ* generation of fluorophores *via* catalysis reactions. The entrapment of a fluorophore can be employed e.g. for determining local packaging zones of SCNPs, whereby the *in situ* generation of fluorophores was exploited as imaging agent in cells.

The first strategy describes an example of the entrapment of fluorescent pyrene molecules. Song *et al.* used SCNPs as nanocontainers to entrap the hydrophobic and fluorescent pyrene in the interior of SCNPs.¹⁷⁶ The entrapment was utilized to determine the local packaging of the hydrophobic interior of the SCNPs. Here, random copolymers with poly(2-hydroxyethylmethacrylate-co-pyridyl disulfide ethyl methacrylate) were utilized to generate the SCNPs *via* reduction of the disulfide groups employing dithiothreitol (DTT) (Figure 2.3.10). The fluorescent pyrene encapsulation was performed by dissolving the pyrene in the polymer solution. Subsequently, the reducing agent DTT was added to entrap the fluorescent pyrene in the SCNP. The release of the pyrene was realized when a redox stimulus was applied.

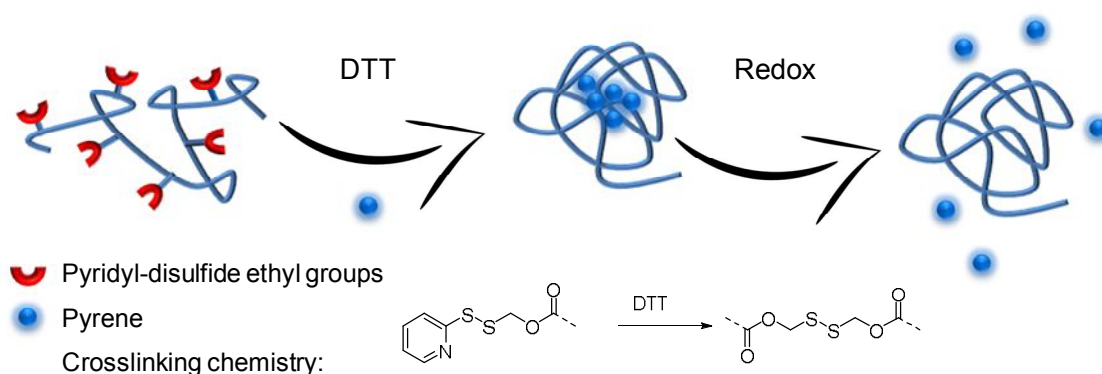


Figure 2.3.10: Formation of water-soluble SCNPs using DTT as reducing agent. The fluorescence pyrene was added during the SCNP formation, causing an entrapment of the fluorescence molecule. By applying a redox stimulus the pyrene moiety could be released. Adapted with permission from reference [176] with permission of the Royal Society of Chemistry (RSC).¹⁷⁶

As already mentioned, the *in situ* generation of fluorophores *via* catalysis reactions were utilized to generate fluorescent molecules in SCNPs. As an example, Liu *et al.* prepared poly(pentafluorophenyl acrylate), which was post-modified with benzene-1,3,5-tricarboxamide-based amine (BTA) as supramolecular recognition motif and poly(etheramine) as water-soluble motif.¹⁹⁰ The BTA moiety allows for the incorporation of Cu^I binding ligands, e.g. 2,2'-bipyridine (Bipy). Upon Cu^I coordination with the introduced ligands, the polymer precursor was collapsed into SCNPs (Figure 2.3.11). Interestingly, the Cu^I coordinated SCNPs were capable to catalyze copper alkyne-azide cycloadditions (CuAAC) reactions.

In order to generate the fluorescent SCNPs, 3-azido-7-hydroxycoumarin and propargyl alcohol were employed as substrates for the CuAAC reaction. With the formation of the triazole ring coupled to the coumarin moiety, the fluorescent linkages were generated.

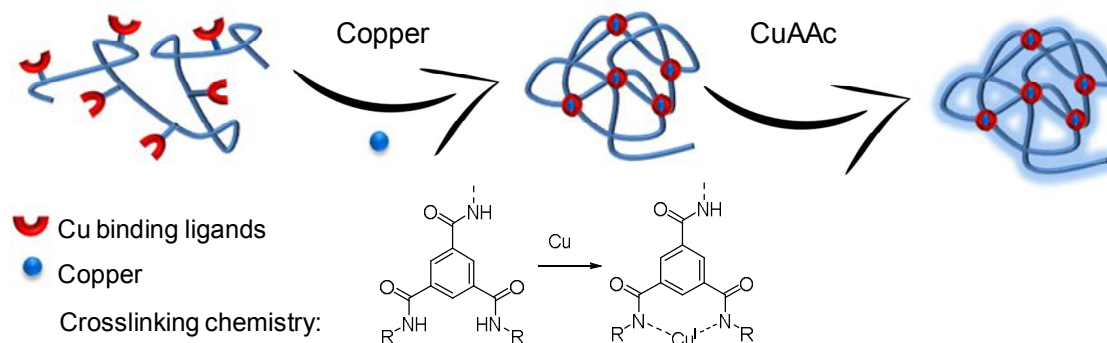


Figure 2.3.11: Schematic overview of the *in situ* generation of fluorophores employing copper as catalyst in a CuAAC reaction. Adapted with permission from reference [190] Copyright (2015) American Chemical Society (ACS).¹⁹⁰

Similarly, Bai *et al.*¹⁹¹ employed Cu^I binding ligands (here α -amino acids) to induce SCNP formation. Specifically, imidazolium and Cu^I binding ligands functionalized norbornene molecules were polymerized in a ROMP reaction, addressing both the water-solubility and the functionality of the polymers. Similar to the aforementioned example, the collapsed polymers were capable to catalyze CuAAC employing as well coumarin moieties to generate the fluorescent molecules. Importantly, the Cu^I loaded SCNPs were able to catalyze the CuAAC reaction in cells, showing an *in-situ* generation of fluorophores in living cell lines.

Thus, the entrapment of fluorescent molecules (e.g. pyrene) or the *in-situ* generation of fluorophores *via* catalysis are powerful methods, where catalysis reactions can be performed in a biological environment. However, in the last case it has to be considered that higher concentrations of copper are toxic for cells, representing not ideal conditions for the application as imaging agents.⁴⁷

2.3.2.3 Post-Modification of SCNPs with Fluorophores

Post-modification of preformed SCNPs with fluorophores is an alternative strategy presented for the preparation of fluorescent SCNPs. In literature, many examples describe post-modification reactions of SCNPs by introducing a fluorophore *i.e.* dansylhydrazine,¹⁹² fluorescein¹⁹³ and naphthalene,¹⁹⁴ or pivaloyl.¹⁹⁵ Of high interest is the example of Harth and colleagues,¹⁹⁶ since the herein prepared SCNPs did not only show fluorescent properties but also enable an application as dendritic transporter of peptides into cells. The polymer system consisted of two macromolecular building blocks with dendritic molecules and a polymeric scaffold. The commercially available fluorophore Alexa Fluor 568 was employed to label the polymeric backbone, where fluorescein was employed to label the peptide. Furthermore, a disulfide anchor was utilized for the fluorescence labeled peptide to release the biomolecule upon a redox stimulus. The cellular uptake of the nanoparticle was monitored *via* confocal fluorescence microscopy.

The post-modification of a previously generated SCNP with a fluorescent dye represents a versatile and simple tool to induce the fluorescent properties into the polymer nanoparticles. In addition, the highlighted example demonstrated that it is possible to generate biocompatible and fluorescent SCNPs using dendritic structures as molecular transporters.

2.3.2.4 Generation of the Fluorescence Properties *via* SCNP formation

The last strategy for the formation of fluorescent SCNPs involves the formation of fluorescent moieties *via* SCNP formation. In comparison to the other approaches, it is one of the most challenging but elegant route to generate fluorescent SCNPs (Figure 2.3.12). There are few examples in literature that fulfill this requirement, which has already been employed in the synthesis of fluorescent SCNPs including *i.e.* triazole-benzene-triazole units,¹³⁷ bipyridine compounds,¹⁶⁶ stilbene units,¹⁹⁷ Pt(II)-porphyrin¹⁹⁸ and tetrazoles.^{6,199} In case of the triazole-benzene-triazole example, poly(styrene) polymers were functionalized with alkyne and azides, which were collapsed subsequently *via* an intramolecular 'click' reaction generating the fluorescent triazole compounds.

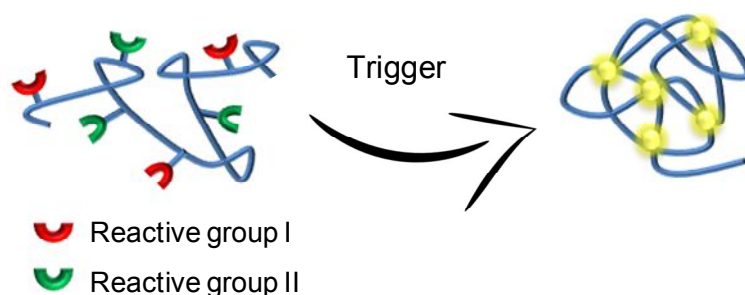


Figure 2.3.12: Schematic overview of the potential synthesis of fluorescent and water-soluble SCNPs during the SCNP collapse, which would fill the gap in the literature.

In summary, there are numerous examples for the generation of fluorescent and water-soluble SCNPs. All described examples incorporate the fluorescent moieties either in the monomers, polymer precursors or were post functionalized in the SCNPs. The advantages employing these methods are the versatility, the use of commercially available fluorophores, the variety of monomers and several more. Regarding the applications as imaging agents, some approaches such as the entrapment of fluorescent molecules or the *in-situ* generation of fluorophores, the application as imaging agent is not feasible, because the nanoparticles are not covalently connected to the fluorescent moiety. One drawback of the post-modification approach is the toxicity of some commercially available fluorophores, limiting the application in a biological environment. The last method discussed was the generation of fluorescence properties *via* SCNP formation. One advantage of this approach is the *in-situ* generation of the fluorophore with the SCNP collapse, however this approach requires a suitable chemistry to induce the fluorescent properties within the SCNP collapse. All the noted examples demonstrate the successful preparation of fluorescent SCNPs, but employing non-water soluble polymers. However, water-solubility is a key criterion for the biological application of these particles. Therefore, the first goal of the current thesis was to fill this gap and design the synthesis of water soluble fluorescent SCNPs employing tetrazole chemistry (refer to Chapter 3).

2.4 Analytical Tools for SCNPs

In the current chapter the key analytical tools are discussed to characterize SCNP formation associated with single polymer chain collapse. Here, size exclusion chromatography (SEC), dynamic light scattering (DLS) and diffusion ordered spectroscopy (DOSY) will be explained. The characterization of SCNPs often focuses on the relative hydrodynamic radius change when a linear precursor polymer collapses into a SCNP. More specifically, the SCNP entails a smaller hydrodynamic radius than the linear polymer chain due to an intramolecular cross-linking process that connects functional moieties either in the side chain or in the end group. For the characterization of SCNPs also atomic force microscopy (AFM), Electrospray ionization mass spectrometry (ESI-MS) and several more methods were employed to characterize the SCNPs, which were not on the focus in the present thesis.

2.4.1 Size Exclusion Chromatography (SEC)

The most widely utilized tool to characterize a SCNP collapse is SEC. Generally, the SEC is a chromatographic method for separating molecules based on their hydrodynamic volume, where a mobile and a stationary phase are employed. The stationary phase consist of a porous material, in particular polymer beads, which are constituted of cross-linked poly(styrene), poly(acrylamide) or cellulose among others, having the ability to swell in the appropriate mobile phase.²⁰⁰ Thus, varied mobile phases can be employed including tetrahydrofuran (THF), *N,N*-dimethylacetamide (DMAc) and water. The separation principle is as follows: Larger particles cannot diffuse into small pores in the column, and thus, elute earlier, while small particles can diffuse into a higher number of pores (including the small ones) and thus elute later. However, polymer separation on the stationary phase is limited. Here, the entire column material volume can be divided into an inner (V_i) and an outer (V_o) volume. The inner V_i describes the pore volume, whereas the V_o denotes the volume outside of the pores. If the polymer chain's hydrodynamic radius is too large to enter any pores (*i.e.* $V_e = V_o$), no separation is achieved due to the upper exclusion limit.

If a polymer sample can enter all available pores of the column material, V_e can be described as $V_e = V_0 + V_i$ representing the lower exclusion limit, resulting again in a non effective separation of the polymeric material. Hence, to separate a suitable polymer size, the elution volume (V_e) is expressed with:

$$K_d = \frac{(V_e - V_0)}{V_i} \quad \text{Eq. (9)}$$

where K_d is the sample distribution coefficient, depending on numerous of parameters e.g. temperature, shape and constitution of the polymer.²⁰¹ A separation takes place if the analyte has a specific fraction between $0 \leq K_d \leq 1$ (being able to access a certain fraction of pores). Since the fraction factor depends on several parameters the SEC is not regarded as an absolute method for molecular weight determination. For the detection of the absolute molecular weight *via* SEC measurements, an universal calibration with the corresponding polymer samples including different narrow molecular weights, is necessary. Furthermore, viscosity and multi angle light scattering detectors are employed to determine the absolute molecular weight of polymers. In contrast, establishing a calibration using multiple polymeric standards such as poly(styrene) or poly(methyl methacrylate) allows for the relative molecular weight determination. Here, the focus is the analytic characterization of SCNPs and therefore the calibration will not be discussed in detail. The interested reader is referred to analytical textbooks, explaining the calibration and how molecular weights can be determined.^{202,203}

SEC measurements are an excellent tool to verify a SCNPs formation, based on the change in the hydrodynamic volume of a collapsed polymer in contrast to its precursor. As discussed earlier, SEC measurements depend on the retention time of a polymeric sample. After a sample is internally cross-linked forming the SCNP, an SEC trace shift to higher retention times occurs, due to a higher diffusion time through the porous material of the SEC column bead, leading to a reduced apparent molecular weight (M_{app}).

It should be noted here that due to several parameters, which can influence the retention time of a polymeric sample (e.g. temperature, pressure, interaction with the column material) the analyzed polymers were measured directly after each other to keep the conditions constant for the determination of the M_{app} of the polymers and SCNPs.

The adjustment of the apparent molecular weight observed by the SEC trace shift can be described with an equation (Eq.10). Pomposo and coworkers have addressed the effect of the apparent molecular weight change.²⁰⁴ The derived law assumes the apparent molecular weight change of fractal soft nano-objects and can be expressed with:

$$M_{app} = c M^{\beta} \quad \text{Eq. (10)}$$

with c as constant and β for the power law exponent, which can further be described as:

$$\beta = \frac{1 + \alpha_f}{1 + \alpha_L} \quad \text{Eq. (11)}$$

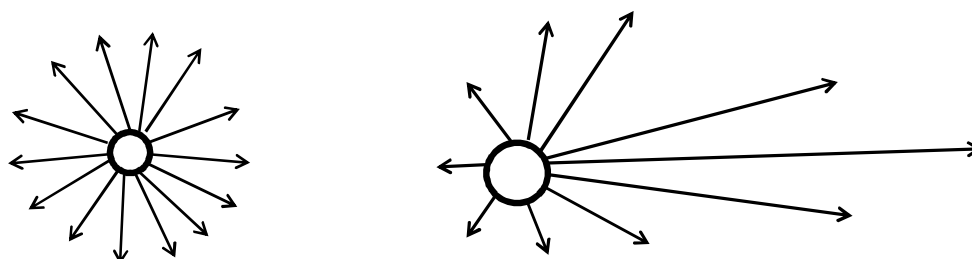
with α_f representing the parameter of the fractal degree and α_L representing the Mark-Houwink-Sakurada exponent. In addition, Pomposo and colleagues assumed two limitations for the fractal soft nano-objects with the minimum ($\beta \approx 0.56$) for perfectly compact polymer samples and the maximum ($\beta \approx 1$) representing nano-objects similar to swollen flexible chains. Further, they observed that a change in the dispersity index \mathcal{D} occurs after the collapse of a linear polymer. The power law of the dispersity change is described as:

$$\mathcal{D}_{app} = \mathcal{D}^{\beta^2} \quad \text{Eq. (12)}$$

for polymer precursors with a log-normal MWD.

2.4.2 Dynamic Light Scattering (DLS)

A further analytical tool for the characterization of SCNPs is DLS, which is also known as photon correlation spectroscopy (PCS). DLS allows to determine the hydrodynamic radius of small molecules as well as macromolecules and large particles in solution or in suspension. The determination of the hydrodynamic radius is based on two phenomena: the Doppler effect and Brownian motion. Brownian motion depends on the particle size, as large particles move slower through the solution than smaller ones.²⁰⁵ The Doppler effect describes the frequency change of moving particles relative to the incident light beam.²⁰⁶ Here, the photons of the incident light beam elastically interact with the particle so that the scattering centers are oscillating in the same frequency as the incident photons. The thus created Hertz dipoles emit photons with the same frequency (referred to as elastic Rayleigh scattering). Rayleigh scattering occurs when the particle size is smaller than 1/10 of the wavelength of the incident light (Figure 2.4.1).



Rayleigh scattering $< 1/10$ of λ

Mie scattering $> 1/10$ of λ

Figure 2.4.1: Overview of the different scattering processes with Rayleigh and Mie scattering dependent on the particle size.

In contrast, the Mie scattering takes place for particles, which are larger than 1/10 of the wavelength of the incident light. Here, the scattering is angle dependent. Ultimately, the diffusion information is encoded in the Lorentzian Rayleigh scattering as the Doppler effect shifts the frequency relative to the particle motion. Light scattering of nanoparticles is proportional with the power of 6 to their radii, leading to a more difficult size determination for smaller particles.

The experimental concept of DLS is implemented with a monochromatic light source and a detector (photonmultiplier), measuring the scattering intensity. Due to the small frequency fluctuations (10^3 Hz compared to 10^{14} Hz Rayleigh intensity) caused by the Doppler effect, the Doppler-broadened frequency spectrum has to be transferred into an autocorrelated spectrum according to the Wiener-Khinchin theorem.²⁰⁷ The autocorrelation function is plotted against short decay intervals (τ) and can be expressed for monodisperse particles with:

$$g(\tau) = 1 + b e^{-2\tau q^2 D_t} \quad \text{Eq. (13)}$$

with b as constant arising from the instrument settings, q as Bragg wave scattering vector and D_t the translational diffusion coefficient. The scattering vector q can be further expressed with:

$$|q| = \frac{4\pi n_0}{\lambda_0 \sin \frac{\theta}{2}} \quad \text{Eq. (14)}$$

with n_0 as the refractive index, λ_0 the wavelength in vacuum and θ the scattering angle. Equation 13 represents the particle motion with the fluctuation of the scattered light. Depending on the detector technology used, the placement of the detector angle can vary.²⁰⁸ Finally, the determination of the hydrodynamic radius can be calculated exploiting the Stokes-Einstein Equation with

$$D = \frac{T k_B}{6\pi\eta R_h} \quad \text{Eq. (15)}$$

with D as diffusion coefficient, T as temperature, k_B as Boltzmann constant and η as the viscosity of the solvent. In the above noted autocorrelation function Eq. (13), only monodisperse samples were considered. For disperse polymers, the correlation function is adapted into a probability-density function.

$$g(\tau) = \int_0^\infty G(\Gamma) e^{-\Gamma t d \Gamma} \quad \text{Eq. (16)}$$

Equation 16 summarizes the different translational diffusion behavior stemming from a disperse sample. Extracting the diffusion coefficient from equation 16 involves an inverse Laplace transformation among other mathematical operations.

Several analytical approaches can be applied to obtain the size information from the correlation function such as non-negative non-linear least-squares (NNLS),²⁰⁹ constrained regularization (CONTIN),^{210,211} cumulant²¹² and exponential sampling.^{213,214} In the present thesis, the cumulative approach was employed to extract the particle size from the disperse correlation function Eq.(16). The cumulative analysis was introduced by Koppel in 1972 and is one of the commonly employed analysis methods due to its reliability.²¹²

Here, an overview of the theoretical consideration and calculations are given. It should be noted that DLS measurements, which determine the size of SCNPs, are a common tool in the SCNP community. However, some disadvantages and limitations of the size determination for SCNPs are noteworthy.

Determining the size of SCNPs *via* DLS can be challenging due to some factors influencing the measurement. The first factor is represented by the choice of the solvent, which can scatter the light during the DLS measurement and can therefore influence the size determination. Furthermore, it has to be considered that the nanoparticles can interact with the solvent leading to undesired changes in size.²⁰⁵ Especially nanoparticles tend to agglomerate and scatter in comparison to the smaller particles much more (as the scattering is proportional to the power of 6 of the radii).²⁰⁵ It should be noted that every change in size or shape of the polymer during the DLS measurement affects the correct determination of the size. Furthermore, colored and fluorescent samples influence the detection of the size in DLS, due to absorption and emission of the particles. In particular, the absorption of light in the range of the incident light beam causes a lower intensity of the scattering and therefore apparent smaller sizes can result.²⁰⁵

2.4.3 Diffusion Ordered Spectroscopy (DOSY)

A further analytical method used for the size determination of SCNPs is the diffusion ordered spectroscopy (DOSY). DOSY NMR represents a well established method to determine diffusion coefficients in nuclear magnetic resonance (NMR) spectroscopy. Single ^1H resonances from a molecule can be directly connected to the diffusion coefficient.²¹⁵ Here, the analysis of polymers is showcased. In particular, the DOSY measurements can be challenging when size distributed samples are analyzed. The assumption of spherical particles in motion is described by the Stokes-Einstein equation (refer to Equation 15), allowing to determine the hydrodynamic radius (R_h) of the sample. In order to determine the translational diffusion coefficient *via* DOSY NMR, a pulsed field gradient (PFG) experiment is employed. In principle, a pair of gradient pulses is employed for de- and encoding the information. First, an encoding gradient pulse is applied to 'label' the spin in the magnetic field. Before the second gradient pulse proceeds the molecules are allowed to diffuse in solution with the diffusion time Δ . After that time the second decoding gradient pulse is applied to determine the new position of the 'labeled' spin in the magnetic field. Before the DOSY experiment will be explained in detail, some general remarks on the NMR measurements are required.

The principle of NMR is that that a nucleus in a magnetic field B causes the nucleic spin to precess in their Lamor frequency, which is defined as

$$\omega(r) = -\gamma B(r) \quad \text{Eq.(17)}$$

with ω the angular frequency, B the magnetic field and γ the gyromagnetic ratio. As mentioned above the DOSY measurements exploit a pulsed field gradient. The spatially resolved ω can be observed if a pulse field gradient is applied causing a magnetization of the spins in z-direction. After the spins are spatially resolved with their Lamor-frequency, the diffusion coefficients can be determined measuring the attenuation of the intensity. The signal intensity is dependent on gradient parameters (g , δ) and the diffusion time Δ .

The signal intensity change can be expressed as:

$$I = I_0 e^{-D\gamma^2 g^2 \delta^2 (\Delta - \frac{\delta}{3})} \quad \text{Eq.(18)}$$

with I is the detected intensity, D the translational diffusion coefficient, γ the gyromagnetic constant of the detected nucleus, g the gradient strength, δ duration of the gradient and Δ the diffusion time. The simplest PFG pulse sequence was described by Stejskal and Tanner in 1965²¹⁶ with the pulse sequence illustrated in Figure 2.3.13.

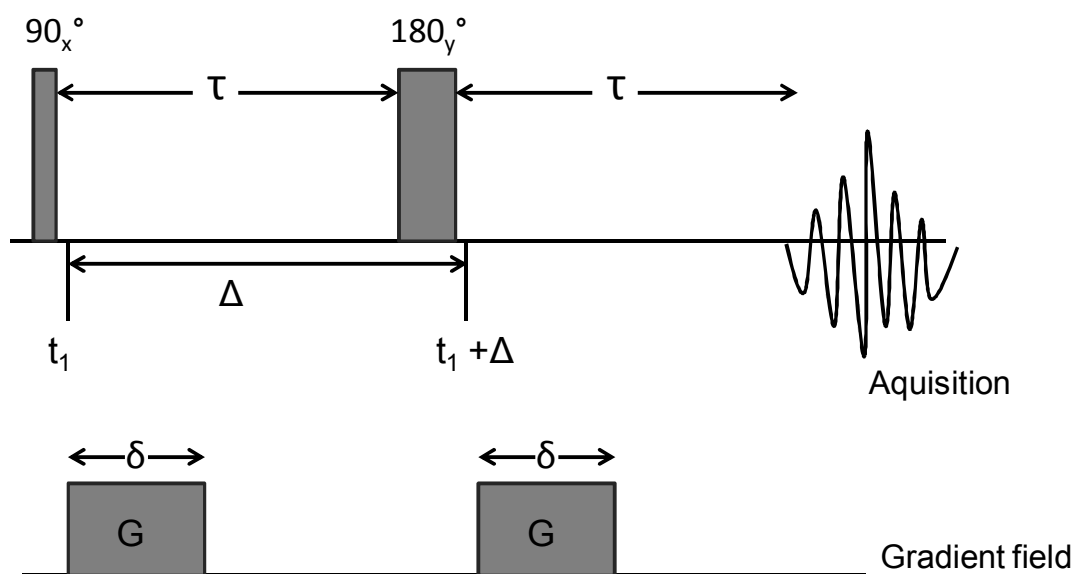


Figure 2.3.13: Simplest pulse sequence for DOSY measurements from Stejskal and Tanner employing the pulsed field gradient spin-echo. Adapted from reference²¹⁷

Initially, the spins are magnetized along the z-axis parallel to the external magnetic field B . After the 90° pulse the spins are flipped into the x, y plane and the molecules diffuse vertically (translational) with a diffusion time Δ . The pulse gradient (G) with a duration of δ is applied at time (t_1) to result in a phase shift. The phase shift of the spins can be expressed with

$$\Phi_i(\tau) = \gamma B_0 + \gamma G \int_{\tau}^{\tau+\delta} z_i(t) dt \quad \text{Eq. (18)}$$

and can be divided in two terms. The left term represents the phase shift induced by the external gradient field B and the right one represents the phase shift induced by the gradient field pulse G . Subsequently, the 180° pulse is applied, inducing a reversed spin precession.

The second gradient pulse that follows the 180° pulse entails the same energy and duration as the first one, causing an interaction, which can be divided in two cases. In the first case, the molecules do not diffuse along the z-axis. Here, the signal is diminished after the two gradient pulses resulting in the detection of the maximum intensity due to the rephased spins along the z-axis. In the second scenario, where the molecules diffuse along the z-axis, the spin shift causes a difference in magnitude after the second period of time τ . Due to the diffusion, the spins entail different positions along the z-axis at different times (t_1 and $t_1 + \delta$) and precess with different frequencies. Here, the spins were not refocused on the z-axis leading to the attenuation of the echo intensity.

As aforementioned the pulse sequence from Stejskal and Tanner represents the generic pulse sequence for DOSY measurements. One drawback employing the Stejskal and Tanner pulse sequence is that the T_2 relaxation time during Δ leads to a decreased intensity of the signal and causes therefore longer experiments. To overcome this drawback the pulse sequence was adapted into three 90° pulses known as stimulated echo (STE). The STE method was named by Hahn and is often applied for macromolecular systems (Figure 2.3.14).²¹⁸

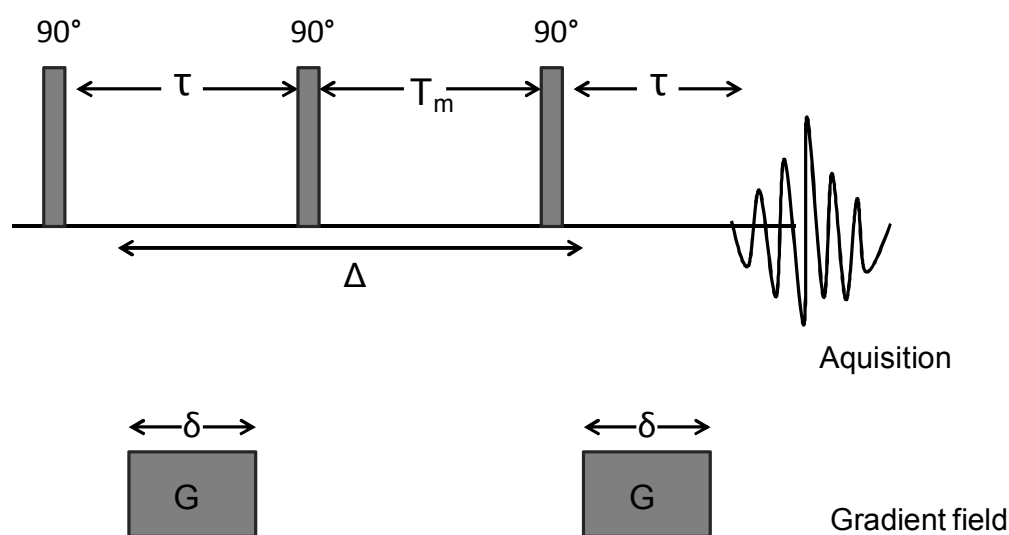


Figure 2.3.14: STE pulse sequence form Hahn. The pulse sequences are split into three 90° pulses. Adapted with permission of Angewandte Chemie-International Edition from reference [219].²¹⁹

The application of three subsequent 90° pulses allows for the extension of the relaxation time. In particular, the short T_2 relaxation times are exchanged with the longer T_1 relaxation times induced by the second 90° pulse.

Here, the T_1 relaxation (Spin-Lattice relaxation) takes place due to a second magnetization in the z-axis. A further adaption of the pulse sequence can be made to improve the measurement of macromolecular species. Specifically, the longitudinal Eddy-current delay (LED) method was introduced, allowing for the discrimination between similar-sized molecules.²²⁰ Eddy currents are electronic currents caused by a change in the magnetic field. Especially for macromolecules, which move slower than small molecules, the employed phase encoding pulses has higher amplitudes causing eddy current effects. To circumvent the issue of eddy currents, the pulse sequence is adapted into five 90° pulses.

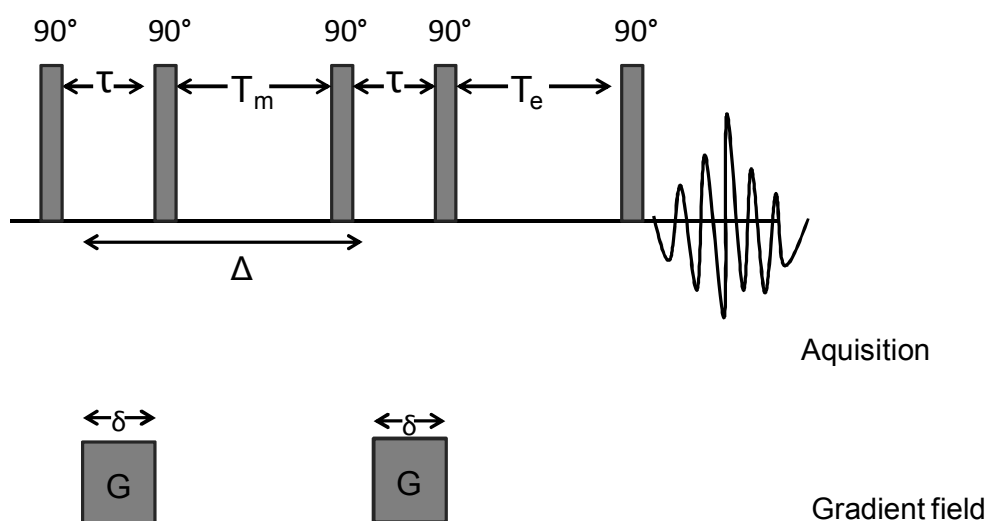


Figure 2.3.15: LED pulse sequence with five 90° pulses to circumvent eddy currents. Adapted with permission of *Angewandte Chemie-International Edition* from reference [219].²¹⁹

In contrast to the STE pulse sequences two 90° pulses is applied. Additionally a delay time (T_e) appears after the fourth 90° pulse. After the second τ period the fourth 90° pulse induces a magnetization in the longitudinal direction, causing a decay of the eddy currents. The delay time T_e can be regarded as a settling period for the eddy currents and afterwards the last 90° pulse is applied for the acquisition. The last modification for an improved measurement can be realized with the bipolar LED (BPLED) sequence.

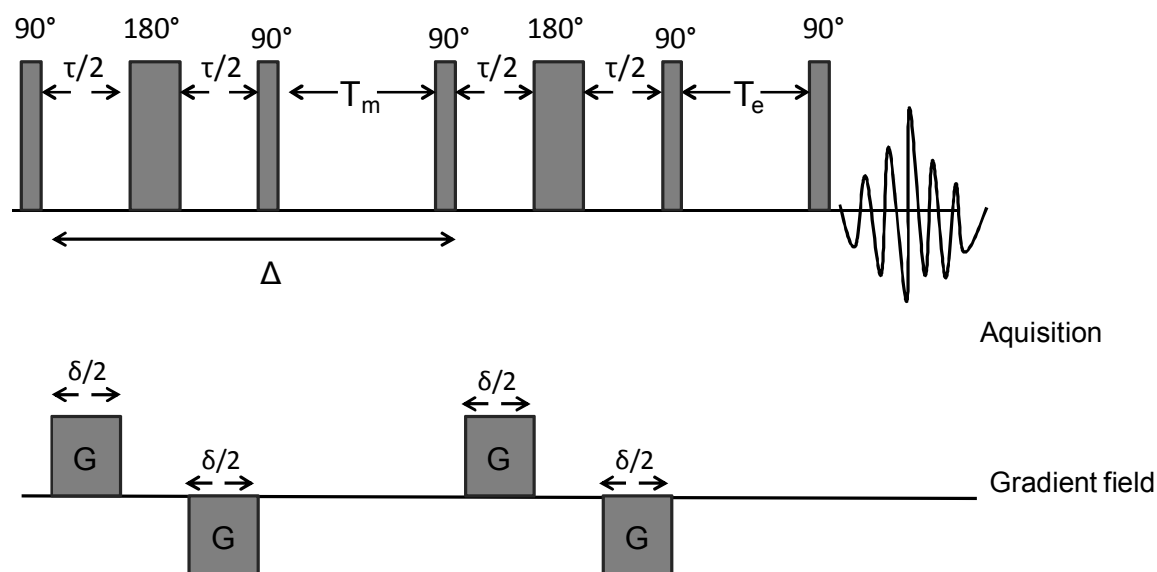


Figure 2.3.16: BPLED pulse sequence with two additional 180° pulses and gradient pulses of different polarity. Adapted with permission of Angewandte Chemie-International Edition from reference [219].²¹⁹

Here, two 90° pulses are replaced in two different polarity (+G,-G) pulsed and were separated with a 180° pulses. The change of the polarity (+G 180° -G) lead to a cancellation of the Eddy currents. The BPLED pulse sequence entails two advantages minimizing the eddy currents and the effective output of the gradient is doubled.

In summary, the analytical tools for determining the size reduction of the SCNPs with respect to their precursor with SEC, DLS and DOSY are described. However, determining the size of SCNPs applying the aforementioned analytical tools can be challenging. A review, regarding the size determination of SCNPs, was recently published, critically investigating the common analytical tools such as SEC, DLS, DOSY, atomic force microscopy (AFM) and transmission electron microscopy (TEM) for SCNPs.²²¹ In the current thesis, SEC, DLS and DOSY methods were employed to characterize the precursor polymers as well as their SCNPs.

For example, in SEC where an absolute molecular weight determination is feasible, employing pure poly(styrene) or poly(methyl methacrylate) coupled to viscosity and multi angle light scattering (MALS) detectors, a variety of different sizes for SCNPs were observed. One example for the variation of the observed size employing SEC as analytical tool is discussed below.

Here, SCNPs with a determined molecular weight of 25kDa ranged from 7.4 nm (for a polyether polymer with 18% thiol-yne cross-links)²²² up to 17.8 nm found for a polycyclooctadiene system with 1% cross-links.²²³ Although a variation of the sizes determined with SEC were expected given the number of cross-links and the coil dynamics, the disparate sizes found for the similar molecular weights in the literature are nevertheless remarkable.

For DLS measurements, the density of the compacted SCNPs were taken into account and compared with size values obtained from literature. In the critical review, they assume that the density estimations of SCNPs based on DLS data should be taken with caution, due to the fact that the calculation requires knowledge about the shape of a collapsed polymer.²²¹ However, when the densities of the SCNPs were compared, contrarily results were obtained with densities ranging from 0.01 g cm⁻³ and densities, which exceed bulk material. In the review, typical densities of ideal SCNPs are at approx. 1 g cm⁻³, which is referred to densities found in bulk material.

In summary, the analytical tools for measuring the size in SCNPs were described and critically discussed. The determination of absolute sizes for SCNPs employing methods such as SEC and DLS is challenging due to the different cross-linking chemistry applied, coil dynamics, scattering and several more (refer to Section 2.4.). Therefore, the determined sizes of SCNPs should be taken with care and represent a relative change in the size of the SCNP to its precursor.



Fluorescent Single Chain Polymer Nanoparticles *via* Tetrazole Photochemistry

During the last years, nature inspired researchers to develop new polymeric soft materials, leading to the generation of bio-functional macromolecules, which can be employed as imaging agents in biological environments.¹⁷¹ The main challenge herein is the synthesis of such sequence-defined natural macromolecules, for instance, proteins or desoxyribonucleic acid (DNA), which entail a complex highly specific linear amino-acid sequence or DNA bases that define their secondary or tertiary structure.

Parts of this section are adapted with permission from Heiler, C.; Offenloch, J.; Blasco, E.; Barner-Kowollik, C. *ACS Macro Lett.* **2017**, *6*, 56-61.²²⁴ and C. Heiler, S. Bastian, P. Lederhose, J. P. Blinco, E. Blasco and C. Barner-Kowollik, *Chem. Commun.*, **2018**, *54*, 3476.²²⁵ The DOSY NMR measurements were carried out from Dr. Eva Blasco. The peptoid synthesis was performed from Stefan Münch and the cells test were carried out from Ilona Wehl.

Therefore, tailor-made polymers mimicking the complexity of proteins, consisting of variable monomers, play a key role in modern polymer science. Polymer chemists aim at the precise folding of well-defined polymer chains into so-called single chain polymer nanoparticles (SCNPs). Here, the SCNP formation is induced *via* an intramolecular collapse of synthetic linear polymer precursor to generate three-dimensional structures, imitating bio-macromolecules.

The central aim of the current thesis includes the synthesis of water-soluble and fluorescent SCNPs for imaging agents in biological systems. However, for *in vivo* applications, several parameters of the polymer system have to be taken into account such as water solubility, toxicity and overall compatibility with components present of a biological system. In order to synthesize fluorescent and water soluble SCNPs with the requested properties, linear water-soluble polymer precursors were equipped with photolabile groups, enabling a mild access to fluorescent SCNPs without the need of a catalyst.

Therefore, the combination of water-soluble polymers equipped with photolabile groups was exploited to generate fluorescent SCNPs. Here, the nitrile imine-mediated tetrazole-ene cycloaddition (NITEC) was chosen as photochemical reaction, providing the highly fluorescent features in the ligation product (a pyrazoline) necessary for application as imaging agent *in vivo*. Two tetrazoles were employed in this thesis: (i) one bearing a phenyl moiety (refer to Section 3.1) that is activated with UV-light at 320 nm (λ_{max}) and (ii) a pyrene functionalized tetrazole (refer to Section 3.2), which can be activated in the range of visible light at 410-420 nm.

3.1 UV-Light Induced Folding of Polymers into SCNPs

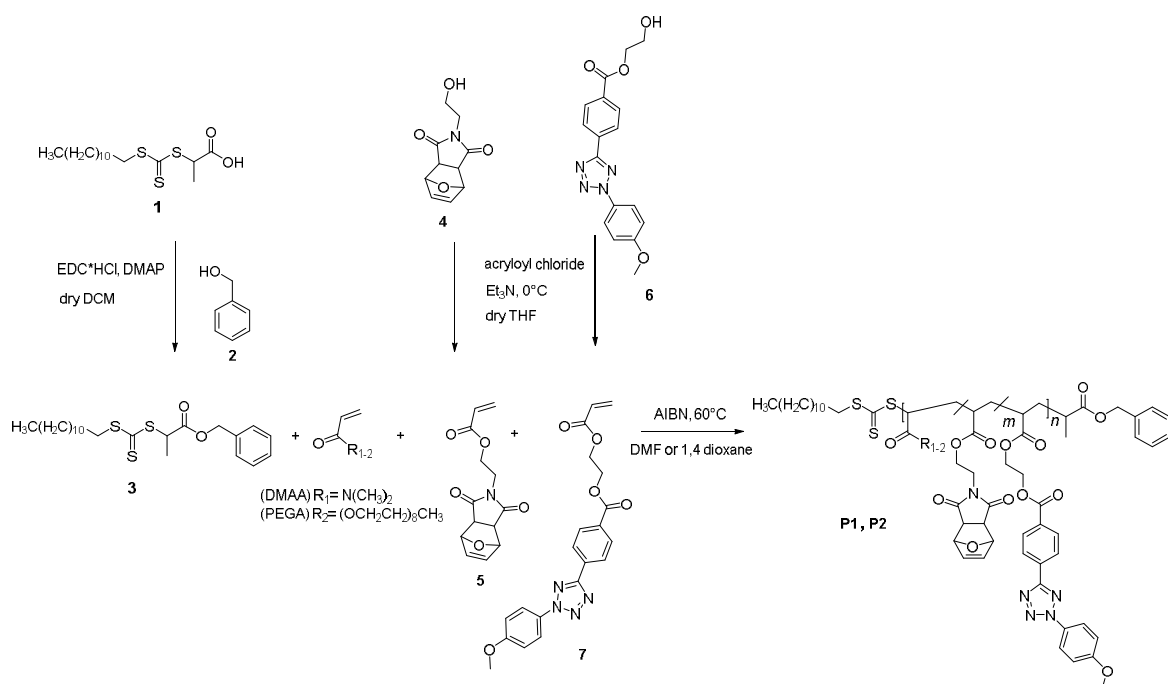
In the current section the UV-induced folding of linear polymer precursor into SCNPs *via* the NITEC reaction is presented. Furthermore, a small molecule study was performed to identify the preferred reactants of the UV-tetrazole. Herein, the main focus was placed on the NITEC reaction, yielding fluorescent pyrazoline adducts.

3.1.1 Photoreactive Monomer and RAFT Agent Synthesis

As the photoreaction of tetrazoles and maleimides result in highly fluorescent pyrazolines (refer to Section 2.2.6.1), a SCNP formation exploiting the NITEC reaction was targeted. Even the fumarate protected maleimide enables the possibility to synthesize the fluorescent pyrazolines utilizing UV-light.⁶ Based on this fact, the direct incorporation of the tetrazole and the protected maleimide *via* functional monomers was prepared to synthesize photoresponsive polymer precursors. The water solubility should be introduced by employing a commercially available water-soluble monomer. A radical polymerization using the functional tetrazole and protected maleimide monomers should be feasible, based on the furan-protected maleimide, where the active double bond is protected. The terpolymerization utilizing the water-soluble and the functional tetrazole and protected maleimide monomers should result in the targeted water-soluble and photoresponsive polymer precursors.

The polymerization method of choice was the reversible addition-fragmentation chain transfer (RAFT) polymerization, addressing the conditions necessary for the direct incorporation of functional monomers. Prior to polymerization, the synthesis of a suitable RAFT agent as well as the synthesis of the functional monomers were conducted. Therefore, the RAFT agent 2-(((dodecylthio)carbonothioyl)thio) propanoate (DoPAT) was modified with a benzylic functionality to determine the number of incorporated monomer units *via* nuclear magnetic resonance spectroscopy (NMR), exploiting the aromatic resonances of the benzyl function (Scheme 3.1.1, **3**). Next, the syntheses of the photoreactive tetrazole (**6**) and the protected maleimide (p-Mal, **4**) were carried out.

The final step prior polymerization entails the monomer synthesis utilizing acryloyl chloride to convert the OH-containing **6** and **4** derivatives into acrylate based monomers herein termed tetrazole acrylate (TetA, **5**) and protected maleimide acrylate (p-MaIA, **7**), respectively (Scheme 3.1.1, **5**, **7**). To impart water solubility, commercially available monomers such as *N,N*-dimethylacryl amide (DMAA) or polyethylene glycol acrylate (PEGA) were utilized.



Scheme 3.1.1: Synthesis of the DoPAT derivative (**3**) and the photoreactive and functional monomers (**5**, **7**) with subsequent RAFT terpolymerization including water-soluble monomers such as DMAA or PEGA, respectively.

The small molecules **3-7** were successfully synthesized (the corresponding characterization data can be found in the appendix, Figure 6.1.1, Figure 6.1.6 and Figure 6.1.9). The focus here is the synthesis of the terpolymerizations employing the newly synthesized compounds **3**, **5** and **7**. Initially, terpolymerizations utilizing the newly generated acrylate-based monomers (**5**, **7**) together with the water soluble DMAA were carried out. The monomer ratio employed for the terpolymerizations was the following, DMAA/MaIA/TetA (70/20/10), featuring a clear excess of the water-soluble part, due to the presence of non-water soluble photoreactive and functional monomers, which would otherwise strongly decrease the water-solubility of the resulting polymers.

The concentrations of the monomers, initiator and RAFT agent were maintained, only solvents or polymerization times were varied (refer to Chapter 5 for the conducted reactions).

Only one terpolymer containing DMAA as monomer could be successfully synthesized with 1,4-dioxane as solvent and 6 hours of polymerization time. The terpolymer DMAA/MaIA/TetA (**P1**) was analyzed *via* DMAc SEC as depicted in Figure 3.1.1. A broad and bimodal molecular weight distribution (MWD) with an average number molecular weight (M_n) with 6.1 kDa ($\mathcal{D} = 1.8$) was observed using poly(methyl methacrylate) (PMMA) as calibration standard (Table 3.1.1). The broad MWD reveals the non-controlled polymer synthesis of **P1** (Figure 3.1.1, **P1**). In all other polymerizations, where the reaction conditions were varied, no well-defined polymer could be synthesized, as the polymerization was limited to either low conversions or a loss of control during polymerization resulting in the Trommsdorff effect (refer to Chapter 5 for the conducted reactions).

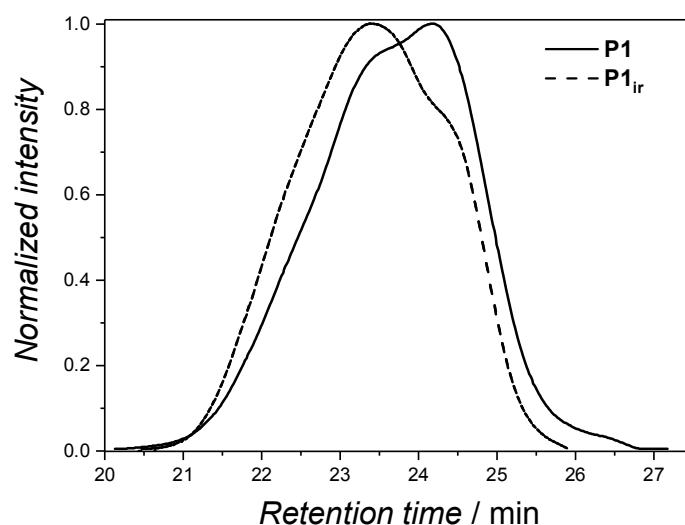


Figure 3.1.1: SEC traces of the DMAA/TetA/*p*-MaIA terpolymerization **P1** (black line) and the UV-light ($\lambda_{\max} = 320$ nm) irradiated polymer **P1_{ir}** (black dashed line) indicating intermolecular cross-linking of the initial polymer **P1**.

Although **P1** could not be synthesized in a controlled fashion, an irradiation with UV-light ($\lambda_{\max} = 320$ nm, refer to Chapter 5) under highly diluted conditions ($c = 0.017$ mg mL⁻¹) was nevertheless attempted. The irradiation of the polymer was conducted in deionized water for 10 h to generate intramolecular cross-linked SCNPs.

To guarantee a successful SCNP collapse, it is important to create only intramolecular linkages, otherwise an insoluble network is formed (refer to Section 2.3). After irradiation of polymer **P1**, the solvent was removed under reduced pressure and analyzed *via* DMAc SEC. As depicted in Figure 3.1.1 (**P1_{ir}**), after irradiation of the polymer, a shift towards lower retention times was obtained. Furthermore, the bimodal character of the SEC trace was maintained and an apparent molecular weight (M_{app}) change of 10.6 kDa ($\mathcal{D} = 1.4$) was observed, which represents an increase in number average molecular weight comparing **P1** to **P1_{ir}** (Table 3.1.1). Regarding the shift in the SEC trace to lower retention times, it can be assumed that undesired intermolecular linkage occurred after irradiation, even in a highly diluted solution. On the basis of the non-successful results obtained *via* SEC, representing one of the most important analytical method for SCNPs, together with the bimodal and broad MWD of the initial polymer **P1**, no further analysis methods were employed.

Table 3.1.1: SEC data of the terpolymer **P1** and the irradiated ($\lambda_{max} = 320$ nm) polymer **P1_{ir}** showing an increase in M_n .

Polymer	M_n	\mathcal{D}
P1	6.1 kDa	1.8
P1_{ir}	10.6 kDa	1.4

The DMAA monomer was exchanged with the PEGA monomer in order to investigate if there is any effect employing the acrylate based monomer. Here, PEGA entails the same acrylate moiety as for the synthesized **5** and **7** species, respectively.

The PEGA terpolymerizations were conducted employing the same monomer ratios as used for **P1** with PEGA/TetA/p-MalA (70/20/10). The PEGA based polymerizations showed similar results with either low or no conversion of the monomers (refer to Chapter 5 for the conducted reactions). In this case, the conditions for a successful terpolymerization employing PEGA/TetA/MalA were found with *N,N*-dimethylformamide (DMF) and a polymerization time of 10 h. Subsequently, SEC was conducted as analytical approach to characterize PEGA/TetA/MalA (**P2**). The obtained SEC trace of **P2** is depicted in Figure 3.1.2.

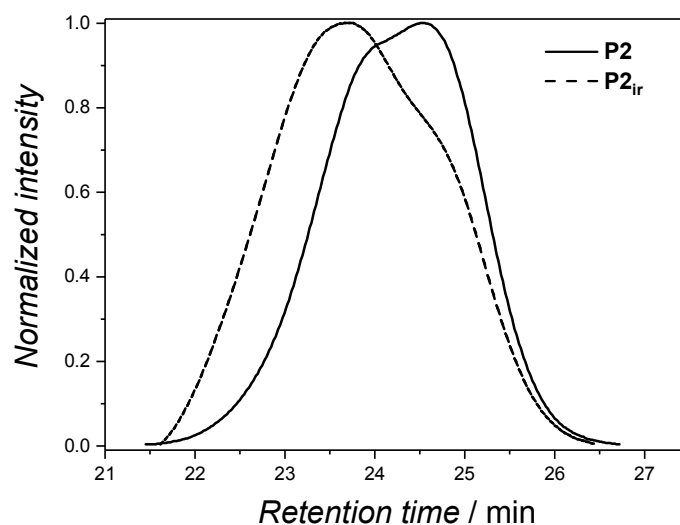


Figure 3.1.2: SEC traces of **P2** (black line) and the UV-light ($\lambda_{max}= 320$ nm) irradiated polymer **P2_{ir}** (black dashed line) indicating an intermolecular cross-linking of the initial polymer **P2**.

Here, a bimodal SEC trace was obtained for the PEGA containing polymer **P2** with a M_n of 3.7 kDa ($\bar{D} = 1.3$) (Table 3.1 2). Subsequently, the photoreaction was carried out under identical conditions as employed for **P1** by irradiation of the polymer under UV-light. As depicted in Figure 3.1.2 a shift towards lower retention times for the irradiated polymer (**P2_{ir}**) is noticed, indicating the same cross-linking reaction as observed for **P1_{ir}**. Furthermore, an increase in M_{app} was determined *via* SEC, resulting in a higher molecular weight for **P2_{ir}** with 4.5 kDa.

Table 3.1 2: SEC values of the terpolymer **P2** and the irradiated ($\lambda_{max}= 320$ nm) polymer **P2_{ir}** showing an increase in M_n and \bar{D} .

Polymer	M_n	\bar{D}
P2	3.7 kDa	1.3
P2_{ir}	4.5kDa	1.5

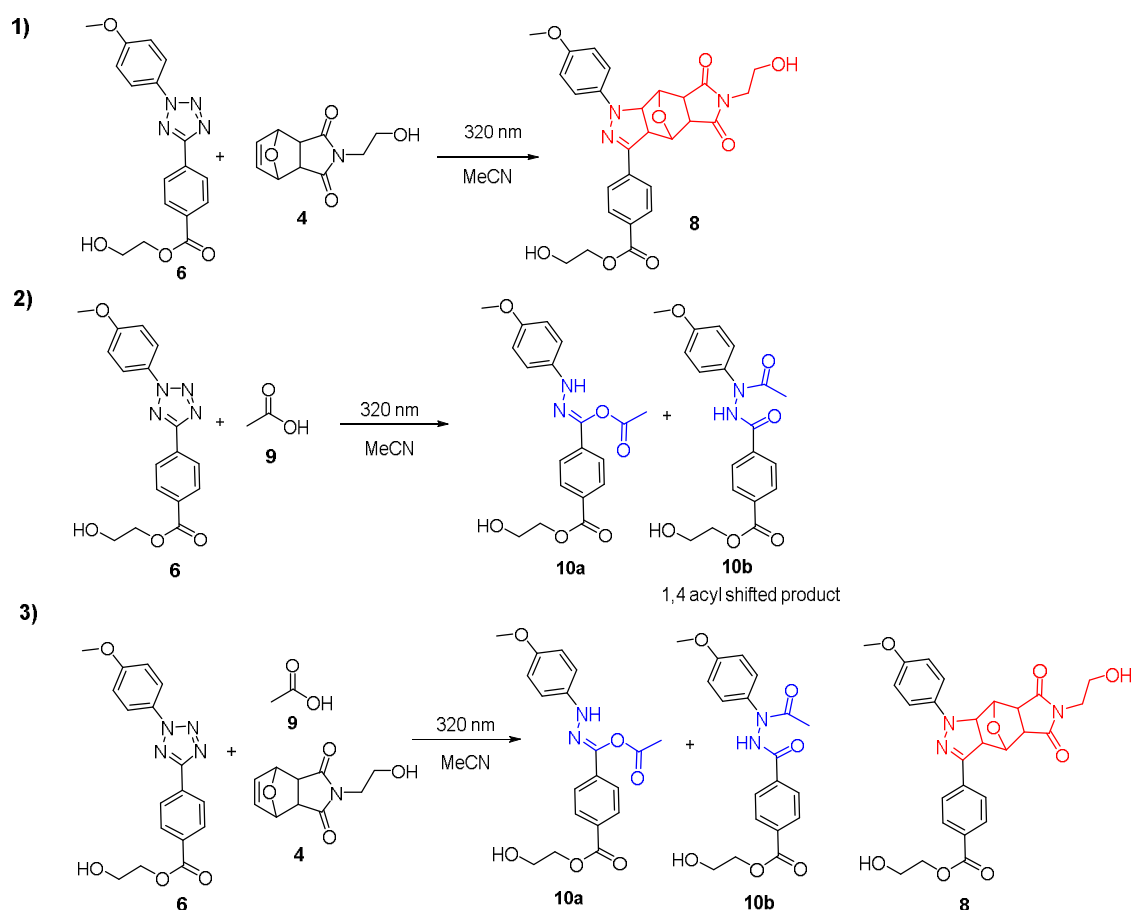
Thus, in summary, it appears that the terpolymerization as envisaged in Scheme 3.1.1 (see above) does not lead to the desired well-defined photoreactive terpolymers capable of undergoing light induced single chain compaction.

In order to regain control over the polymerization reaction itself, the initial approach employing direct incorporation of functional monomers *via* terpolymerizations was adapted to a post-modification of water soluble polymers. Recent studies by Lin *et al*¹²³ demonstrated that carboxylic acids are suitable reaction partners in a nitrile imine carboxylic acid ligation (NICAL), offering an alternative approach to utilize tetrazole photochemistry for SCNP formation. Thus, a post-modification of poly(acrylic acid) (PAA) with a subsequent functionalization of the photoresponsive groups was targeted, enabling the folding *via* a dual folding mechanism employing NITEC and NICAL. PAA is a well-known water-soluble polymer with many applications in consumer and biomedical products.^{226,227} Furthermore, PAA readily imparts water-solubility during homopolymerization in contrast to the terpolymerization with PEGA or DMAA, respectively.

3.1.2 Small Molecule Study of the UV-Tetrazole

Prior to the controlled RAFT polymerization of acrylic acid (AA), small molecule assessment were performed to investigate the reactivity of the nitrile imine generated by the photolysis of the parent tetrazole (**6**) with two reactants, *i.e.* *p*-Mal (**4**) and acetic acid (**9**) (Scheme 3.1.2). The reaction was performed in acetonitrile (MeCN) and irradiated with a UV-lamp ($\lambda_{\text{max}} = 320 \text{ nm}$).

The detailed reaction conditions for the small molecule study are located in Chapter 5. In total, three reactions were conducted employing **6**, **4** and **9**. In the first reaction 1) employing **6** + **4**, the solution was irradiated with UV-light to investigate the NITEC reaction. If a successful NITEC reaction proceeds, the pyrazoline derivative (**8**) is formed. In the second reaction 2), **6** + **9** are converted with UV-light to investigate the NICAL reaction. As mentioned above, the reaction between a carboxylic acid with the nitrile imine should lead to a substitution of **9** yielding a hydrazone derivative (**10a**) with a subsequent 1,4-acyl shift forming the hydrazine derivative (**10b**). The last reaction contained both reactants (**4** + **9**) in equimolar ratios to identify if either the NITEC or NICAL reaction is preferred.



Scheme 3.1.2: Overview of the small molecule study of the UV-active tetrazole **6** with 1) *p*-Mal (**4**) and 2) acetic acid (**9**) as reaction partner as well as the competitive reactions with both 3) *p*-Mal (**4**) and carboxylic acid (**9**). The irradiation was carried out in MeCN with UV-light ($\lambda_{max} = 320 \text{ nm}$) until the reactions were completed. Adapted with permission from reference [224]. Copyright (2015) American Chemical Society (ACS).²²⁴

The characterization of the NITEC and NICAL reaction products was investigated via ^1H NMR spectroscopy. The first reaction between **6** and **4** was analyzed via ^1H NMR spectroscopy (Figure 3.1.3). Here, the resonances at 4.93 (d) and 4.49 ppm (e) were highlighted in red and were identified as the resonances arising from the pyrazoline moiety. In proton NMR, the resonances were assigned to compound **8** arising from the reaction of **4** + **6**. In the aromatic region (7–8 ppm) of **8** with l (8.02 ppm), k (7.91 ppm), c (7.14 ppm) and b (6.95 ppm), evidence for an exclusive NITEC formation was found. The initial tetrazole **6**, employed for the small molecule study, differs in the aromatic region in ^1H NMR spectroscopy. In particular, the ^1H NMR resonances of **6** with e (8.30 ppm), d (8.22 ppm) c (8.07 ppm) and b (7.22 ppm) were completely different (refer to the appendix Figure 6.1.4).

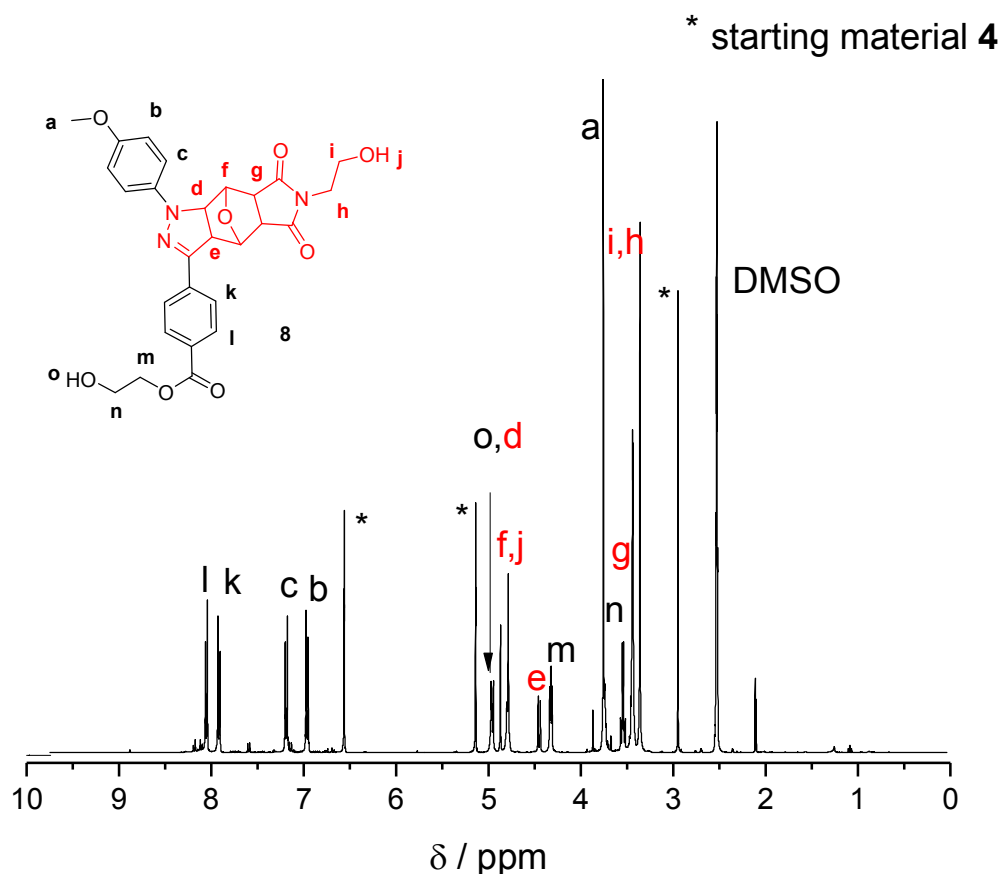


Figure 3.1.3: ^1H NMR spectrum of the raw product arising from the photoreaction with **6** and **4** generating the pyrazoline product **8** recorded in $\text{DMSO-}d_6$ at 400 MHz. The irradiation was conducted by applying UV-light ($\lambda_{\text{max}} = 320 \text{ nm}$). Adapted with permission from reference [224]. Copyright (2015) American Chemical Society (ACS).²²⁴

It can be assumed that a full conversion of the tetrazole and an exclusive formation of the NITEC reaction with the protected maleimide took place.

Subsequently, the second reaction was analyzed *via* ^1H NMR spectroscopy to investigate the reactivity of **9** towards **6** (Scheme 3.1.2). The proton NMR spectrum of reaction 2) revealed two NICAL species after irradiation with UV-light. The proposed hydrazine and hydrazone reaction products containing **10a** and **10b** were observed showing different proton resonances in ^1H NMR spectroscopy (Figure 3.1.4). In the low-field of the NMR spectrum, different NH resonances at 11.7 (e) and 11.2 ppm (n) were detected. The assignment to either **10a** or **10b** could be performed, due to the different chemical constitution after the acyl-shift. Specifically, the NH resonance of **10b** was assigned to 11.7 ppm, due to the presence of the acyl-group leading to a shift into the lower field of the ^1H NMR spectrum compared to **10a**.

The NH resonance of compound **10a** was assigned to 11.2 ppm based on the absence of an electron-withdrawing group, which is in direct proximity of the NH resonance (11.2 ppm). The assignment of the NH-resonances (11.2 and 11.7 ppm) of **10a** + **10b** can be utilized to identify the corresponding aromatic residues (7-8.5 ppm) by setting the aromatic as well as the NH integrals into proportion.

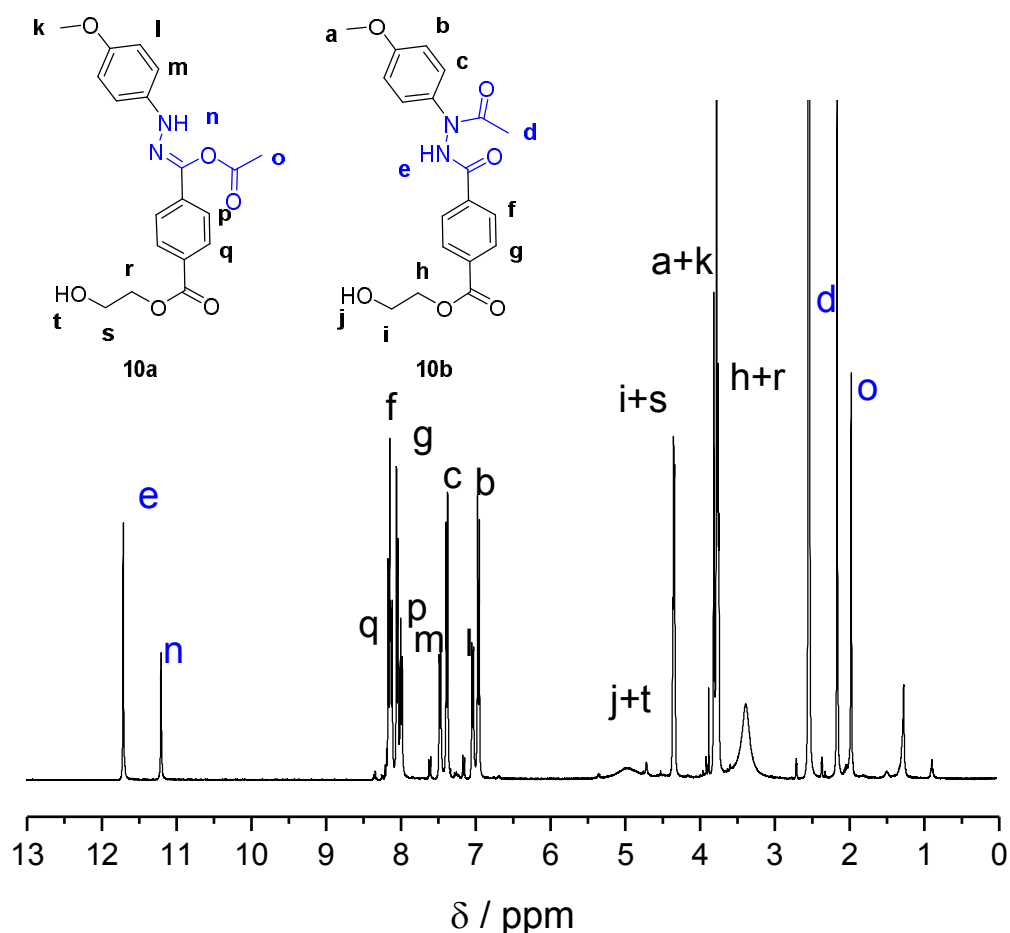


Figure 3.1.4: ^1H NMR spectrum of the NICAL raw products (**10a** + **10b**) recorded in $\text{DMSO-}d_6$ at 400 MHz. Adapted with permission from reference [224]. Copyright (2015) American Chemical Society (ACS).²²⁴

Subsequently, **4** and **9** were irradiated together in a one pot reaction with **6** to establish, if one reaction partner is preferred by the light-generated nitrile imine. The reaction was carried out employing 1.3 eqs. of each reactive partner with respect to the tetrazole (refer to Chapter 5 for detailed reaction conditions). To identify whether the NITEC or NICAL reaction is preferred, the recorded ^1H NMR spectra of the three reactions were plotted together.

In particular, the aromatic region of **8** and **10a** + **10b** as well as the competitive reaction were stacked and plotted in one figure to ease the comparison of the reaction products. (Figure 3.1.5). The NMR spectra in the aromatic region (6.8-8.4 ppm) from **8** or **10a** + **10b** indicate different proton resonances. Especially the aromatic resonance from **8** at 7.2 ppm (Figure 3.1.5, 1, b) can be utilized to determine the ratios of the preferred reaction pathways. To calculate the NITEC/NICAL ratio of the competitive reaction channels, the respective and relevant integrals from **8** (7.2 ppm) and **10a** + **10b** (7.4 and 7.36 ppm) were set into relation. The product percentages were calculated utilizing the above mentioned resonances and a ratio of the NICAL vs. the NITEC reaction of 1: 4.8 (**8:10**) were determined, indicating a clear preference for the NICAL pathway in the presence of p-Mal (Figure 3.1.5).

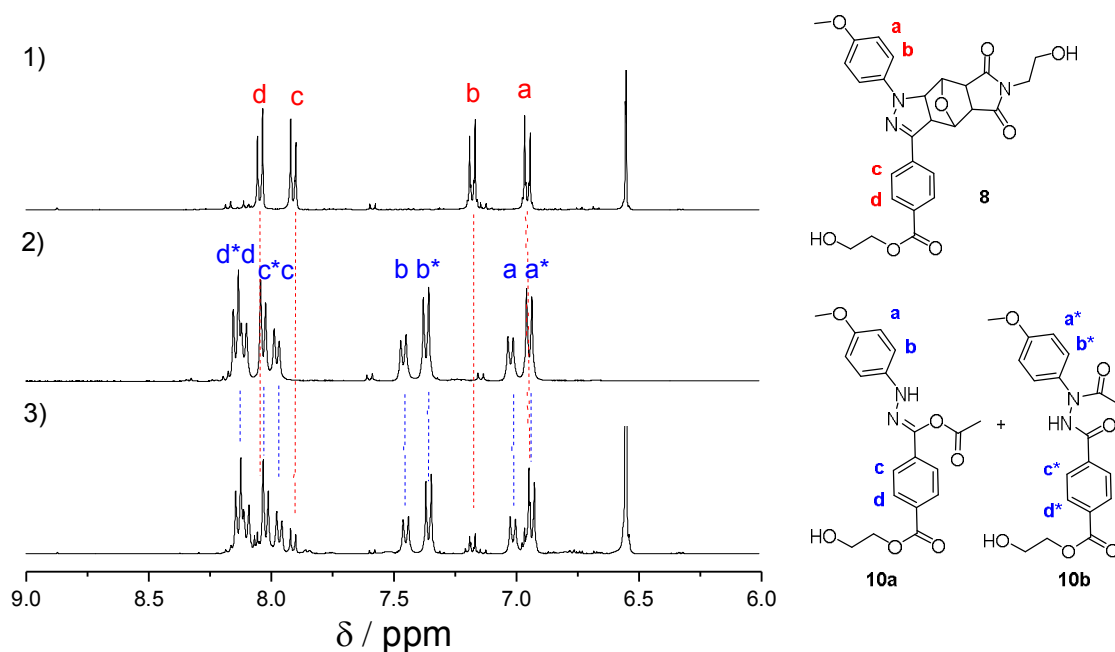


Figure 3.1.5: ^1H NMR spectra (9-6 ppm.) of the photo-induced raw products of 1) **8**, 2) **10a** + **10b** and 3) **8**, **10a** + **10b** recorded in $\text{DMSO-}d_6$ at 400 MHz. The reactions were irradiated with UV-light ($\lambda_{\text{max}} = 320 \text{ nm}$). Adapted with permission from reference [224]. Copyright (2015) American Chemical Society (ACS).²²⁴

After successful assessment *via* proton NMR, the reaction products were further analyzed employing UV/Vis spectroscopy. Here, the starting material **6** as well as the products **8**, **10a** + **10b** were investigated *via* UV/Vis spectroscopy (Figure 3.1.6). The absorbance maximum of **6** was detected at close to 290 nm. For **8**, a local maximum at 415 nm could be observed, which is characteristic for pyrazolone adducts.

In the case of **10a** + **10b**, the absence of the typical pyrazoline maximum at 415 nm was observed, instead a different maximum in the UV range at close to 265 nm is seen. In the competitive reaction, where **8**, **10a** + **10b** are present, both absorbance maxima were observed. However, the absorbance maximum at 415 nm of the competitive reaction 3) was significantly reduced in comparison to the absorbance maximum when only **8** was employed. These results are congruent with the obtained data from ^1H NMR, showing a minor NITEC reaction pathway during the competitive reaction in comparison to pure NITEC. The most important feature in the context of generating fluorescent SCNPs is discussed next, *i.e.* the inherent fluorescence of the system recorded by fluorescence spectroscopy.

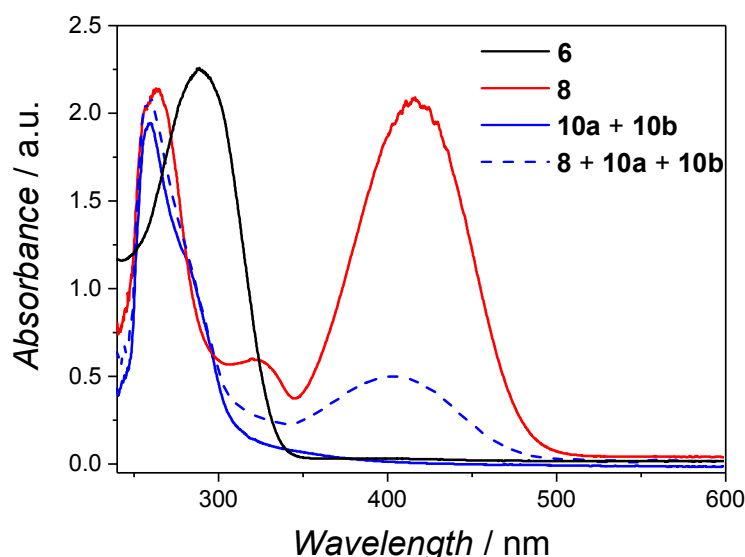


Figure 3.1.6: UV/Vis spectra of **6** (black line) ($c = 0.5 \text{ mg L}^{-1}$) and the irradiated ($\lambda_{\text{max}} = 320 \text{ nm}$) reaction products from the small molecule study with **8** (red line), **10a** + **10b** (blue line), and the reaction mixture **8** + **10a** + **10b** (blue dashed line) recorded in DMSO ($c = 0.016 \text{ mol L}^{-1}$) Adapted with permission from reference [224]. Copyright (2015) American Chemical Society (ACS).²²⁴

To identify the fluorescence behavior of the generated reaction products **8** and **10a** + **10b**, fluorescence measurements were performed. In order to compare both reaction products regarding the fluorescence, the excitation wavelength was kept in the visible range at 440 nm. This wavelength was determined utilizing fluorescence spectroscopy to yield the highest fluorescence emission for **8**. As depicted in Figure 3.1.7 (a), **8** shows a fluorescence emission band at 575 nm, when excited with a wavelength of 440 nm.

The highly fluorescent features of **8** can also be readily detected by exciting the molecule with a hand-held UV-lamp ($\lambda_{em} = 366$ nm), making the pyrazoline structural element highly attractive for exploitation in SCNPs for *in vivo* imaging.

For **10a** + **10b**, an emission band at 525 nm was observed (Figure 3.1.7). Regarding the emission intensity of product **8**, it can be stated that the products **10a** + **10b**, representing the pure NICAL reaction, show only low fluorescence intensities. The NICAL chemistry therefore represents a non-suitable tool for the generation of imaging agents. The almost non-fluorescent NICAL (**10a** + **10b**) reaction products were also irradiated with a hand-held UV-lamp ($\lambda_{em} = 366$ nm), underpinning the low fluorescence emission found *via* fluorescence spectroscopy (Figure 3.1.7, b). Comparing both fluorescence features found for **8** and **10a** + **10b**, only **8** represents a potential chemistry, which can be applied for imaging in biological environments. The excitation wavelength in the visible range of 440 nm together with the intense emission band at 575 nm offers a perfect combination for cell imaging without the need of high energetic UV-light. After successful investigation of the small molecule study using the UV-active tetrazole (**6**), the polymerization of acrylic acid to generate the water-soluble backbone polymer was carried out.

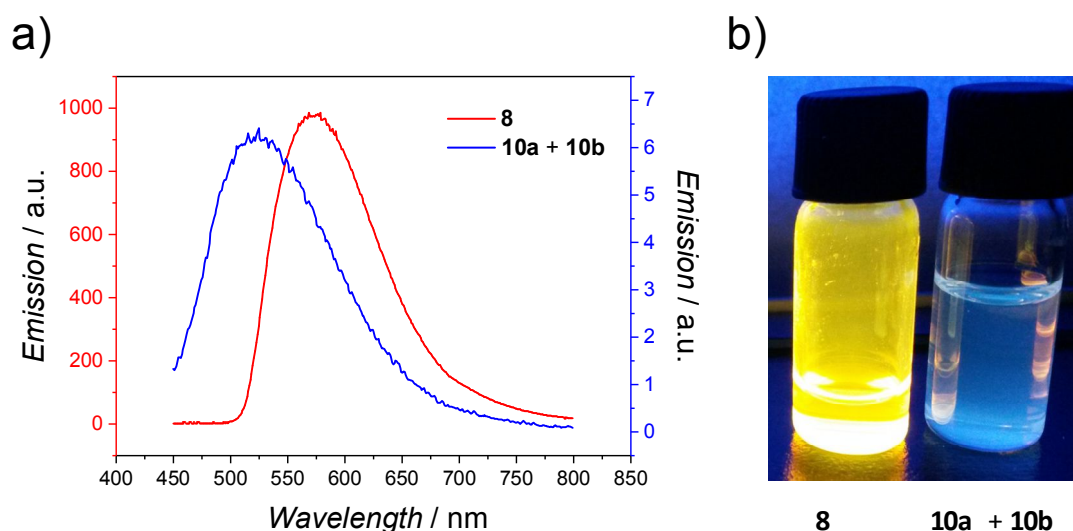
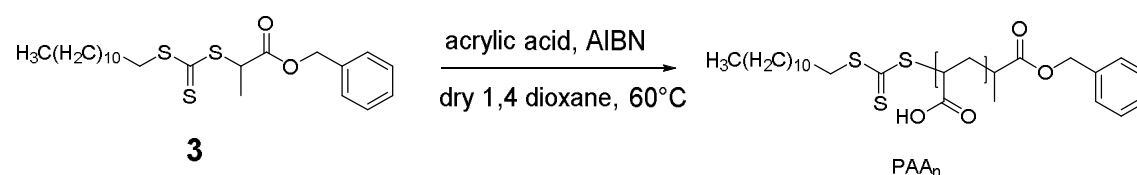


Figure 3.1.7: a) Fluorescence spectra of the reaction products **8** and **10a** + **10b** recorded in DMSO ($c = 0.016$ mol L⁻¹) with the excitation wavelength of 440 nm, b) Image of the fluorescent reaction products **8** and **10a** + **10b** irradiated with a hand-held UV-lamp ($\lambda_{em} = 366$ nm). Adapted with permission from reference [224]. Copyright (2015) American Chemical Society (ACS).²²⁴

3.1.3 Preparation of PAA Polymers Containing the UV-Light Active Tetrazole

Once the small molecule study was successfully completed, the synthesis of the precursor polymers constituting the SCNPs was targeted. The previously synthesized RAFT agent equipped with the benzylic end group (**3**) was also employed for the polymerization. The preparation of PAA with high conversion and low \bar{D} via RAFT polymerization is challenging due to chain transfer reactions of the monomer leading to potentially low conversions or branching of the polymer.²²⁸

For the polymerization of acrylic acid the previously functionalized DoPAT-RAFT agent (**3**) was exploited. In total, three PAA polymers (**P3-P5**) with different chain lengths were synthesized (refer to Chapter 5 for the polymerization conditions). The PAA_n polymers were analyzed via ¹H NMR spectroscopy to determine M_n .



Scheme 3.1.3: RAFT polymerization employing the previously synthesized RAFT agent (**3**) with acrylic acid in dry 1,4 dioxane at 60°C.

As noted above, the calculation of M_n was targeted by utilizing the previously introduced benzylic end-group in the RAFT agent. Here, only an exemplary ¹H NMR spectrum is shown, due to the identical chemical constitution of the PAA based polymers (Figure 3.1.8). The analysis of the ¹H NMR spectrum indicates the resonances associated with the acrylic acid backbone with d (12.2 ppm), e (4.1 ppm) and f (1.7 ppm) as well as the resonances of the benzylic end-group j (7.3 ppm) after polymerization. The calculation of the repeating units in the polymer was performed using the integrals of the introduced benzylic end-group j (7.3 ppm), which were set into proportion with the integrals of the polymer backbone e (4.1 ppm).

The estimation of M_n for the different **P3-P5** utilizing ^1H NMR resulted in 13.4 kDa for **P3** with a chain length of 180 monomer units, 6.9 kDa for **P4** with a chain length of 80 monomers and 5.4 kDa for **P5** involving 69 acrylic acid monomer units. Based on these calculations, resulting in different M_n for the PAA based polymers (**P3-P5**), the post-modification reaction with the functional groups were conducted. The SEC measurements were performed *via* *N,N*-dimethyl acetamide (DMAc) SEC, after anchoring of the corresponding functional groups to the PAA polymers. Here, the reaction conditions for the DMAc SEC measurements are maintained allowing for to detect a change in M_{app} .

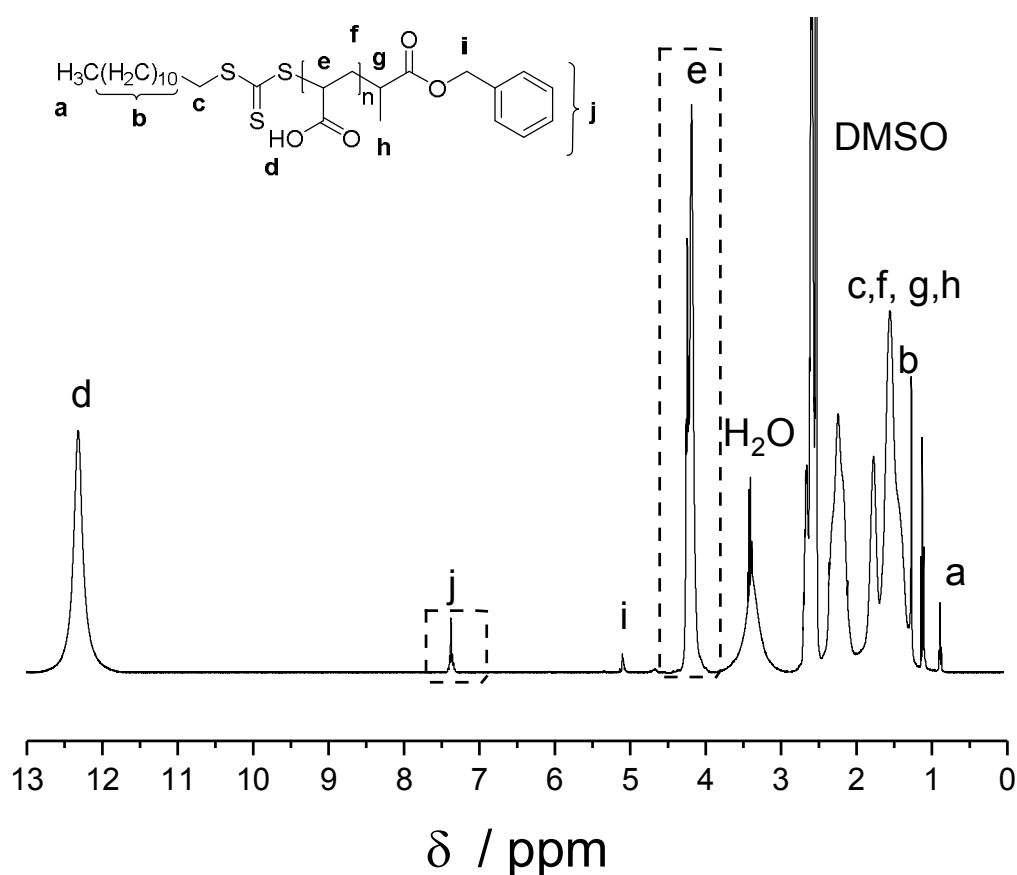
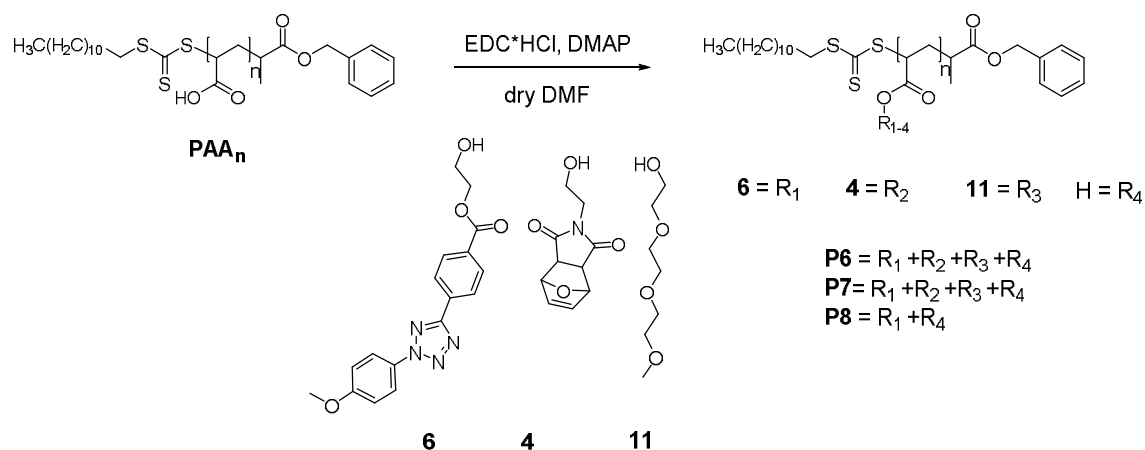


Figure 3.1.8: Exemplary ^1H NMR spectrum of the linear **P3** precursor. The integral of the aromatic resonance at 7.36 ppm (*j*) and the integral of the resonance at 4.1 ppm associated with the polymer backbone, were employed for estimating M_n of the polymers by ratioing the integrals. **P3** was measured in $\text{DMSO-}d_6$ at 400 MHz. Adapted with permission from reference [224]. Copyright (2015) American Chemical Society (ACS).²²⁴

In subsequent Steglich esterifications, **P3-5** were statistically functionalized with the OH derivatives **4**, **6** and triethyleneglycol monomethylether (TEG) (Scheme 3.1.4). Polymer **P3** and **P4** were functionalized with **6**, **4** and TEG (**11**) to obtain the photoresponsive polymer precursor **P6** and **P8**, respectively.

The TEG moiety was incorporated in the p-Mal containing polymers, which have the potential to collapse *via* NITEC. Trapping more carboxylic acids from the polymeric backbone with **11** may increase the biocompatibility for further application as fluorescent SCNPs in cells.

The next post-modification employing **P5** as initial polymer with a chain length of 69 monomer units was conducted with **6** only, since a NICAL triggered folding of the polymer with the carboxylic acid backbone was targeted. The functionalization of **P5** resulted in the photoresponsive polymer **P8**. The functionalization of the polymers **P6**, **P7** and **P8** was characterized *via* ^1H NMR spectroscopy to verify the successful post-modification.



Scheme 3.1.4: Statistical functionalization *via* Steglich esterification of **P3-P5** in DMF employing **6**, **4** and **11** leading to **P6**, **P7** and **P8**. **P6** and **P8** were additionally equipped with **4** and **11**, and **P8** contains only **6**.

First, **P6** was analyzed *via* ^1H NMR spectroscopy, which should be functionalized with **6**, **4** and **11** (Figure 3.1.9). In the recorded ^1H NMR spectrum, all incorporated groups from the post-modification reaction could be assigned to **6**, **4** and **11**. However, one signal in the aromatic region at 8.2 ppm, which could be attributed to **6** was reduced, and in parallel a new resonance at 6.9 ppm appeared, indicated with g'.

When **P8** was recorded *via* ^1H NMR (Figure 3.1.9, b) even a completely vanished resonance at 8.2 ppm was observed. In addition, the resonance at 6.9 ppm (g') as observed for **P6** was recorded.

Before the molar ratios of the functional groups in **P6-8** were calculated, a verification for the successful incorporation of **6** was necessary. To verify the

successful post-modification of **6** in the PAA polymers **P6-8**, correlation spectroscopy (COSY) measurements were carried out. To compare the correlations of **P6** and **P8**, an additional correlation COSY spectrum of **6** was recorded. In summary, three COSY spectra of **6**, **P6** and **P8** investigating the phenomenon of the shifted proton resonance at 6.9 ppm were measured. To simplify the observed correlations, only the aromatic region of **6**, **P6** and **P8** is illustrated. First, the COSY NMR of **6** was recorded, as illustrated in Figure 3.1.10.

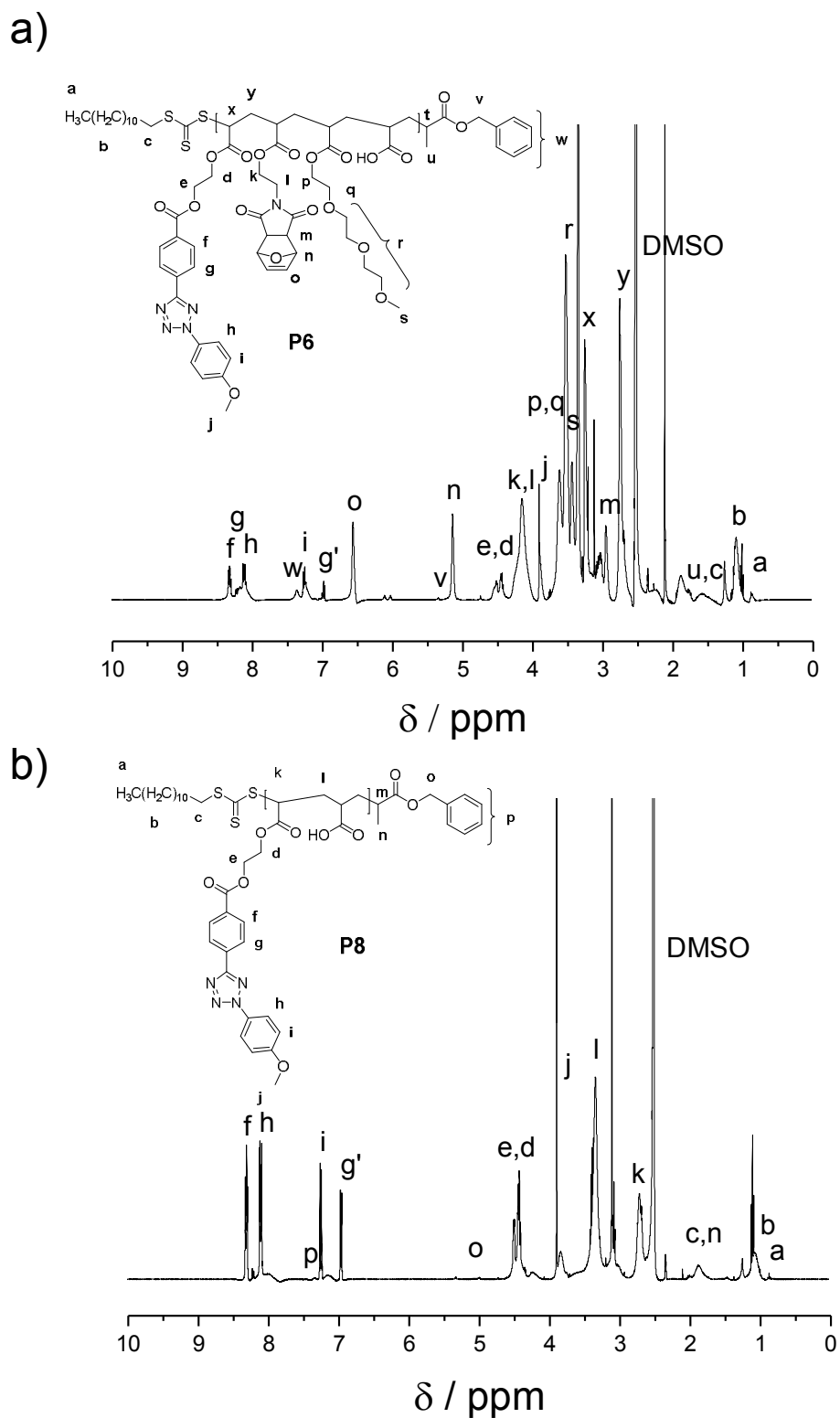


Figure 3.1.9: ^1H NMR spectra of **P6** and **P8** showing the incorporated resonances associated with the incorporated groups of **4,6** and **11**. **P6** and **P8** were recorded in $\text{DMSO-}d_6$ with 400 MHz. The shifted signal 'g' to 6.96 ppm was investigated via COSY NMR afterwards indicating a shift of the resonances due to an interaction with the polymer backbone. Adapted with permission from reference [224]. Copyright (2015) American Chemical Society (ACS).²²⁴

The small molecule **6** was analyzed showing interactions of the aromatic proton resonances associated with the aryl-flanked tetrazole. In particular, the interactions are clearly distinguishable from each other and can be divided in the two benzylic groups of the tetrazole. The proton resonances of the aryl group bearing the methoxy moiety correlate with each other and are highlighted with h (8.1 ppm) and i (7.2 ppm) in the spectrum. A second correlation, involving the carboxyl containing aromatic resonances was found. These signals are indicated with f (8.3 ppm) and g (8.2 ppm) The 2D COSY NMR spectrum of **6** indicates the correlation of each benzylic group with each other.

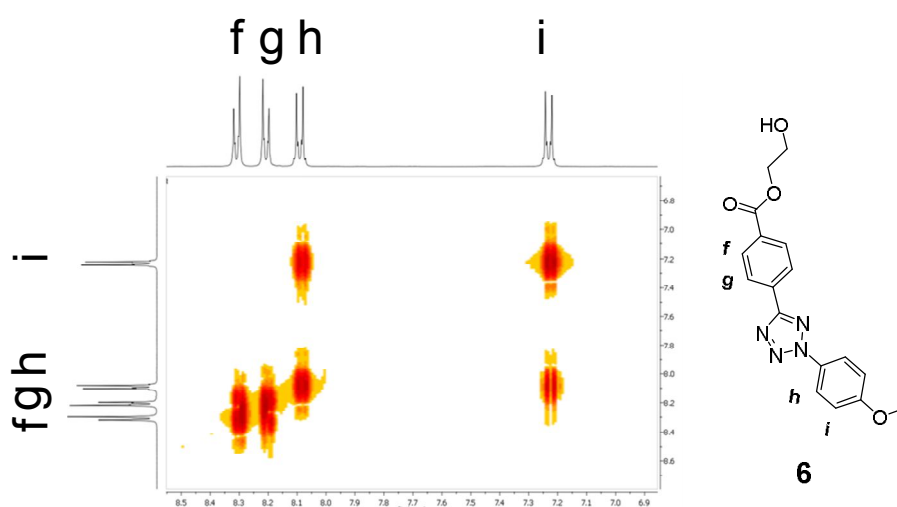


Figure 3.1.10: COSY NMR spectrum of **6** of the aromatic region measured in DMSO-*d*₆ at 400 MHz. Adapted with permission from reference [224]. Copyright (2015) American Chemical Society (ACS).²²⁴

The investigated correlations of **6** were compared with **P6** and **P8** to verify if the tetrazole was incorporated. Therefore, COSY NMR spectra were recorded of **P6** and **P8** illustrated in Figure 3.1.11. In the case of **P6**, more correlations compared to the small molecule **6** were observed. The correlations found for **6**, involving the correlation of f (8.3 ppm) with g (8.2 ppm), and h (8.1 ppm) with i (7.2 ppm), were also observed for polymer **P6**, even when the original signal g (8.2 ppm) was reduced. Furthermore, additional interactions including the new resonance g' (6.9 ppm) were detected. In particular, the resonance g' (6.9 ppm) interacts with both the original resonance g (8.2 ppm) as well as with the resonance f (8.3 ppm).

In the case of **P8**, the origin resonance g, which should be found at 8.2 ppm was completely vanished. Only interactions between the new resonance g' (6.9 ppm) with the resonance f (8.3 ppm) were observed. Comparing these results it seems that the presence of the TEG and the p-Mal groups have an influence on the aromatic signal g' (6.9 ppm).

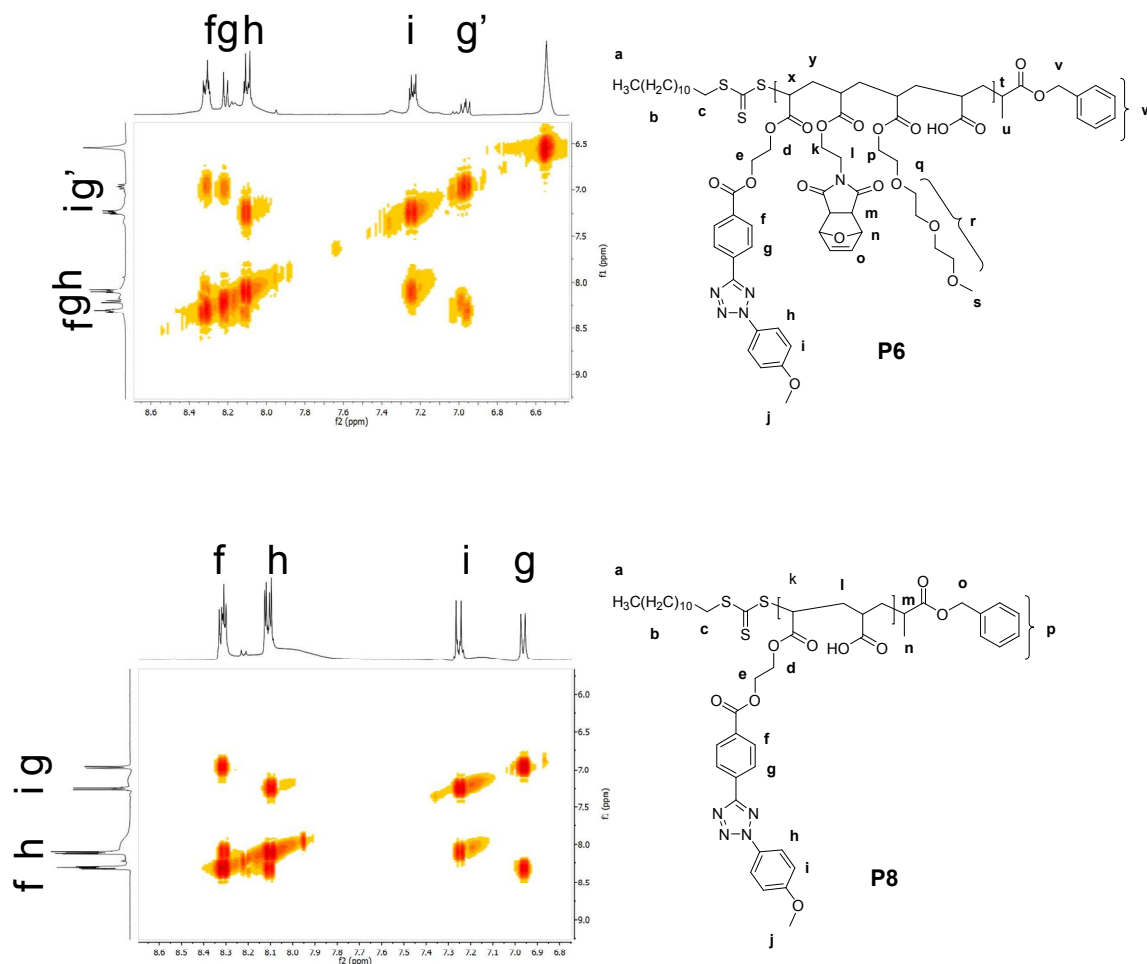


Figure 3.1.11: COSY NMR spectra of **P6** and **P8** showing the correlation in the aromatic region of the NMR spectrum. Correlations between f and g, h and i were found in both polymers. Adapted with permission from reference [224]. Copyright (2015) American Chemical Society (ACS).²²⁴

In summary, the correlation signals between f and g were clearly distinguishable in both polymers **P6** and **P8**, showing the same resonances as found for **6**, indicating the successful incorporation of **6**. Nevertheless, a second analytical method was employed to ensure the incorporation of the important photoreactive compound **6**. To verify the incorporation of **6** in **P6** and **P8**, UV/Vis spectroscopy measurements were conducted as depicted in Figure 3.1.12.

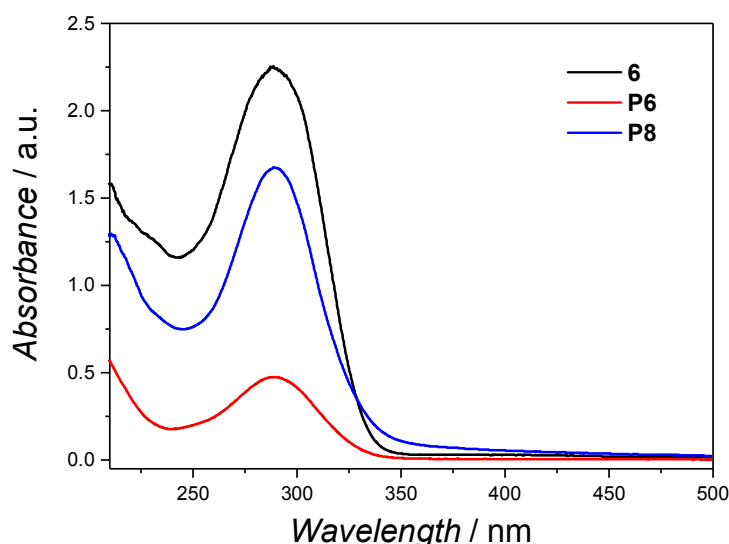


Figure 3.1.12: Exemplary UV/Vis spectra of the UV tetrazole **6** ($c = 0.016 \text{ mol L}^{-1}$) and the polymer precursor **P6** and **P8** ($c = 0.03 \text{ mg mL}^{-1}$.) recorded in MeCN. Adapted with permission from reference [224]. Copyright (2015) American Chemical Society (ACS).²²⁴

The obtained UV/Vis spectrum for **6** was plotted together with the absorbance spectra of **P6** and **P8**. The photoreactive compound **6** showed an absorbance maximum at 290 nm, which was already investigated in Section 3.1.2. In the case of the post-modified polymers **P6** and **P8**, the same absorbance maximum was detected at 290 nm, indicating the successful incorporation of **6** in **P6** and **P8**. The measurement of **P6** was exemplarily performed, due to identical functional groups employed in the post-modification reaction with **4**, **6** and **11** leading to **P7**. The incorporation of the photoreactive compound **6** was evidenced *via* COSY NMR and UV/Vis spectroscopy, leading to the successful synthesis of the photoreactive precursors **P6-8**.

Finally, the functionalization degree of the incorporated functional groups were calculated employing again the benzylic end group in the polymers **P6-8**. In Table 3.1.1, the functionalization degree of the polymers are collated, which were calculated *via* ^1H NMR spectroscopy. In the case of **P6**, 9 mol% of **6**, 12 mol% of **4** and 26 mol% of **11** in the acrylic acid backbone were incorporated suggesting an overall functionalization degree of 47 mol%. The post-modified polymer **P7** posses almost the same ratio as found for **P6** with 8 mol% of **6**, 12 mol% of **4** and 24 mol% of **11**. The complete functionalization degree of **P8** was calculated to close to 44 mol%.

For **P8** an overall functionalization degree of 60 mol% of **6** was determined via ^1H NMR spectroscopy. The post-modification resulted in a non-quantitative functionalization of the polymer precursor **P6-8**. Furthermore, only an overall functionalization of less than 50 mol% could be achieved in polymer **P6** and **P7**, leading to a slight excess of the carboxylic acid groups in those polymers. In the case of **P8**, an excess of the tetrazole moiety was determined in contrast to the acid groups. After successful investigation of the polymer precursors **P6-8**, the photo-induced compactations were performed.

Table 3.1.1: Functionalization degrees of the post-modified polymer precursor **P6-8**. The calculations are performed via ^1H NMR spectroscopy utilizing the previously introduced benzylic end group of the RAFT agent. Adapted with permission from reference [224]. Copyright (2015) American Chemical Society (ACS).²²⁴

Polymer	Tet (mol%)	p-Mal (mol%)	TEG (mol%)	Total (mol%)
P6	9	12	26	47
P7	8	14	24	44
P8	60	-	-	60

3.1.4 UV-light Induced Folding of PAA Polymers and their Characterization

Finally, the preparation of the SCNPs employing UV-light was carried out (for detailed conditions refer to Chapter 5). Based on the water soluble PAA backbone of **P6-8**, the precursors showed excellent solubility in water. Thus, **P6-8** were dissolved separately in deionized water under high dilution ($c = 0.017 \text{ mg mL}^{-1}$) and irradiated for 17 h with UV-light ($\lambda_{\text{max}} = 320 \text{ nm}$). Subsequently, the water was removed under reduced pressure and the SCNPs were analyzed. To characterize the fluorescent SCNPs, UV/Vis and fluorescence spectroscopy were employed as initial analytical methods. To verify the successful photochemical reaction, in particular NITEC and NICAL reaction, the UV/Vis and fluorescence spectroscopic analysis of the small molecule study is illustrated together with the data obtained from the polymers **P6-8** before and after irradiation (**SCNP6** + **SCNP8**) (Figure 3.1.13).

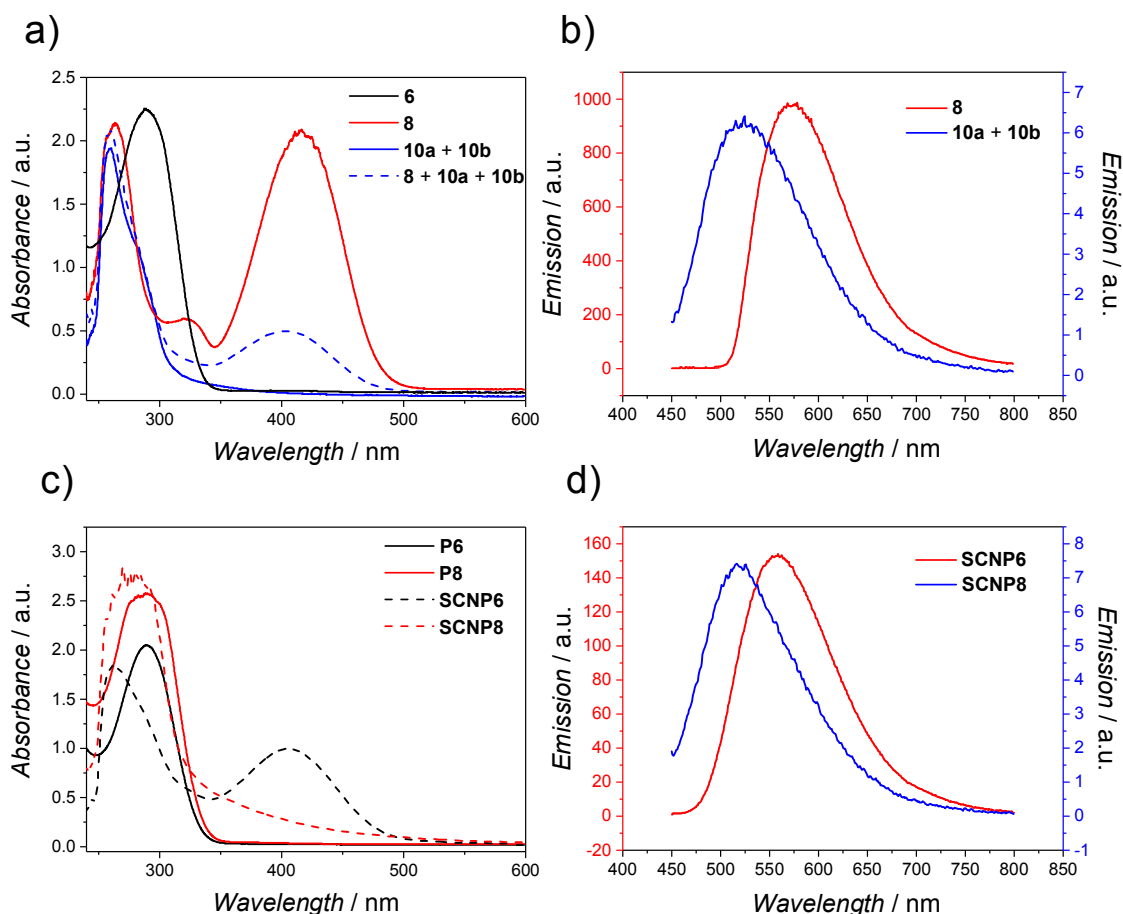


Figure 3.1.13: a) UV/Vis spectra of **6** (black), **8** (red) and **10a + 10b** (blue) as well as the reaction products **8 + 10a + 10b** (blue dashed line) indicating different absorbance maxima corresponding to **8** or **10a + 10b**, b) fluorescence spectra of **8** and **10a + 10b** showing different emission maxima corresponding to either NITEC or NICAL, c) UV/Vis absorbance spectra of the polymer precursors **P6** and **P8** and the corresponding **SCNP6** and **SCNP8** indicating the same absorbance properties as found for **8** and **10**, d) fluorescence spectra of **SCNP6 + SCNP8** giving the characteristic emission as found for **8** and **10a + 10b**. The measurements were recorded in DMSO with a concentration of 0.016 mol L^{-1} for the small molecules and 0.5 mg mL^{-1} for the polymer samples. Adapted with permission from reference [224]. Copyright (2015) American Chemical Society (ACS).²²⁴

As mentioned previously (Section 3.1.2), the absorbance (Figure 3.1.13, a) maximum of the tetrazole was observed at 290 nm. The reaction product **8** obtained from the small molecule study showed a specific absorption maximum at 415 nm, which is characteristic for pyrazolines. For **10a + 10b**, an absence of these absorption maximum at 415 nm was found, showing only a maximum at 265 nm. The same absorbance maximum c) at 290 nm was observed for the functionalized polymers **P6** and **P8** as already stated (Section 3.1.2).

Importantly, the same absorption properties were detected, comparing **8** and **10a + 10b** with the prepared **SCNP6** and **SCNP8**, showing either the maximum at 415 nm or 265 nm, respectively.

Here, the presence of the local absorbance maximum at 415 nm for **SCNP6** was observed. For **SCNP8**, the absence of this maximum was detected. Both UV/Vis spectra of **SCNP6** and **SCNP8** are congruent with the absorbance spectra obtained for **8** and **10a + 10b**. In addition, the fluorescent features for **SCNP6** and **SCNP8** are in perfect agreement with the fluorescent features found for **8** and **10a + 10b** with emission maxima of 475 nm or 575 nm, respectively. Moreover, the excitation with a UV-lamp ($\lambda_{em} = 366$ nm) of **SCNP6** and **SCNP8** indicated the same fluorescent features as observed for **8** and **10a + 10b** (Figure 3.1.14).

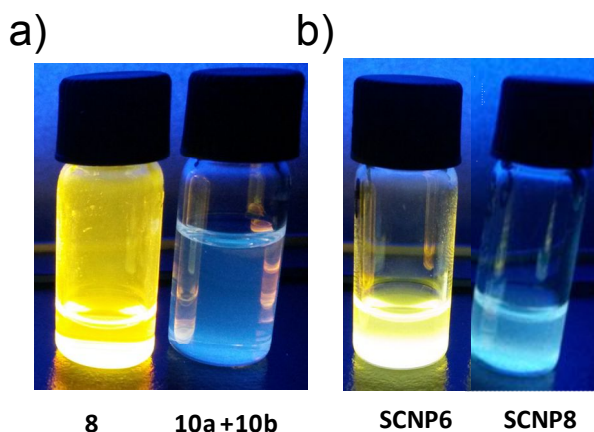


Figure 3.1.14: Image of the fluorescent reaction products **8**, **10a + 10b** and **SCNP6** and **SCNP8** indicating the same fluorescence properties, when excited with a UV-lamp ($\lambda_{em} = 366$ nm). Adapted with permission from reference [224]. Copyright (2015) American Chemical Society (ACS).²²⁴

The first evidence for the successfully conducted photoreactions of **P6-8** were found in UV/Vis and fluorescence spectroscopy. The results must, however, be verified applying more analytical approaches such as ^1H NMR spectroscopy. Therefore, ^1H NMR spectroscopy was employed to examine the UV-irradiated polymers **SCNP6-8**. **SCNP6** was plotted together with **P6** to investigate the pyrazoline formation *via* ^1H NMR spectroscopy (Figure 3.1.15). To verify the NITEC reaction in **SCNP6**, a zoom of the important region (5.3-4.6 ppm) was performed. In the upper part of the spectrum, where **P6** is illustrated, only evidence for the protected maleimide signal a at 5.1 ppm was observed. In contrast, **SCNP6** showed two additional signals at 4.93 ppm (b) and 4.81 ppm (c).

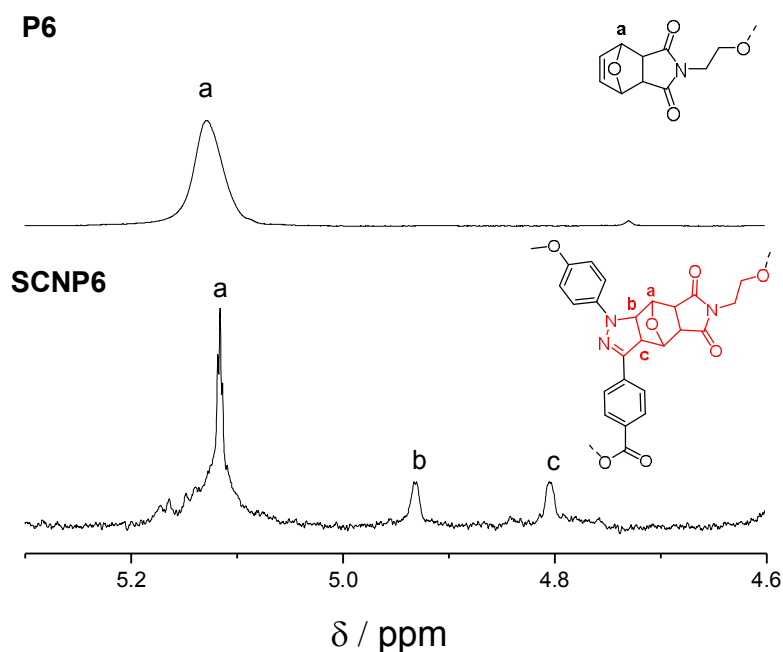


Figure 3.1.15: ¹H NMR spectra of **P6** and the corresponding **SCNP6** showing the newly generated pyrazoline signals after irradiation ($\lambda_{\max} = 320$ nm) of the polymer. The polymer precursor was measured in DMSO-*d*₆ with 400 MHz. Adapted with permission from reference [224]. Copyright (2015) American Chemical Society (ACS).²²⁴

The resonances b (4.93 ppm) and c (4.81 ppm) of **SCNP6** are not in perfect agreement with the pyrazoline resonances from **8**, which were observed at 4.5 and 4.8 ppm. However, it has to be considered that the pyrazoline signals were anchored on the PAA polymer, representing a different chemical environment as for the small molecule **8**. Based on the results from UV/Vis, fluorescence and NMR spectroscopy, it can be assumed that the NITEC reaction took place after irradiation with UV-light of **P6**.

It has to be noted that the nitrile imine reaction is a non-orthogonal (refer to Section 2.2) reaction and therefore several side reactions such as dimerization of the tetrazole as well as reaction with solvents can lead to unexpected resonances in the aromatic region. Therefore, the pyrazoline integrals b (4.93 ppm) and c (4.81 ppm) and the reduced p-Mal integral a (5.1 ppm) in the NITEC driven collapsed SCNPs (**SCNP6** and **SCNP7**) were employed to determine, whether the NICAL or NITEC reaction pathway was preferred. These integrals were set into proportion, in order to calculate the dual folding mechanism ratios. The ratio of the NITEC reaction was calculated for **P6** to 70 % and for **P7** to 55 %, suggesting to a preferred NITEC reaction in the polymers **P6** and **P7**.

These results are in contrast to the small molecule studies, which resulted in a clear preference of the NICAL reaction in presence of **4**. One explanation for the preferred NITEC reaction in the SCNPs could be the accessibility of the carboxylic acids compared to the incorporated p-Mal in the polymer. Thus, the bulky tetrazole has only limited access to the acids, leading to a decreased NICAL driven reaction. As a result, a local excess of the incorporated p-Mal groups is present and would lead to the NITEC preference in the polymer.

In addition, it has to be considered that the tetrazole could self-dimerize upon irradiation with UV-light, thus affecting the calculated ratio. However in the small molecule study no dimerization products, neither in the presence of **4** nor in the presence of **9**, were observed. Due to the highly functionalized polymers **P6-8** containing both reactants (**4** and carboxylic acids), a compaction *via* the dimerization of **6** is very unlikely. The complete ^1H NMR spectra of **SCNP6-8** can be found in the appendix Figure 6.1.36.

Since the polymers **P6-8** and the **SCNP6-8** were analyzed *via* ^1H NMR spectroscopy, one of the most important analytical tools characterizing the SCNP formation was employed, *i.e.* SEC. To verify the successful collapse, SEC measurements of **P6-8** and **SCNP6-8** in DMAc were conducted. It has to be noted that the SEC values were calculated employing PMMA standards and do not display the absolute molecular weights. However, the important feature in the field of generating SCNPs is the determination of the relative change in size (or hydrodynamic volume) after the collapse of its precursor. The obtained values from SEC measurements are collated in Table 3.1.3.

Table 3.1.3: DMAc SEC values based molecular weight data of **P6**, **SCNP6**, **P7** and **SCNP7** are shown, employing a PMMA calibration. Adapted with permission from reference [224]. Copyright (2015) American Chemical Society (ACS).²²⁴

Polymer	M_n (kDa)	D_M
P6	20	1.5
SCNP6	14	1.5
P7	12	1.2
SCNP7	10	1.7

First, **P6** and **SCNP6** were analyzed *via* SEC and plotted together in Figure 3.1.16, a). Here, the red line represents the polymer precursor **P6** with a molecular weight of close to 20 kDa ($\bar{D} = 1.5$) and the red dashed line indicates the corresponding **SCNP6** with a molecular weight of 14 kDa ($\bar{D} = 1.5$). A shift in the retention time for **SCNP6** in contrast to **P6** was observed, suggesting – jointly with the previously conducted analytical measurements – an intramolecular collapse, which can be attributed mainly to the NITEC reaction. Subsequently, **P7** and the corresponding **SCNP7** were analyzed utilizing DMAc SEC. The same phenomenon as found for **SCNP6** could be detected here for **SCNP7**, indicating an increase in retention time in contrast to the precursor **P7**. For **P7** (green line) a M_n of 12 kDa ($\bar{D} = 1.2$) was observed. A change in M_{app} for **SCNP7** to 10 kDa ($\bar{D} = 1.7$) was detected, indicating the intramolecular collapse of **P7**.

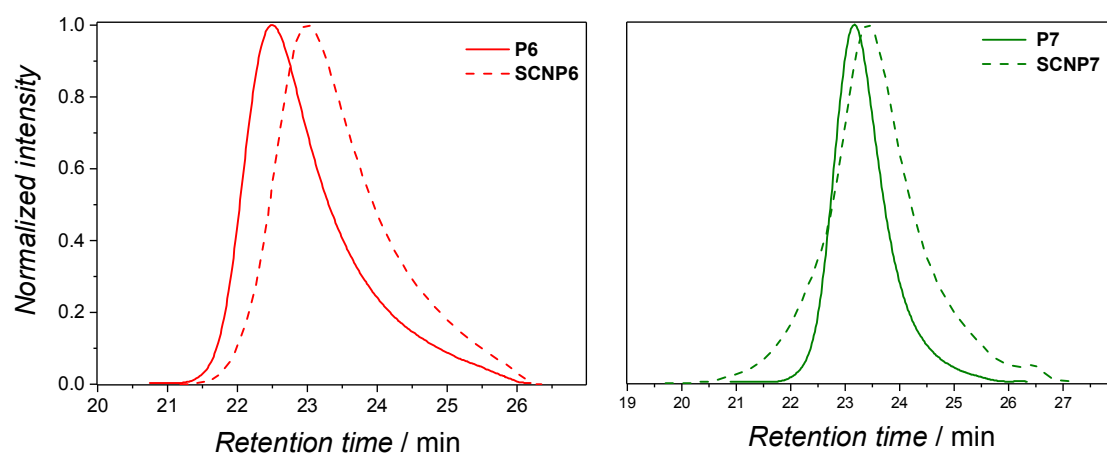


Figure 3.1.16: DMAc SEC traces of **P6** and **P7** and the corresponding irradiated ($\lambda_{max} = 320$ nm) **SCNP6** and **SCNP7** indicating an increase in retention time due to a smaller hydrodynamic volume of the irradiated polymers compared to its precursor. Adapted with permission from reference [224]. Copyright (2015) American Chemical Society (ACS).²²⁴

Here, the SEC shift of **SCNP7** in comparison to its precursor was not as significant as for **SCNP6**, which can be clearly seen in Figure 3.1.16. The polymers **P6** and **P7** as well as their SCNPs were soluble in DMAc except **P8** and the irradiated **SCNP8**. Although a functionalization degree of 60 mol% was reached for **P8** with **6**, which increases the solubility in organic solvents, both polymer samples (**P8** and **SCNP8**) could not be analyzed *via* DMAc SEC.

To verify the intramolecular collapse of **P8** independently from SEC, dynamic light scattering (DLS) and diffusion ordered spectroscopy (DOSY) measurements were conducted.

First, the polymeric precursors (**P6-8**) and their irradiated species (**SCNP6-8**) were investigated *via* DLS measurements (Figure 3.1.17). The values obtained are collated in Table 3.1.4. For **P6** (a, red line), a hydrodynamic diameter (D_h) of 4.3 nm was observed. The irradiated polymer sample **SCNP6** (red dashed line) showed a D_h of 2.3 nm, suggesting the compaction of the irradiated polymer sample. For polymer **P7** (b, green line), featuring a reduced chain length in comparison to **P6**, a D_h with 2.4 nm was observed. The D_h of **P6** (4.3 nm) and **P7** (2.4 nm) are reasonable relative to each other, when the reduced chain length of **P7** with almost the same functionalization degree is taken into account. The irradiated **SCNP7** (green dashed line) revealed a relatively small D_h of ~ 1 nm. When the D_h of **SCNP7** (~ 1 nm) is compared with the D_h of **SCNP6** (2.3 nm) the relative values are reasonable, taking again the doubled chain length into account. For **P8** (c, blue line), a slightly higher D_h was observed with 3.2 nm in contrast to **P6** and **P7**. Although **P8** originates from the PAA polymer (**P5**) containing the shortest chain length with 69 acrylic acids, the highest D_h was observed. The higher D_h of **P8** in comparison to **P6** and **P7** can be explained with the higher functionalization degree employing the bulky tetrazole groups. For **SCNP8**, a smaller D_h in the range of ~ 1 nm was found, which appears unrealistically small and might suggest that the DLS measurement have to be taken with caution (see below).

Table 3.1.4: D_h found employing DLS measurements of **P6-8** and their irradiated ($\lambda_{max} = 320$ nm) **SCNP6-8**. Adapted with permission from reference [224]. Copyright (2015) American Chemical Society (ACS).²²⁴

Polymer	D_h (nm)
P6	4.3
SCNP6	2.3
P7	2.4
SCNP7	~ 1
P8	3.2
SCNP8	~ 1

It should be considered that the functionalization degree of **P8** was calculated close to 60 mol% leading to a higher compaction of the precursor to **SCNP8** after irradiation. The DLS measurements need to be taken with caution, due to the polyelectrolyte polymers together with the fluorescent and colored SCNPs. PAA is known as polyionic polymer, which can pH dependently differ in the size as Pohlmeier and coworkers demonstrated.²²⁹ Critically, the polymer samples were fluorescent and colored, which can interfere with the light scattering process of the polymer samples and therefore influence the results as stated in literature (refer to Section 2.4.2).²⁰⁵ In summary, it can be noted that the results of the DLS measurements only indicate a relative decrease of the hydrodynamic diameter of the polymers in comparison to the SCNPs and do likely not represent absolute values.

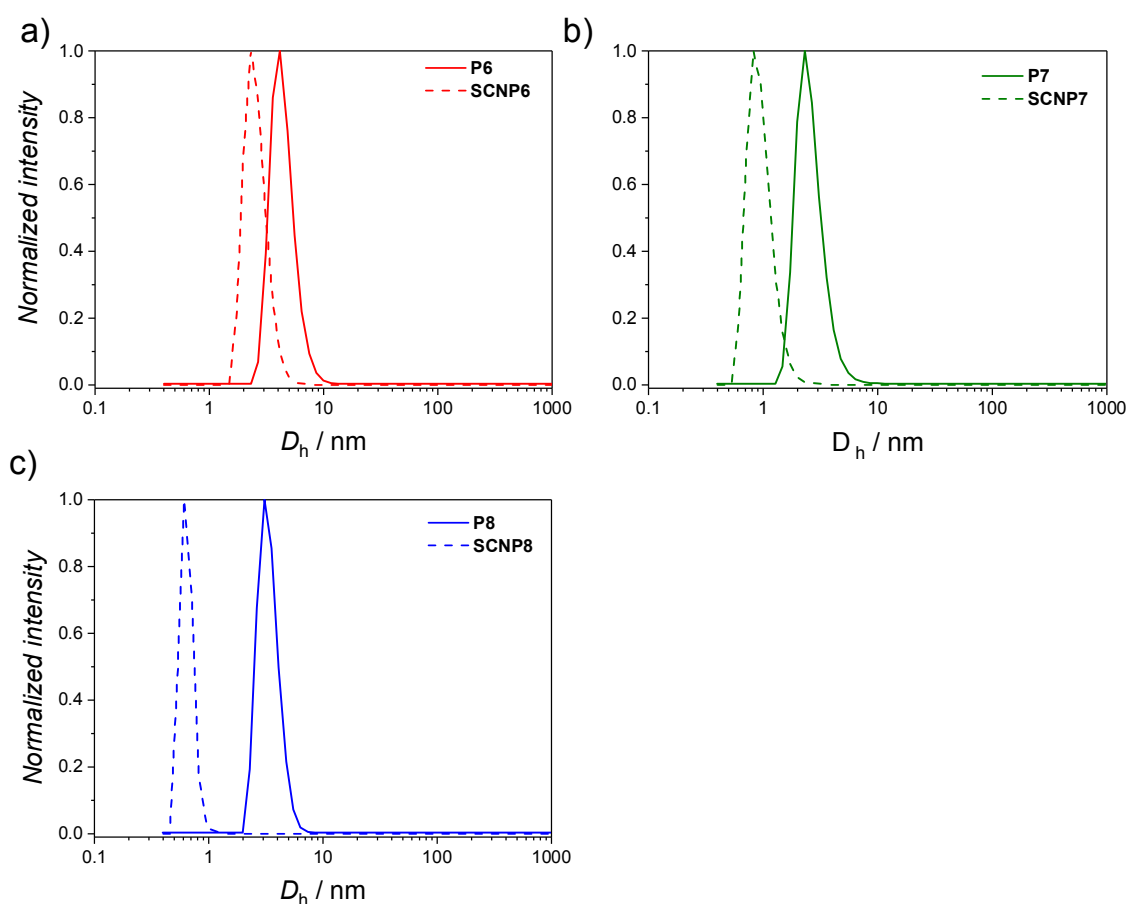


Figure 3.1.17: DLS measurements of **P6-8** and the corresponding **SCNP6-8** measured in MeCN with a concentration of 0.5 mg mL^{-1} . Adapted with permission from reference [224]. Copyright (2015) American Chemical Society (ACS).²²⁴

As already mentioned, SEC measurements for **P8** and **SCNP8** could not be implemented due to solubility issues. Thus, to verify the D_h of **P8** and **SCNP8**, a second analytic method had to be introduced. Therefore, DOSY measurements were recorded to confirm the SCNP collapse for **P8**. Both **P8** and **SCNP8** were analyzed with DOSY NMR resulting in different diffusion coefficients. To calculate D_h , the tetrazole resonances were utilized in DOSY NMR, representing a permanent feature in both polymers **P8** and **SCNP8**. For calculating D_h via the measured diffusion coefficient, employing DOSY NMR refer to Section 2.4. For **P8**, a D_h of 1.7 nm and for the corresponding **SCNP8** a D_h of 1.0 nm was found, which is in good agreement with the DLS measurements.

Table 3.1.5: Diffusion coefficients of **P8** and **SCNP8** with the corresponding hydrodynamic diameter (D_h) calculated with DOSY NMR. For the calculation please refer to Section 2.4. Adapted with permission from reference [224]. Copyright (2015) American Chemical Society (ACS).²²⁴

Polymer	D ($\text{m}^2 \text{s}^{-1}$)	D_h (nm)
P8	$1.33 \cdot 10^{-10}$	1.7
SCNP8	$1.98 \cdot 10^{-10}$	1.0

3.1.5 Application as Imaging Agents

The application as imaging agent is one of the potential uses of the prepared fluorescent SCNPs. In collaborative work (KIT, team of Prof. Dr Ute Schepers), the highly fluorescent **SCNP7** is currently investigated as imaging agent and carrier molecule for drug delivery in *in vivo* cells and in zebra fish embryos. Therefore, the ability to penetrate a cell as well as the intracellular accumulation of **SCNP7** was tested on HeLa, SK-MEL 28, RAW and HUVEC cells. **SCNP7** was able to penetrate the cell membrane of the tested HeLA cells and accumulated in the cytosol (Figure 3.1.18). Furthermore, toxicity tests of SCNPs were investigated on HeLa cells displaying moderate toxicity ($\text{LD}_{50} \sim 200 \mu\text{g mL}^{-1}$).

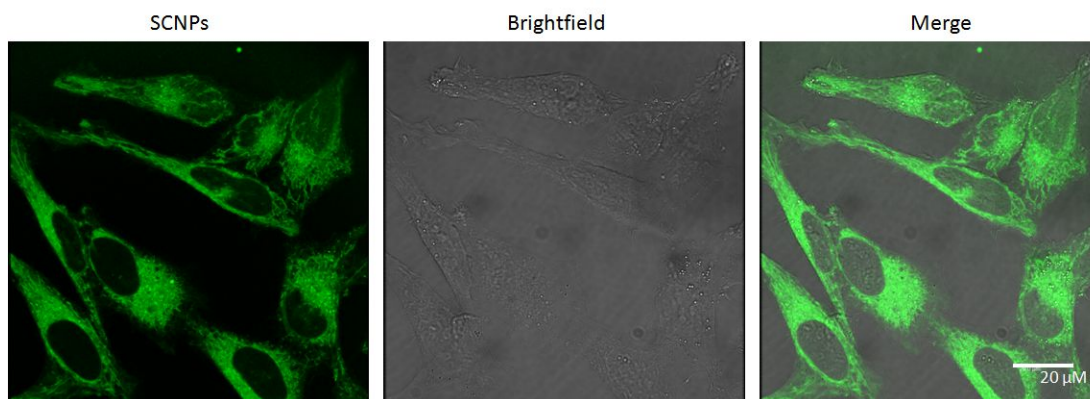


Figure 3.1.18: Confocal fluorescence microscopy measurements showing 1×10^4 HeLa cells treated with $150 \mu\text{g}$ **SCNP7** for 24 h at 37°C . Leica SPE, Lens ACS APO 63x/1.30 OIL, Ex.: 405 nm, Em.: 450-550 nm. Conducted by Ilona Wehl (KIT).

A second *in vivo* test, analyzing organ specificity and specific uptake in the brain of 2 days post fertilized (dpf) zebrafish embryos, was conducted (Figure 3.1.19). Therefore, **SCNP7** was injected into the brain ventricle of the zebra fish embryo and the localization of **SCNP7** was analyzed 1 h and 24 h after injection. As a result, the nanoparticles were accumulating in the brain ventricle and probably in the brain tissue (1 h after injection) and finally concentrated in endothelial cells and macrophages (24 h after injection). Further investigations are ongoing.

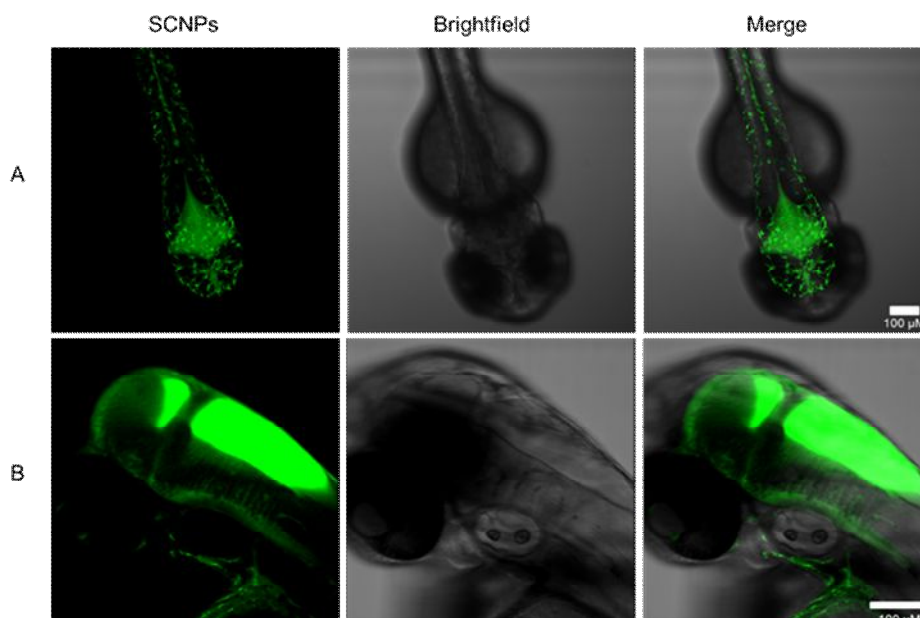
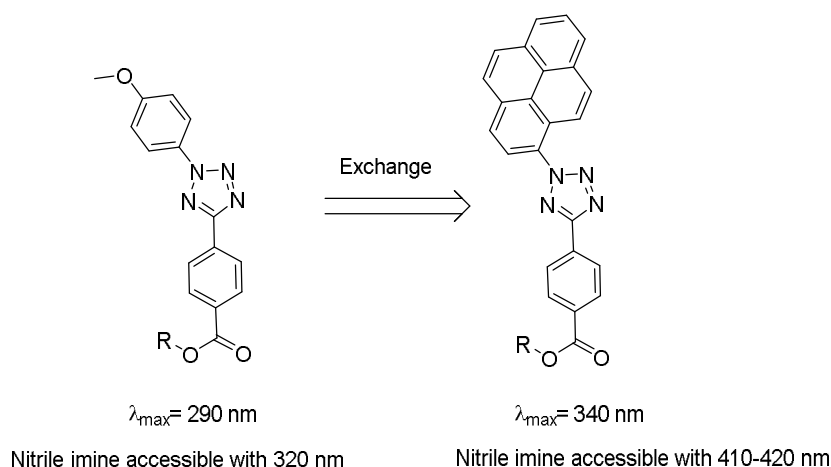


Figure 3.1.19: 2 days post fertilized old zebrafish, 1 h after ventricle injections of 15 mg ml^{-1} **SCNP7** A: Dorsal view of brain ventricle, Leica TCS-SPE, Lens: 10x DRY. 1. SCNPs, Ex.: 405 nm, Em.: 450-550 nm 2. Brightfield 3. Merge: B: Close-up view of brain ventricle and brain, Leica TCS-SPE, Lens: 20x DRY. 1. SCNPs, Ex.: 405nm, Em.: 450-550 nm 2. Brightfield 3. Merge. Conducted by Ilona Wehl (KIT).

3.2 Visible Light Induced Folding of Polymers into SCNPs

In the following chapter a mild access route to the visible light triggered formation of single chain polymer nanoparticles (SCNPs) is introduced. Here, the UV-light tetrazole was exchanged with the visible light active tetrazole, offering a mild access to trigger photochemical reactions (Scheme 3.2.1) as previously introduced by our team.¹²⁴ Wavelengths shorter than 300 nm entail high levels of energy, which can cause a variety of side reactions, e.g. UV bleaching, cell damage or induce polymer degradation. To minimize side reactions based on the high-energy irradiation wavelength, a mild triggerable tetrazole compound is introduced termed pyrene-aryl-tetrazole (PAT). PAT entails a pyrene moiety extending the π -system of the chromophore resulting in the red-shifted absorption of light ($\lambda_{\max} = 340$ nm), allowing for high cleavage efficiency under visible light irradiation. The fundamental reactivity of PAT is described in Section 2.2.6.1. PAT was utilized as a photoreactive compound, which benefits from an increased control over the photochemical reaction with its ability to absorb lower levels of energy. The lower energy is of major interest especially in biological applications. Here, UV-light can cause cell damage, where visible light is not harmful for cells. Furthermore, longer wavelengths can penetrate deeper into materials, which make the PAT tetrazole a perfect candidate for the usage in biological applications, possibly even for photochemistry within living organisms.



Scheme 3.2.1: Changing the reactivity of the tetrazole employing pyrene instead of the methoxy benzyl group enabling a visible light accessible tetrazole.

Prior exploring the PAT chemistry in a comparatively complex polymeric system (*i.e.* single chain collapse), the relevant reactivities were assessed in a small model molecule study. In particular, the photoinduced coupling towards different reactive compounds such as a furan-protected maleimide (p-Mal), fumarate (fum), acetic acid, as well as potential PAT self-dimerization were investigated. The small molecule study was utilized to assess a collection of potential linkers for the generation of fluorescent SCNPs.

Here, the previously tested NITEC photochemistry was utilized on water-soluble poly(acrylic acid) (PAA) as well as in poly(styrene) (PS) based polymers. The following section is focused on PAA based polymers, entailing a biomolecule with specific cell targeting abilities as an end group. The cell targeting molecule design and synthesis was a collaborative effort with Prof. Dr. Stefan Bräse (KIT). The last section (Section 3.2.2) entails the formation of SCNPs *via* visible light employing PS based polymers. Here, the previously investigated photochemistry of the visible light accessible tetrazole were applied to PS polymers to induce the SCNP formation.

3.2.1 Small Molecule Study of the Visible Light Tetrazole

The photochemistry of tetrazoles entails a broad reaction variety with a plethora of reactive partners such as electron deficient double bonds, nucleophiles, and carboxylic acids (refer to Section 2.2.6.1). In the following section, certain reactants were selected for the small molecule study, which could later be incorporated into polymers as anchors for photochemically induced intramolecular folding. The different reactions are organized as follows: 1) the reaction between tetrazole (**12**) and p-Mal (**4**); 2) the reaction between tetrazole (**12**) and fumarate (**14**) 3) the dimerization of tetrazole (**12**) and 4) reaction between tetrazole (**12**) and a carboxylic acid (**9**) and 5) the reaction between tetrazole (**12**) and 2,4-bismaleimidotoluene (**18**). The small molecule study was carried out in DCM utilizing LEDs with a narrow emission spectrum of 410-420 nm. Reaction mixtures were irradiated for 3 h and kinetic samples were taken in one hour intervals.

The photoinduced reactions (1-5, refer to Scheme 3.2.2) were investigated *via* ^1H NMR spectroscopy to analyze the resulting reaction products. For reaction 1), the pyrazoline related resonances are highlighted in red and were observed at 3.24 and 3.01 ppm (Figure 3.2.1, **13**). It must be noted that in contrast to the UV-driven small molecule study, the presented ^1H NMR spectrum was recorded in $\text{DMSO-}d_6$ instead of CDCl_3 , where the chemical shifts might differ. A second ^1H NMR spectrum of **8** was recorded as a reference, indicating the similar high-field shifted resonances at 3.17 and 3.26 ppm (refer to the appendix Figure 6.1.14 for the zoomed ^1H NMR spectrum recorded in CDCl_3 of **8**).

Reaction 2) was performed with a fumarate (**14**) as reaction partner for the PAT. The highlighted signals in blue indicate the pyrazoline adduct **15**, showing resonances with chemical shifts of 5.63 and 4.85 ppm (Figure 3.2.1, **15**). The shift into the low field of the ^1H NMR spectrum can be explained by the presence of the electron-withdrawing ester groups, which are in direct proximity to the formed pyrazoline bond.

In reaction 3), converting **12** with visible light, the dimerization of the nitrile imine, yielding a tetrazine moiety, was investigated. The present thesis showcases a detailed analytical elucidation of this important reaction pathway. Here, no significant changes were observed in ^1H NMR except of a broadening of the PAT resonances at 4.47 and 3.63 ppm highlighted in green (Figure 3.2.1, **16**). Furthermore, compared to the other conducted photoreactions, a more narrow aromatic (8.40-8.04 ppm) region was observed compared to the other adducts **13**, **15**, **17** and **19**. The complete analysis of **16** *via* ^1H NMR spectroscopy cannot be accomplished and further investigations such as ESI-MS has to be applied for a full verification of the tetrazine formation.

Reaction 4) of **12** and **9** was analyzed to investigate the reactivity of the visible light tetrazole towards carboxylic acids, a process known as nitrile imine carboxylic acid ligation (NICAL). In the resulting NICAL reaction products (Figure 3.2.1, **17a + 17b**), the NH-resonances at 9.03 and 10.0 ppm are clearly detectable, which were already observed for the UV-driven NICAL reaction (refer to Chapter 3.1).

The same 1,4-acyl shift of **17a** was also detected in the visible light driven NICAL reaction. The NH-resonance from the hydrazone (**17a**) adduct (10.0 ppm) was almost completely vanished in contrast to the hydrazine (**17b**) NH-resonance (9.03 ppm), indicating an efficient 1,4-acyl-shift.

For reaction 5), investigating the reactivity towards unprotected maleimides, **12** was converted with **18**. As the reactivity of tetrazoles towards maleimides is already known (refer to Section 2.2.6.1), pyrazoline formation with the maleimide was expected. Indeed, the characteristic resonances for **19** were observed at 5.15 and 5.68 ppm (Figure 3.2.1, **19**). The same shift to higher ppm was observed for **19** in comparison to **13**. Here, the maleimide, which is in direct proximity to the formed pyrazoline bond, is effecting a resonance shift, due to the electron-withdrawing character of maleimides. The investigations *via* ^1H NMR spectroscopy together with COSY NMR (refer to the appendix, Figure 6.1.17- Figure 6.1.24) indicate the successful formation of the reaction products. To confirm the reaction products found *via* ^1H NMR spectroscopy, the resulting raw products were additionally analyzed *via* high resolution ESI-MS.

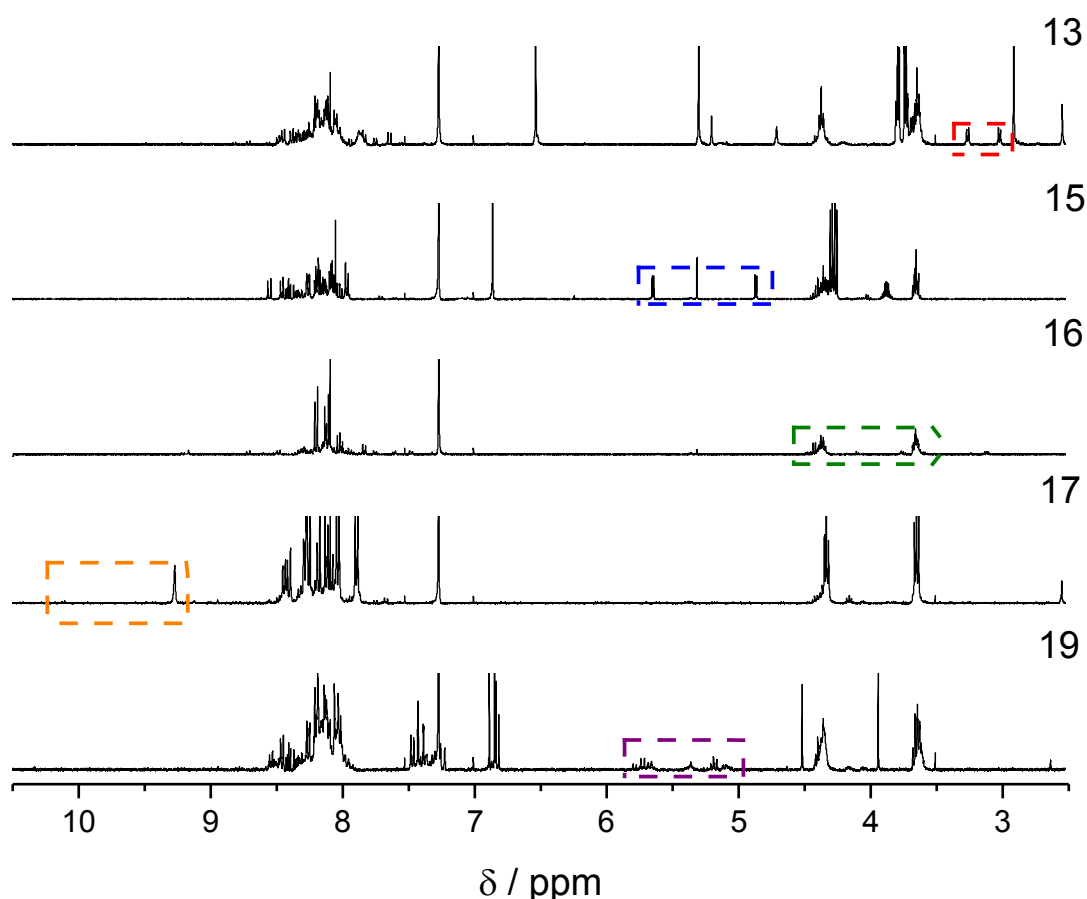
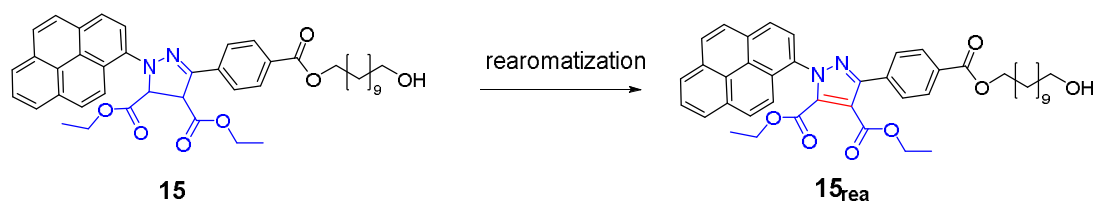


Figure 3.2.1: ^1H NMR spectra of the irradiated ($\lambda = 410\text{-}420\text{nm}$) raw products of the small molecule study, employing **12** as reactant, were recorded in CDCl_3 at 400 MHz. The characteristic signals are highlighted in the spectra with the corresponding colors with **13** (red), **15** (blue), **17** (green), **17** (orange) and **19** (purple).

The first pyrazoline derivative **13** was observed in ESI-MS with a singly sodiated molecule $[\text{M} + \text{Na}]^+$. The characteristic isotopic pattern was found, indicating the successful reaction of **4** with **12**. The second reaction, where the reactivity towards fumarates (**14**) was tested, the singly sodiated molecule $[\text{M} + \text{Na}]^+$ **15** was found in ESI-MS. Furthermore, a second species was observed, which was identified as the rearomatized product (Scheme 3.2.3, **15_{rea}**). This rearomatization of unprotected enes was already identified in the reaction between tetrazoles and maleimides (refer to Section 2.2.6.1).



Scheme 3.2.3: Rearomatization of **15** after irradiation with visible light ($\lambda = 410\text{-}420\text{nm}$). The rearomatized species was observed during high resolution ESI-MS after 1h of irradiation.

In reaction 3), the formed tetrazine adducted was investigated employing ESI-MS. A low ionization tendency was observed for the dimerization reaction, yielding the tetrazine adduct **16**. The low ionization in ESI-MS is caused by the non-polar character of the tetrazine adduct. Nevertheless, the characteristic isotopic pattern was identified as the dimerized PAT molecule with a singly sodiated adduct $[M+\text{Na}]^+$.

In the next assessment, of reaction 4), verifying compound **17** via ESI-MS, the ionization efficiency was drastically increased. A reason for the enhanced ionization could be the polarity of the formed products (**17a** + **17b**) in comparison to the other reaction products **13**, **15** and **16**. The singly ionized reaction product and even the species including two molecules sharing one sodium ion $[2M + \text{Na}]^+$ were identified via ESI-MS.

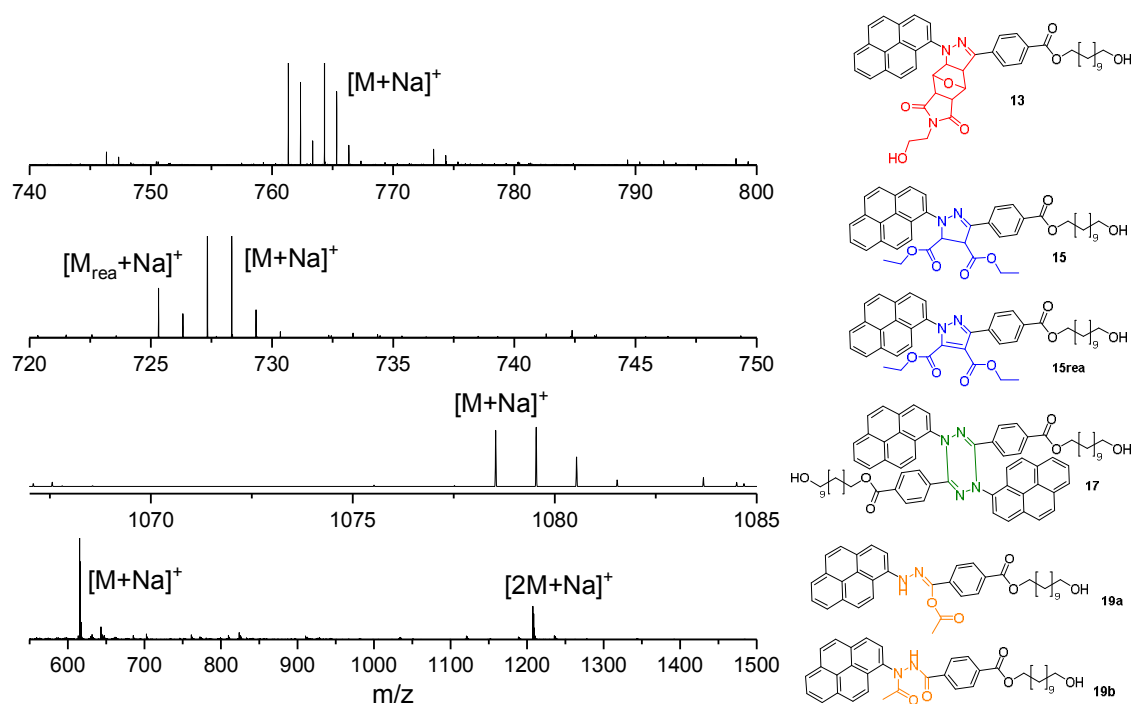


Figure 3.2.2: Mass spectra of the small molecule study showing the corresponding reaction products with **13** (red), **15** (blue), **17** (green) and **17** (orange).

The data obtained *via* ESI-MS of the photo-induced reactions 1-4) are collated in Table 3.2.1. All reaction products, except **19**, were identified in the small molecule study, as their respective sodium adducts. The non-polar properties of **19** and the doubly reacted PAT in respect to one bismaleimide molecule, preventing an efficient ionization during the ESI-MS measurements. However, the successful reaction of the maleimide with the PAT tetrazole was already confirmed in previous work of the Barner-Kowollik group.¹²⁴ The confirmation of this reaction, including a maleimide, has been conducted in a separate study, where a much more narrow focus was placed on the mass spectrometric investigation of tetrazole reactions as such.¹²⁴ Here, the reaction with a maleimide equipped with a polar hydroxy group could be identified in mass spectrometry. As the identification of **19** was not the focus of the present thesis, investigation *via* NMR was deemed adequate and **18** displays a suitable candidate to trigger SCNP folding.

Table 3.2.1: Overview of the assigned reaction products **13**, **15**, **16** and **17** obtained after irradiation with visible light in presence of **12** ($\lambda = 410\text{-}420\text{nm}$, $0\text{-}3\text{h}$) detected with high resolution ESI-MS.

Sample	Species	$(m/z)^{theo}$	$(m/z)^{exp}$	$\Delta (m/z)$
13	[M+Na] ⁺	764.33117	764.33250	0.00133
15	[M+Na] ⁺	727.33537	727.33617	0.0008
15_{rea}	[M+Na] ⁺	725.31972	725.32038	0.00066
16	[M+Na] ⁺	1087.53441	1087.53613	0.00172
17	[M+Na] ⁺	615.28294	615.28481	0.00187
17	[2M+Na] ⁺	1207.57667	1207.58135	0.00468

The photophysical properties of PAT and the corresponding adducts were investigated *via* UV/Vis and fluorescence spectroscopy to examine the absorbance and fluorescence properties of the products resulting from reactions 1-5) depicted in Scheme 3.2.2. First, UV/Vis was conducted to investigate the absorbance properties of the reaction products arising from the visible light small molecule study (Figure 3.2.3, a). In the case of the pyrazoline containing structures induced *via* visible light (**13**, **15**, **19**), a maximum at approx. 400 nm was expected, based on the previously conducted UV-driven small molecule study (refer to Section 3.1). In the conducted UV/Vis measurements of **13**, **15** and **19** the characteristic local absorbance maximum at 400 nm were observed. Surprisingly, the same local absorption maximum was seen for the self-dimerization (**16**) reaction of PAT resulting in the tetrazine adduct.

In addition, the results obtained for the visible light driven NICAL reaction (**17**) were congruent with the findings for the UV tetrazole reactions regarding the absorbance characteristics (refer to Section 3.1.2). Here, no absorption maximum at 400 nm could be detected. Only sharp local absorbance maxima at 350 and 325 nm were observed.

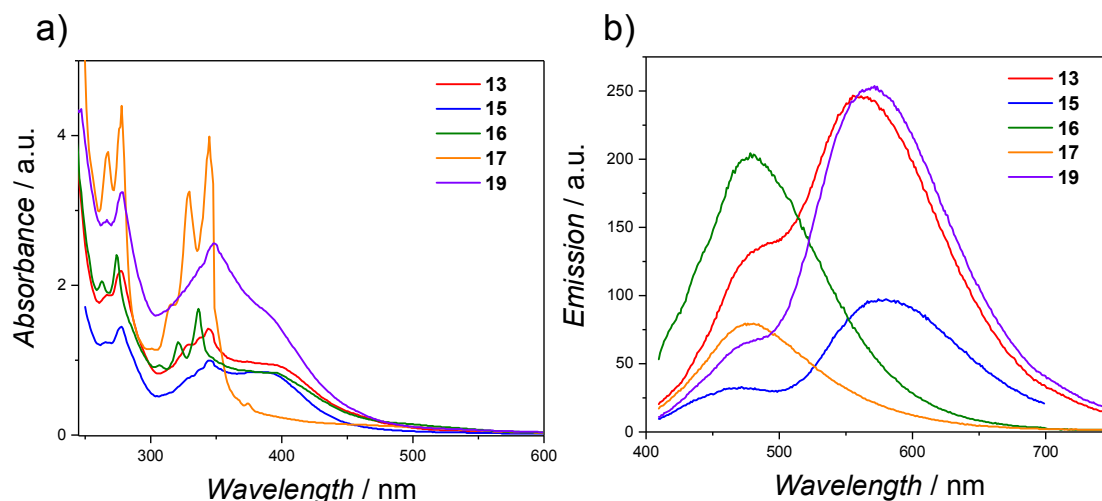


Figure 3.2.3: a) UV/Vis and b) fluorescence spectra of the raw products **13**, **15**, **16**, **17** and **19** ($c = 0.2 \text{ mg mL}^{-1}$) after the irradiation with visible light ($\lambda = 410\text{-}420 \text{ nm}$). The irradiation conditions as well as the geometry are located in the appendix (Figure 6.1.51-Figure 6.1.53). Adapted with permission from reference [225] with permission from The Royal Society of Chemistry (RSC).²²⁵

In addition, all photo-products were analyzed *via* fluorescence spectroscopy. Here, samples were excited at 400 nm (Figure 3.2.3, b). The fluorescent pyrazoline adducts **13**, **15** and, **19** exhibited intense emission bands with a global maximum at 575 nm. A second local maximum at 475 nm was also observed, which is not characteristic for the pyrazoline molecules. It has to be considered that the reaction products were not purified after irradiation with visible light and several side reactions (see Section 2.2.6.1) can occur during the photoreaction employing tetrazoles. In the case of the dimerization reaction resulting in compound **16**, only one emission maximum at 475 nm was detected. Comparing the emission intensities of **16** with **13**, **15** and **19**, similar intensities were obtained. In contrast to the pyrazoline containing compounds **13**, **15** and **19** with an emission maximum at 575 nm, a difference of $\sim 100 \text{ nm}$ was observed. The emission intensity of the compounds **13**, **15** and **19** together with the red shifted emission of 575 nm underpin the potential usage of the pyrazolines as imaging agents.

For the conducted NICAL reaction yielding **17**, the same absorbance maximum at 475 nm was found as for **16**. Here, the lowest emission intensity was observed compared to the other photo-products. It has to be noted that the excitation wavelength was kept to 400 nm, due to the potential application as imaging agents in cells.

Furthermore, the fluorescence properties were determined from the visible light small molecule study using a UV-lamp ($\lambda = 366$ nm). An image of the fluorescent vials is shown in Figure 3.2.4. As already seen by fluorescence spectroscopy, the pyrazoline products showed the highest fluorescence indicating an orange color (**13**, **19**). In contrast, a different color (blue) was observed for product **15**. It can be assumed that the rearomatization of the product leads to different emission intensities. Furthermore, it has to be taken into account that **12**, including the highly fluorescent pyrene moiety, could still be present in the raw products, hence, influencing the color. Nevertheless, the products **13** and **19** revealed excellent fluorescence properties, with emission bands in the visible light regime.

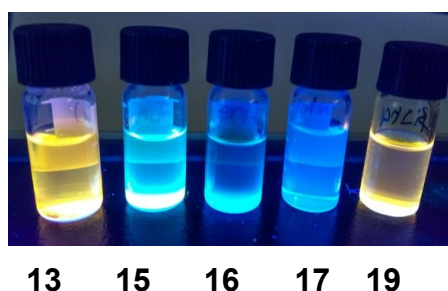


Figure 3.2.4: Image of the fluorescent raw products **13**, **15**, **16**, **17** and **19** excited with a UV-lamp ($\lambda = 366$ nm) recorded in DCM at a concentration 0.2 mg mL^{-1} .

In addition, to trigger the PAT derivative under mild conditions, a sufficient imaging performance of the corresponding adduct in the biological environment needs to be ensured. Therefore, a direct comparison of the fluorescent pyrazoline adduct **8** (Figure 3.2.5, **8**, **13**) formed *via* cycloaddition of the UV tetrazole (**6**) and p-Mal (**4**) as well as the newly introduced cycloadduct **13** was carried out. The pyrazoline derivative of adduct **8** was demonstrated to be a suitable imaging agent in literature as well as in the current thesis (refer to Section 3.1.2) and was applied as a benchmark in the imaging performance study. The pyrazoline adducts **8** and **13** were investigated *via* fluorescence spectroscopy, to compare the pyrazoline molecules obtained with p-Mal (**4**).

The measurements were conducted in DCM and may therefore slightly differ to the previous obtained results regarding **8**. Here, the normalized emission spectra of **8** and **13** are displayed, revealing a small shift of the emission maximum of **13** in comparison to **8**. The emission maximum of **8** was observed at 545 nm, where in **13** an emission maximum at 575 nm was detected, showing a difference of 30 nm. A red shifted emission of **13** was observed and it can be assumed that an improved imaging performance is feasible. Especially the advantages of the mild trigger together with the slightly red shifted emission spectrum, flags the PAT tetrazole (**12**) as a potentially powerful tool for the synthesis of fluorescent SCNPs.

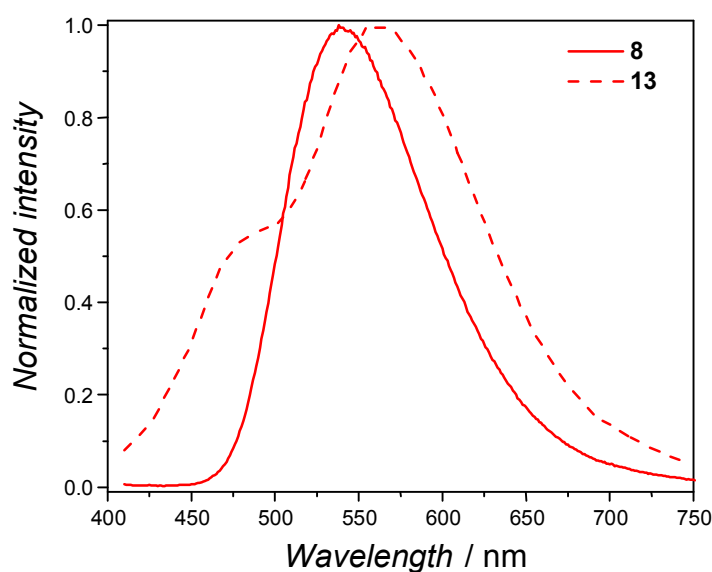
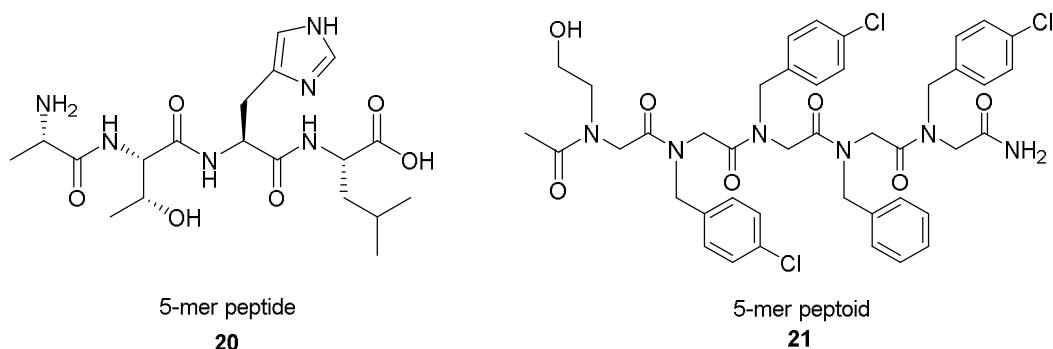


Figure 3.2.5: Normalized fluorescence spectra of the pyrazoline containing products using *p*-Mal (**8**, **13**) indicating a different emission maximum ($\lambda_{\text{ex}} = 400 \text{ nm}$). Both measurements were carried out in DCM ($c = 0.2 \text{ mg mL}^{-1}$).

3.2.2 Preparation of PAA Polymers Containing the Visible Light Active Tetrazole

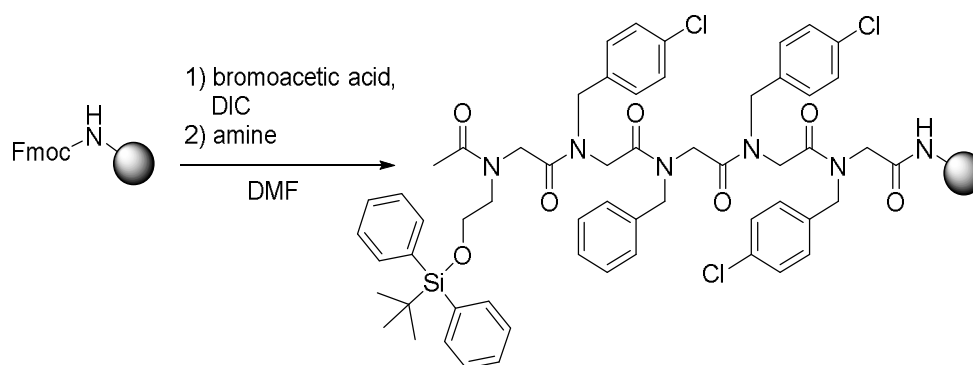
Since the small molecule study of the visible light PAT showcased promising results during the formation of highly fluorescent cycloadducts, a water-soluble PAA polymer was prepared entailing acid functionalities for subsequent esterification of the PAT motif to the polymer chain. As the fluorescent SCNPs were envisaged to act as imaging agents in cells, a biomolecule was previously introduced in the RAFT agent. These biomolecules – named as peptoids – are known to act as a molecular transporters in cells. In particular, peptoids are peptidomimetika and exhibit similar properties as peptides – however – bearing an increased stability against enzymatic degradation.²³⁰ The preparation is based on a versatile solid-phase²³¹ synthesis and was carried out by Stefan Münch (KIT, Team of Prof. Dr. Stefan Bräse). The enhanced stability results from the absence of a chiral carbon atom, which is introduced by the amino acids in the peptide synthesis. Peptoids, however, bear a non-chiral backbone (Scheme 3.2.4). The biomimetic property of peptoids is realized with the specific interaction with cell compartments, which depends on the molecular composition of the peptoid.



Scheme 3.2.4: Comparison of an exemplary peptide structure of a 5-mer amino acid sequence and the 5-mer peptoid sequence employed.

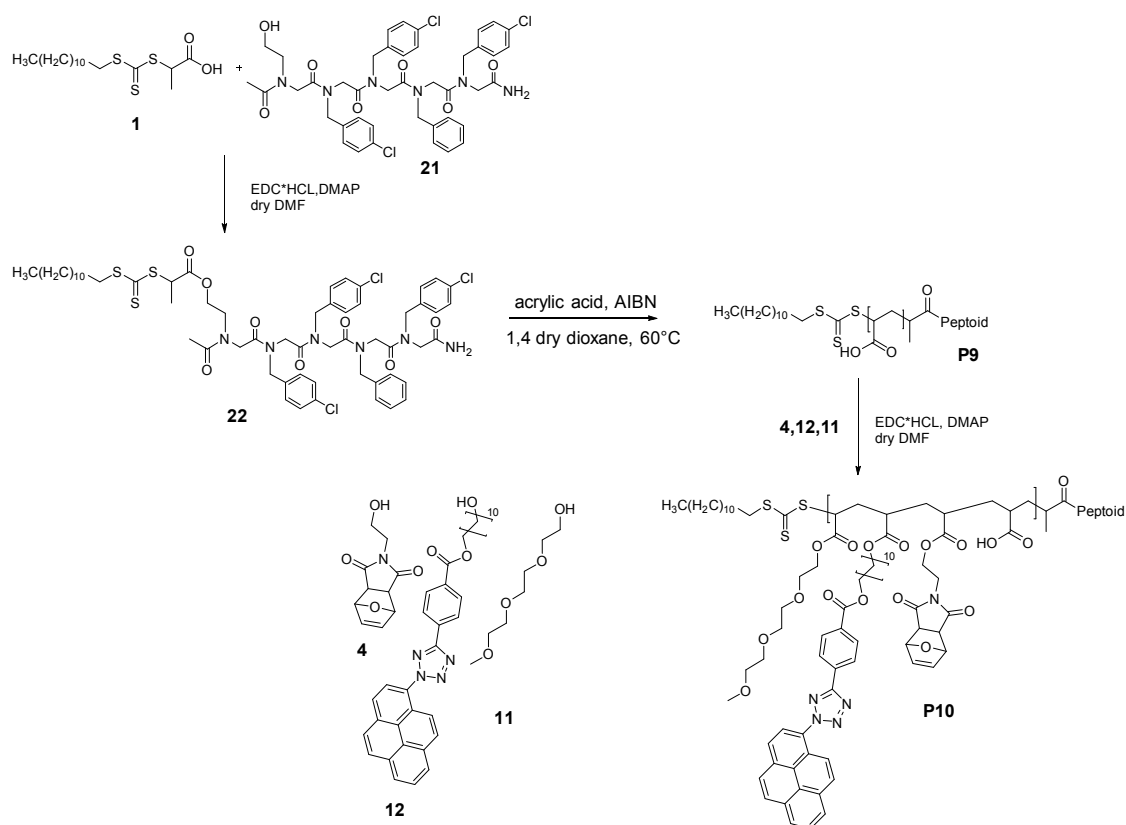
Here, the molecular composition of the synthesized peptoids contained lipophilic motifs, which were known to show increased localization into mitochondria in cells when more lipophilic residues, are used.²³² A solid phase submonomer synthesis comprising a solid phase and a liquid phase was employed for the peptoid synthesis. For the solid phase synthesis, a rink-amide resin equipped with an amide as an anchor for the peptoid was employed.

Subsequently, primary amines and bromoacetic acid were alternately introduced to generate the peptoid in consecutive nucleophilic substitutions. The solid phase products can readily be purified after every step by washing the resin with the appropriate solvents. The last step of the synthesis entails the cleavage of the resin under acidic or basic conditions, depending on the resin used for the synthesis (refer to Chapter 5 for the full synthesis procedure and characterization). One disadvantage of the solid phase synthesis is the low yield, resulting from the alternately sequenced synthesis and the loading capacity of the employed resin.



Scheme 3.2.5: Solid phase submonomer synthesis employing different amines such as *p*-chlorobenzylamine, benzylamine and the silyl-group protected ethanolamine.

After deprotection of the silyl-group and cleavage of the amide bond between the solid phase and the peptoid, the peptoid was obtained. For further information regarding the characterization refer to Chapter 5. Subsequently, the obtained peptoid was converted into a biologically active RAFT agent with **1** (Scheme 3.2.6). The combination of the RAFT agent with the peptoid bears two advantages. First, the incorporation of a biomolecule including the specific transport ability, and second the use of the aromatic residues for calculation of the molecular weight *via* ^1H NMR spectroscopy. The esterification of **1** and **21** into the end-group modified RAFT agent **22** was achieved under Steglich conditions (Scheme 3.2.6). Subsequently, the polymerization with AA was carried out to obtain the PAA polymer **P9**. The functionalization with the photoreactive (**4**, **12**) and non-photoreactive (**11**) compounds was conducted under mild esterification conditions (Scheme 3.2.6, **13**) yielding polymer **P10**.



Scheme 3.2.6: Overview of the synthetic approach featuring a Steglich esterification of the peptoid (**21**) and DoPAT (**1**) with subsequent polymerization of acrylic acid. The linear polymer was modified with a statistical esterification with **4**, **12** and **11** leading to the photoreactive polymer (**P10**).

In order to evidence the successful polymerization of **P9**, ^1H NMR spectroscopy was employed. Thus, ^1H NMR spectra were recorded to determine the number average molecular weight (M_n) of **P9** with the introduced peptoid (Figure 3.2.6, **P9**). Therefore, the integrals of the aromatic resonances at 7.00-8.60 ppm (i) were integrated and compared with the polymer backbone signal (d). Comparing these resonances, a M_n of 16 kDa with a chain length of 210 monomer units was calculated.

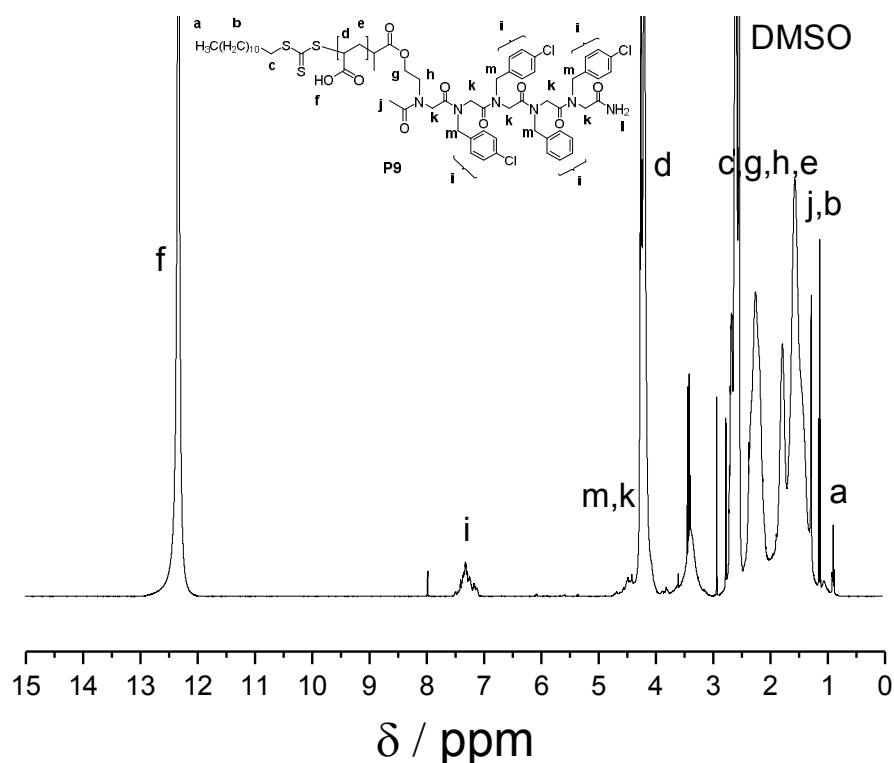


Figure 3.2.6: ^1H NMR spectrum of **P9** measured in $\text{DMSO-}d_6$ at 400 MHz. The aryl resonances *i* associated with the peptoid and the polymer backbone signal *d* were used for calculation of M_n .

Subsequently, the statistical functionalization reactions *via* Steglich esterification were carried out. The successful post-polymerization modification was verified by specific resonances in the ^1H NMR spectrum (Figure 3.2.7). These resonances were assigned to the functional groups PAT, p-Mal and TEG. As noted in Section 3.1.3, an identical shift of the tetrazole proton resonances was observed in **P10** (Figure 3.2.7, k), revealing the same chemical environment as found for **P6** and **P8**. A further investigation of this previously studied phenomenon applying COSY NMR was not performed, due to the most probable interaction of the PAA backbone with the incorporated tetrazole as already stated in section 3.1.3.

As the peptoid was attached to the reinitiating group of the RAFT agent and the trithiocarbonate group is susceptible to hydrolysis, the end group fidelity is a crucial aspect to consider. Therefore, the ^1H NMR spectra of **P9** and **P10** were stacked to identify the peptoid resonances.

In the expanded spectrum it is clearly evident that the end-group of polymer **P10** exhibits the same aromatic resonances found as observed for **P9**, indicating the presence of the peptoid after functionalization. However, the calculation of the installed linker was not feasible *via* the peptoid-group, due to slightly overlapping resonances arising from the tetrazole shift at 6.96 ppm. Therefore, the methyl group of the RAFT agent (Figure 3.2.7, a) was used instead, yielding a functionalization degree of the introduced reactive compounds of 8 mol% for PAT, 6 mol % for p-Mal and 16 mol% for the TEG units.

Importantly, the fluorescence of the NITEC cycloadduct is sufficient to utilize SCNPs as a potential imaging agent for cells. However, due to the non-quantitative esterification of the reactive linker, the remaining carboxylic acid functionalities would compete with the NITEC reaction. As shown in the previous SCNP formation using UV-light (Chapter 3.1), a NITEC-type folding of the polymers was achieved even with an excess of carboxylic acids groups present. Since the post-modification resulted in photoresponsive polymer precursors, the irradiation of **P10** was performed with visible light.

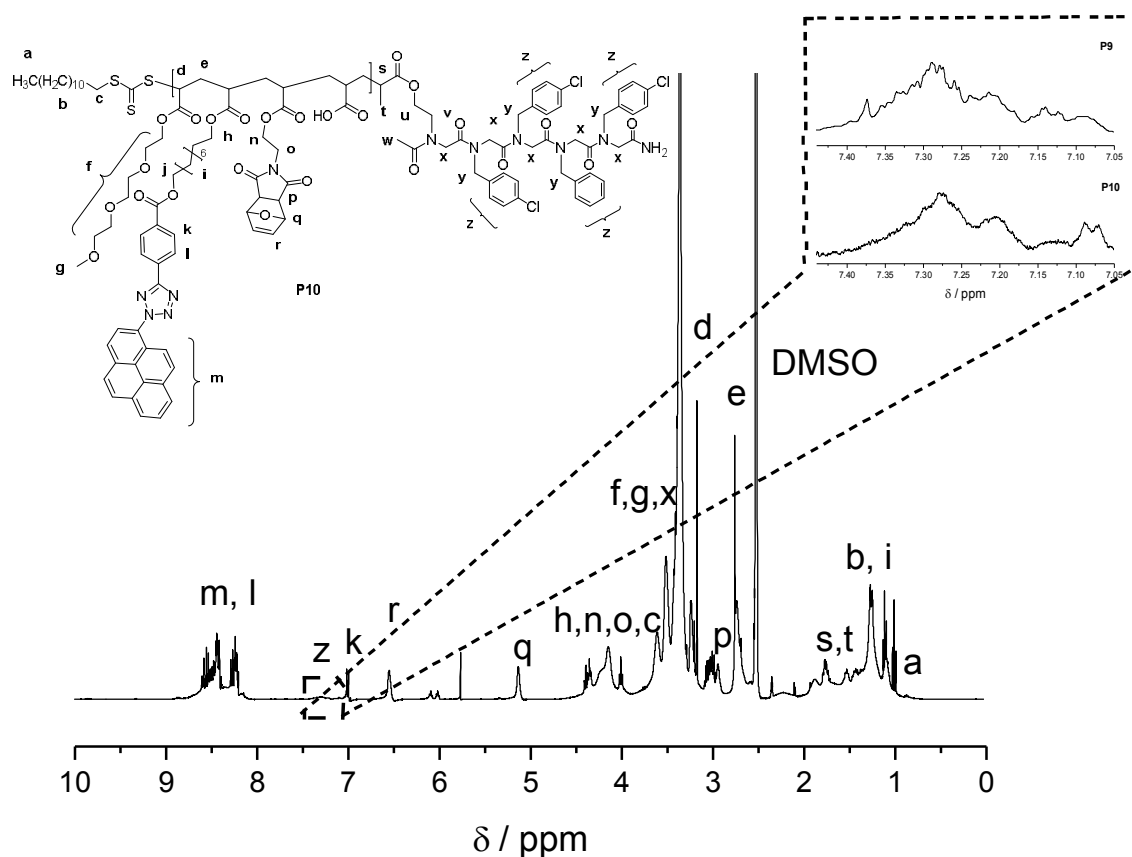


Figure 3.2.7: ^1H NMR spectrum of **P10** measured in $\text{DMSO-}d_6$ at 400 MHz showing the resonances arising from the introduced **4**, **6** and **11**. Zoom: Verification of the end group comparing the initial **P9** with **P10**.

3.2.3 Visible Light Induced Folding of PAA Polymers and their Characterization

The irradiation of the synthesized **P10** was carried out to obtain fluorescent SCNPs. Although the polymer was soluble in water, the highly volatile DCM was preferred enabling the fast removal of the solvent. Polymer **P10** was therefore dissolved in DCM at a concentration of 0.017 mg mL^{-1} and irradiated with 3 blue LED lamps in the visible light regime for 90 min (refer to Chapter 5 for the detailed irradiation conditions). Afterwards the solvent was removed and the polymer was analyzed *via* SEC, UV/Vis and fluorescence spectroscopy. The first analytical method applied was DMAc SEC. The initial polymer **P10** and the irradiated polymer sample **SCNP10** were analyzed *via* SEC (Figure 3.2.8). For **P10**, a M_n of 28 kDa ($\mathcal{D} = 1.3$) was calculated applying PMMA calibration. The SEC trace of **SCNP10** was shifted towards higher retention times in contrast to polymer **P10**.

Furthermore, the apparent molecular weight (M_{app}) changed to 19.1 kDa ($\bar{D} = 1.6$), which was calculated employing a PMMA calibration. A difference of ~ 10 kDa to the initial polymer **P10** was observed, which indicates an efficient compaction.

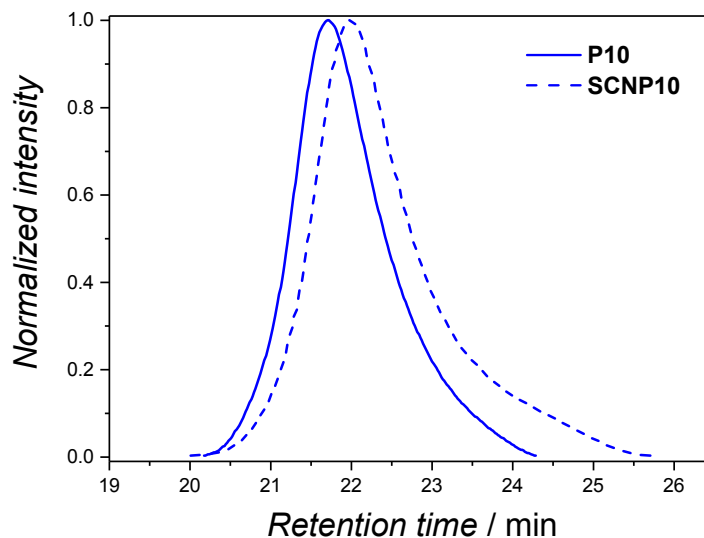


Figure 3.2.8: DMAc SEC traces of **P10** and the irradiated ($\lambda = 410\text{-}420\text{ nm}$) **SCNP10** indicating a shift towards higher retention times after irradiation.

In order to assess whether NICAL or NITEC reactions occurred, UV/Vis and fluorescence spectroscopy measurements were performed. Thus, **SCNP10** was analyzed with UV/Vis and fluorescence spectroscopy and the resulting spectra were plotted jointly with the spectra resulting from the small molecule study of the PAT tetrazole with **13** and **17** (Figure 3.2.9). The previously performed reactions producing NITEC adduct **13** and NICAL adduct **17** (Section 3.2.1) provide the absorption characteristics as a reference.

When the UV/Vis spectra of **13**, **17** and **SCNP10** are compared, the absence of the local absorbance maximum around 400 nm is evident in **SCNP10**. The local absorbance maximum at 400 nm is typical for NITEC products. Therefore, it can likely be assumed that the SCNP collapse of **P10** predominantly took place *via* the NICAL reaction route. Further confirmation of this hypothesis is provided by the fluorescence spectra of **13**, **17** and **SCNP10**. Here, the characteristic emission maximum at approx. 475 nm indicates that the NICAL reaction pathway was kinetically favored.

Although the dimerization reaction of the tetrazole shows the same emission band at 475 nm, it can be excluded as a photochemical reaction path, due to the absence of the 400 nm maximum observed in the UV/Vis spectrum.

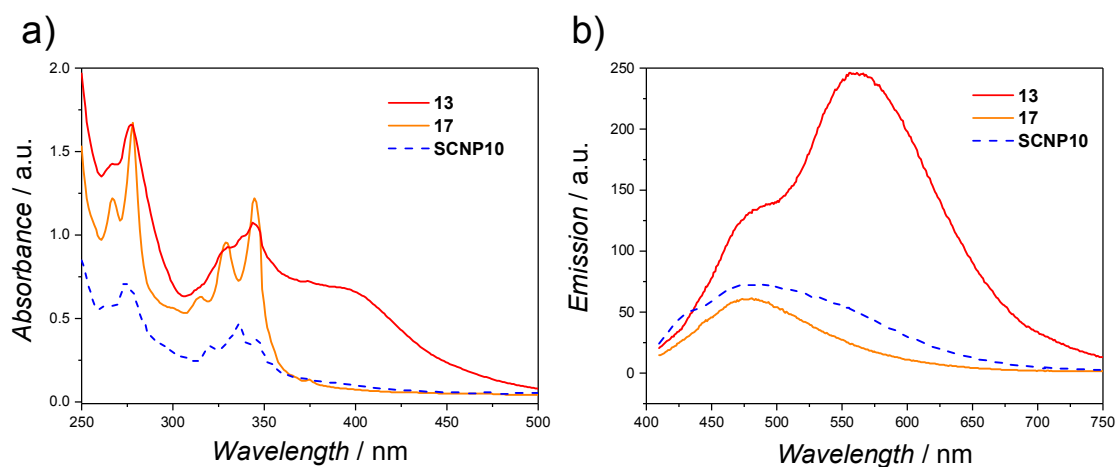
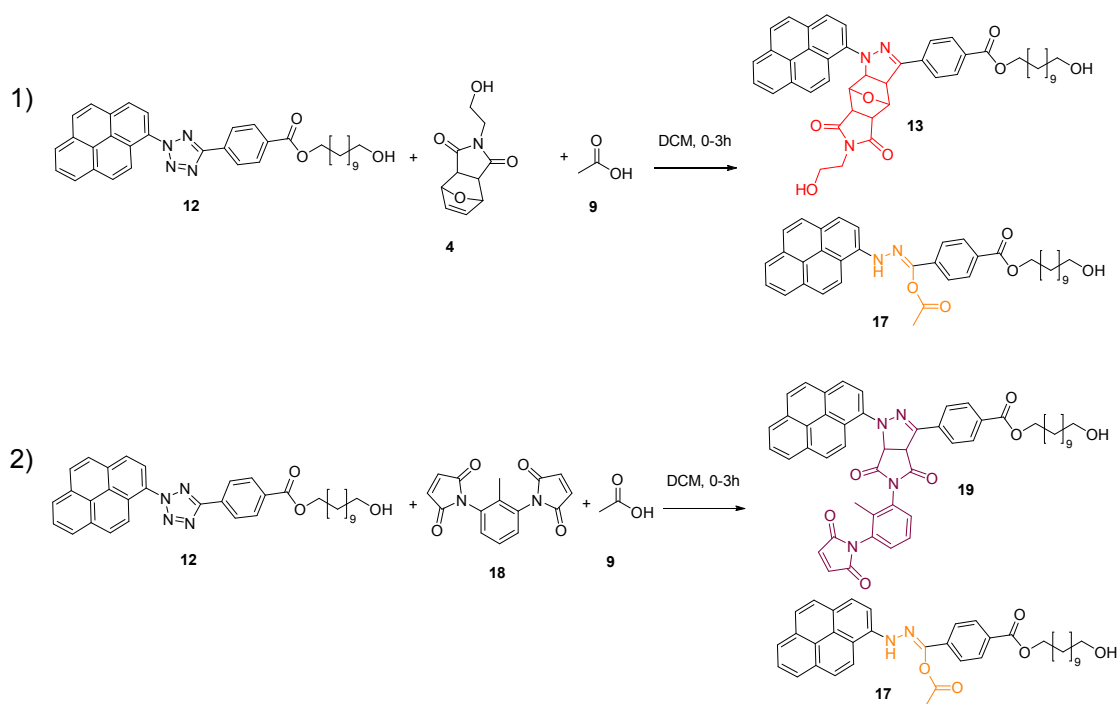


Figure 3.2.9: a) UV/Vis and b) fluorescence spectra of **13**, **17** and **SCNP10** recorded in DCM at a concentration of 0.2 mg mL^{-1} for the small molecules and 0.5 mg mL^{-1} for **SCNP10**, indicating a NICAL driven reaction. The irradiation conditions as well as the irradiation geometry are included in the appendix, Figure 6.1.51-Figure 6.1.53.

Resulting from the predominantly NICAL driven SCNP formation of **P10**, only little fluorescence intensity can be detected for **SCNP10**. Thus, **SCNP10** is not a suitable candidate as imaging agent due to insufficient fluorescent properties after the collapse of the polymer chain. Therefore, a second approach was envisaged to favor the NITEC based collapse of the polymer by using the 2,4-bismaleimidotoluene (**18**) as a dilinker. An investigation of the competitive reaction of **18** and acetic acid (**9**) was conducted in order to elucidate the preferred reaction pathway (Scheme 3.2.7). If the NITEC reaction employing the unprotected maleimide **18** is preferred, the dilinker could be used as a suitable reaction partner in the NITEC reaction. Additionally, for completion of the small molecule study a competitive reaction with **4** and **9** was also carried out to investigate the preferred reaction pathway. In summary, two competitive reactions were conducted with the PAT tetrazole **12** with reaction 1) employing **4** and **9** and reaction 2) employing **18** and **9** (Scheme 3.2.7). For simplicity reasons only the initial NICAL product (**17**) is illustrated.



Scheme 3.2.7: Competitive reactions of PAT (**12**) with 1) *p*-Mal (**4**) and acetic acid (**9**) and 2) with 2,4-bismaleimidotoluene (**18**) and acetic acid (**9**).

The reactions 1) and 2) were conducted using a 1.3-fold excess of each reactant with respect to PAT (refer to Chapter 5 for the detailed reaction conditions). Based on the two potential coupling sites in **18**, only 0.65 eq. were used instead of 1.3 eq. All competitive small molecule reactions were conducted under otherwise identical conditions to previous studies (refer to Section 3.2.1).

To investigate the resulting photo-reaction products, ^1H NMR spectroscopy was performed. A summary of the obtained spectra of the competitive small molecule study is shown in Figure 3.2.10. The proton resonances of the previously recorded reaction products **13**, **17** and **19** are provided as a reference together with the competitive reaction products (**13** + **17** and **17** + **19**). In the ^1H NMR spectrum of reaction 1) (**13** + **17**), representing the NITEC and NICAL reaction, characteristic resonances in both products are found. The proton resonance of **17** corresponding to the NICAL reaction (9.01 and 10.0 ppm, orange) as well as of **13** corresponding to the NITEC reaction (3.01 and 3.24 ppm, red) were observed. It can be assumed that the formation of both adducts proceeded. Furthermore, the ratio of the NITEC and NICAL reaction extent was determined by comparing the characteristic resonances at 3.01 ppm with 10.0 ppm, resulting in a 1:0.5 (**17**:**13**) ratio, indicating a clear preference of the NICAL pathway.

Here, a minor preference of the NICAL vs. the NITEC reaction was identified in comparison to the UV-induced NICAL and NITEC reactions, where a ratio of 1: 4.8 (**10:8**) was determined (refer to Section 3.1.2).

Reaction 2) employing **18** and **9** was carried out and analyzed *via* ^1H NMR spectroscopy. In this case, no evidence for both reaction products were observed, due to an absence of the NICAL resonances (**17** + **19**, orange). Here, the ^1H NMR spectrum could only provide the information for the resonances corresponding to reaction product **19** (5.15 and 5.68 ppm, purple).

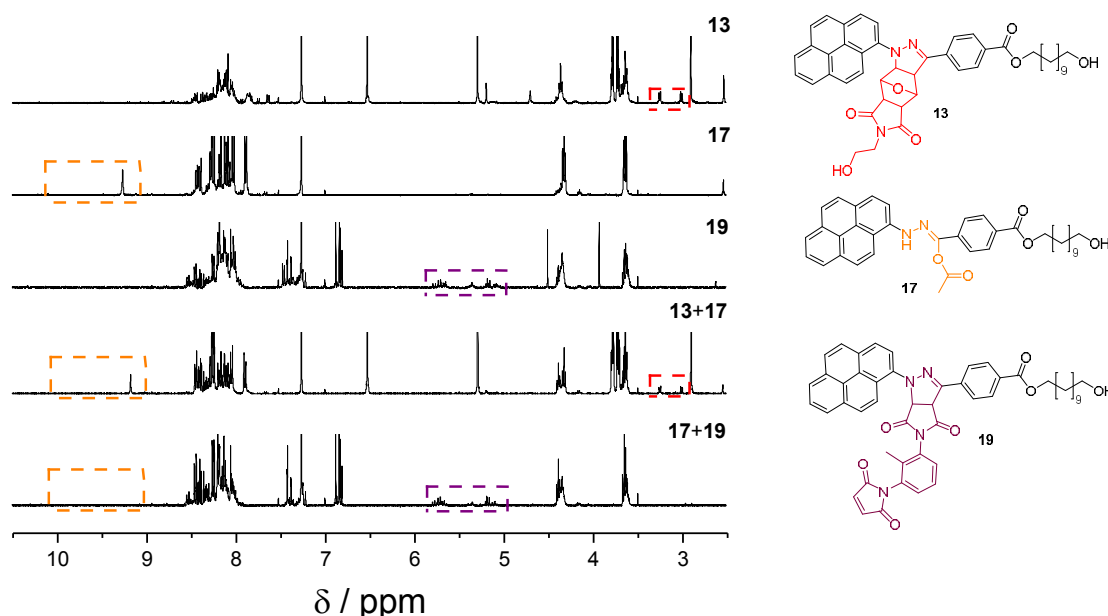


Figure 3.2.10: NMR spectra of the irradiated ($\lambda = 410\text{-}420\text{ nm}$) reaction products **13**, **17** and **19** as well as the competitive reactions products **13** + **17**, **17** + **19** recorded in CDCl_3 at 400 MHz.

The competitive reaction products were additionally investigated *via* UV/Vis and fluorescence spectroscopy. In Figure 3.2.11, the spectra of **13** (red), **17** (orange), **19** (purple) as well as the competitive reactions **13** + **17** (red dashed line), **17** + **19** (orange dashed line) are depicted. For the first competitive reaction 1), both absorbance features were observed. On one hand the 400 nm local absorbance maximum and on the other hand the local absorbance maxima at 350 and 325 nm were detected. By comparing the fluorescence spectra of the competitive reaction 1), both characteristic fluorescence emission maxima at 475 and 575 nm were observed (**13** + **17**, red dashed line), indicating a dual NITEC and NICAL reaction pathway.

For reaction 2), the absorbance spectra of the small molecule adducts **17** and **19** as well as the competitive reaction (**17** + **19**) are illustrated in Figure 3.2.11, a). As the ^1H NMR measurements already indicated, no evidence was found in UV/Vis spectroscopy for the formation of the NICAL adduct (**17** + **19**, orange dashed line). The analogue absorption maximum as observed for reaction **19** was found for the competitive reaction (**17** + **19**). In the recorded fluorescence spectra, no evidence for a NICAL reaction was seen, which is congruent with the data from ^1H NMR and UV/Vis spectroscopy. It has to be noted that **19** displays a higher emission intensity compared to **17**, which might mask the fluorescence of **17**. On the balance of all analytical evidence, however, no suggestion for the formation of **17** in the competitive reaction was found.

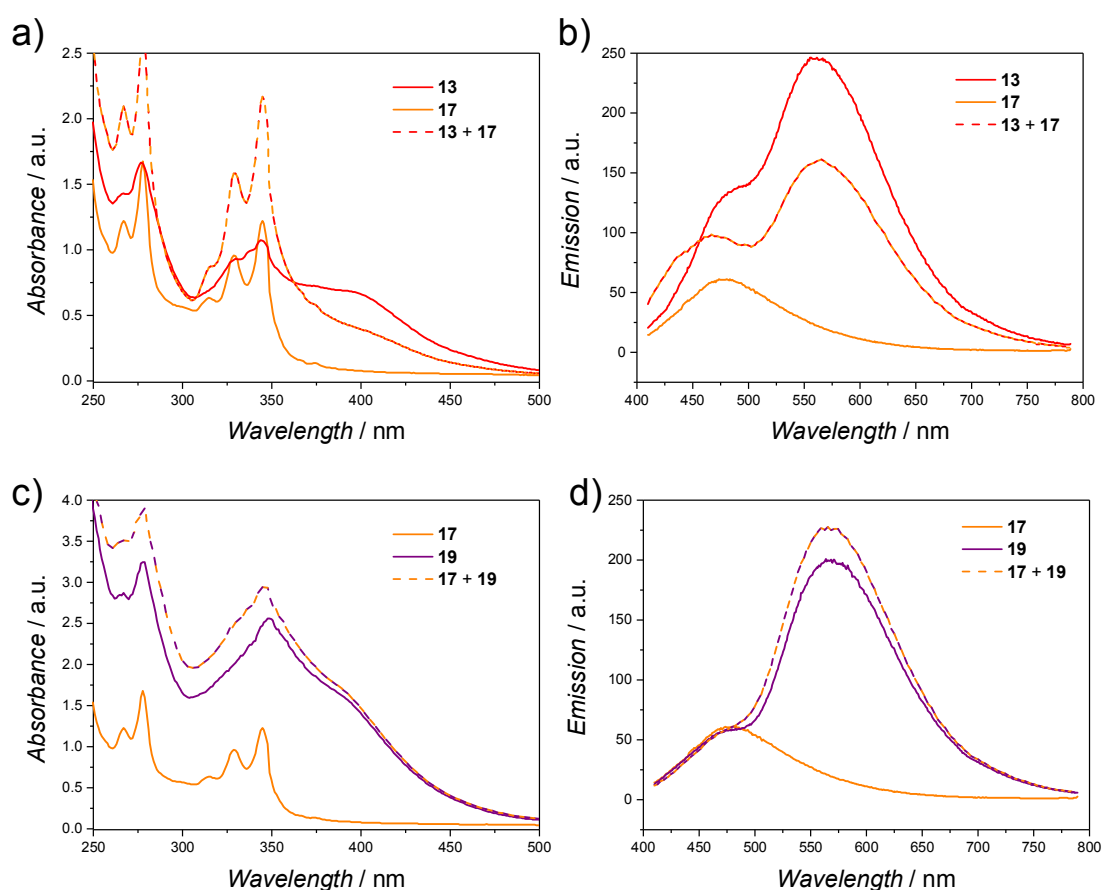
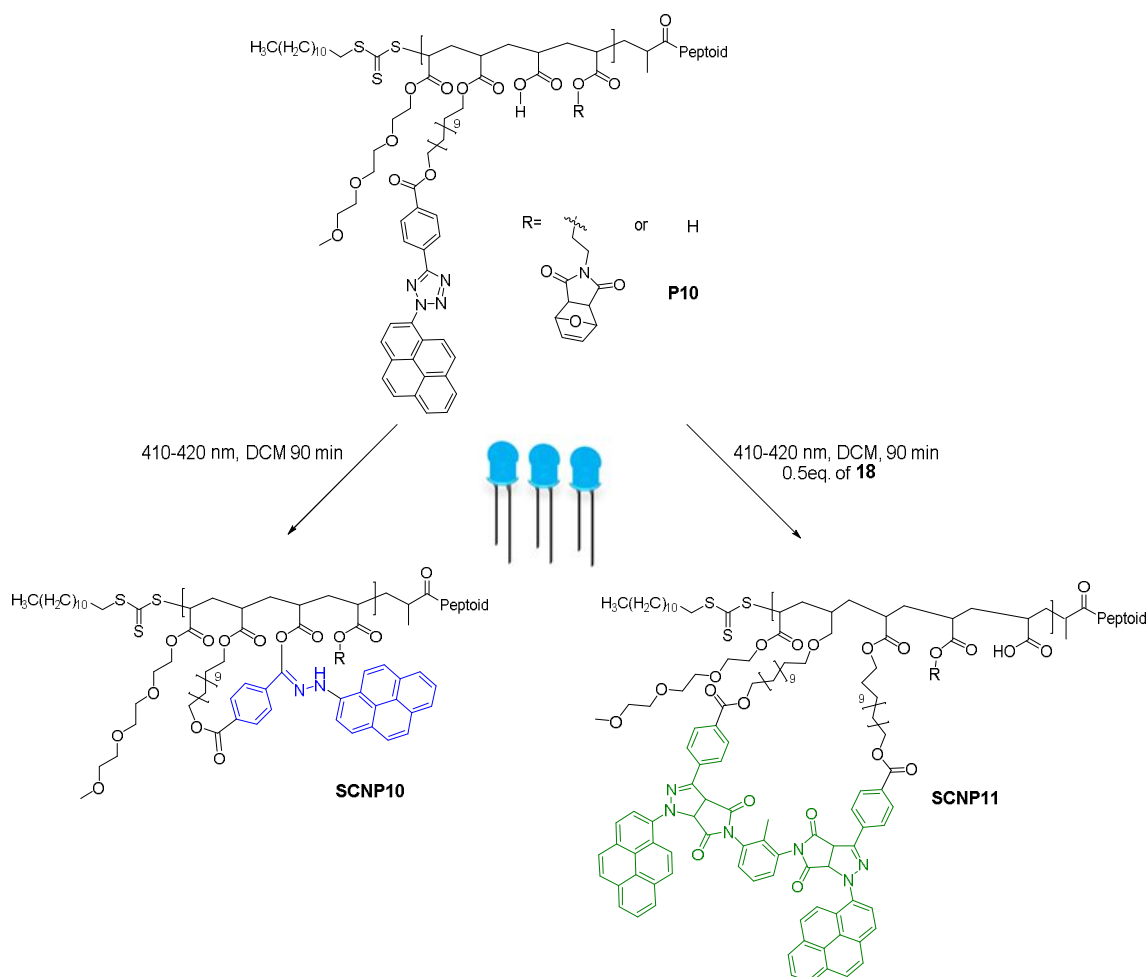


Figure 3.2.11: a) UV/Vis spectra of **13**, **17** and the competitive reaction products (**13** + **17**). b) Fluorescence spectra of **13**, **17** and the competitive reaction products (**13** + **17**). c) UV/Vis spectra of **17**, **19** and the competitive reaction products (**17** + **19**). d) Fluorescence spectra of **17**, **19** and the competitive reaction products (**17** + **19**). The samples were recorded in DCM at a concentration of 0.2 mg mL^{-1} . The spectra of **13**, **17** and **19** were plotted as a reference. The irradiation conditions as well as the geometry can be found in the appendix (Figure 6.1.51-Figure 6.1.53).

The competitive reaction study demonstrated that **18** represents a potential tool for triggering the NITEC driven collapse of **P10**. Resulting from the competitive studies, a small preference for the visible light tetrazole reaction partners can be established as follows **18** > **9** > **4** > **12**. The reaction of the unprotected maleimide (**18**) is the most kinetically preferred reactant for **12**, followed by the reaction with the carboxylic acid (**9**). The reaction of protected maleimide (**4**) is preferred over the tetrazine dimerization **16** reaction. The reaction with fumarate was not considered in this order. Based on the kinetics study results, the **P10** collapse was repeated in the presence of the bismaleimide linker **18** (Scheme 3.2.8). A schematic overview is given to illustrate the conducted and the planned folding of polymer **P10** (Scheme 3.2.8).



Scheme 3.2.8: Overview of the obtained (**SCNP10**) and the targeted **SCNP11** employing the bismaleimide linker (**18**). The conducted reactions were irradiated with 3 LED lamps ($\lambda = 410\text{-}420\text{ nm}$). Refer to the appendix (Figure 6.1.51-Figure 6.1.53) for the geometry and energies employed for irradiation.

The synthesis of **SCNP11** was conducted under highly diluted conditions ($c = 0.0017 \text{ mg L}^{-1}$) in presence of 0.5 eq. of **18** to trigger the intramolecular collapse. The stoichiometry was selected to account for two linking points per linker. Similar irradiation conditions as used for **SCNP10** were applied for the preparation of the targeted **SCNP11**. To verify the intramolecular collapse of **P10** to **SCNP11**, DMAc SEC was measured (Figure 3.2.12). A M_n of 28 kDa ($\mathcal{D} = 1.3$) for polymer **P10** was estimated applying a PMMA calibration. The DMAc SEC traces of **P10** and **SCNP11** indicate a shift to higher retention times for **SCNP11**. Furthermore, M_{app} of **SCNP11** was determined to 21.5 kDa ($\mathcal{D} = 1.4$), revealing an efficient compaction compared to **P10**. Based on the SEC results, a successful SCNP collapse is likely.

To investigate the photophysical characteristics of the collapsed polymer, UV/Vis and fluorescence measurements were conducted.

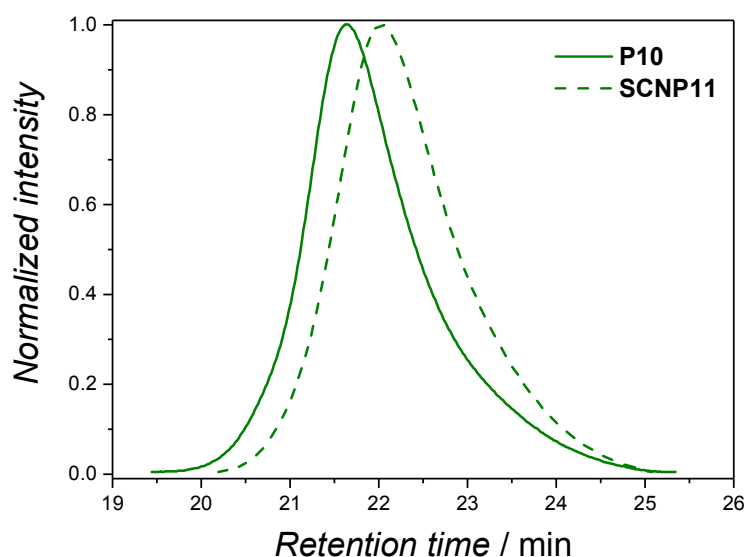


Figure 3.2.12: SEC traces of **P10** and **SCNP11** measured in DMAc. The irradiation conditions as well as the geometry can be found in the appendix (Figure 6.1.51-Figure 6.1.53).

The UV/Vis measurements of **17**, **19** and **SCNP11** are collated in Figure 3.2.13. UV/Vis measurements confirm the occurrence of the preferred NITEC reaction for **SCNP11** formation, when the bismaleimide linker **18** was added to the solution. In UV/Vis spectroscopy, the global absorbance maximum at 400 nm as observed for **19** was found, representing a first hint for a successful NITEC reaction.

To confirm the assumed photochemical collapse *via* NITEC in **SCNP11**, a fluorescence spectrum was recorded and compared with the spectra measured for **17** and **19**. The emission spectrum recorded for **SCNP11** showed an emission equally to the emission band found for **19** with a maximum at 575 nm.

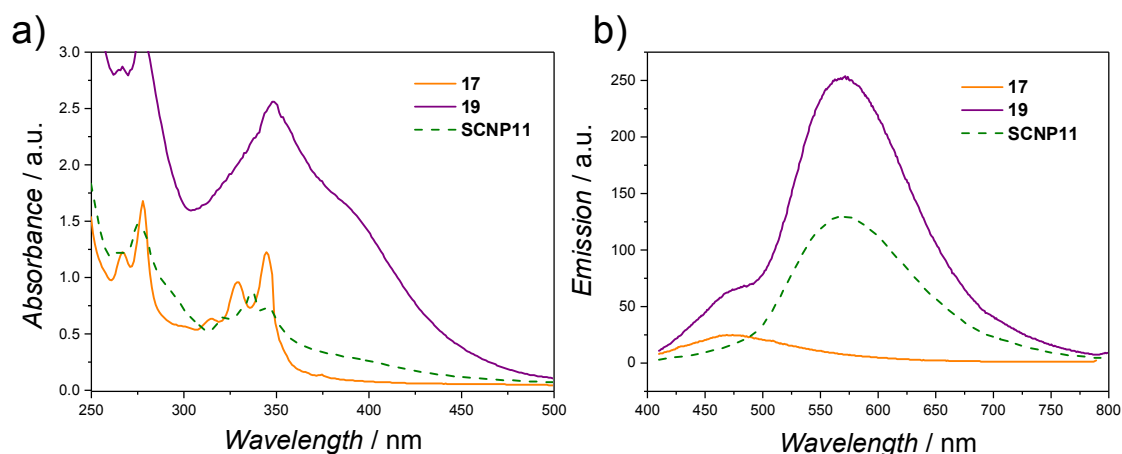


Figure 3.2.13: a) UV/Vis and b) fluorescence spectra of **17**, **19** and **SCNP11** recorded in DCM at a concentration of 0.2 mg mL^{-1} for the small molecules and 0.5 mg mL^{-1} for **SCNP11** indicating a NITEC driven reaction. The irradiation conditions as well as the geometry are located in the appendix (Figure 6.1.51-Figure 6.1.53).

Based on these first promising results, the folding of **P10** was repeated and scaled up to characterize the resulting SCNPs in more detail. However, it was found that the PAT tetrazole in the initial polymer **P10** was not stable over time and a change in the SEC trace as well as in ^1H NMR spectroscopy was detected (Figure 3.2.14, **P10_{ch}**).

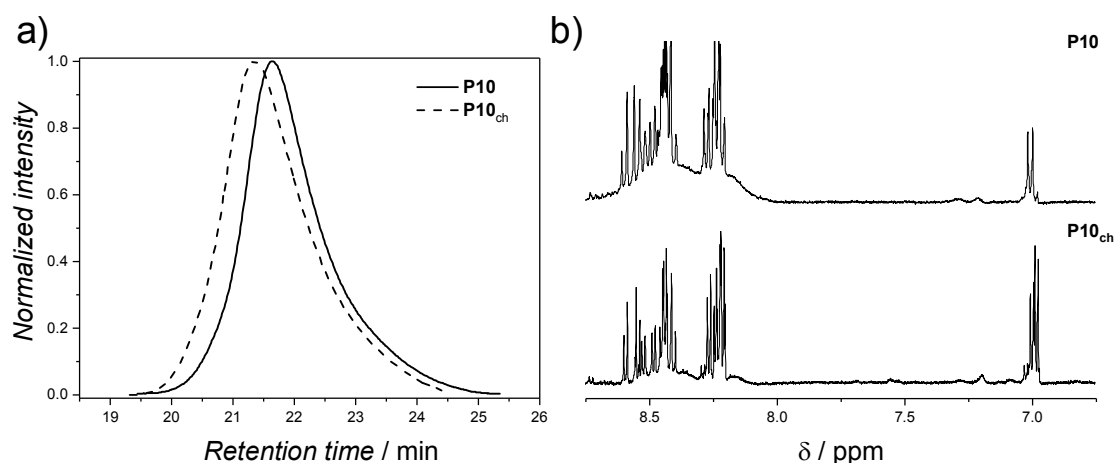


Figure 3.2.14: a) SEC Trace of **P10** and the changed **P10_{ch}** revealing a non-stable polymer **P10** over time b) ^1H NMR spectra of both polymers indicating a change in the aromatic region at 8.75 - 8.1 ppm as well as for the resonance at 7.0 ppm.

The shift to higher retention times together with the observed change in ^1H NMR indicate an intermolecular reaction of the incorporated tetrazole. An apparent change in molecular weight of 10 kDa was observed in DMAc SEC in comparison to the initial polymer **P10**.

Since initial promising results were obtained, several acrylic acid polymerizations were conducted. However, a repetition of the previous promising folding experiments could not be achieved, even with adapted reaction conditions such as varying the chain length of PAA or the equivalents of the bismaleimide, increasing the functionalization degrees, applying different solvents for the photochemical reaction, changing the photoreactor and utilizing a new bismaleimide linker. One exemplary SEC trace is depicted in Figure 3.2.15, where the equivalents of the dilinker were varied. The obtained data suggest that up to a 10-fold excess of dilinker, a shift to lower retention times is observed, indicating intermolecular cross-linking of the precursor. In previous literature it has been stated that the folding of polymers is more efficient when applying higher equivalents of a dilinker,²²² yet these findings could not be confirmed in the present thesis.

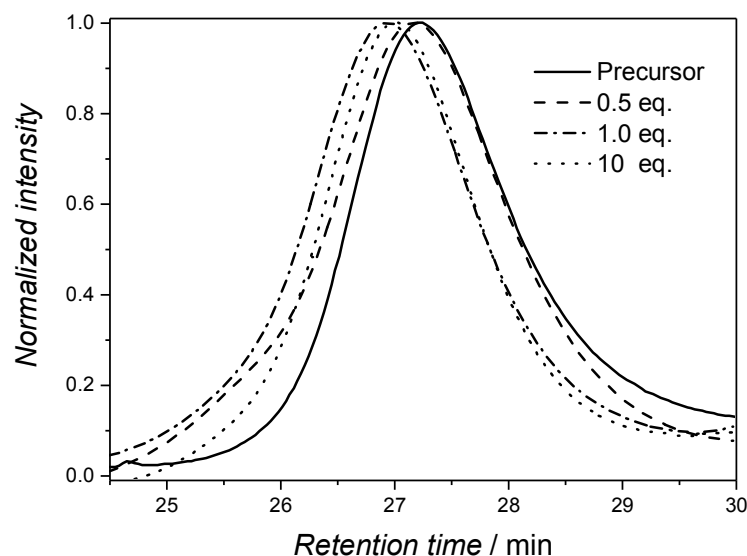


Figure 3.2.15: Exemplary SEC traces of the conducted irradiation experiments employing **18** as dilinker. The dilinker equivalents with respect to the tetrazole groups were varied with 0.5, 1.0 and 10.0.

Although the dilution and the equivalents of the dilinker were extensively varied, no successful SCNP formation was reached. One explanation could be that the statistical functionalization of the PAA based polymer is poor, achieving a non-fully functionalized polymer. Since the construction of SCNPs from PAA based polymers entails significant challenges with regard to reproducibility, a change regarding the polymer backbone became necessary. Thus, poly(styrene) (PS) polymers are inert and thus significantly simpler to handle and process, representing a sturdy starting point for a new approach. A visible light induced approach for the formation of SCNPs would open a multitude of photochemically based reactions e.g. λ -orthogonal approaches employing different activation wavelengths.

3.2.4 Polymerization of Polystyrene *via* NMP

Since the small molecule study resulted in mostly fluorescent derivatives, an introduction of these previously tested photoreactions should be utilized for the generation of fluorescent SCNPs on the basis of PS. For introducing the functional compounds, again the simple post-modification route was chosen. Before the post-modification was conducted, linear PS based polymers were synthesized in a controlled fashion. Therefore, nitroxide mediated polymerization (NMP) was employed as polymerization method. Prior to the polymerization, a suitable NMP initiator (**25**) was synthesized with 1-bromo ethyl benzene (**23**) and TEMPO (**24**) (Figure 3.2.16). The characterization of the NMP initiator can be found in the appendix (Figure 6.1.12). In this case, a copolymerization *via* NMP was carried out with styrene (**26**) and 4-chloromethylstyrene (CMS, **27**) as monomers (Figure 3.2.16). The obtained (**P11**) copolymer was characterized *via* SEC. Here, a monomodal molecular weight distribution (MWD) was observed. Employing PS calibration from THF SEC a M_n of 12.5 kDa ($\mathcal{D} = 1.3$) was determined.

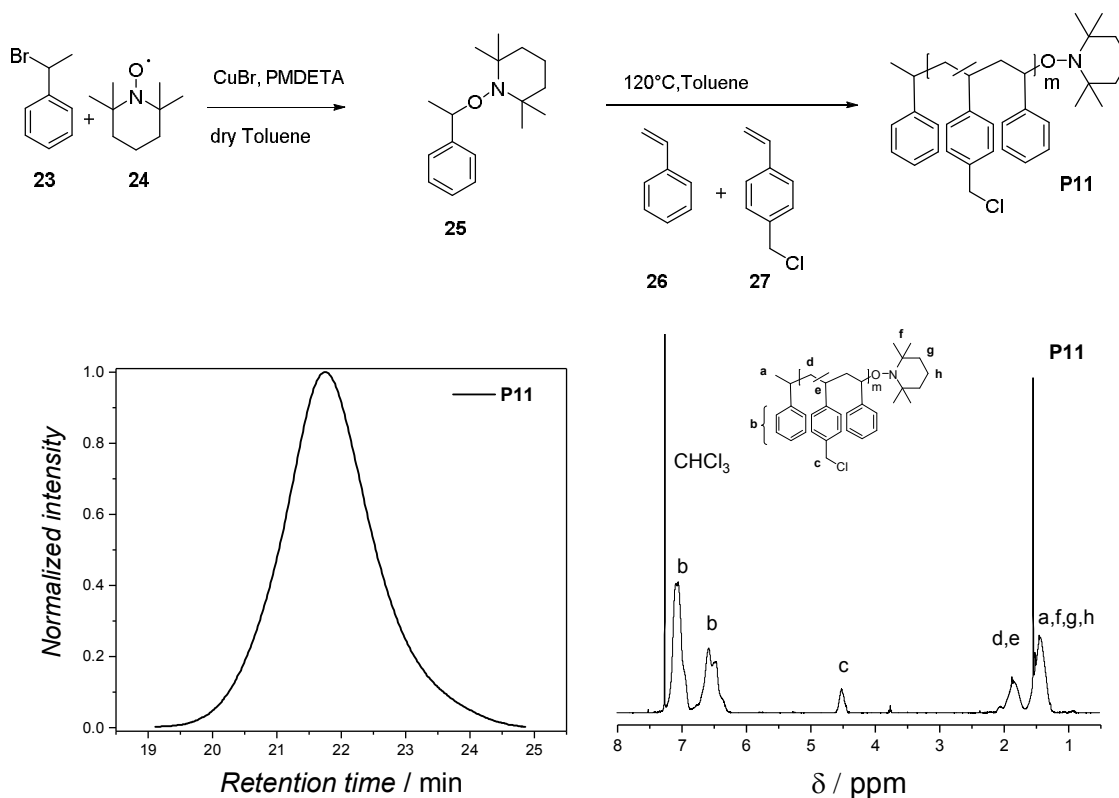


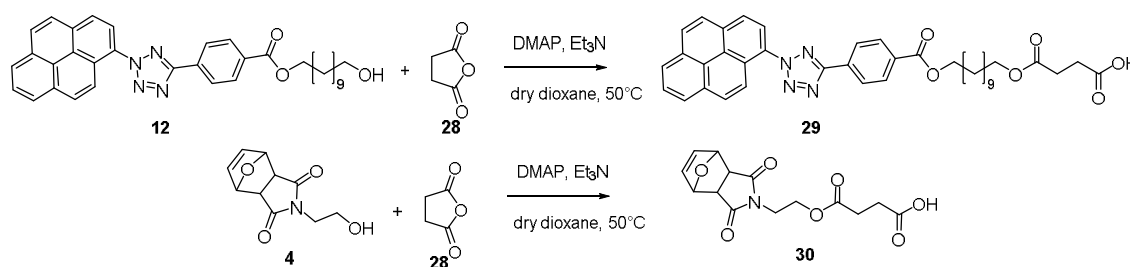
Figure 3.2.16: Overview of the synthetic pathway for the NMP initiator **25** and polymer **P11**. The copolymer **P11** was synthesized using **25**, **26** and **27** in toluene at 120°C. SEC trace and ¹H NMR spectrum of **P11** indicate a controlled copolymerization. Adapted with permission from reference [225] with permission from The Royal Society of Chemistry (RSC).²²⁵

The ¹H NMR spectrum showed resonances for **P11**, which are in agreement with the literature.⁶ The introduction of chlorine moiety *via* CMS allows for further post-modifications of the polymer, which was already performed in Barner-Kowollik team, with nucleophilic substitution and azide transformation among others.^{233,6} In the present approach, the functionalization of the copolymer with functional moieties required for the visible light folding was executed. Therefore, the modification of the chlorine content in the polymer was performed to allow for the precise post-modification of **P11**. Here, the integral of the proton resonances of the methylene group of the CMS monomer at 4.50 ppm (Figure 3.2.14, c) and the integral of the aromatic region at 7.28 - 6.23 ppm (Figure 3.2.14, b) was set into proportion to quantify the number of CMS units per polymer chain. To calculate the molar ratio of the chlorine groups in the copolymer, the following equation was utilized:

$$\%(\text{CMS}) = \frac{5c}{2b+c} * 100 \quad \text{Eq.(17)}$$

Based on Eq. (17) and with the measured integrals in ^1H NMR spectrum of **P11**, the molar ratio of the CMS groups was determined to 14 mol%. All further post-modification reactions using the photochemically active compounds are based on the ratio calculated for polymer **P11**.

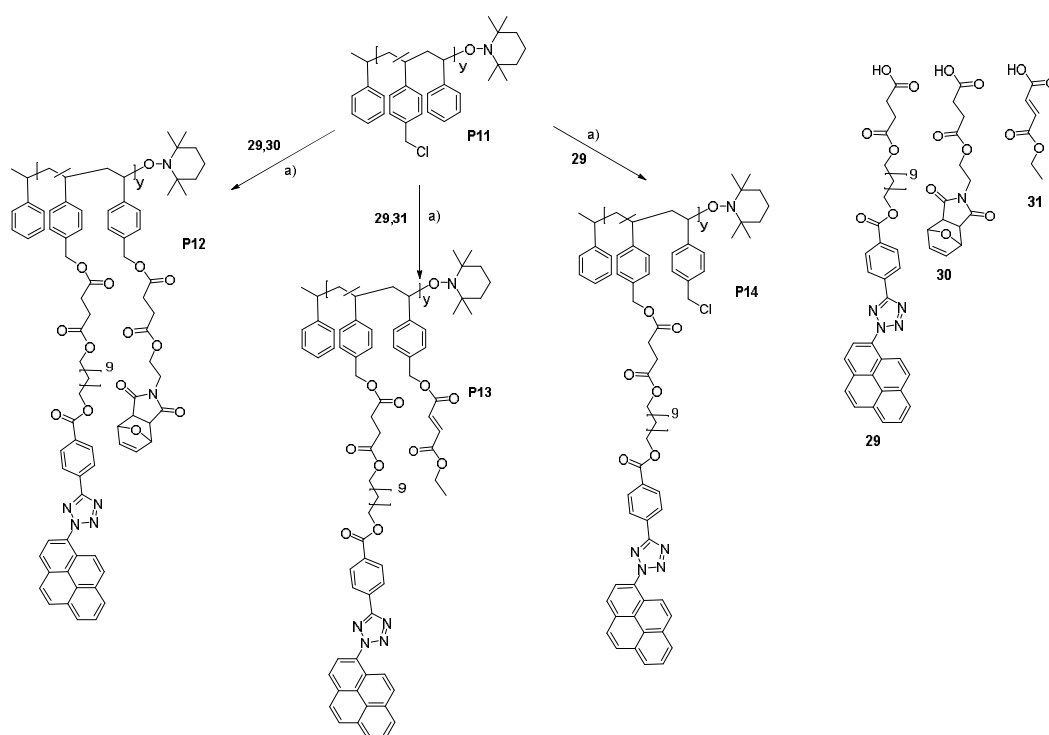
In the next step, the functionalization of **P11** with moieties suitable for visible light coupling to form SCNPs was carried out. Prior to the post-modifications, the OH derivatives of PAT (**12**) and protected maleimide (**4**) were converted into carboxylic acids for introduction in the PS based polymer **P11** (Scheme 3.2.9). The selection of the protected maleimide **4** as reagent was based on the observations made in the small molecule study (refer to Section 3.2). Here, the NITEC reaction of PAT and **4** resulted in the formation of a fluorescent pyrazoline adduct under mild reaction conditions. The acid derivatives of **12** and **4** were prepared *via* conversion of the hydroxy moieties in the presence of maleic anhydride **28** to yield compounds **29** and **30**.



Scheme 3.2.9: Synthesis of the PAT-*p*-Mal acid derivatives **29** and **30** applying ring-opening esterification with maleic anhydride.

The full synthesis procedure of **29** and **30** as well as the fully characterized ^1H NMR spectra can be found in Chapter 5. Once the suitable photoreactive linkers were synthesized, the esterification reactions with **P11** were carried out to connect the different linkers to the copolymer. Polymer species **P12**, **P13** and **P14**, bearing functional groups suitable for folding reactions *via* visible light, were prepared *via* esterification reactions with the chlorine moiety of the CMS unit (Scheme 3.2.10). First, the functionalization with **29** and **30** was carried out with a mild esterification method employing CsCO_3 .

For the second post-modification reaction, a commercially available monoethyl fumarate (**31**), was utilized. The incorporation of the fumarate was chosen, due to the formation of the fluorescent pyrazoline (**15**) after conversion with the PAT tetrazole. The last post-modification was performed with **29** only, yielding the polymer precursor **P14**. The detailed reaction conditions for the conducted post-modification reactions can be found in Chapter 5.



Scheme 3.2.10: Synthesis of the polymeric precursors **P12**, **P13** and **P14** bearing either PAT (**26**) and *p*-Mal (**27**), the monoethyl fumarate (**28**) or only PAT. * Cs_2CO_3 , 40°C dry DMF 48h.

The precursors **P12**, **P13** and **P14** were initially characterized via THF SEC and ^1H NMR spectroscopy to verify the coupling reactions with the photoreactive compounds. First, **P12** was analyzed to verify the successful post-modification reaction. In the THF SEC assessment, the initial polymer **P11** was also analyzed as a reference. As depicted in Figure 3.2.17, a shift towards lower retention times was found when **P11** and **P12** were compared. The difference in the retention time of polymer **P11** to polymer **P12** was monitored with a change in M_{app} from 12.5 kDa for **P11** to 18.5 kDa for **P12**.

The ^1H NMR spectrum of polymer **P12** reveals the resonances corresponding to the incorporated **29** with q (8.0–8.46 ppm), n (4.37 ppm), p (4.08 ppm) and o

(1.99-1.20 ppm) and **30** with m (6.44 ppm), l (5.24 ppm), i (4.25 ppm), j (3.72 ppm) and k (2.84 ppm) representing the successful post-modification of the initial polymer **P11** (Figure 3.2.17, b). The former resonance at 4.51 ppm, originating from the chlorine group vanished, indicating a complete functionalization. The ratio of the introduced groups was readily calculated by comparing the resonances associated with PAT with p-Mal in the copolymer resulting in a ratio PAT/p-Mal of 1:1.

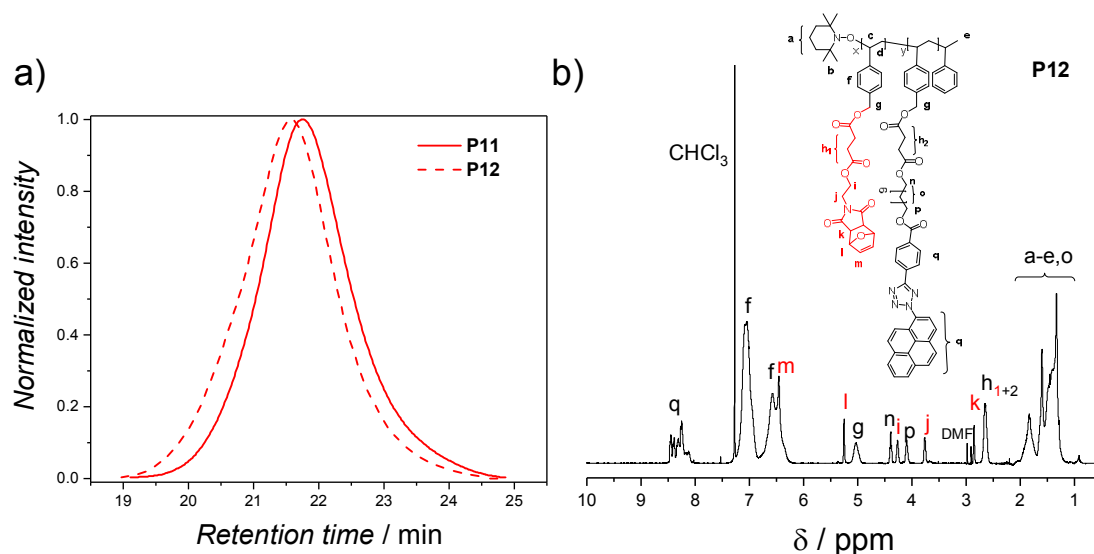


Figure 3.2.17: a) THF SEC traces of polymer **P11** (red line) and **P12** (red dashed line) indicating a shorter retention time for the substituted polymer **P12**. b) ¹H NMR spectrum of the functionalized polymer **P12** with the incorporated PAT (**29**) and p-Mal (**30**) groups measured in CDCl₃ with 400 MHz. Adapted with permission from reference [225] with permission from The Royal Society of Chemistry (RSC).²²⁵

Next, polymer **P13** was characterized with the analytical approaches as applied for **P12**. In SEC, the functionalized copolymer **P13** showed again a shift towards lower retention time in comparison to **P11**, giving a first hint at the successful post-modification. An estimated molecular weight change, employing PS calibration of the SEC, indicated an increase to a M_n of 15.5 kDa. A molecular weight change of ~ 3.3 kDa compared to the native **P11** (Figure 3.2.18, a)) was determined. Furthermore, ¹H NMR spectrum indicated the successful functionalization evidenced by the appearance of the PAT with q (8.0-8.46 ppm), n (4.37 ppm), p (4.08 ppm) and o (1.99-1.20 ppm) and monoethyl fumarate i (4.22 ppm) resonances (Figure 3.2.18, b)).

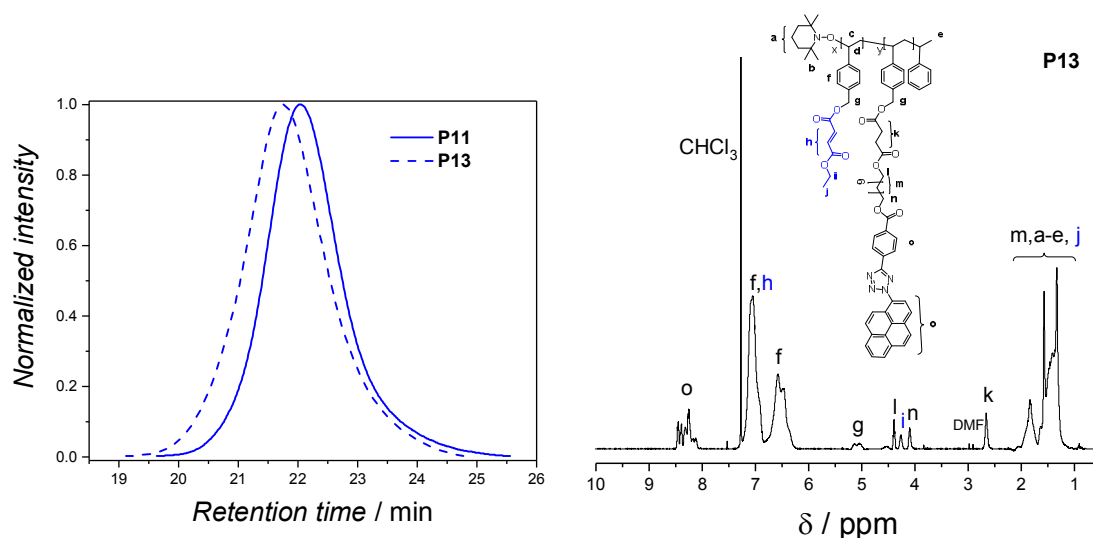


Figure 3.2.18: a) THF SEC traces of polymer **P11** (blue line) and **P13** (blue dashed line) indicating a decrease in retention time. b) ¹H NMR spectrum of the functionalized polymer **P13** with the incorporated PAT (**29**) and monoethyl fumarate (**31**) groups recorded in CDCl₃ with 400 MHz. Adapted with permission from reference [225] with permission from The Royal Society of Chemistry (RSC).²²⁵

A full functionalization of the 14mol% of the CMS groups in **P11** was observed for **P13**. The ratio of the incorporated PAT and fumarate groups was calculated for **P13** with PAT/monoethylfumarate of 1:1.

The last polymeric precursor synthesized (**P14**) features a functionalization with PAT only (Figure 3.2.19). When SEC measurements were conducted, **P14** showed an increase in M_n of ~6 kDa in comparison to the original polymer **P11**. Here, a broadening of the SEC trace was observed, leading to a polydispersity of 1.4. In ¹H NMR spectroscopy, the successful functionalization of **P11** was established, showing the resonances arising from the PAT molecule. However, no quantitative functionalization was realized, which was probably caused by the exclusive introduction of the bulky PAT groups. By comparing the aromatic resonances before and after functionalization with the signal at 4.51 ppm, the degree of functionalization was calculated to be close to 12 mol %. The previously functionalized precursor **P12** and **P13** featured a complete functionalization of 14 mol %.

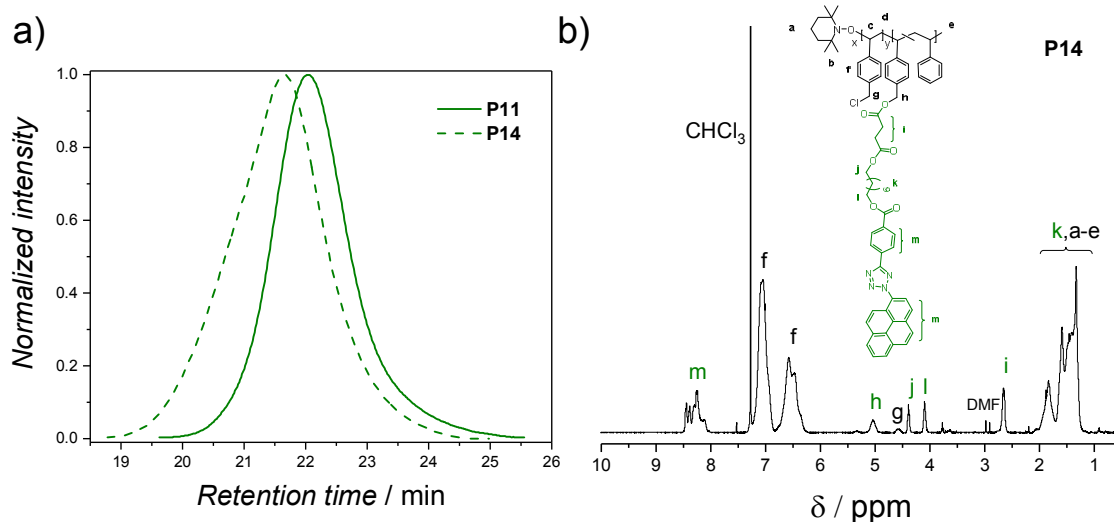


Figure 3.2.19: a) THF SEC traces of polymer **P11** (green line) and **P14** (green dashed line) indicating a decrease in retention time b) ¹H NMR spectrum of the functionalized polymer **P14** with the incorporated PAT (**29**) group measured in CDCl₃ with 400 MHz. Adapted with permission from reference [225] with permission from The Royal Society of Chemistry (RSC).²²⁵

The values obtained from SEC and ¹H NMR measurements are collated in Table 3.2.2, showing the different functionalization degrees as well as the mol % of the incorporated compounds. An increase of the molecular weight ranging from 3-6 kDa was observed for **P12**, **P13** and **P14** compared to the original polystyrene copolymer **P11**. Although a non-quantitative functionalization was found for **P14** with 12 mol%, here the highest difference in the molecular weight was observed in SEC. One possible explanation could be the exclusive introduction of the high molecular weight (660 Da) PAT tetrazole (**29**), representing the heaviest compound used for the post-modification reactions.

Table 3.2.2: Characterization data obtained from THF SEC and ^1H NMR spectroscopy measurements for **P11-P14**. The post-modified polymers **P12-14** indicate an increase in M_n after the functionalization reaction. The percentage of incorporated groups was calculated via ^1H NMR spectroscopy. Adapted with permission from reference [225] with permission from The Royal Society of Chemistry (RSC).²²⁵

Polymer	M_n (kDa)	D_M	Tet (%)	p-Mal (%)	Fum (%)
P11	12.5	1.3	-	-	-
P12	18.5	1.4	7	7	-
P13	15.5	1.3	7	-	7
P14	18.3	1.4	12	-	-

After successful conversion of **P11** to photoreactive **P12**, **P13** and **P14**, the light induced formation of the fluorescent nanoparticles was performed. The polymers **P12-P14** were irradiated with three Avonec LED lamps (λ_{em} = 410-420 nm) for 90 minutes without any additives expecting either the NITEC or dimerization reaction, respectively (Scheme 3.2.11). Furthermore, a NICAL driven collapse of **P14** was targeted by the usage of a diacid (**32**)

The irradiation of the photoreactive polymers were conducted at a concentration of 0.017 mg L⁻¹ in DCM, representing the highly diluted conditions necessary to enforce the intramolecular chain collapse. Based on the small molecule study, an irradiation time of 90 minutes was chosen for the SCNP formation, which was adequate to convert the PAT tetrazole. Subsequently, the solvent was removed under reduced pressure and the SCNPs were dissolved in the appropriate solvent for analysis. The detailed irradiation conditions can be found in Chapter 5.

For polymer **P12**, a NITEC driven folding of the PS precursor was envisaged, driven by the incorporation of the protected maleimide (**30**). An alternative approach for triggering NITEC is represented with polymer **P13**, where a NITEC folding was expected with the incorporated ene (**31**). The polymer collapse of **P14** was targeted *via* the dimerization reaction of the activated tetrazole.

3.2.5 Visible Light Induced Folding of PS Polymers and their Characterization

For analysis of the potential SCNPs, UV/Vis, fluorescence and NMR spectroscopy as well as SEC were employed. The spectroscopic methods entail the information of the photochemical reactions and the SEC measurements indicate if an intramolecular collapse took place. Additionally, diffusion ordered spectroscopy (DOSY) measurements were conducted to confirm the decrease of the hydrodynamic diameter (D_h) compared to their precursors. A first hint at the expected photochemistry after irradiation of the polymers can be established *via* UV/Vis and fluorescence spectroscopy measurements. Therefore, the irradiated polymer samples (**SCNP12-15**) were dissolved in DCM and the spectroscopic measurements were performed (Figure 3.2.20). In fluorescence spectroscopy, the samples were excited with a wavelength of 400 nm.

First, the UV/Vis and fluorescence spectra of **SCNP12** and **SCNP13** were recorded. For comparison of the envisaged NITEC photoreactions, absorbance and emission characteristics of **13** and **15** from the small molecule study are plotted together with the observations found for the corresponding **SCNP12** and **SCNP13**.

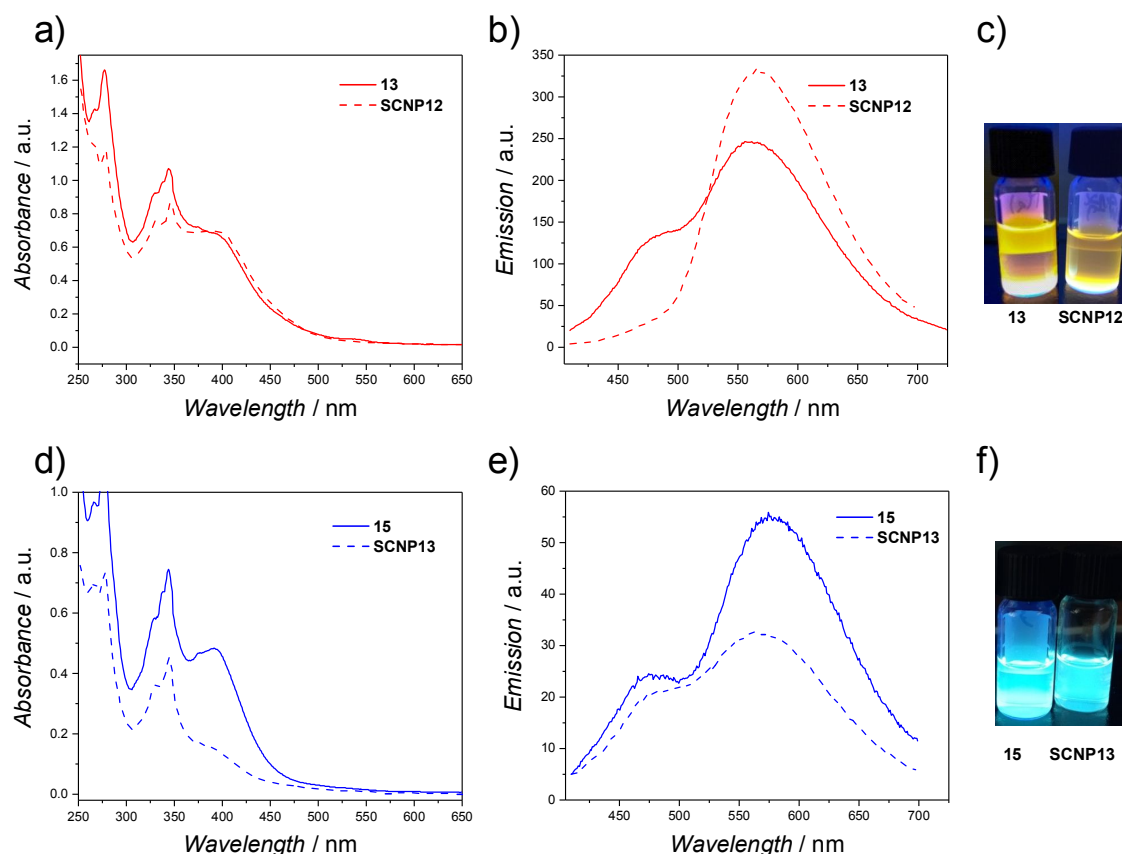


Figure 3.2.20: a) UV/Vis spectra of **13** and **SCNP12**. b) Fluorescence spectra of **13** and **SCNP12** ($\lambda_{\text{ex}} = 400$ nm). c) Image of **13** and **SCNP12**. d) UV/Vis spectra of **15** and **SCNP13**. e) Fluorescence spectra of **15** and **SCNP13** ($\lambda_{\text{ex}} = 400$ nm) f) image of **15** and **SCNP13**. UV/Vis and fluorescence spectra were recorded in DCM ($c = 0.2$ mg mL⁻¹). Images of the fluorescent small molecules and SCNPs were irradiated with a hand-held UV-lamp ($\lambda_{\text{em}} = 366$ nm). The irradiation conditions as well as the geometry can be found in the appendix (Figure 6.1.51-Figure 6.1.53). Adapted with permission from reference [225] with permission from The Royal Society of Chemistry (RSC).²²⁵

In UV/Vis spectroscopy, the global absorbance maximum at 400 nm – representing the pyrazoline formation – was observed for both measured SCNPs (**SCNP12** + **SCNP13**) (Figure 3.2.20, a), d)). These results fit perfectly with the observed absorption spectrum obtained for the small molecules **13** and **15**, respectively (refer to Section 3.2.1).

In the conducted fluorescence measurement (Figure 3.2.20, b) of **SCNP12**, similar fluorescence properties were observed as for **13**. In particular, the characteristic emission spectrum of the potential **SCNP12** was obtained with an emission maximum at 575 nm. The emission wavelength at 575 nm can be attributed to the pyrazoline formation.

Moreover, the fluorescence properties were detected *via* excitation of the adducts, employing a hand-held UV-lamp ($\lambda_{em} = 366$ nm). For **SCNP12** the same fluorescence features found as observed for **13** were detected, giving a yellow color.

In the conducted fluorescence measurement (Figure 3.2.20, e) of **SCNP13** both emission maxima at 475 and 575 nm were observed. The fluorescence features of **SCNP13** are congruent with the emission maxima found for the fumarate adduct **15**, indicating a successful NITEC reaction. Furthermore, the similar fluorescence properties for **15** and **SCNP13** were demonstrated, with the excitation of these products employing a UV-lamp ($\lambda_{em} = 366$ nm).

Next, **SCNP14** and **SCNP15** were analyzed *via* UV/Vis and fluorescence spectroscopy. In order to compare the reactions induced by visible light, the data collected for **16** and **17** in UV/Vis and fluorescence spectroscopy are plotted with the polymer samples (Figure 3.2.21). The spectra of **16** and **17** originate from the visible small molecule study and are plotted as a reference. In UV/Vis measurement (Figure 3.2.21, a) of **SCNP14** a local absorbance maximum at 400 nm is recorded, which is in good agreement with the UV/Vis spectrum for the dimerized PAT (**16**). In the recorded fluorescence spectrum of **SCNP14** the same emission band as found for **16** was observed. Here, an emission maximum at 475 nm is recorded for **SCNP14**, which is congruent with the collected data from fluorescence measurements of **16**.

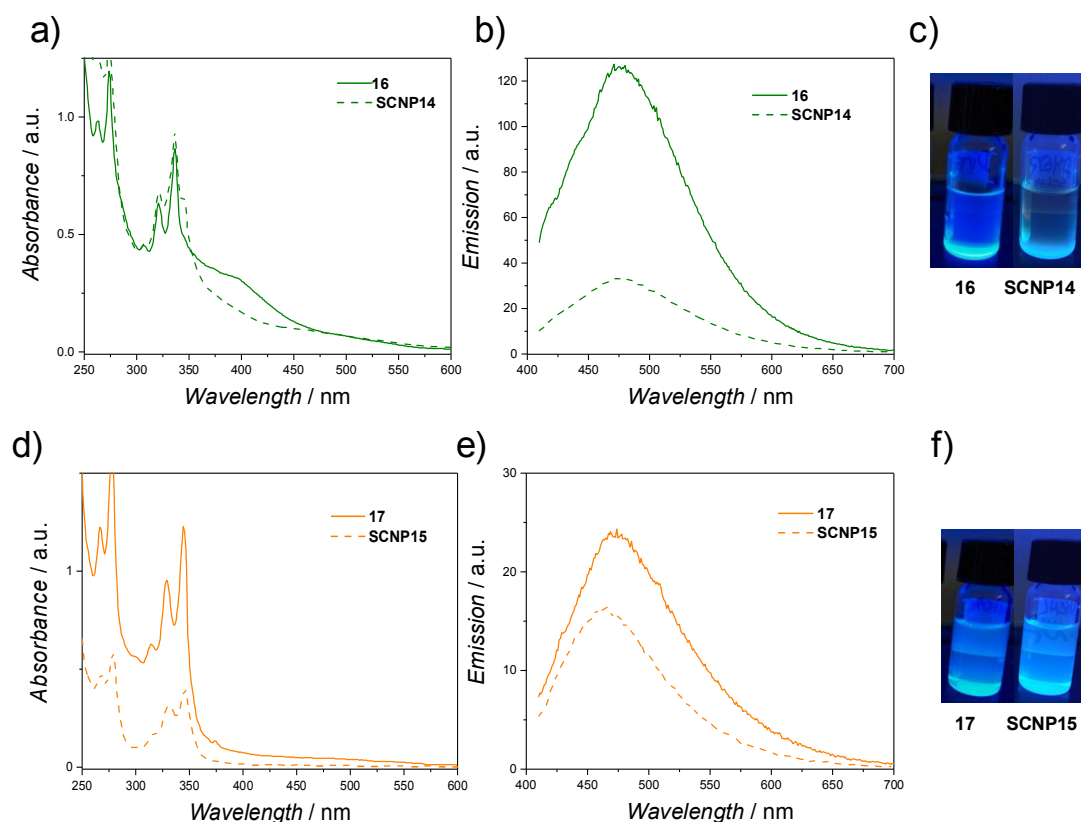


Figure 3.2.21: a) UV/Vis spectra of **16** and **SCNP14**. b) Fluorescence spectra of **16** and **SCNP14** ($\lambda_{ex} = 400$ nm) c) image of **16** and **SCNP14**. d) UV/Vis spectra of **17** and **SCNP15**. e) Fluorescence spectra of **17** and **SCNP15** ($\lambda_{ex} = 400$ nm) f) image of **17** and **SCNP15**. UV/Vis and fluorescence spectra were recorded in DCM ($c = 0.2$ mg mL⁻¹) Images of the fluorescent small molecules and SCNPs were irradiated with a hand-held UV-lamp ($\lambda_{em} = 366$ nm). The irradiation conditions as well as the geometry can be found in the appendix (Figure 6.1.51-Figure 6.1.53). Adapted with permission from reference [225] with permission from The Royal Society of Chemistry (RSC).²²⁵

As observed in the small molecule study of the NICAL reaction resulting in **17**, no absorbance maximum at 400 nm was detected. Here, the same lack of an absorbance maximum at 400 nm was detected for **SCNP15**. Only the characteristic absorbance maxima of 350 and 325 nm were observed, indicating a NICAL process between PAT and the carboxylic acid. In the recorded fluorescence spectra (Figure 3.2.21, e), an emission maximum at 475 nm was obtained, indicating the NICAL reaction of **SCNP15**.

All measured fluorescent properties were readily observed by irradiation with a hand-held UV-lamp ($\lambda_{em} = 366$ nm). The conducted spectroscopic methods indicate the successful photochemistry after irradiation of the polymers.

The application of visible light instead of UV light causes less side reactions allowing a more versatile characterization of the irradiated polymers *via* ^1H NMR spectroscopy. ^1H NMR measurements were conducted for better insight in the performed photo-induced reactions. First, **SCNP12** was analyzed *via* ^1H NMR spectroscopy to verify the pyrazoline formation after irradiation of the incorporated PAT tetrazole (Figure 3.2.22). To compare the initial polymer **P12** with **SCNP12**, the ^1H NMR spectra were plotted in one graph. In **P12**, the resonances of the incorporated p-Mal groups are highlighted with a (6.44 ppm) and b (5.24 ppm) and the aromatic tetrazole groups are highlighted with c (8.48-8.04 ppm). In the irradiated sample **SCNP12**, a shift of the aromatic region (8.29 ppm-7.71 ppm) was observed indicating the conversion of the tetrazole.

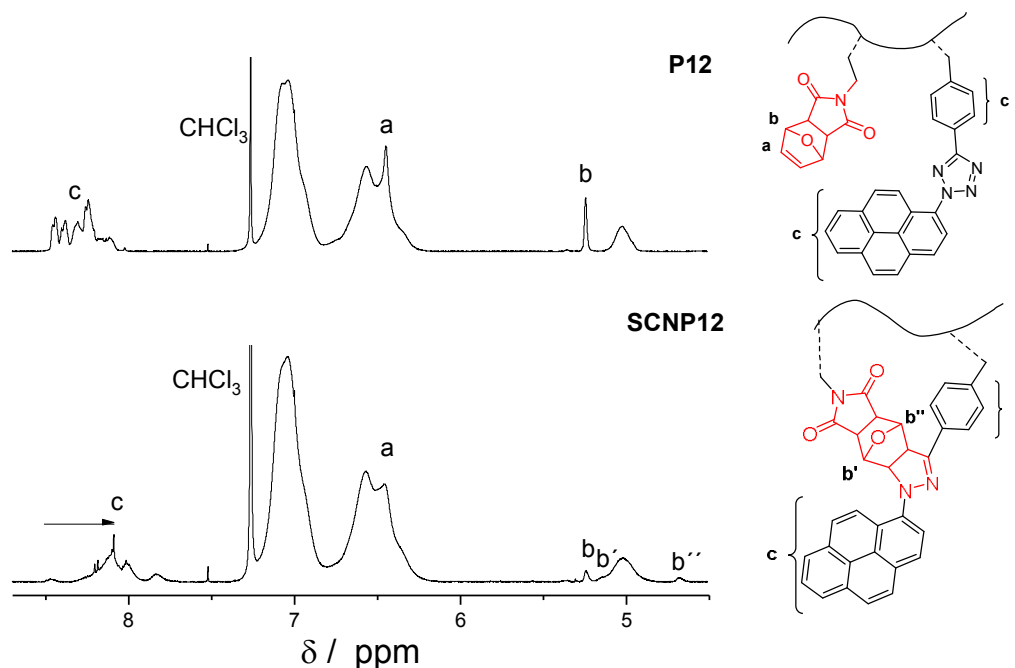


Figure 3.2.22: ^1H NMR spectra of **P12** and **SCNP12** indicating the consumption of the incorporated p-Mal after irradiation. The resonances a (6.44 ppm) and b (5.24 ppm) from p-Mal illustrated in the upper spectrum of **P12** were reduced after treatment with visible light. A reduction of these signals together with newly arising resonances b' (5.14 ppm) and b'' (4.66 ppm) indicate the successful formation of the pyrazoline adduct. The irradiation conditions as well as the geometry can be found in the appendix (Figure 6.1.51-Figure 6.1.53). Adapted with permission from reference [225] with permission from The Royal Society of Chemistry (RSC).²²⁵

Furthermore, a decrease of the incorporated p-Mal group resonances (a and b) comparing **P12** with **SCNP12** supports the assumption of the expected reaction product. A reduction of these signals together with newly arising resonances b' (5.14 ppm) and b'' (4.66 ppm), which can be attributed to the pyrazoline adduct, indicate the successful pyrazoline formation. In addition, the ¹H NMR resonances of **SCNP12** indicate the same resonances as found for the pyrazoline adduct **13** in the small molecule study (refer to Chapter 5), underpinning the successful formation of the pyrazoline adduct.

In the case of **SCNP13** – bearing the fumarate species – no significant resonances which were highlighted in blue for the NITEC reaction, were observed (Figure 3.2.23, b). The reason for no detectable resonances in the region of 5.6 ppm and 4.8 ppm for **SCNP13** from the pyrazoline product can be explained with the rearomatization of the irradiated sample. As mentioned before in the small molecule study, a rather rapid (1h) rearomatization takes place, if the nitrile imine reacts with the fumarate. Although the fumarate pyrazoline resonances in **SCNP13**, were not found, UV/Vis and fluorescence spectroscopy provided information for a successful pyrazoline formation of the incorporated fumarate **31**.

The ¹H NMR spectrum of **SCNP14** revealed a narrow aromatic region (8.0-8.4 ppm) and additionally a broadening of the tetrazole signals g (4.4 ppm) and i (4.2 ppm). These observations are congruent with the resonances found for the tetrazine species **16** (refer to Section 3.2.1) in the small molecule study.

For the NICAL triggered reaction employing the PEG diacid (**32**), the ¹H NMR spectrum is illustrated in (Figure 3.2.23, d)). The resonances, which can be attributed to the PEG diacid linker, were observed as indicated by l (5.0 ppm), m (3.7 ppm) and n (4.3 ppm). As mentioned above, the polymer was precipitated after the photoreaction to remove possible residual PEG. The ¹H NMR spectrum indicates after precipitation the presence of the small PEG chain in **SCNP15**, indicating the successful connection of the of **32** to the polymer *via* NICAL.

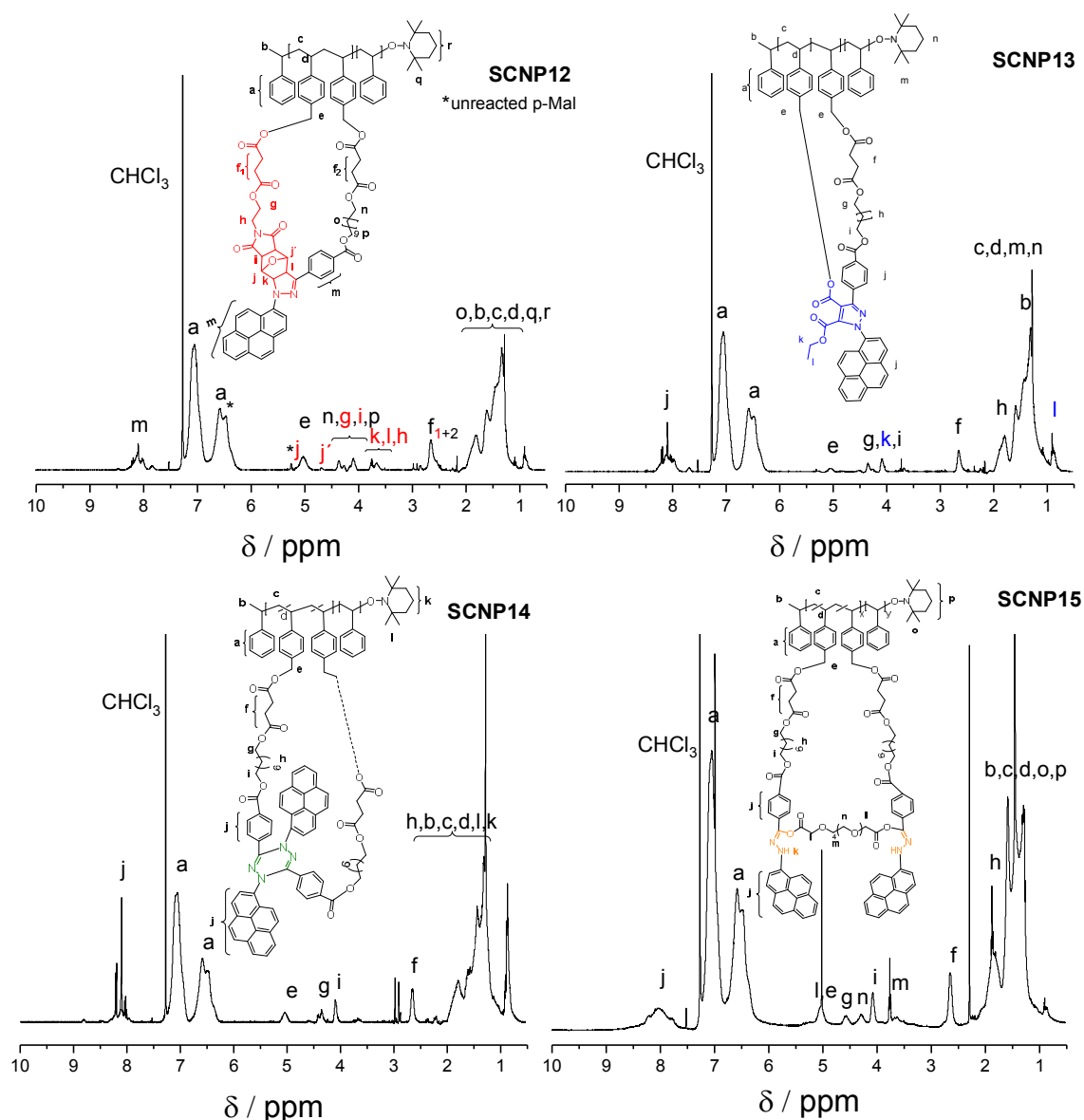


Figure 3.2.23: ^1H NMR spectra of **SCNP12-15** measured in CDCl_3 at 400 MHz. The significant resonances of the molecules are highlighted in the color according to the color of the structure. Adapted with permission from reference [225] with permission from The Royal Society of Chemistry (RSC).²²⁵

So far, only evidence for the expected photochemistry reactions were found performing UV/Vis, fluorescence and NMR spectroscopy of the irradiated polymer samples. To verify the intramolecular collapse of the polymers towards SCNPs, SEC measurements were conducted. Here, the polymer precursors **P12-14** are depicted and highlighted with the color of the applied photoreaction (Figure 3.2.24). In particular, **P12** (red line) functionalized with **29** and **30**, results in a number average molecular weight of 18.5 kDa using the polystyrene calibration in THF SEC.

The irradiated sample **SCNP12** (red dashed line) illustrates the shifted SEC trace to longer retention times. Employing a PS calibration, a M_n of 15 kDa was determined, resulting in a change in M_{app} of 3.5 kDa. This change indicates a compaction for **SCNP12** compared to **P12** and it can be assumed that an intramolecular crosslink *via* the NITEC reaction took place.

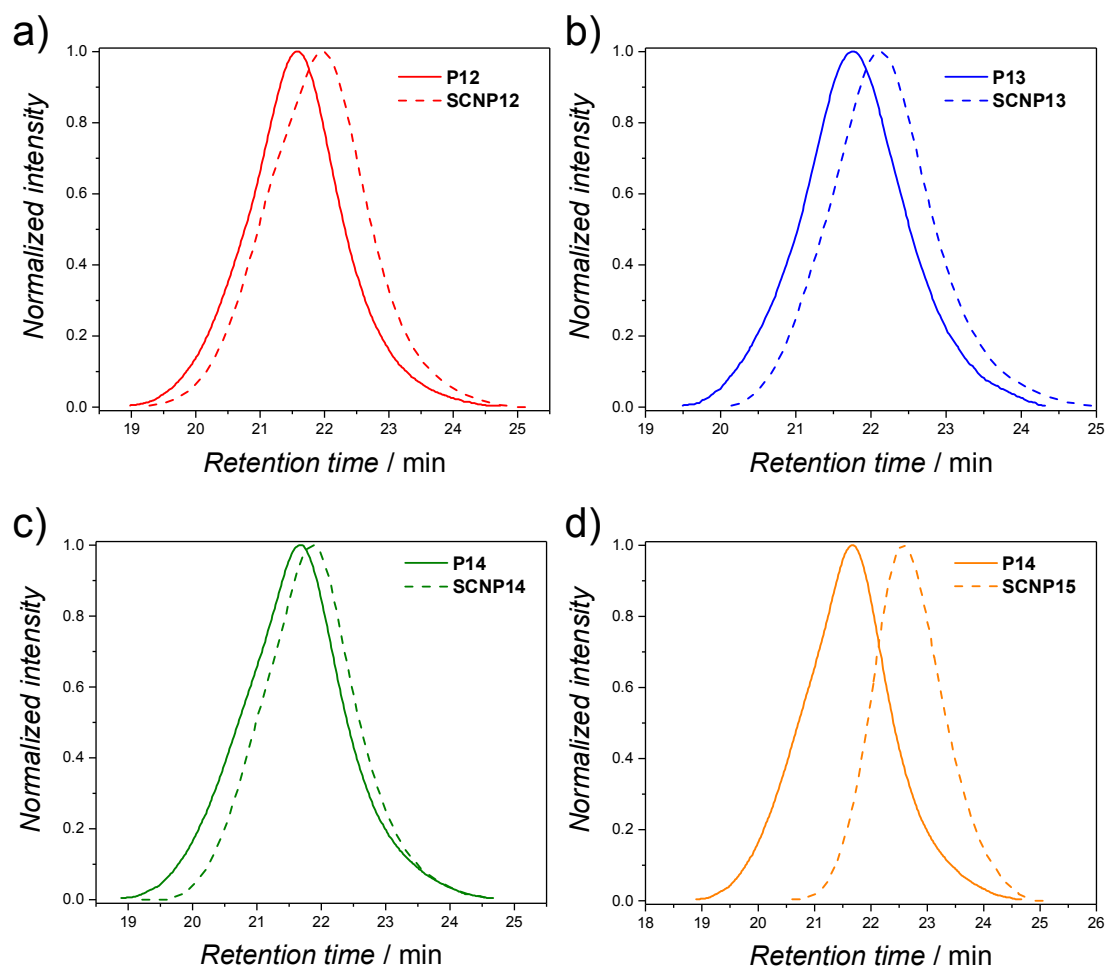


Figure 3.2.24: a-d) SEC traces of the polymer precursors **P12-14** (lines) and their corresponding visible light irradiated samples **SCNP12-15** (dashed lines). The SCNPs indicate a higher retention time with respect to their precursors, verifying the successful SCNP collapse. The color code indicates the photochemistry employed. a) PAT + *p*-Mal, b) PAT + fumarate, c) PAT dimerization and d) PAT + PEG diacid. Adapted with permission from reference [225] with permission from The Royal Society of Chemistry (RSC).²²⁵

Next, the linear polymer **P13** was investigated *via* THF SEC (Figure 3.2.24, b). As mentioned before (Section 3.2.4), a monomodal MWD for **P13** with a M_n of 15.5 kDa was determined. For the irradiated polymer sample **SCNP13**, a shift to higher retention times compared to the initial polymer **P13** was found. The M_{app} was calculated to 12 kDa, representing a change of 3 kDa to the polymer

precursor **P13**. It can be carefully assumed that an intramolecular collapse of **P13** took place after irradiation.

As already mentioned (refer to Section 3.2.4), the PAT functionalized polymer **P14** showed a M_n of 18.3 kDa. The first SCNP collapse employing **P14** was targeted *via* the dimerization reaction of the tetrazoles upon irradiation. Here, the irradiated sample **SCNP14** indicated a shift to higher retention time compared to **P14**. Employing the PS calibration, a M_{app} of 15.6 kDa for **SCNP14** was calculated, representing a difference compared to **P14** with 2.7 kDa, indicating a compaction of **P14** after irradiation with light. The next photoreaction employed was achieved with the addition of the previous mentioned PEG diacid linker to the DCM solution carrying **P14**. Polymer **P14** was again measured *via* THF SEC and compared with the irradiated sample **SCNP15** (Figure 3.2.24, d). The obtained SEC data revealed an efficient compaction of **SCNP15** in comparison to the linear **P14**. Here, a M_{app} of 9 kDa was observed for **SCNP15**, indicating an efficient collapse.

Table 3.2.3: Number average molecular weight (M_n) and dispersity (\mathcal{D}_M) values obtained from THF SEC showing the molecular weight of the polymer precursors **P12-P14** and their corresponding **SCNP12-15**.

Polymer	M_n (kDa)	\mathcal{D}_M
P12	18.5	1.3
SCNP12	14.7	1.4
P13	15.5	1.3
SCNP13	12	1.3
P14	18.3	1.3
SCNP14	15.6	1.4
SCNP15	9	1.2

Due to the fact that the SEC instrument is calibrated with linear PS, its application to the present polymers has to be taken with caution. The change in molecular weight of the SCNPs is based on the relative decrease of the hydrodynamic volume and presents as already mentioned the apparent change M_{app} .

In order to verify the nanoparticle formation independently from SEC, DOSY NMR measurements were performed. This spectroscopic method determines the diffusion coefficient for molecules in solution (refer to Section 2.3.3). *Via* the application of the Stokes-Einstein equation, which describes the relation between diffusion coefficient and radius (refer to the Section 2.3.3), the D_h of the polymers and their corresponding SCNPs can be determined.

First, the polymer precursors **P12-14** were analyzed *via* DOSY NMR and the obtained values are collated in Table 3.2.4. Different D_h were observed for the polymer precursors with 6.2 nm for **P12**, 5.5 nm for **P13** and 10.6 nm for **P14**. The differences in D_h can be explained based on the functionalization degrees and functionalization groups, which were varied in **P12-14**. For **P12** and **P13**, similar D_h were obtained, due to identical functionalization degrees of 14 mol% and similar PAT to ene ratios. Although a minor functionalization degree of 12 mol % was reached for **P14**, a higher D_h in comparison to **P12** and **P13** was found. It has to be considered that in **P14** only the bulky PAT tetrazole was incorporated, which could be the reason for the higher diffusion coefficient measured in DOSY.

Table 3.2.4: Hydrodynamic diameters obtained from DOSY measurement of the polymer **P12-14** and the corresponding **SCNP12-15**. The measurements were conducted in $CDCl_3$ at 400 MHz.

Polymer	D_h (nm)
P12	6.2
SCNP12	2.9
P13	5.5
SCNP13	2.7
P14	10.6
SCNP14	5.0
SCNP15	3.8

Importantly, the SCNPs should feature a lower D_h in comparison to the previously analyzed **P12-14**. The corresponding **SCNP12-15** were subsequently analyzed *via* DOSY NMR, resulting in D_h ranging from 2.7-5.0 nm. In the case of **SCNP12**, a D_h of 2.9 nm was found, indicating an efficient compaction of **P12**, where a D_h of 6.2 nm was determined.

For **SCNP13**, a smaller diameter with 2.7 nm indicated the successful intramolecular collapse in comparison to the measured precursor **P13** with 5.5 nm. For **SCNP14** and **SCNP15**, which were based on **P14**, D_h values with 5.0 for **SCNP14** and 3.8 nm for **SCNP15** were recorded, respectively. The relative reduction of the detected values indicate that the photochemistry employed led to an intramolecular collapse of the linear polymer **P14**.

4.

Concluding Remarks and Outlook

In the present thesis, the investigation of the tetrazole photochemistry as well as its application for the formation of fluorescent single chain polymer nanoparticles (SCNPs) employing light of different wavelengths is explored. Initially, a UV-light driven approach led to water-soluble and fluorescent nanoparticles (Section 3.1), which are currently under investigation in *in vivo* experiments. Secondly, a new visible light system was developed, demonstrating the compaction of hydrophobic polymers (Section 3.2).

In the first approach, terpolymerizations *via* reversible addition-fragmentation chain transfer polymerization (RAFT) employing functional and water-soluble monomers were prepared. The obtained polymers, however, showed broad and bimodal molecular weight distributions (MWDs) during size exclusion chromatography (SEC) measurements. In addition, the UV-light induced folding of the polymers indicated an apparent molecular weight change to higher molecular weights, suggesting undesired network formation.

Thus, the synthetic strategy was changed and water-soluble poly(acrylic acid) (PAA) was found to function as a good candidate since it combines two important properties: water-solubility and the presence of functional groups, *i.e.* carboxylic acid moieties. These groups were employed for the incorporation of enes (protected maleimides) and UV active tetrazoles into the polymer *via* esterification reactions. Prior to the folding experiments, the reactivity of the UV-light active tetrazole with the corresponding ene and carboxylic acid (acetic acid) was investigated in small molecule studies. The reaction of the ene resulted in the nitrile imine-mediated tetrazole-ene cycloaddition (NITEC) and the reaction with the acetic acid in the nitrile imine carboxylic acid ligation (NICAL). It was demonstrated that in a competitive reaction (mixture of tetrazole, ene and acetic acid) the NICAL reaction is preferred over the NITEC reaction. Furthermore, the fluorescent features for the NITEC and NICAL reaction products were investigated, indicating highly fluorescent properties for the NITEC pyrazoline adduct with an emission maximum at 575 nm when excited in the visible range. For the NICAL reaction, only a minor fluorescent adduct was observed with an emission maximum at 475 nm.

Once the model studies were concluded, the functional polymers were employed for the preparation of SCNPs under diluted conditions. In particular, polymers containing both tetrazole and ene and only tetrazole units were irradiated with UV-light ($\lambda_{\text{max}} = 320$ nm). Interestingly, although an excess of carboxylic acids was present in the polymer, a predominantly NITEC driven formation of SCNPs was found in the case of the dual functionalized polymer. Possible reasons include the reduced accessibility of the bulky tetrazoles towards the carboxylic acids in the polymeric chain, making the protected maleimide more attractive towards the nitrile imine.

In order to confirm the intramolecular collapse, all polymeric precursors and their corresponding SCNPs were analyzed *via* SEC, dynamic light scattering (DLS) and diffusion ordered spectroscopy (DOSY). In SEC, the measured SCNPs displayed a strong change to lower apparent molecular weights compared to their polymer precursors, evidencing the desired intramolecular bonds after irradiation with UV-light. Furthermore, all polymers and their SCNPs were analyzed using DLS.

The obtained hydrodynamic diameter (D_h) from DLS measurements indicated for all SCNPs an efficient compaction compared to their precursors. However, very small sizes (~ 1 nm) were obtained for two SCNPs, which were folded with the dual folding mechanism (NITEC and NICAL) or the NICAL reaction only. The small sized SCNPs were further analyzed with DOSY NMR spectroscopy, where the small sizes were confirmed. In addition to the size determination of the SCNPs, the fluorescence properties of the collapsed polymers were investigated. The fluorescent features found for the SCNPs are congruent with the fluorescent properties observed in the small molecule study, corresponding to either NITEC or NICAL reaction, respectively.

Importantly, the highly fluorescent SCNPs were tested in HeLA cells and zebra fish embryos, showing good cellular uptake in the initial biological tests in a collaboration with the group of Prof. Ute Schepers. Further imaging experiments are currently under way in the Schepers laboratories.

Subsequently, the UV-active tetrazole was replaced with a visible light active tetrazole bearing a pyrene unit, which was employed for the preparation of fluorescent SCNPs (Section 3.2). Similarly to the previous approach, a small molecule study was carried out to investigate the reactivity of the pyrene aryl tetrazole (PAT) with different functional groups *i.e.* furan protected maleimide, fumarate, acetic acid and maleimide. The small molecule study revealed that the protected and non-protected maleimide groups led to highly fluorescent pyrazoline adducts, which emit light at a wavelength of approx. 575 nm after excitation with 400 nm, leading to a suitable fluorophore for cell imaging. The fumarate adduct showed similar absorption and emission (475 nm and 575 nm) properties as the maleimide adducts, however with a lower emission intensity in the fluorescence spectrum. The products of the PAT dimerization and NICAL reaction showed the lowest fluorescence intensities, with an emission maximum at 475 nm. The successful formation of the photoinduced reaction products associated with the small molecule study was evidenced employing ^1H NMR spectroscopy, electrospray ionization mass spectrometry (ESI-MS) and UV/Vis and fluorescence spectroscopy.

Once the small molecules were successfully investigated, the preparation of the polymer precursors was conducted. First, a bioactive molecule, here a peptoid, was introduced in the RAFT agent, which was evidenced *via* ^1H NMR spectroscopy and ESI-MS. The successful polymerization of acrylic acid with the peptoid loaded RAFT agent was confirmed *via* ^1H NMR spectroscopy, where the peptoid end-group was maintained after polymerization. Analogue to the UV-approach, the functional groups along the polymer backbone were introduced *via* a mild Steglich esterification and analyzed utilizing SEC and ^1H NMR spectroscopy. The functionalized PAA polymer was subsequently irradiated – under high dilution conditions – with visible light ($\lambda = 410\text{-}420\text{ nm}$) and analyzed *via* SEC, UV/Vis and fluorescence spectroscopy. Here, a predominantly SCNP formation *via* the NICAL reaction was observed. In order to favor the NITEC reaction, the folding was carried out in the presence of a bismaleimide linker. Initial SEC measurements as well as UV/Vis and fluorescence spectroscopy indicated an intramolecularly linked SCNP *via* NITEC. However, the visible light tetrazole was not stable over time in the PAA polymer. The SEC trace as well as the ^1H NMR spectrum showed different results compared to the recorded analytical data from the initial polymer precursor.

Thus, the polymer backbone was replaced with poly(styrene). First, a polymerization of styrene and chloromethylstyrene was carried out, controlled *via* nitroxide-mediated polymerization (NMP). The chloromethylstyrene moiety was exploited to introduce the functional groups into the copolymer. Specifically, a statistical functionalization of the chlorine units of the copolymer, employing carboxylic acid derivatives from the PAT and a protected maleimide, PAT and fumarate or PAT only was successfully carried out, leading to three functional polymers. Subsequently, a highly diluted solution of these functionalized polymers was employed for the preparation of the visible light induced SCNPs. In addition, the polymer containing only PAT units was irradiated in the presence of a PEG diacid linker to trigger a NICAL-driven folding. In summary, four SCNPs were prepared and analyzed employing SEC, UV/Vis and fluorescence as well as ^1H NMR and DOSY NMR spectroscopy.

The successful photoreactions leading to the formation of the SCNPs were confirmed employing ^1H NMR spectroscopy, where all resonances were identified, underpinning the SCNPs formation.

To confirm the intramolecular reaction of the SCNPs, SEC and DOSY as analytical tools were employed. During SEC, an apparent molecular weight change towards lower molecular weights was observed for all SCNPs, evidencing a successful compaction of the corresponding polymer precursors. Interestingly, the collapse utilizing the PEG diacid linker showed the most efficient collapse upon irradiation with visible light. A reason for the efficient collapse (approx. 50%) could be the flexible PEG linker, able to connect the incorporated tetrazoles in the polymer, having a greater distance in one polymer chain. Furthermore, the collapse of the polymers was independently confirmed *via* DOSY NMR experiments. Here, a size reduction for all polymers was observed, evidencing the intramolecular linkage upon irradiation with light. In addition, the fluorescent features found in the small molecule study employing the visible light active tetrazole were congruent with the fluorescent properties found for the prepared SCNPs with emission maxima at 475 nm or 575 nm, respectively

In summary, two tetrazole based systems were employed to synthesize fluorescent SCNPs utilizing different wavelengths. Specifically, the visible light approach is offering new pathways for the synthesis of fluorescent SCNPs employing mild and biocompatible conditions. Importantly, all synthesized SCNPs showed fluorescent properties, especially those prepared *via* the NITEC reaction, opening new possibilities in biological applications, e.g. as imaging agents.

A future perspective using the explored tetrazole chemistry could be the investigation of a λ -orthogonal folding of polymer chains, employing two different wavelengths. In particular, a suitable reaction system represents the *ortho*-quinodimethanes (UV region) and the visible light induced tetrazole chemistry. As described in Section 2.2 *ortho*-quinodimethanes are able to undergo photoinduced Diels-Alder reaction when a wavelength of approx. 350 nm is employed. The advantage of employing *ortho*-quinodimethanes and PAT is the reactivity of both reactive groups towards electron deficient bonds e.g. maleimides.

The reactivity towards maleimides can be exploited either in a Diels-Alder reaction with the *ortho*-quinodimethanes or in a 1,3-dipole based system using the PAT tetrazole.

Therefore, an introduction of both photoreactive compounds together with the electron deficient maleimide in one polymer chain should lead to a precursor polymer, which is able to collapse in a step-wise manner (Figure 4.1.1).

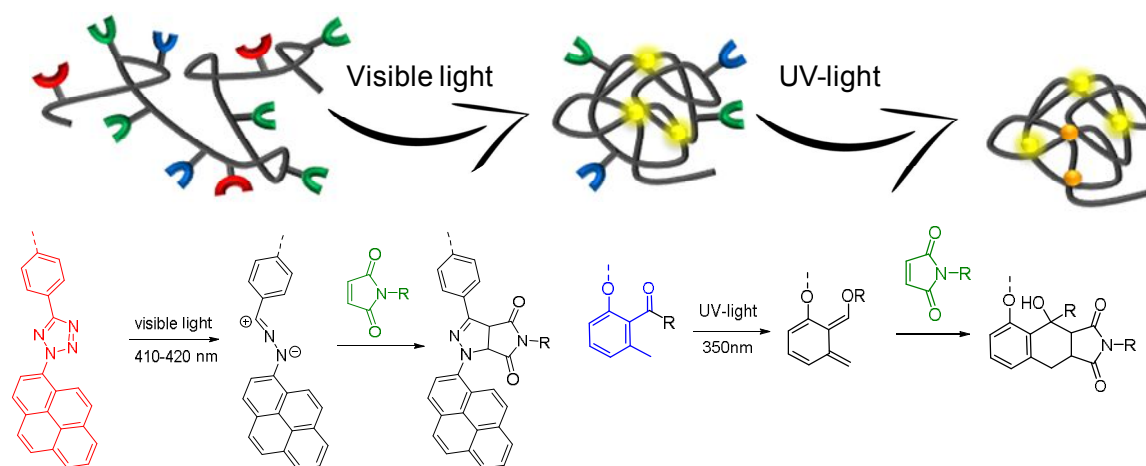


Figure 4.1.1: Proposed λ -orthogonal folding approach for the step-wise induced folding employing visible and UV-light. First, the tetrazole reacts with the incorporated maleimide upon irradiation with visible light followed by the photoreaction of the *ortho*-quinodimethanes with the residual maleimides using UV-light.

5

Experimental Part

5.1 Materials and Methods

Acetic anhydride (>97%, Acros Organics), acrylic acid (99%, Fluka), acryloyl chloride (97%, Sigma Aldrich), aminopyrene (97%, Sigma Aldrich), p-anisidine (99%, Sigma Aldrich), azobis(isobutyronitril) (98%, TCI) (purification via recrystallization before use), benzyl alcohol (99%, Sigma Aldrich), bromoethanol (95%, Sigma Aldrich), bromoacetic acid (98.5%, J&K Scientific) 11-bromo-1-undecanol (99%, Sigma Aldrich), cesium carbonate (99.9% Roth), diethyl fumarate (98% Alfa Aesar), diisopropylethylamine (99%, Alfa Aesar), N,N-dimethylaminopyridine (99%, Sigma Aldrich), 2-(((dodecylthio)carbonothioyl)thio)propanoate (DoPAT) was obtained from Lanxess GmbH, EDC·HCL (Roth, >99%), ethanolamine (99%, Acros organics), formyl benzoic acid (97%, Sigma Aldrich), furan (> 99%, Sigma Aldrich), hydrochloric acid 37% (Roth), imidazole (99%, Carbolution Chemicals) magnesium sulfate (> 99% extra dry, Roth), maleic anhydride (99% Acros), monoethyl fumarate (95%, Sigma Aldrich), poly (ethylene glycol) bis(carboxymethyl) ether ($M_n=250$, Sigma Aldrich), pyridine (99%, Acros Organics), sodium nitrite (97%, Acros organics), sodium hydrogen carbonate (> 99.5%, Roth), sodium tetrafluoroborate (97%, Sigma), tert-butyl diphenylchlorosilane (97%, Fluorochem), tetrabutylammonium fluoride (TBAF) solution, 1 M in THF (Sigma Aldrich), trifluoroacetic acid (99%, Abcr), p-toluenesulfonyl hydrazide (97%, Acros),

succinic anhydride (> 95%, TCI) tetraethylene glycol monomethyl ether (> 98%, TCI). All solvents such as dry DMF, dry DCM, dry 1,4 dioxane, ethylacetate, cyclohexane, diethyl ether, acetonitrile (MeCN), piperidine were used in p.a degree. Peptide grade DMF was obtained from Iris Biotech and dried over Na₂SO₄ prior use.

Nuclear Magnetic Resonance (NMR): Nuclear magnetic resonance (NMR) measurements were performed on a Bruker Avance III Microbay 400 at an operating frequency of 400 MHz (¹H) and 100 MHz (¹³C), respectively. All spectra were recorded at ambient temperature. The residual proton signals of the deuterated solvents were used as an internal standard. The solutions were prepared with a concentration of 10 mg in 0.50 mL in the respective deuterated solvent. The NMR solvents used were purchased from Eurisotop (deuteriochloroform, d6- dimethylsulfoxide,).

THF Size Exclusion Chromatography (THF SEC): Polymer Laboratories (Varian) PL-SEC 50 Plus Integrated System, comprising an autosampler, a PLgel 5 mm bead-size guard column (50 × 7.5 mm), one PLgel 5 mm Mixed E column (300×7.5 mm), two PLgel 5 mm Mixed C columns (300 × 7.5 mm), and a differential refractive index detector using THF (with 0.01% BHT as additive) as eluent at 35 °C with a flow rate of 1 mL min⁻¹. The present SEC system was calibrated using narrow linear polystyrene standards ranging from 476 to 2.5·10⁶ g mol⁻¹ and linear poly(methyl methacrylate) standards ranging from 700 to 2·10⁶ g mol⁻¹ (Polymer Standard Service, PSS). The resulting molar mass distributions were determined using Mark-Houwink parameters for polystyrene ($K= 14.1 \cdot 10^{-5}$ dL g⁻¹, $\alpha = 0.7$) or poly(methyl methacrylate) ($K= 12.8 \cdot 10^{-5}$ dL g⁻¹, $\alpha = 0.69$)²³⁴, respectively. Experimental molar mass (M_n) and dispersity (\mathcal{D}) values were analyzed using the Varian software.

DMAc Size Exclusion Chromatography (DMAc SEC): Size exclusion chromatography (SEC) measurements were performed on a Polymer Laboratories PLGPC 50 Plus Integrated System, comprising an autosampler, a PLgel 5 μm bead-size guard column (50 x 7.5 mm) followed by three PLgel 5 μm MixedC columns (300x7.5 mm) and a differential refractive index detector using *N,N*-dimethylacetamide (DMAc) containing 0.03 wt% LiBr as eluent at 50 °C with a flow rate of 1.0 mL min⁻¹. The SEC system was calibrated against linear poly(methylmethacrylate) standards with molecular weights ranging from 700 to 2·10⁶ g mol⁻¹. All SEC calculations were carried out relative to a poly(methylmethacrylate) calibration. (Mark-Houwink-Parameters $K = 14.1 \cdot 10^{-5}$ dL g⁻¹; $\alpha = 0.7$).

UV/Vis Spectroscopy (1): UV/Vis measurements of single spectra were carried out on OceanOptics USB4000 spectrometer with a USB-ISS-UV-Vis detecting unit. The measurement interval had a range from 200 to 800 nm with a resolution of 1 nm and slit width of 2 nm in a precision cell made of quartz SUPRASIL from HELLMMA with a light path of 2 mm.

UV/Vis Spectroscopy (2): UV/Vis spectra were recorded on a Varian Cary 300 spectrometer. Spectra were recorded in DCM at 20 °C with a concentration of 0.2 mg mL⁻¹. Spectra were collected between 200 and 800 nm. Samples were baseline corrected with respect to the pure solvent. A cuvette with an optical path length of 2 mm was used for the UV/Vis measurements.

Fluorescence Spectroscopy: Fluorescence spectra were measured on a Varian Cary Fluorescence Spectrometer with a step width of 1 nm and an integration time of 0.2 s. All spectra for the water-soluble SCNPs were recorded in DMSO-d₆ or H₂O ($c = 0.0016$ mol L⁻¹ small molecules, $c = 0.5$ mg L⁻¹ polymer precursors) at 20 °C and are corrected for Raman emission from water. The spectra of containing the visible light tetrazole were recorded in DCM ($c = 0.2$ mg mL⁻¹) at 20 °C. The fluorescence emission spectra were recorded in quartz cuvettes loaded with a sample volume of 700 μL and an optical path length of 10 mm.

Diffusion Ordered NMR (DOSY-NMR): DOSY experiments based on ^1H NMR were performed in CDCl_3 or $d_6\text{-DMSO}$ at 298.00 K on a Bruker Avance III Microbay 400 at an operating frequency of 400 MHz (^1H) using a stimulated echo sequence incorporating bipolar gradient pulses and a longitudinal eddy current delay (BPP-LED) with the standard Bruker pulse program, ledbpgp2s. The gradient strength was linearly incremented in 96 steps from 5 % up to 95 % of the maximum gradient strength. Diffusion times and gradient pulse durations were optimized for each experiment in order to achieve a 95% decrease in the signal intensities at the largest gradient amplitude. After Fourier transformation and phase correction, the diffusion dimension of the 2D DOSY spectra was processed by means of the Bruker Topspin software package (version 3.2) and analyzed with the Bruker Dynamic Center. Spectra for the polymers and their corresponding single-chain nanoparticles were measured and mean values were taken from the found diffusion coefficients of characteristic NMR-peaks.

$$r = \frac{k_B T}{6\pi \eta D}$$

k_B = Boltzmann constant

T = Temperature

η = Viscosity of solvent

r = Radius

Dynamic Light Scattering (DLS): The apparent hydrodynamic diameters ($D_{h,app}$) were determined at 25 °C by means of a dynamic light scattering (DLS) analysis using a Zetasizer Nano ZS light scattering apparatus (Malvern Instruments, UK) equipped with He-Ne laser (at a wavelength of 633 nm, 4 mW). The Nano ZS instrument incorporates a non-invasive backscattering (NIBS) optic with a detection angle of 173°. The polymer solutions were prepared in MeCN and were subsequently filtered into PS cuvettes. The prepared samples were stabilized prior to DLS analysis at ambient temperature. All values of the apparent hydrodynamic diameter for the polymer and the single-chain nanoparticles were averaged over triplicate measurements (10 runs/measurement), and were automatically provided by the instrument using a cumulative analysis.

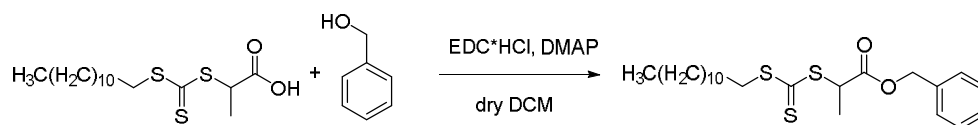
Matrix Assisted Laser Desorption Ionization-Time of Flight (MALDI-TOF): MALDI-TOF measurements were performed on an Axima Confidence (Shimadzu Biotech). The machine was operated in positive reflection mode. As a matrix, MALDI-Universal Matrix was dissolved in 50:50 acetonitrile/water with 0.1% TFA and put on a ground steel target. The spots were crystallized at room temperature. The peptide calibration standard II from Bruker Daltonik was used. The used software was MALDI-MS Application by Shimadzu Biotech version 2.9.3.20110624.

Analytical High Pressure (Performance) Liquid Chromatography (HPLC): Determination of purity was done using an Agilent 1100 series HPLC system with a G1322A degasser, G1311A pump, G1313A autosampler, G1316A column oven and G1315B diode array detector. An analytical C₁₈-column (VDSpher C18-M-SE, C₁₈, 5 µm, 4.0 mm × 250 mm from VDS Optilab) was used as stationary phase with a flow rate of 1 mL/min. Analytical runs were done with a linear gradient from 5% acetonitrile with 0.1% TFA in water to 95% acetonitrile with 0.1% TFA in water in 20 min at 25 °C. Purity was determined by integration of all signals at 218 nm.

Electro-Spray Ionization Mass Spectrometry (ESI-MS): High-resolution mass spectra (HRMS) were obtained using a Q Exactive (Orbitrap) mass spectrometer (Thermo Fisher Scientific, San Jose, CA, USA) equipped with a HESI II probe. The instrument calibration was carried out in the m/z range 74 -1822 using calibration solutions from Thermo Scientific. A constant spray voltage of 4.7 kV and a dimensionless sheath gas of 5 were applied. The capillary temperature and the S-lens RF level were set to 320 °C and 62.0, respectively. The samples were dissolved in a solvent mixture of THF/MeOH (v:v, 3/2) with sodium triflate and injected with a flow of 5 to 15 $\mu\text{L}\cdot\text{min}^{-1}$, respectively.

5.2 Small Molecule Synthesis

5.2.1 RAFT Agent Synthesis

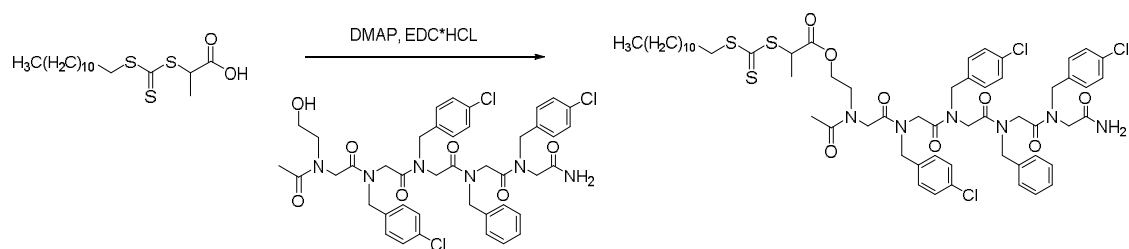


Scheme 5.2.1: Steglich esterification of the DoPAT derivative using benzyl alcohol.

In a flame dried Schlenk flask 3.0 g of DoPAT (8.55 mmol, 1.00 eq.), 0.20 g of *N,N*-dimethylaminopyridine (DMAP) (1.71 mmol, 0.2 eq.) and 1.85 g of benzylic alcohol (17.11 mmol, 2.00 eq.) were dissolved in 80 mL of dry DCM. The reaction mixture was cooled with crushed ice to 0°C and 1.64 g of EDC·HCL (8.55 mmol, 1.00 eq.) were added. The mixture was stirred over night at ambient temperature. The solution was washed with 5% hydrochloric acid solution as well as brine and dried over magnesium sulfate. For purification, silica gel column chromatography employing a solvent mixture CH/EE (10:1) was performed yielding a yellow solid (yield 3.60 g, 82%).

¹H NMR (400 MHz, CDCl₃) δ [ppm]: 7.35 – 7.20 (m, 5H), 5.18 – 5.03 (s, 2H), 4.80 (q, J = 7.4 Hz, 1H), 3.37 – 3.10 (m, 2H), 1.66 – 1.56 (m, 2H), 1.54 (d, J = 7.4 Hz, 3H), 1.37 – 1.13 (m, 19H), 0.81 (t, J = 6.8 Hz, 3H). ¹³C NMR (101 MHz, CDCl₃) δ [ppm]: 221.1 (CS₃), 167.9 (COOH), 129.03 (Benzyl), 128.81 (Benzyl), 128.59 (Benzyl), 47.2 (S-CH₂), 37.7 (CH₂), 32.1 (CH₂), 29.6 (CH₂), 29.1 (CH₂), 28.0 (CH₂), 22.8 (CH₂), 16.5 (CH₂), 14.3 (CH₃).

Synthesis of the DOPAT-peptoid (22)



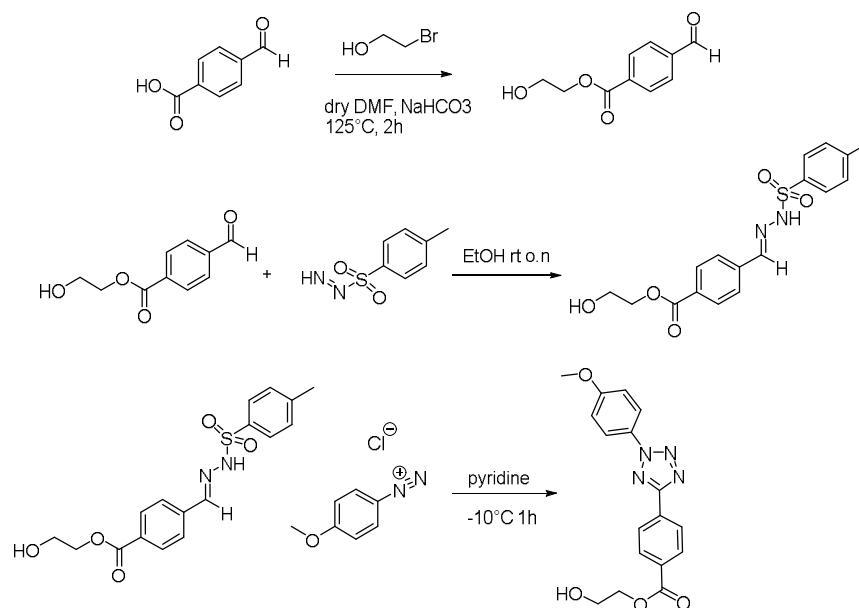
Scheme 5.2.2 Steglich esterification with DoPAT (1) and the peptoid (23)

In a flame dried Schlenk flask 0.028 g of **1** (79.8 μmol , 1.00 eq.), 1.95 mg of *N,N*-dimethylaminopyridine (DMAP) (15.9 μmol , 0.2 eq.) and 68.1 mg of the peptoid (79.8 μmol , 1.00 eq.) were dissolved in 7 mL of DMF. The reaction mixture was cooled with crushed ice to 0°C and 30.6 mg of EDC·HCL (0.159 mmol, 2.00 eq.) were added. The mixture was stirred over night at ambient temperature. The solution was washed with 5% hydrochloric acid solution as well as brine and dried over magnesium sulfate (50mL). For purification, silica gel column chromatography employing a solvent mixture DCM/MeOH (4:1) was performed yielding a yellow solid (28 mg, 32%).

^1H NMR (400 MHz, CDCl_3) δ [ppm]: 7.80 – 6.83 (m, 17H), 4.94 – 3.15 (m, 22H), 3.00 (s, 2H), 2.29 – 1.46 (m, 8H), 1.46 – 1.10 (m, 20H), 1.00 – 0.62 (m, 3H).
 MS (ESI-MS): m/z : MS calc. $[\text{M}+\text{Na}]^+$ 1205.36098, MS found 1205.36234, MS calc. $[\text{2M}+\text{Na}]^+$ 2390.73314, MS found 2390.72949

5.2.2 Synthesis of the Photoreactive Compounds

Synthesis of the UV-tetrazole (6)

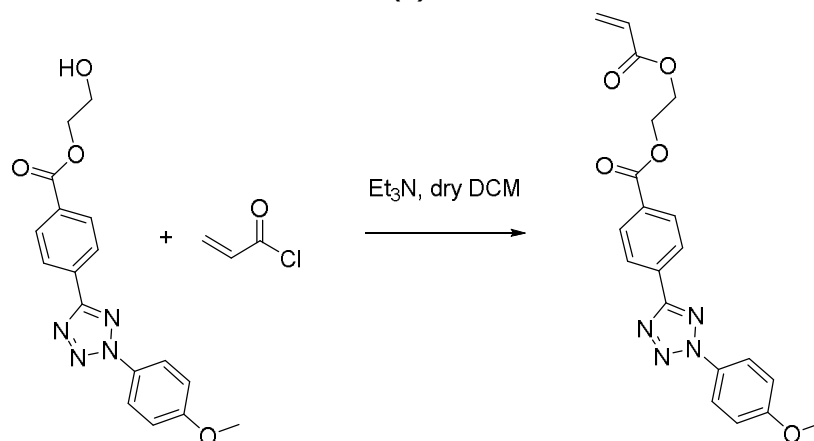


Scheme 5.2.3: Tetrazole synthesis including the nucleophilic substitution of bromoethanol with subsequent reaction with the *para*-toluenesulfonylhydrazide. The last step of the tetrazole synthesis entails the reaction with the diazonium salt with the previously synthesized activated *para*-toluenesulfonylhydrazide to yield tetrazole (6).

5.0 g of formylbenzoic acid (33.3 mmol, 1.00 eq.), 5.59 g of sodium hydrogen carbonate (66.6 mmol, 2.00 eq.) and 5.41 g of bromoethanol (43.3 mmol, 1.30 eq.) were dissolved in 200 mL of DMF and heated to 125 °C for 2 h. Subsequently, 300 mL ethyl acetate were added and the crude reaction mixture was washed with brine 2 to 3 times (50 mL). The organic layer was dried over magnesium sulfate and the solvent was evaporated under reduced pressure. The obtained yellow oil was used without further purification. The compound was dissolved in 100 mL of ethanol and 5.40 g of *p*-toluenesulfonylhydrazide (29.0 mmol, 1.1 eq.) was added to the solution and stirred over night. Subsequently, ethanol was evaporated under reduced pressure and the obtained white powder was dissolved in 100 mL of pyridine. Initially, 2.0 g of *p*-anisidine (16.2 mmol, 1.00 eq.) was dissolved in a solvent mixture of HCl/water/ethanol (1:3:3). Subsequently, 1.12 g sodium nitrite (16.2 mmol, 1.00 eq.) was dissolved in a second round bottom flask in the same solvent mixture of methanol and water. The solutions were slowly combined and stirred for 10 minutes at 0 °C. In the next step, the pyridine solution was cooled to -10 °C with ice and sodium chloride and the prepared diazonium salt was slowly added.

The combined reaction mixture was stirred for 1h and then precipitated into 1 L of a 1 M hydrochloric acid solution. The raw product was recrystallized 3 times from cyclohexane / ethanol to yield a solid. 2.2 g (33%).

^1H NMR (400 MHz, $\text{d}_6\text{-DMSO}$) δ [ppm]: 8.35 – 8.26 (d, 2H), 8.24 – 8.16 (d, 2H), 8.12 – 8.02 (m, 2H), 7.29 – 7.16 (m, 2H), 4.98 (t, $J = 5.4$ Hz, 1H), 4.40 – 4.26 (m, 2H), 3.87 (s, 3H), 3.74 (dd, $J = 9.6, 5.0$ Hz, 2H). ^{13}C NMR (101 MHz, $\text{d}_6\text{-DMSO}$) δ [ppm]: 166.37 (COOR), 164.07 (C=N-N), 160.72 (C-O- CH_3), 131.64 (Benzyl-C), 131.43 (Benzyl), 130.33 (Benzyl), 126.94 (Meo-p-Benzyl), 121.50 (Meo-m-Benzyl), 114.77 (MeO-o-Benzyl), 66.93 (OCR), 61.42 ($\text{CH}_2\text{-OH}$), 55.71 (CH_3).

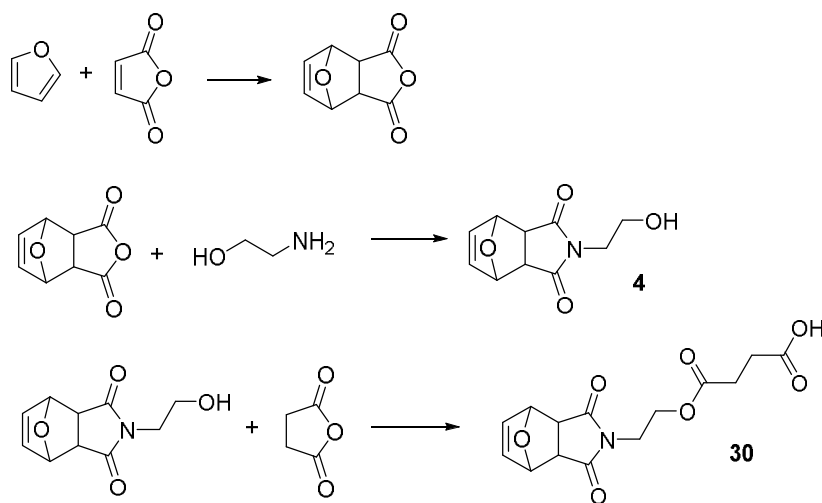
Synthesis of the tetrazole monomer (7)

Scheme 5.2.4: Synthesis of the acrylate based monomer employing tetrazole (6) and acryloyl chloride.

In a flame dried Schlenk flask 2.2 g of the tetrazole (6) (6.46 mmol, 1.00 eq.), 5.9 g of Et₃N) (71.1 mmol, 11.0 eq.) were dissolved in 20mL dry THF and cooled to 0°C with crushed ice. Subsequently, 5.96 g of acryloyl chloride (65.9 mmol, 10.2 eq) were slowly added. The reaction mixture was stirred over night at ambient temperature. The salt was removed by filtration and the solvent was evaporated under reduced pressure using 30°C water temperature. For purification, silica gel column chromatography employing a solvent mixture CH/EE (3:1) was performed yielding a pile solid (yield 2.54 g, 28%).

¹H NMR (400 MHz, CDCl₃) δ [ppm]: 8.31 (d, *J* = 8.7 Hz, 1H), 8.18 (d, *J* = 8.7 Hz, 1H), 8.10 (d, *J* = 9.2 Hz, 1H), 7.06 (d, *J* = 9.2 Hz, 1H), 6.46 (dd, *J* = 17.3, 1.4 Hz, 1H), 6.17 (dd, *J* = 17.3, 10.4 Hz, 1H), 5.87 (dd, *J* = 10.4, 1.4 Hz, 1H), 4.71 – 4.47 (m, 2H), 3.89 (s, 2H).

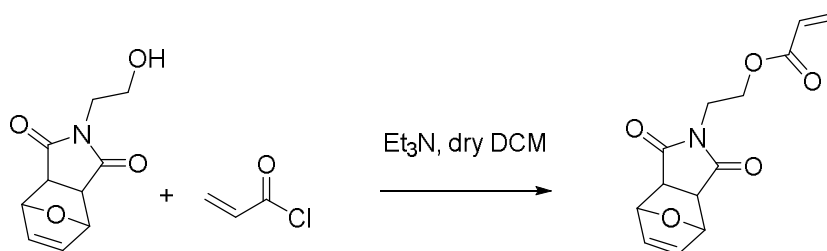
Synthesis of 2-(2-hydroxyethyl)-3a,4,7,7a-tetrahydro-1H-4,7-epoxyisoindole-1,3(2H)-dione (4) and 4-(2-(1,3-dioxo-1,3,3a,4,7,7a-hexahydro-2H-4,7-epoxyisoindol-2-yl)ethoxy)-4-oxobutanoic acid (30)



Scheme 5.2.5: Synthesis of the furan protected maleimides (**4**, **30**).

The synthesis was carried out according to the synthesis procedure found in literature.⁶

2-(1,3-dioxo-1,3,3a,4,7,7a-hexahydro-2H-4,7-epoxyisoindol-2-yl)ethyl acrylate (5)

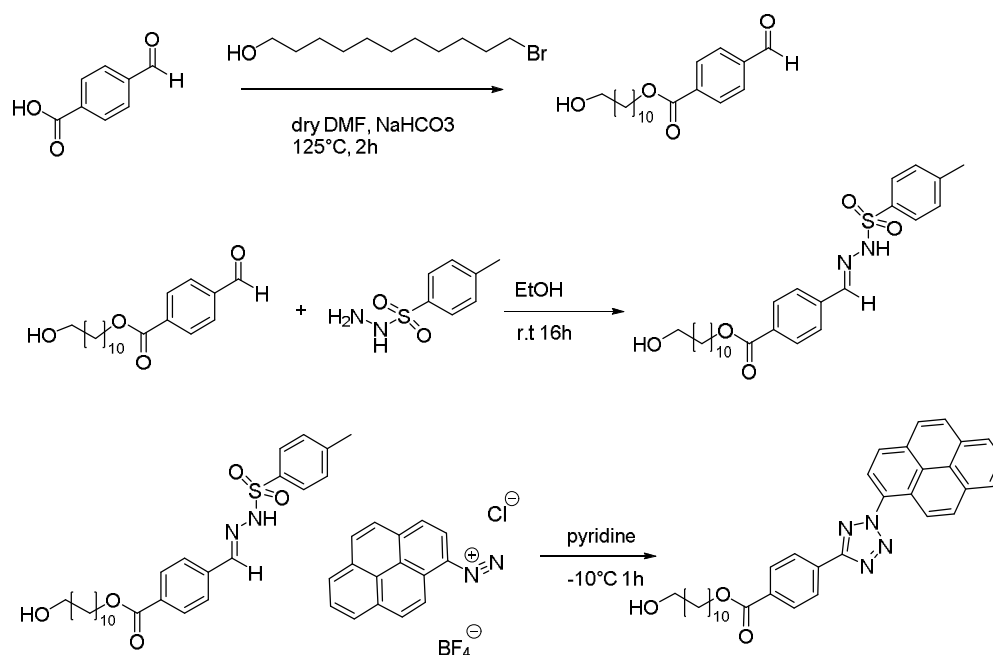


Scheme 5.2.6: Synthesis of the acrylate based monomer employing the protected maleimide (**4**) and acryloyl chloride.

In a flame dried Schlenk flask 4.55 g of the p-Mal-OH (**4**) (21.7 mmol, 1.00 eq.), 4.56 g of Et₃N) (54.4 mmol, 2.5 eq.) were dissolved in 40 mL dry THF and cooled to 0°C with crushed ice. Subsequently, 4.72 g of acryloyl chloride (52.2 mmol, 2.40 eq.) were slowly added. The reaction mixture was stirred over night at ambient temperature. The salt was removed by filtration and the solvent was evaporated under reduced pressure using 30°C water temperature. For purification, silica gel column chromatography employing a solvent mixture CH/EE (3:1) was performed yielding a white solid (yield 2.0 g, 35%).

¹H NMR (400 MHz, CDCl₃) δ [ppm]: 6.50 (t, 2H), 6.36 (dd, *J* = 17.3, 1.4 Hz, 1H), 6.04 (dd, *J* = 17.3, 10.5 Hz, 1H), 5.82 (dd, *J* = 10.5, 1.4 Hz, 1H), 5.24 (t, 2H), 4.39 – 4.19 (m, 1H), 3.79 (s, 1H). ¹³C NMR (101 MHz, CDCl₃) δ 176.06 (O=C-N), 165.84 (O=C-O), 136.66 (R-C=C-R), 131.41 (H₂C=), 128.08 (C=CH₂), 81.03 (C-O-C), 60.83 (C-O-C=O), 47.57 (C-C), 37.91 (CH₂-N).

Synthesis of the pyrene-aryl tetrazole (12)¹²⁴



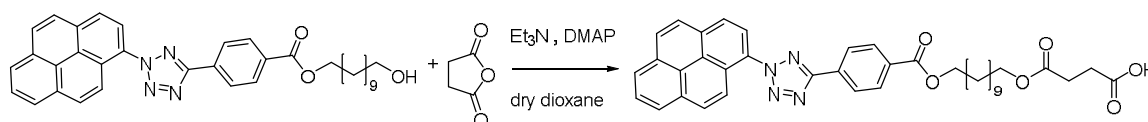
Scheme 5.2.7: Tetrazole synthesis including the nucleophilic substitution of 11-bromoundecanol with subsequent reaction with the *para*-toluenesulfonylhydrazide. The last step of the tetrazole synthesis entails the reaction with the diazonium salt with the previously synthesized activated *para*-toluenesulfonylhydrazide to yield the pyrene-aryl-tetrazole (12).

6.0 g of formylbenzoic acid (39.9 mmol, 1.00 eq.), 6.71 g of sodium hydrogen carbonate (79.9 mmol, 2.00 eq.) and 13.0 g of 11-bromoundecan-1-ol (51.9 mmol, 1.30 eq.) were dissolved in 50 mL of DMF and heated to 125 °C for 2 h. Subsequently, 300 mL of ethyl acetate were added and the crude reaction mixture was washed with brine 3 times (50 mL). The organic layer was dried over magnesium sulfate and the solvent was evaporated under reduced pressure and dried under high vacuum. The obtained yellow oil was used without further purification. The compound was dissolved in 100 mL of ethanol and 6.96 g of *para*-toluenesulfonylhydrazide (37.4 mmol, 1.1 eq.) was added to the solution and stirred overnight. Subsequently, ethanol was evaporated under reduced pressure and the obtained yellow solid was dried under high vacuum. 0.7 g of the previously synthesized compound was dissolved in 8 mL of pyridine. The first solution contained 0.258 g of aminopyrene (1.18 mmol, 1.00 eq.) in 30 mL of THF and was cooled to -21 °C under argon atmosphere. In a second round bottom flask 1.04 g of sodium tetrafluoroborate (9.50 mmol, 8.00 eq.) was dissolved in 15 mL of 50 wt % fluoroboric acid and water (7:3) under argon atmosphere.

This solution was slowly added to the aminopyrene solution and stirred for 20 min at -21°C . Subsequently, 94.0 mg of sodium nitrite (1.36 mmol, 1.15 eq.) was dissolved in a third round bottom flask in 2 mL of water under argon atmosphere. The sodium nitrite solution was slowly combined and stirred for 10 min at -21°C . The orange diazonium salt formed was collected and added to the pyridine solution. The combined reaction mixture was stirred for 1h and subsequently precipitated into 80 mL of a 1 M HCl solution. The raw product was recrystallized 3 times from ethanol to yield a brown solid. 220 mg (yield: 33 %).

^1H NMR (400 MHz, CDCl_3) δ [ppm]: 8.81 – 7.78 (m, 13H), 4.38 (t, 2H), 3.64 (t, 2H), 1.87 – 1.73 (m, 2H), 1.69 – 1.22 (m, 18H). MS calc. $[\text{M}+\text{Na}]^+$ 583.26853, MS found 583.26929, MS calc $[\text{2M}+\text{Na}]^+$ 1143.54725, MS found 1143.55005

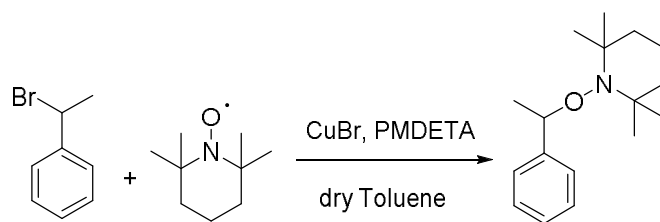
Synthesis of 4-oxo-4-((11-((4-(2-(pyren-1-yl)-2H-tetrazol-5-yl)benzoyl)oxy)undecyl)oxy)butanoic acid (29)²³⁵



Scheme 5.2.8: Ring opening esterification of the PAT derivative yielding the PAT acid derivative 29.

632.2 mg of PAT-OH (1.13 mmol, 1.0 eq.) were dissolved in 10 mL of dry 1,4 dioxane under argon atmosphere. Subsequently, 677 mg of succinic anhydride (6.78 mmol, 6.0 eq.), 303 mg of DMAP (2.48 mmol, 2.20 eq.) and 1.58 mL of triethylamine (11.3 mmol, 10 eq.) were added to the solution. The reaction mixture was stirred for 4 d at 50°C . After evaporation of the solvent the crude product was recrystallized and washed with brine. The organic solvent was removed and recrystallized from ethanol 2x 80 mL yielding a brown solid 451 mg (Yield: 61%).

^1H NMR (400 MHz, CDCl_3) δ [ppm]: 8.50 – 8.16 (m, 13H), 4.38 (t, 2H), 4.09 (t, 2H), 2.65 (m, $J = 12.7, 6.0$ Hz, 4H), 1.82 (s, 2H), 1.65 – 1.43 (m, 4H), 1.32 (dd, $J = 30.1, 11.8$ Hz, 12H).



Scheme 5.2.9: Synthesis of the NMP-initiator according to the synthesis procedure found in the literature.⁶

5.3 Small Molecule Studies

5.3.1 UV-Tetrazole

The irradiation tests were performed in a 50 mL round bottom flask equipped with a stirrer. 10.0 mg of **6** (0.029 mmol, 1.0 eq.) was dissolved in 30 mL MeCN and the corresponding molecules were added, (1) 7.9 mg furan-protected maleimide (p-Mal) (0.038 mmol, 1.3 eq.), (2) (2.29 mg AcOH (0.038 mmol, 1.3 eq.) and (3) 7.9 mg p-Mal (0.038 mmol, 1.3 eq.) + 2.29 mg AcOH (0.038 mmol, 1.3 eq.). The solution was irradiated with an Arimed B6 lamp ($\lambda_{\text{max}} = 320 \text{ nm}$).

Table 5.3.1: Irradiation conditions for the small molecule study employing the UV tetrazole (**6**) with p-Mal (**4**) and acetic acid (**9**).

Reaction	Tet	p-Mal	Acetic acid	Irradiation time
1)	1.0 eq.	1.3 eq.-	-	5 h
2)	1.0 eq.	-	1.3 eq.	17 h
3)	1.0 eq.	1.3 eq.	1.3 eq.	5 h

5.3.2 Visible Light active Tetrazole

The irradiation tests were performed in a 50 mL round bottom flask equipped with a stirrer. 10.0 mg of **12** (0.017 mmol, 1.0 eq.) were dissolved in 30 mL of DCM and the corresponding molecules were added for the different tests: 1) 4.8 mg of furan-protected maleimide (**4**) (0.023 mmol, 1.3 eq.), 2) 4.0 mg of diethylfumarate (**14**) (0.023 mmol, 1.3 eq.) 4) 1.3 μ L of acetic acid (**9**) (0.023 mmol, 1.3 eq.) or 5) 3.2 mg of bismaleimidotoluene (**18**) (0.011 mmol, 0.65 eq.). The solution was irradiated with 3 Avonec LED lamps (λ = 410-420 nm) for 90 minutes each (refer to the appendix Figure 6.1.51-Figure 6.1.53) for the geometry of the reaction). An overview of the conducted reactions are collated in Table 5.3.2.

Table 5.3.2: Reaction conditions for the small molecule studies employing the visible light active tetrazole (**12**). The reaction were carried out with *p*-Mal, diethylfumarate, acetic acid and bismaleimidotoluene.

Reaction	PAT	<i>p</i> -Mal	Diethyl fumarate	Acetic acid	Bismaleimidotoluene
1)	1.0 eq.	1.3 eq.-	-	-	-
2)	1.0 eq.	-	1.3 eq.	-	-
3)	1.0 eq.	-	-	-	-
4)	1.0 eq.	-	-	1.3 eq.	-
5)	1.0 eq.	-	-	-	0.65 eq.

5.3.3 Competitive Irradiation Studies (PAT)

The irradiation tests were performed in a 50 mL round bottom flask equipped with a stir bar. 10.0 mg of PAT-OH (0.017 mmol, 1.0 eq.) were dissolved in 30 mL of DCM and the corresponding molecules were added for the different tests: 1) 4.8 mg of furan-protected maleimide (**4**) (0.023 mmol, 1.3 eq.) and 1.3 μ L of acetic acid (**9**) (0.023 mmol, 1.3 eq.) 2) 3.2 mg of bismaleimidotoluene (**18**) (0.011 mmol, 0.65 eq.) and 1.3 μ L of acetic acid (0.023 mmol, 1.3 eq.). The conditions of the reactions are collated in Table 5.3.3.

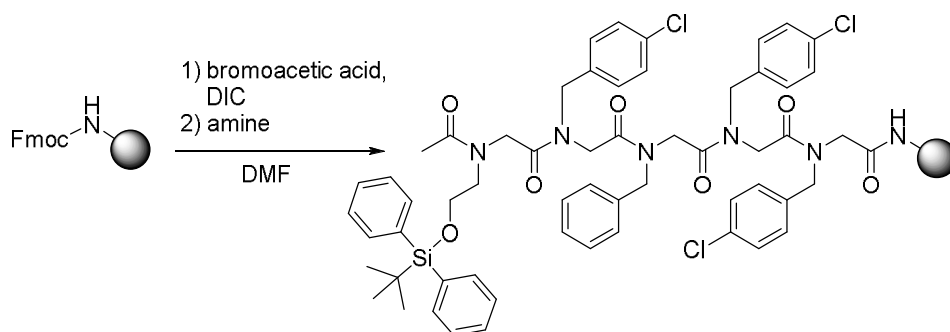
Table 5.3.3: Competitive small molecule study employing the PAT tetrazole, bismaleimidotoluene, acetic acid and *p*-Mal.

Reaction	PAT	<i>p</i> -Mal	Acetic acid	Bismaleimido-toluene
1)	1.0 eq.	1.3 eq.	1.3 eq.	-
2)	1.0 eq.	-	1.3 eq.	0.65 eq.

5.4 Peptoid Synthesis

The peptoid synthesis was carried out from Stefan Münch (Prof. Dr. Stefan Bräse KIT)

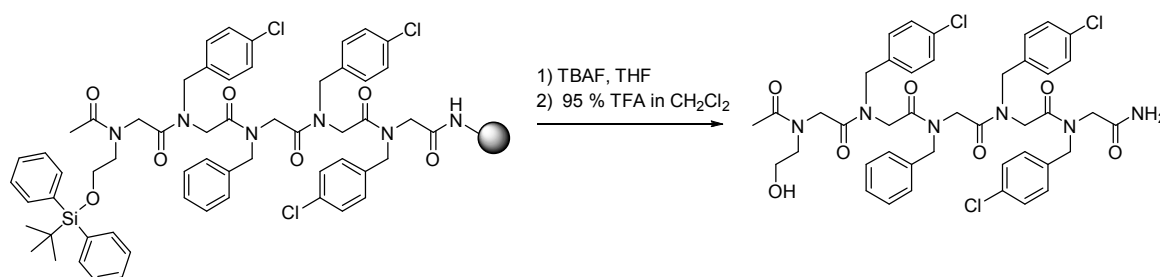
Synthesis of the peptoid conjugate Ac-(N2oh^{TBDPS})-(N1Pc)-(N1ph)-(N1Pc)₂-SP

**Scheme 5.4.1:** Submonomer synthesis of the peptoid employing different amines.

984 mg of Rink-Amide resin was swollen in a syringe equipped with frit in 10 mL of DMF for 1 h. The solvent was removed and the resin was incubated with 3 × 5.0 mL of 20% piperidine in DMF for 5 min each. The resin was washed four times with 10 mL of DMF and one time with 10 mL of peptide grade DMF. The pentameric peptoid was synthesized by alternating acylation and substitution steps. For the following acylation, 4.00 mL of 1.2 M bromo acetic acid (667 mg, 4.80 mmol, 8.00 eq.) solution in peptide grade DMF and 743 μ L of DIC (606 mg, 4.80 mmol, 8.00 eq.) were added and shaken for 30 min. Afterwards, the resin was washed two times with DMF and one time with peptide grade DMF. For the following substitution step, 4.8 mL of 1 M amine solution was given to the resin and this mixture was put on the shaker for 30 min. Afterwards, the resin was washed two times with DMF and one time with peptide grade DMF.

These acylation and substitution steps were repeated five times each in total to give the pentameric peptoid. Amines used for the substitution steps in order are two times 4-benzylamine (584 μL , 680 mg, 4.80 mmol, 8.00 eq.), benzylamine (524 μL , 514 mg, 4.80 mmol, 8.00 eq.), 4-benzylamine (584 μL , 680 mg, 4.80 mmol, 8.00 eq.) and TBDPS-protected ethanolamine (1.44 g, 4.80 mmol, 8.00 eq.). After the peptoid synthesis, the N-terminus was capped by adding 567 μL of acetic anhydride (613 mg, 6.00 mmol, 10.0 eq.) and 1.57 mL of DIPEA (1.16 g, 9.00 mmol, 15.0 eq.) in 5 mL of DMF overnight. The resin was washed three times with DMF and two times with DCM and used for the next reaction.

Deprotection of the peptoid conjugate Ac-(N2oh^{TBDPS})-(N1Pc)- (N1ph)-(N1Pc)₂-SP



Scheme 5.4.2: Deprotection and cleavage from the solid phase.

6.0 mL of 1 M TBAF (6.00 mmol, 10.0 eq.) in THF was added to the product and was shaken for 3 h at room temperature. The solvent was removed and the resin was washed 2 times with THF, DMF and DCM each. The product was cleaved from solid support with 95% TFA in DCM for 16 h. The filtrate was collected and the resin was extensively washed with DCM. The wash solutions and the filtrate were combined and the solvent was evaporated. The crude product was purified by preparative HPLC yielding 112 mg of a white solid (23% yield over 12 steps) as product. MS (MALDI-TOF): m/z = calc. 873.23075 $[\text{M}+\text{Na}]^+$, found 873.2835 Analytical HPLC (5–95% acetonitrile + 0.1% TFA in 20 min, detection at 218 nm): $t_{\text{Ret}} = 12.46$ min.

5.5 Polymerizations

5.5.1 RAFT Polymerizations

RAFT Polymerization of P1

The terpolymerization of DMAA was carried out in 1,4 dioxane with a monomer concentration of 1.5 mol L^{-1} . 1,4-dioxane were passed through a short column of basic alumina to remove peroxides or stabilizers, respectively. 0.8 mg of AIBN (0.5 μmol , 1.4 eq.), 11.0 mg of **3** (25 μmol , 7.0 eq.), 0.17 g of DMAA (1.75 mmol, 490 eq.), 0.131 g of p-MalA (0.5 mmol, 140 eq.) and 98.5 mg of TetA (0.25 mmol, 70 eq.) were dissolved in 1.5 mL 1,4-dioxane. The vial was sealed with a crimping tong and the solution was percolated with nitrogen for 30 minutes. The reaction was allowed to proceed for 8 h at 60 °C. After 8 h, the reaction was terminated by rapidly reducing the temperature by immersion in liquid nitrogen, opening the flask and letting the solution stir at ambient conditions for several minutes. The crude product was purified *via* precipitation in ice cold diethyl ether yielding a pile solid. The solid was dried for 2 days in a vacuum oven at 70°C.

RAFT Polymerization of P2

The terpolymerization of PEGA was carried out in dry DMF with a monomer concentration of 0.6 mol L^{-1} . 0.1 mg AIBN (0.62 μmol , 0.7 eq.). Subsequently, 2.7 mg of **3** (6.25 μmol , 7.0 eq.), 0.15 g of PEGA (1.75 mmol, 350 eq.), 65.8 mg of p-MalA (0.25 mmol, 280 eq.) and 49.2 mg of TetA (0.12 mmol, 140 eq.) were dissolved in 1 mL dry DMF. The vial was sealed with a crimping tong and the solution was percolated with nitrogen for 30 minutes. The reaction was allowed to proceed for 10 h at 60 °C. After 10 h, the reaction was terminated by rapidly reducing the temperature by immersion in liquid nitrogen, opening the flask and letting the solution stir at ambient conditions for several minutes. The crude product was purified *via* precipitation in ice cold diethyl ether yielding a pile gel. The gel was dried for 2 days in a vacuum oven at 70°C.

Table 5.5.1: Terpolymerizations performed utilizing TetA, MalA and the water-soluble PEGA or DMAA. The monomer, initiator and RAFT agent concentration were maintained (see above) only the reaction time and the solvent was varied.

Monomer	M_n [g mol ⁻¹]	\bar{D}	Time [h]	Solvent
PEGA/TetA/p-MalA (70/10/20)	1000	1.6	7 h	DMF
PEGA/TetA/p-MalA (70/10/20)	7000	1.3	10 h	DMF
PEGA/TetA/p-MalA (70/10/20)	-	-	o. 24h	DMF
DMAA/TetA/MalA (70/10/20)	3900	1.4	7h	DMF
DMAA/TetA/MalA (70/10/20)	-	-	6h	1,4 dioxane
DMAA/TetA/MalA (70/10/20)	gel	-	20h	1,4 dioxane

RAFT Polymerization of P3, P4 and P5

The polymerizations of acrylic acid were carried out in 1,4 dioxane with a monomer concentration of 1.80 mol L⁻¹. 1,4-dioxane and acrylic acid were passed through a short column of basic alumina to remove peroxides or stabilizers, respectively. 0.5 mg AIBN (3.5 μmol, 0.7 eq.), 0.015 mg (**3**) (35 μmol, 7.0 eq.) and 0.720 mg acrylic acid (10.0 mmol, 2000 eq.) were dissolved in 5 mL 1,4-dioxane. The vial was sealed with a crimping tong and the solution was percolated with nitrogen for 30 minutes. The reaction was allowed to proceed for 6 h at 60 °C. After 6 h, the reaction was terminated by rapidly reducing the temperature by immersion in liquid nitrogen, opening the flask and letting the solution stir at ambient conditions for several minutes. The crude product was purified *via* precipitation three times each in ice cold diethyl ether yielding a yellow powder. The powder was dried for 2 days in a vacuum oven at 70°C. The benzylic resonance (j, 7,36 ppm) and the backbone signal (e, 4.17 ppm) were used for calculating of the absolute molecular weight.

RAFT Polymerization of P10

The polymerization of acrylic acid were carried out in 1,4-dioxane with a monomer concentration of 1.80 mol L⁻¹. 1,4-Dioxane and acrylic acid were passed through a short column of basic alumina to remove peroxides or stabilizers, respectively. 0.15 mg AIBN (0.93 μmol, 0.7 eq.), 11.05 mg (DoPAT-Peptoid) (9.30 μmol, 7.0 eq.) and 0.280 mg acrylic acid (4.00 mmol, 3000 eq.) were dissolved in 2 mL 1,4-dioxane. The vial was sealed with a crimping tong and the solution was percolated with nitrogen for 30 minutes. The reaction was allowed to proceed for 6 h at 60 °C. After 6 h, the reaction was terminated by rapidly reducing the temperature by immersion in liquid nitrogen, opening the flask and letting the solution stir at ambient conditions for several minutes. The crude product was purified *via* precipitation three times each in ice cold diethyl ether yielding a yellow powder. The powder was dried for 2 days in a vacuum oven at 70°C. The aromatic resonance of the peptoid end group (i, 7.52-7.08 ppm) and the backbone signal (d, 4.17 ppm) were used for calculating of the molecular weight

5.5.2 Post Functionalization of PAA based Polymers

Post-modification of P3 yielding P6

In a flame dried Schlenk flask 150 mg of **P3** (0.01 mmol, 1.00 eq.), 50.9 mg of DMAP (0.41 mmol, 0.2 eq. respective to COOH groups), 106.4 mg of **6** (0.31 mmol, 0.15 eq. respective to COOH groups), 152.5 mg of **11** (0.72 mmol, 0.35 eq. respective to COOH groups) and 273.0 mg of **4** (1.66 mmol, 0.8 eq. respective to COOH groups) were dissolved in 8 mL of dry DMF. The reaction mixture was cooled with crushed ice to 0°C and 798.7 mg EDC·HCl (4.15 mmol, 2.00 eq. respective to the COOH groups) were added and stirred over night at ambient temperature. The solvent was removed under reduced pressure and the residual oil was dissolved in DCM. The solution was washed with 5% hydrochloric acid solution as well as brine and dried over magnesium sulfate. For purification the polymer was precipitated in ice-cold diethyl ether three times.

Post-modification of P4 yielding P7

The synthesis of **P7** was prepared by following the same procedure as before using 150 mg of **P4** (0.02 mmol, 1.00 eq.), 50.9 mg of DMAP (0.41 mmol, 0.2 eq. respective to COOH groups), 106.4 mg of **6** (0.31mmol, 0.15 eq. respective to COOH groups), 152.5 mg of **4** (0.72 mmol, 0.35 eq. respective to COOH groups) and 171.0 mg of **13** (1.04 mmol, 0.5 eq. respective to COOH groups).

Post-modification of P5 yielding P8

In a flame dried Schlenk flask, 107 mg of **P5** (0.02 mmol, 1.00 eq.), 36.3 mg of DMAP (0.29 mmol, 0.2 eq. respective to COOH groups), 151.85 mg of **6** (0.44 mmol, 0.35 eq. respective to COOH groups) were dissolved in 8 mL of dry DMF. The reaction mixture was cooled with crushed ice to 0°C and 341.8 mg of EDC·HCL (1.78 mmol, 2.00 eq. respective to the COOH groups) were added and stirred over night at ambient temperature. The solvent was removed under reduced pressure and the residual solid was dissolved in DCM. The solution was washed with 5% hydrochloric solution and brine and dried over magnesium sulfate. For purification, the polymer was precipitated in ice-cold diethyl ether three times.

Post-modification of P9 yielding P10

In a flame dried Schlenk flask 100 mg of **P9** (0.01 mmol, 1.00 eq.), 50.9 mg of DMAP (0.41 mmol, 0.2 eq. respective to COOH groups), 106.4 mg of **12** (0.31 mmol, 0.15 eq. respective to COOH groups), 152.5 mg of **4** (0.72 mmol, 0.35 eq. respective to COOH groups) and 273.0 mg of **11** (1.66 mmol, 0.8 eq. respective to CCOH groups) were dissolved in 8 mL of dry DMF. The reaction mixture was cooled with crushed ice to 0°C and 798.7 mg EDC·HCl (4.15 mmol, 2.00 eq. respective to the COOH groups) were added and stirred over night at ambient temperature. The solvent was removed under reduced pressure and the residual oil was dissolved in DCM. The solution was washed with 5% hydrochloric acid solution as well as brine and dried over magnesium sulfate. For purification the polymer was precipitated in ice-cold diethylether three times.

5.5.3 NMP Polymerizations

NMP Polymerization of Polymer P11

The polymerization of styrene/cms was performed in a 50 mL vial. The stabilizers were removed with basic alumina before use. 6.37 g of styrene (61.2 mmol, 160 eq.), 1.75 g of 4-chloromethylstyrene (11.5 mmol, 30 eq.) and 100 mg of the NMP initiator (0.38 mmol, 1 eq.) were dissolved in 4 mL toluene. The vial was sealed with a crimping tong and the solution was percolated with nitrogen for 30 min. The reaction was allowed to proceed for 20 h at 125 °C. Afterwards, the reaction was terminated by rapidly reducing the temperature by immersion in liquid nitrogen, opening the flask and letting the solution stir at ambient conditions for several minutes. The crude product was purified *via* precipitation three times each in ice cold methanol yielding a white powder. The powder was dried under high vacuum. The percentage of CMS in the polymer was calculated as reported in literature resulting in 14 % of CMS units.

Post-modification of P11 yielding P12, P13 and P14

200 mg of the copolymer **P11** (0.016 mmol, 1.00 eq) were dissolved in 8 mL dry DMF and functionalized with the corresponding carboxylic acid derivatives as follows: a) (**P12**) 46.1 mg of **30** (0.151 mmol, 0.6 eq) and 83.4 mg of the **29** (0.094 mmol, 0.5 eq.); b) (**P13**) 21.8 mg of **31** (0.151 mmol, 0.6 eq.) and 83.4 mg of **29** (0.094 mmol, 0.5 eq.) and c) (**P14**) 150 mg of **29** (0.227 mmol, 0.9 eq.) and were used for functionalization. To the prepared solutions 247.7 mg of cesium carbonate (0.757 mmol, 3.0eq) was added and stirred at 40°C for 48 hours. The solvent was removed under reduced pressure. The crude product was purified *via* precipitation three times each in ice cold methanol yielding a pile powder.

5.6 General Procedure for the Photo-induced SCNP Formation

Solutions of the functionalized linear precursor polymers were prepared in DCM or pure water, respectively under high dilution ($c = 0.017 \text{ mg mL}^{-1}$) and irradiated with a 36 W compact low-pressure UV-A lamp emitting at 320 nm (λ_{max}) for the UV-driven approach or with an Avonec LED setup using 3 lamps, emitting at 410-420 nm, for the visible light approach, in a custom build photoreactor. The solvent was removed under reduced pressure to afford the fluorescent single-chain polymer nanoparticles, which were directly dissolved in the appropriate solvent for analysis.

6

Appendix

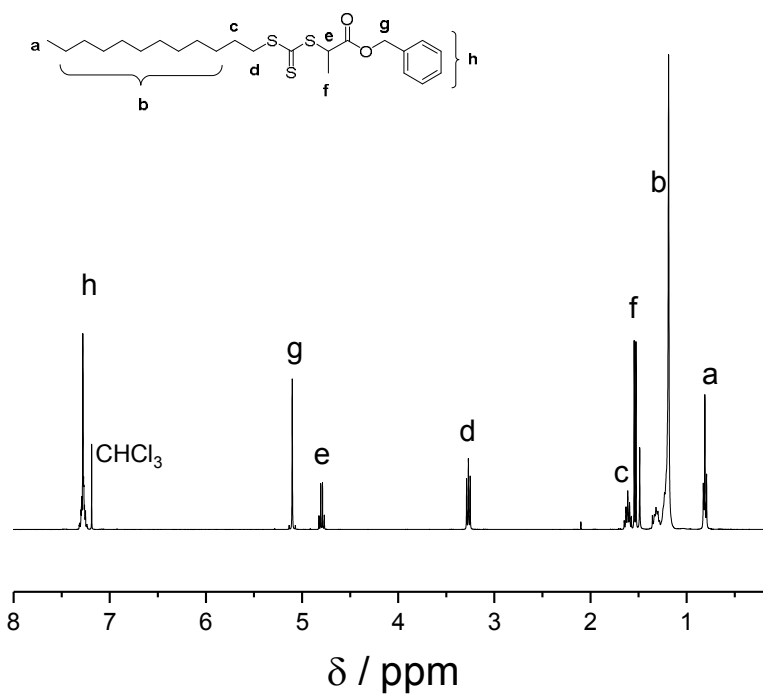


Figure 6.1.1: ^1H NMR of the DoPAT RAFT (3) agent recorded in CDCl_3 at 400 MHz. Adapted with permission from reference [224]. Copyright (2015) American Chemical Society (ACS).²²⁴

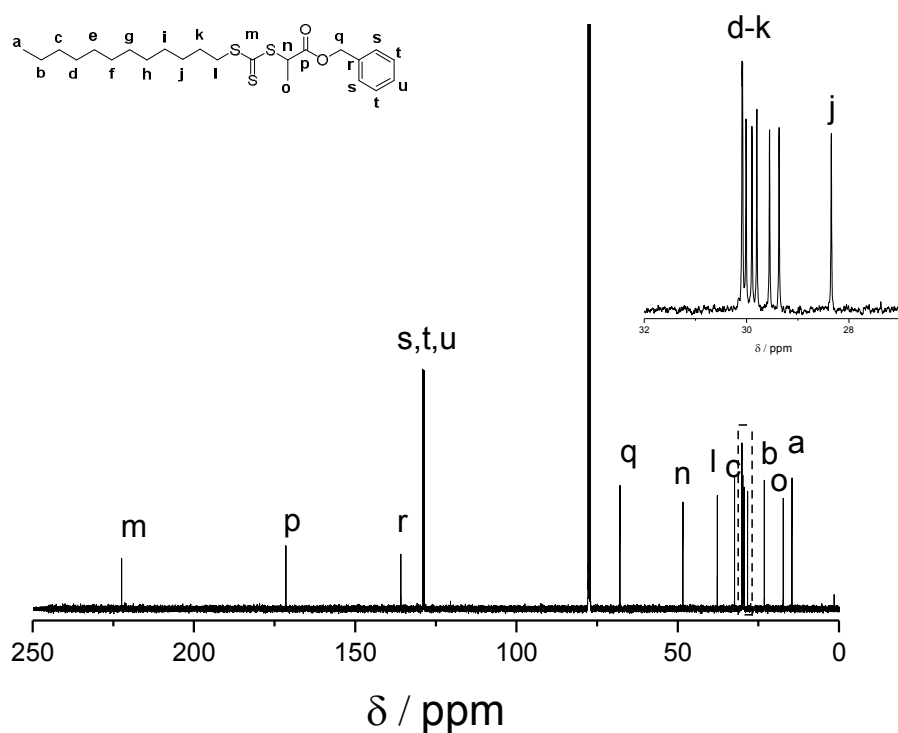


Figure 6.1.2: ^{13}C NMR of the DoPAT RAFT (3) agent recorded in CDCl_3 at 100 MHz. Adapted with permission from reference [224]. Copyright (2015) American Chemical Society (ACS).²²⁴

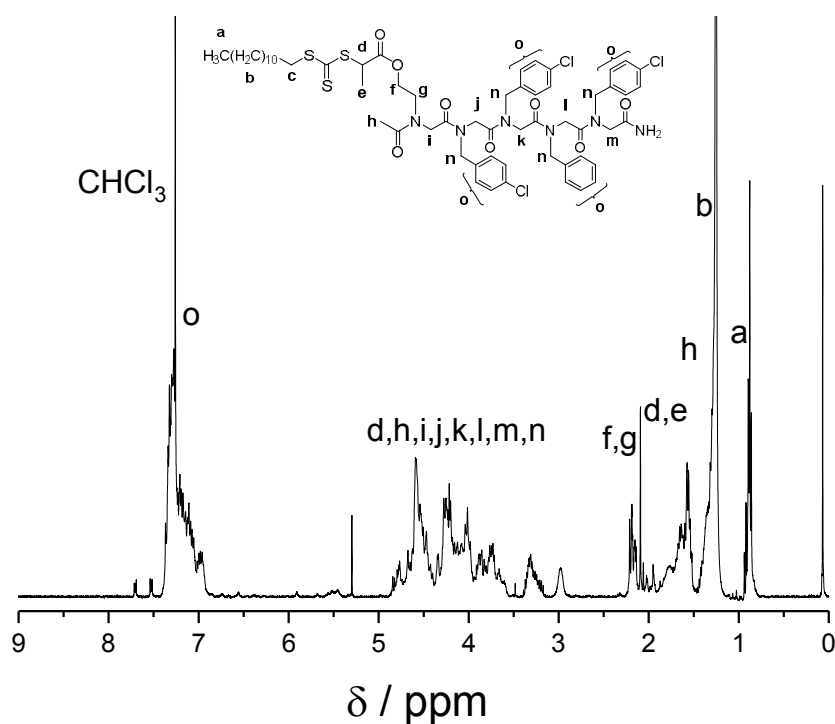


Figure 6.1.3: ^1H NMR spectrum of the DoPAT-peptoid RAFT agent (22) recorded in CDCl_3 at 400 MHz.

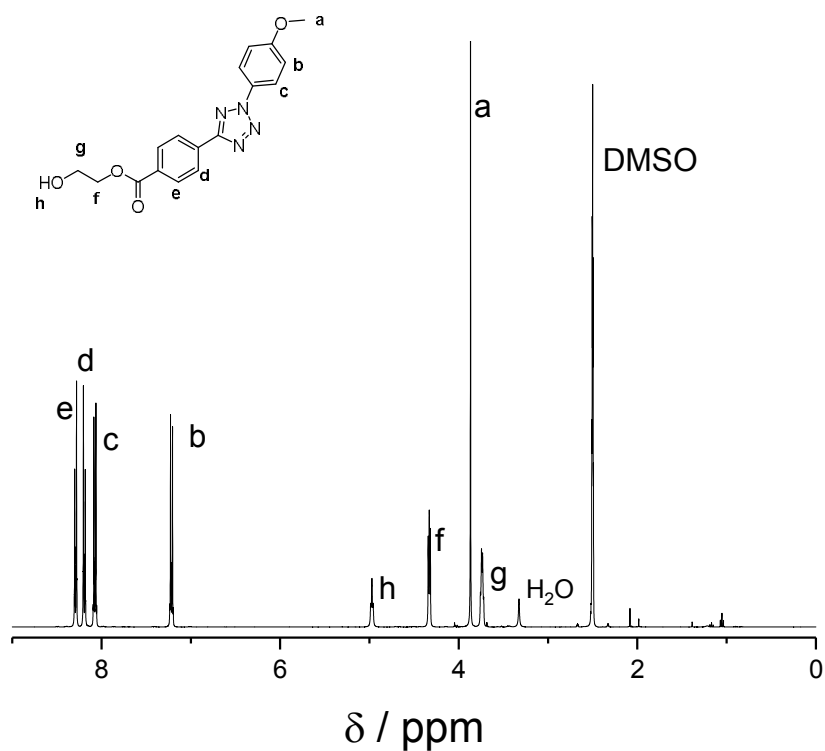


Figure 6.1.4: ^1H NMR spectrum of Tet (**6**) recorded in $\text{DMSO-}d_6$ at 400 MHz. Adapted with permission from reference [224]. Copyright (2015) American Chemical Society (ACS).²²⁴

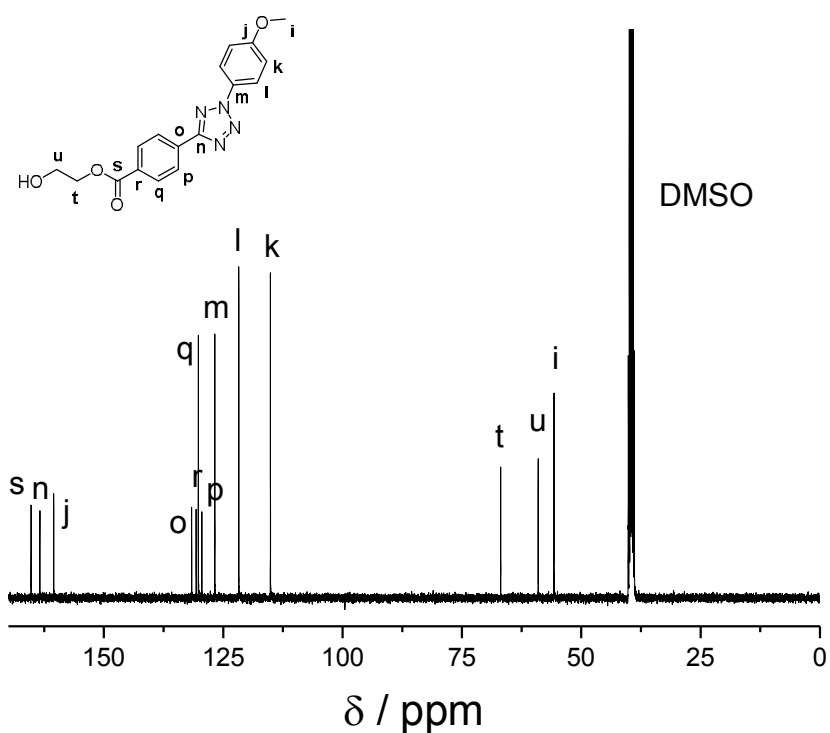


Figure 6.1.5: ^{13}C NMR spectrum of Tet (**6**) recorded in $\text{DMSO-}d_6$ at 100 MHz. Adapted with permission from reference [224]. Copyright (2015) American Chemical Society (ACS).²²⁴

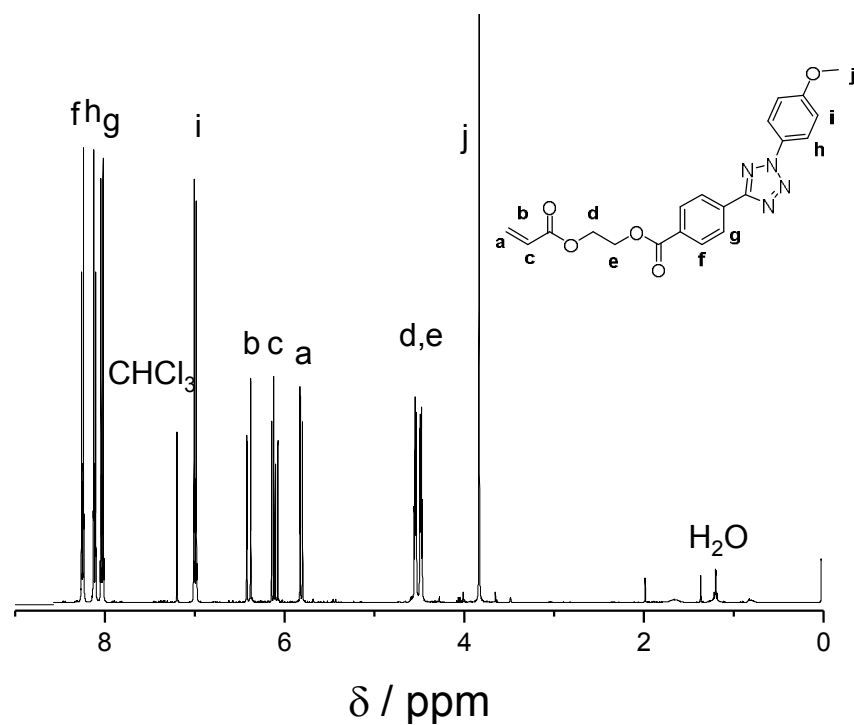


Figure 6.1.6: $^1\text{H-NMR}$ spectrum of the tetrazole monomer (7) measured in CDCl_3 at 400 MHz.

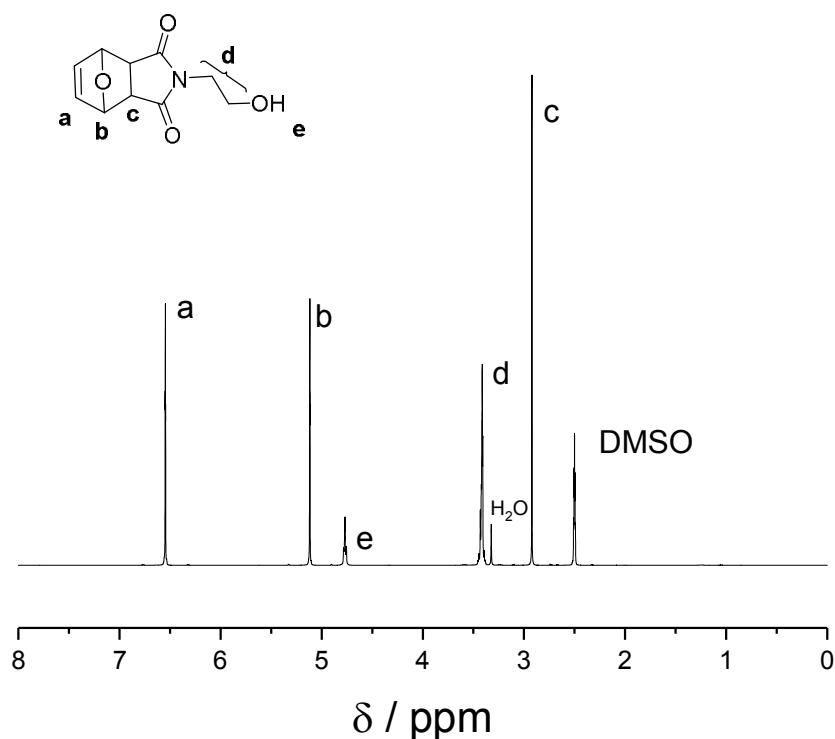


Figure 6.1.7: $^1\text{H-NMR}$ spectrum of *p*-Mal (4) recorded in $\text{DMSO-}d_6$ at 400 MHz. Adapted with permission from reference [224]. Copyright (2015) American Chemical Society (ACS).²²⁴

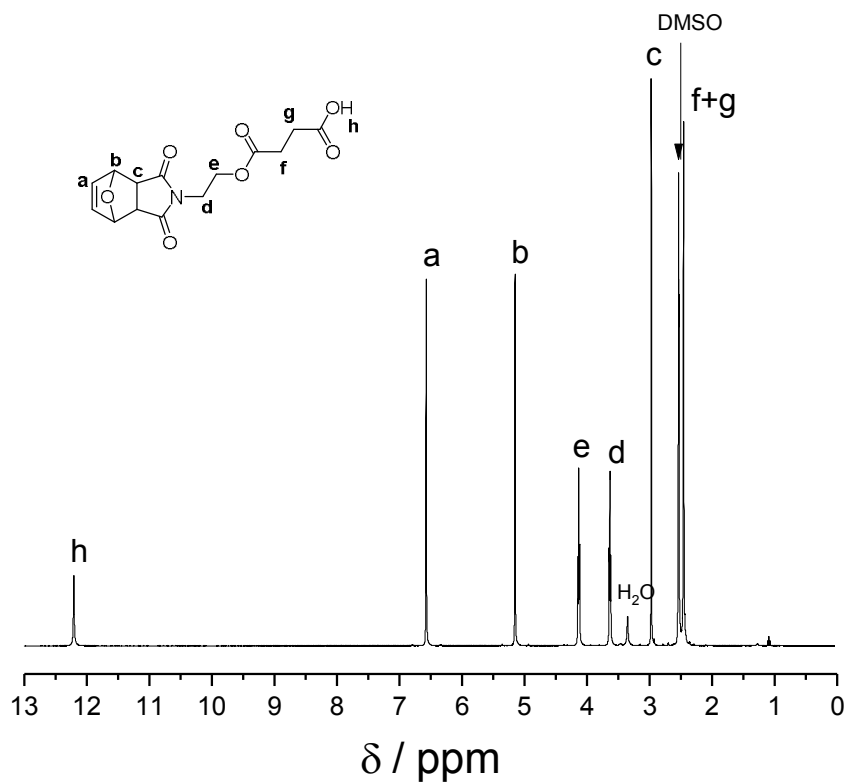


Figure 6.1.8: $^1\text{H-NMR}$ spectrum of *p*-Mal-acid (30) recorded in $\text{DMSO-}d_6$ at 400 MHz. Adapted with permission from reference [225] with permission from The Royal Society of Chemistry (RSC).²²⁵

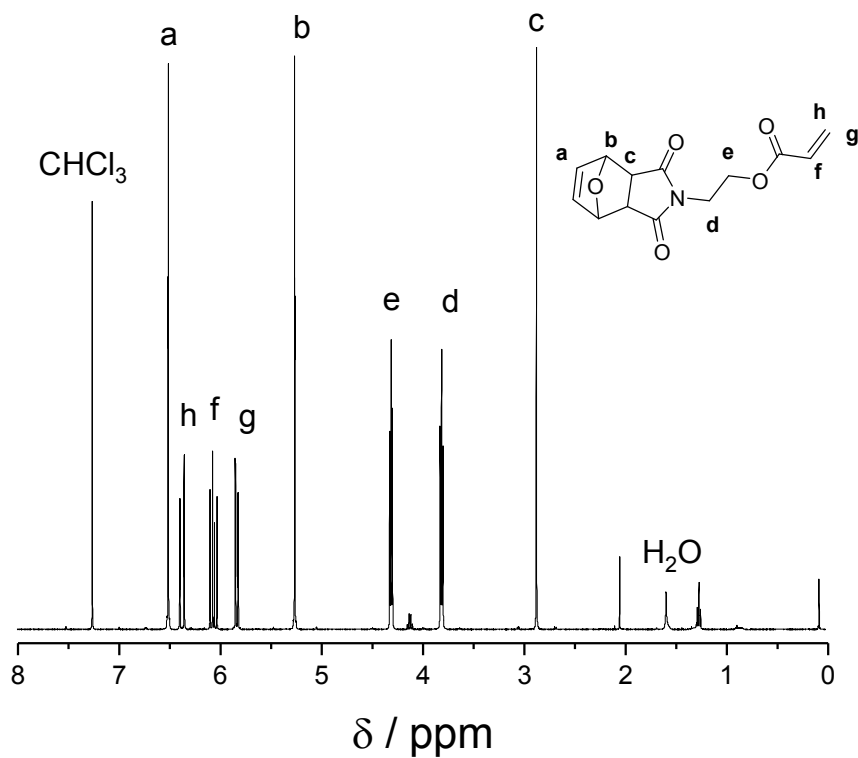


Figure 6.1.9: $^1\text{H-NMR}$ spectrum of the synthesized *p*-Mal monomer (5) recorded in CDCl_3 at 400 MHz.

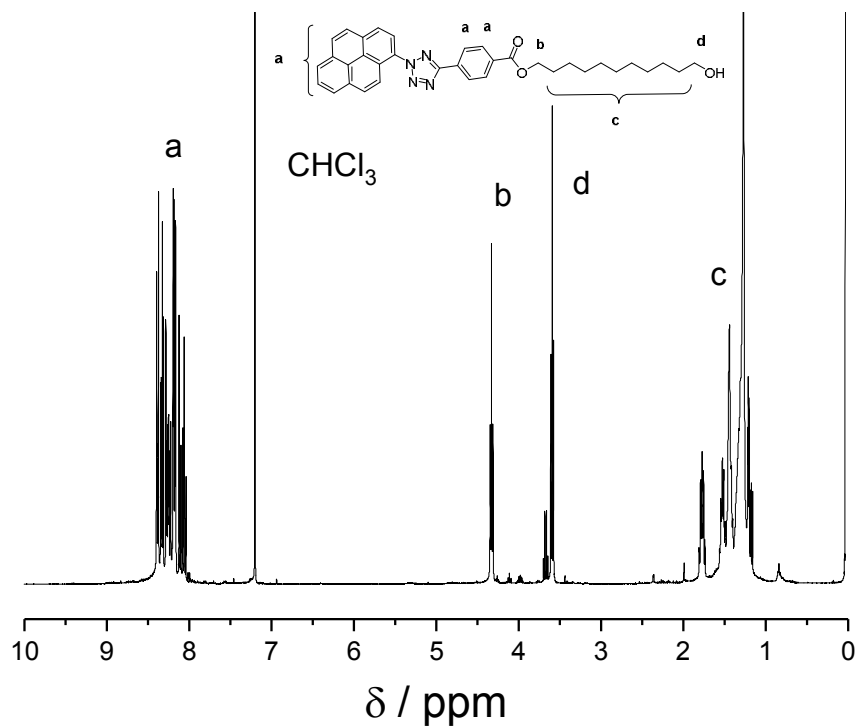


Figure 6.1.10: ^1H NMR spectrum of the PAT tetrazole (12) recorded in CDCl_3 at 400 MHz. Adapted with permission from reference [225] with permission from The Royal Society of Chemistry (RSC).²²⁵

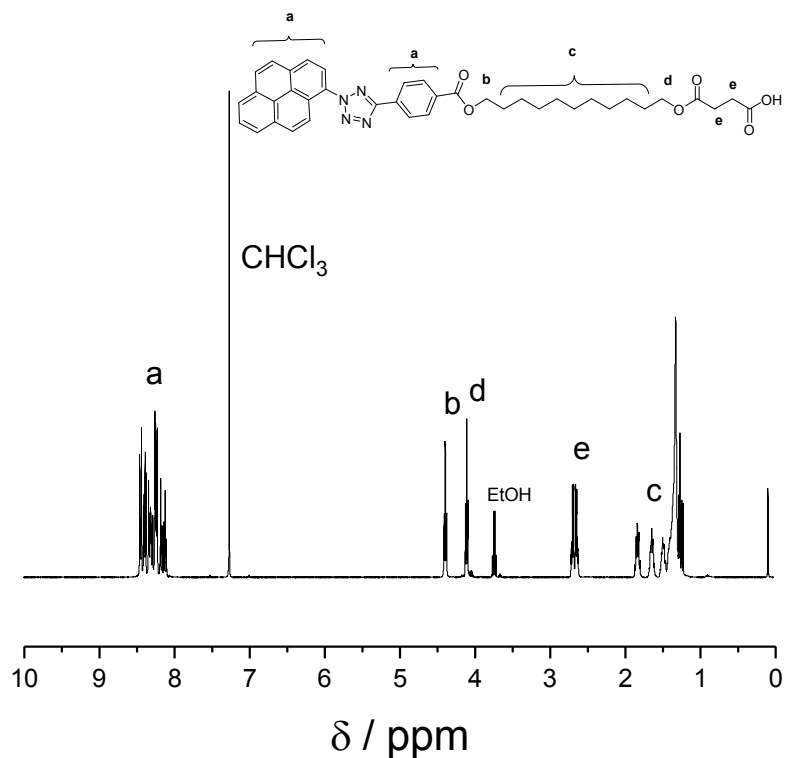


Figure 6.1.11: ¹H NMR of the PAT acid (29) recorded in CDCl₃ at 400 MHz. Adapted with permission from reference [225] with permission from The Royal Society of Chemistry (RSC).²²⁵

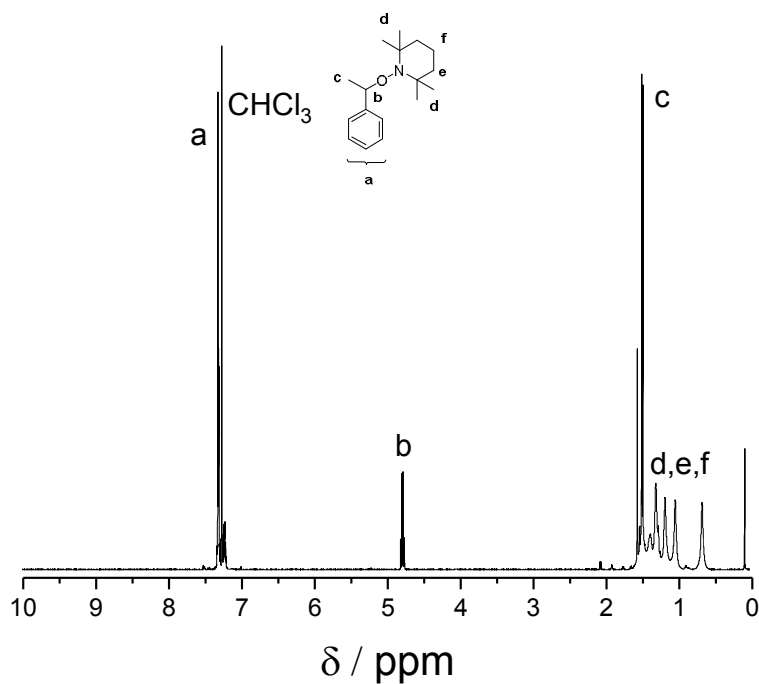


Figure 6.1.12: ¹H NMR spectrum of the synthesized NMP-initiator (25) recorded in CDCl₃ at 400 MHz. Adapted with permission from reference [225] with permission from The Royal Society of Chemistry (RSC).²²⁵

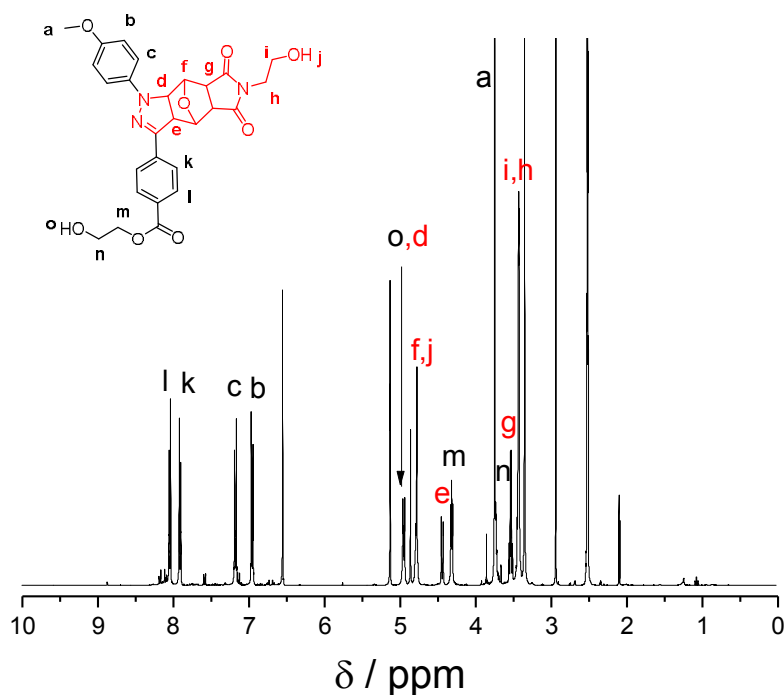


Figure 6.1.13: ^1H NMR spectrum of the reaction product **8** recorded in $\text{DMSO-}d_6$ at 400 MHz. Adapted with permission from reference [224]. Copyright (2015) American Chemical Society (ACS).²²⁴

^1H NMR (400 MHz, DMSO): δ [ppm] : 8.09 – 7.99 (d, 2H), 7.97 – 7.83 (d, 2H), 7.22 – 7.13 (d, 2H), 7.01 – 6.87 (d, 2H), 4.94 (d, $J = 9.6$ Hz, 2H), 4.77 (s, 3H), 4.43 (d, $J = 9.6$ Hz, 1H), 4.34 – 4.27 (t, 2H), 3.56 – 3.48 (m, 2H), 3.41 (m, $J = 6.2$ Hz, 4H).

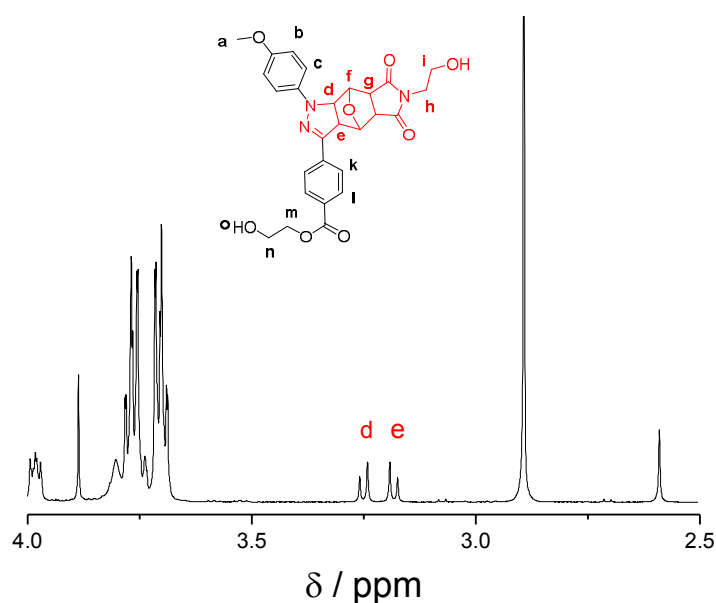


Figure 6.1.14: ^1H NMR spectrum (4.0-2.5 ppm) of the reaction product **8** recorded in CDCl_3 at 400 MHz, showing only the relevant pyrazoline resonances for comparison with the visible light driven pyrazoline formation.

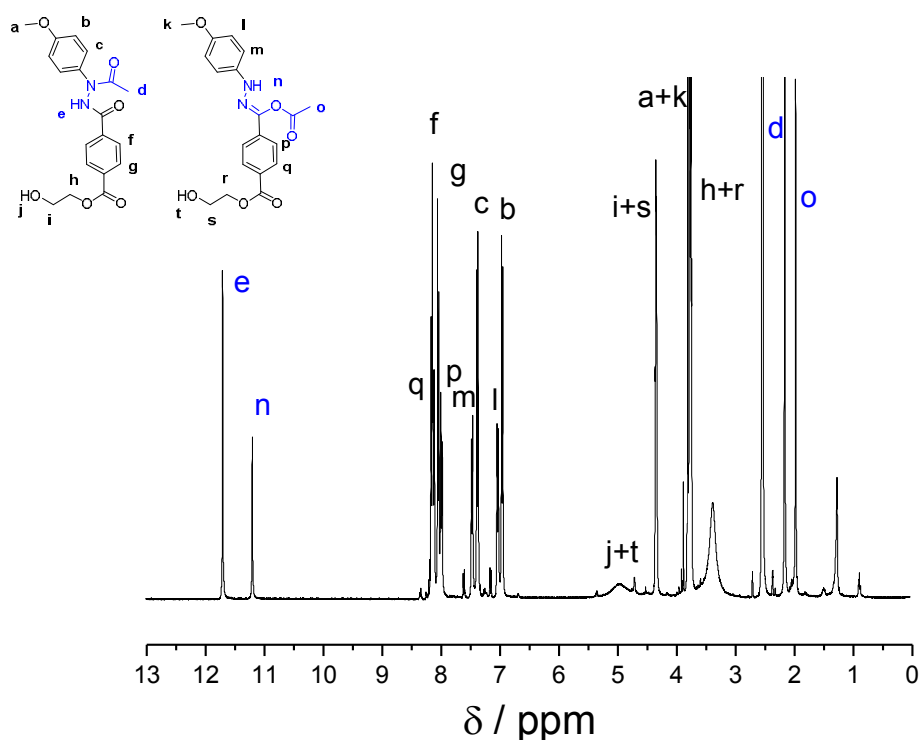


Figure 6.1.15: ^1H NMR spectrum of the reaction products **10a** + **10b** recorded in $\text{DMSO-}d_6$ at 400 MHz. Adapted with permission from reference [224]. Copyright (2015) American Chemical Society (ACS).²²⁴

^1H NMR (400 MHz, d_6 -DMSO) δ [ppm] : Acyl shifted product = 11.70 (s, 1H), 8.12 (d, $J = 4.9$ Hz, 2H), 8.06 – 7.99 (d, 2H), 7.34 (d, $J = 11.6$ Hz, 2H), 6.94 (d, $J = 9.0$ Hz, 2H), 4.87 (bs, $J = 76.8$ Hz, 1H), 4.37 – 4.24 (m, 2H), 3.74 – 3.70 (m, 3H), 3.71 – 3.7 (m, 2H), 2.13 (s, 3H).

^1H NMR (400 MHz, d_6 -DMSO) δ [ppm]: 11.19 (s, 1H), 8.11 (d, $J = 2.0$ Hz, 2H), 7.96 (dd, $J = 8.4, 4.1$ Hz, 2H), 7.46 (dd, $J = 11.6, 5.1$ Hz, 2H), 6.99 (t, $J = 11.0$ Hz, 2H), 4.87 (bs, $J = 76.8$ Hz, 1H), 4.36 – 4.25 (m, 2H), 3.78 (m, $J = 4.0$ Hz, 3H), 3.73 – 3.72 (m, 2H), , 1.93 (s, 3H).

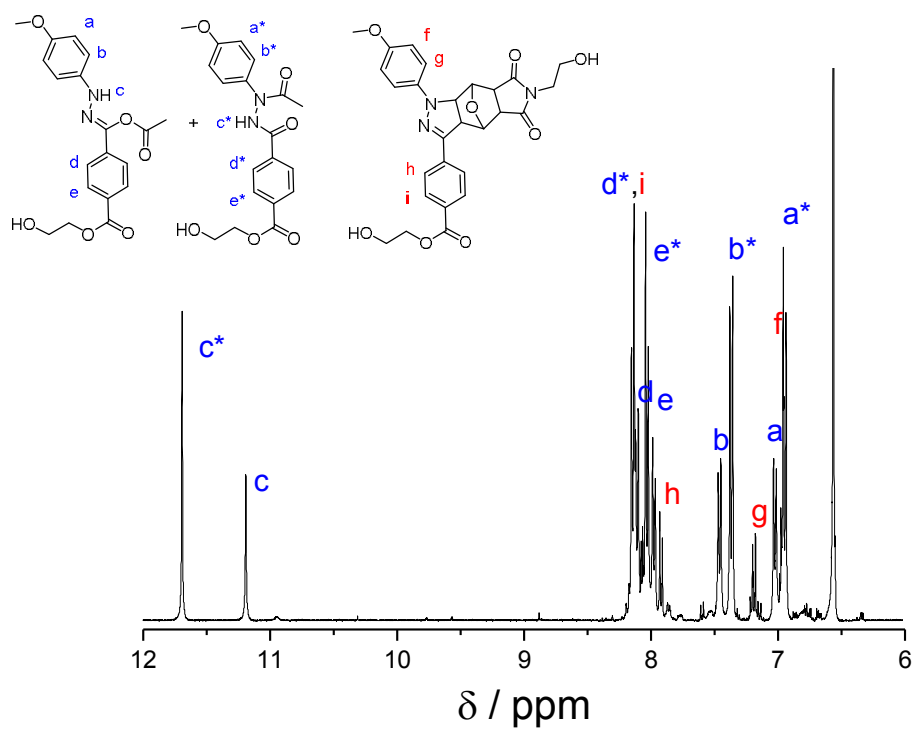


Figure 6.1.16: ¹H NMR spectrum (6-12 ppm) of the reaction products **8**, **10a** + **10b** recorded in DMSO-*d*₆ at 400 MHz. Adapted with permission from reference [224]. Copyright (2015) American Chemical Society (ACS).²²⁴

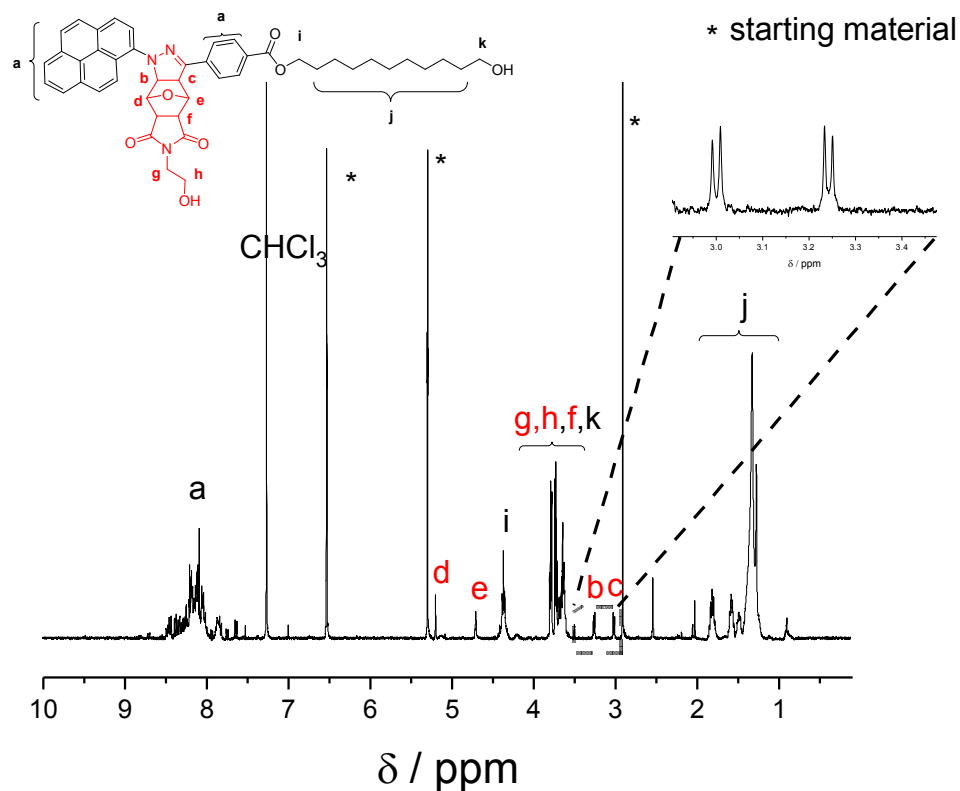


Figure 6.1.17: ^1H NMR spectrum of reaction product **13** (NITEC adduct between PAT and *p*-Mal) recorded in CDCl_3 at 400 MHz. The zoom shows the corresponding signals of the pyrazoline product with the furan protected maleimide. Adapted with permission from reference [225] with permission from The Royal Society of Chemistry (RSC).²²⁵

^1H NMR (400 MHz, CDCl_3) δ [ppm]: 8.81 – 7.78 (m, 13H), 5.20 (s, 1H), 4.63 (s, 1H) 4.35 (t, 2H), 3.78 – 3.72 (m, 4H), 3.67-3.64 (m, 2H), 3.63-3.61 (t, 2H), 3.24 (d, $J = 6.9$ Hz, 1H), 3.00 (d, $J = 7.0$ Hz, 1H). 1.87 – 1.22 (m, 18H). ESI-MS [m/z]: MS calc. $[\text{M}+\text{Na}]^+$ 764.33117, MS found 764.33250

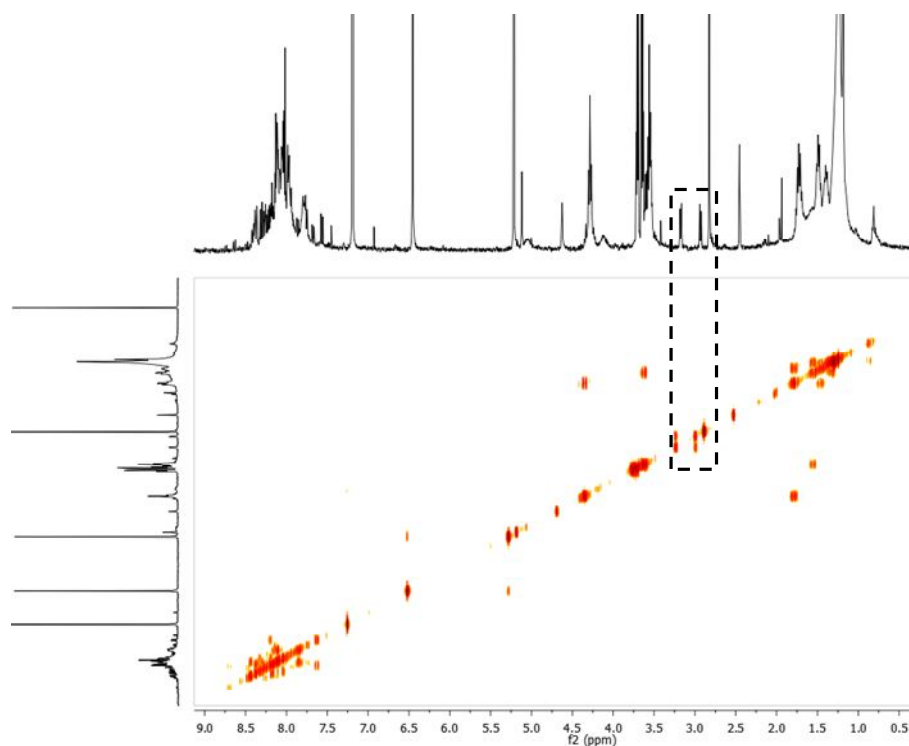


Figure 6.1.18: COSY NMR spectrum of reaction 13 (NITEC adduct between PAT and *p*-Mal) reaction after 3h, showing the correlation of the newly generated pyrazoline formation at 3.0 ppm and 3.2 ppm. Adapted with permission from reference [225] with permission from The Royal Society of Chemistry (RSC).²²⁵

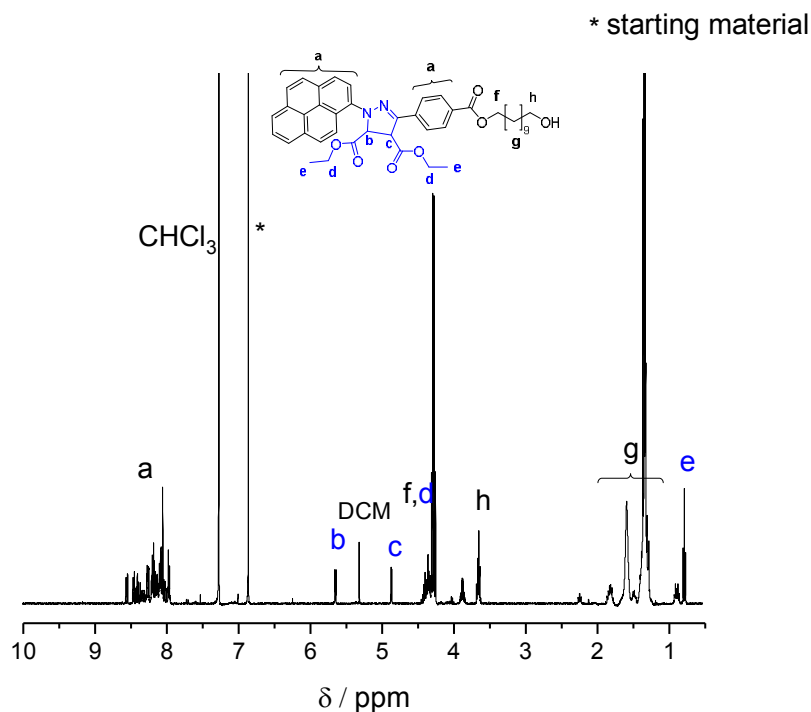


Figure 6.1 19: ¹H NMR spectrum of reaction 15 (NITEC adduct with diethyl fumarate) recorded in CDCl₃ at 400 MHz. The rearomatized reaction product is not shown. Adapted with permission from reference [225] with permission from The Royal Society of Chemistry (RSC).²²⁵

^1H NMR (400 MHz, CDCl_3) δ [ppm]: 8.77 – 7.50 (m, 13H), 5.63 (d, $J = 5.0$ Hz, 1H), 4.85 (d, $J = 4.9$ Hz, 1H), 4.57 – 4.01 (m, 6H) 3.63 (m, $J = 9.0, 4.2$ Hz, 2H), 2.07 – 0.92 (m, 18H), 0.76 (t, $J = 7.1$ Hz, 6H). ESI-MS [m/z]: MS calc. $[\text{M}+\text{Na}]^+$ 727.33537, MS found 727.33617, MS calc rearomatized $[\text{M}+\text{Na}]^+$ 725.31972, MS found 725.32038

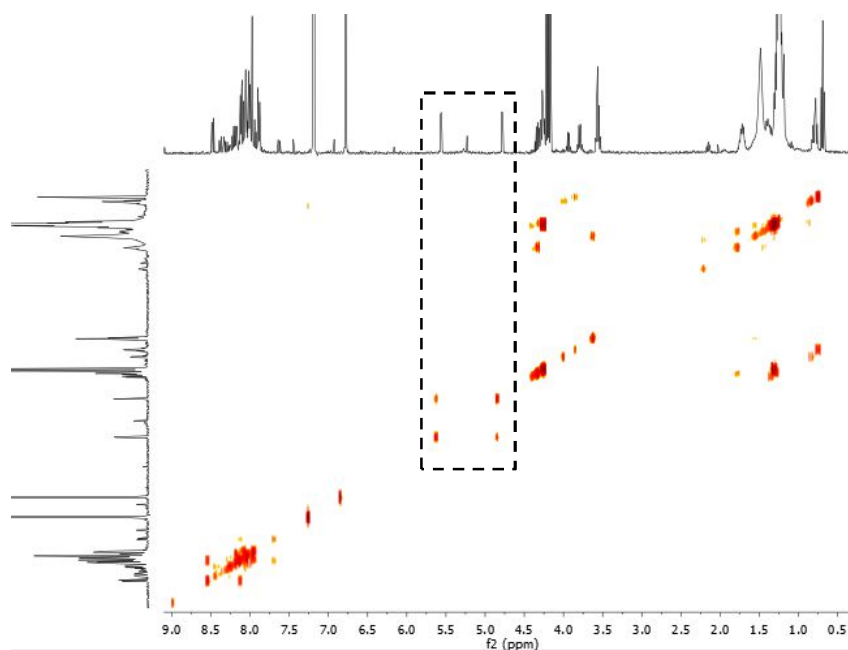


Figure 6.1.20: COSY NMR of reaction **15** (NITEC adduct with diethyl fumarate) after 2h, showing the correlation of the newly generated pyrazoline formation at 5.5 ppm and 4.8 ppm. Adapted with permission from reference [225] with permission from The Royal Society of Chemistry (RSC).²²⁵

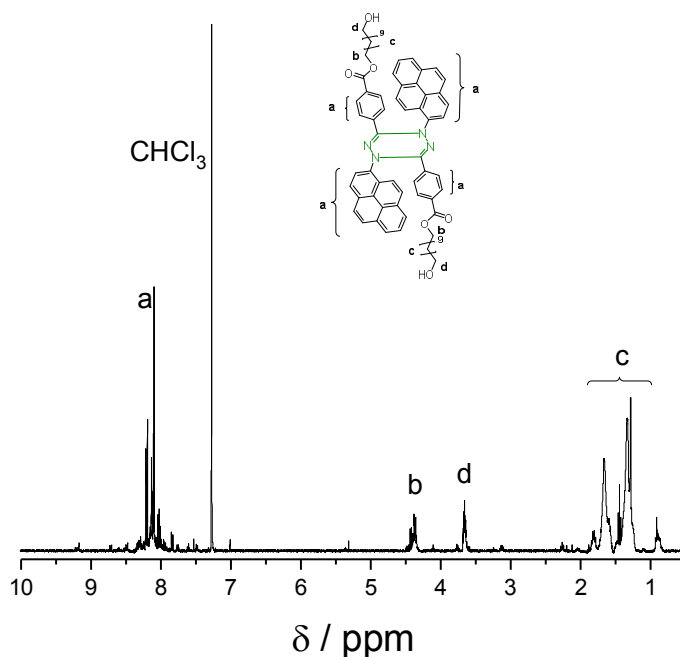


Figure 6.1.21: ^1H NMR spectrum of reaction product **16** (PAT tetrazole dimer) recorded in CDCl_3 at 400 MHz. Adapted with permission from reference [225] with permission from The Royal Society of Chemistry (RSC).²²⁵

^1H NMR (400 MHz, CDCl_3) δ [ppm]: 8.99 – 7.35 (m, 26H), 4.47 – 4.30 (dt, $J = 14.8, 6.9$ Hz, 4H), 3.63 (m, 4H), 1.80 (dd, $J = 22.5, 15.1$ Hz, 4H), 1.53 – 1.15 (m, 36H). ESI-MS [m/z]: MS calc. $[\text{M}+\text{Na}]^+$ 1087.53441, MS found 1087.53613, MS calc. $[\text{M}+\text{H}]^+$ 1065.55246 MS found 1065.55146.

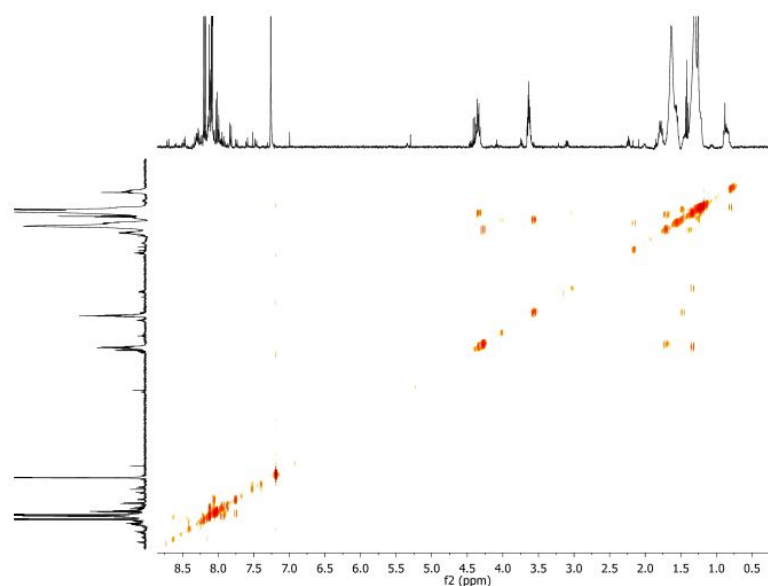


Figure 6.1.22: COSY NMR spectrum of reaction product **16** (PAT tetrazole dimer) recorded in CDCl_3 at 400 MHz. Adapted with permission from reference [225] with permission from The Royal Society of Chemistry (RSC).²²⁵

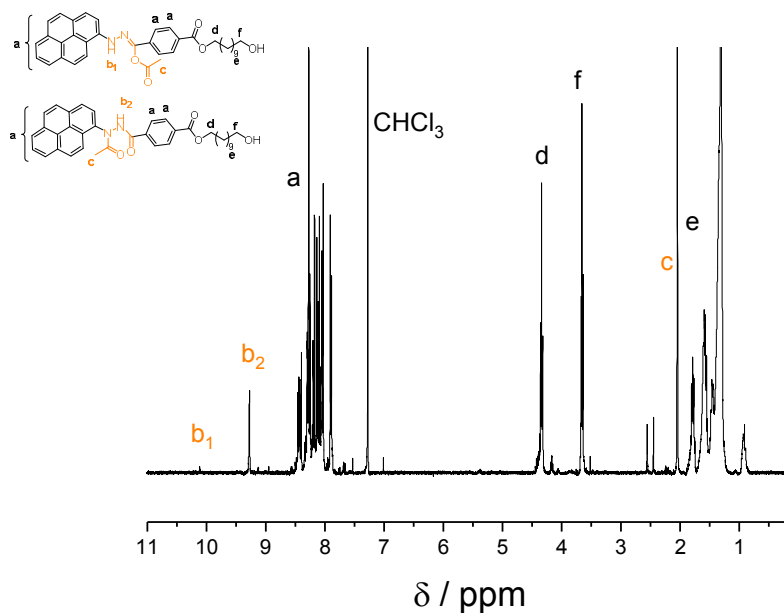


Figure 6.1.23: ^1H NMR spectrum of reaction product **17a** and **17b** (NICAL adduct) recorded in CDCl_3 at 400 MHz. Adapted with permission from reference [225] with permission from The Royal Society of Chemistry (RSC).²²⁵

^1H NMR (400 MHz, CDCl_3) δ [ppm]: 10.0 (s, 1H), 9.03 (s, 1H), 8.81 – 7.78 (m, 13H), 4.38 (t, 2H), 3.64 (t, 2H), 1.87 – 1.73 (m, 2H), 1.69 – 1.22 (m, 18H). ESI-MS [m/z]: MS calc. $[\text{M}+\text{Na}]^+$ 615.28294, MS found 615.28481, MS calc $[2\text{M}+\text{Na}]^+$ 1207.57667, MS found 1207.58135.

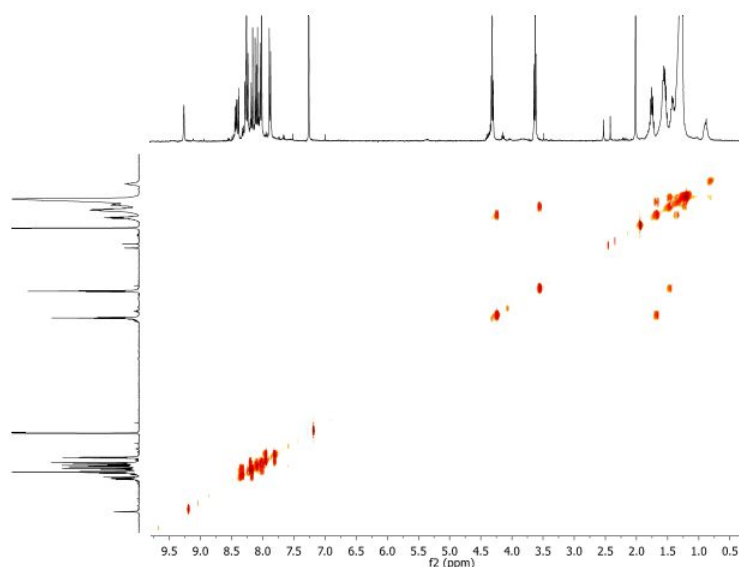


Figure 6.1.24: COSY NMR spectrum of reaction product **17a** and **17b** (NICAL adduct) recorded in CDCl_3 at 400 MHz. Adapted with permission from reference [225] with permission from The Royal Society of Chemistry (RSC).²²⁵

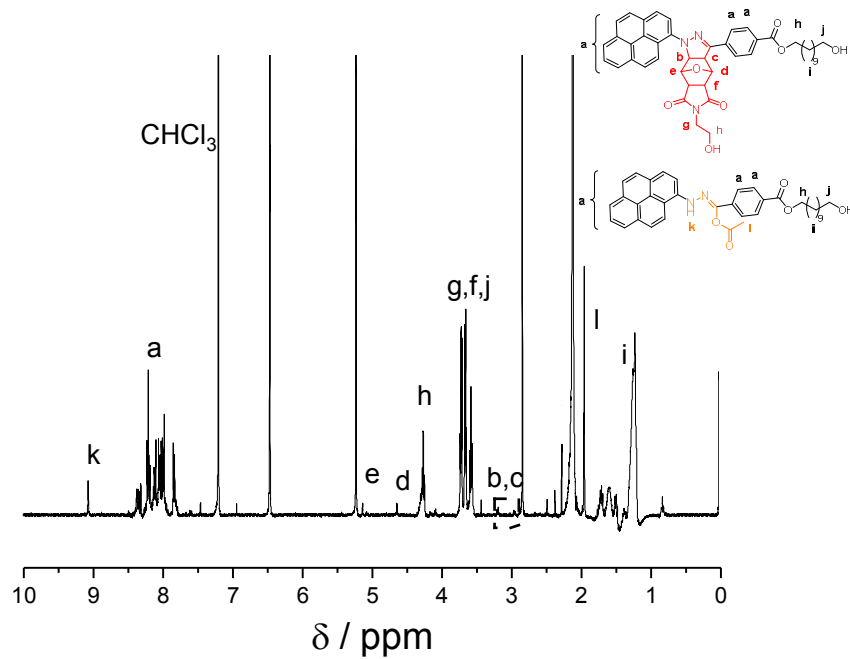


Figure 6.1.25: ^1H NMR spectrum of reaction product **17** and **13** recorded in CDCl_3 at 400 MHz.

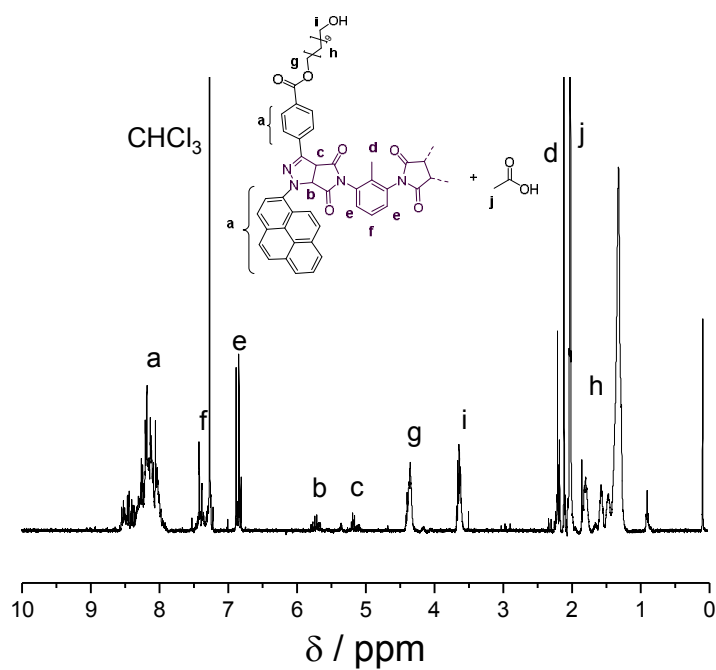


Figure 6.1.26: ^1H NMR spectrum of the competitive reaction with the products **17** and **21** recorded in CDCl_3 at 400 MHz.

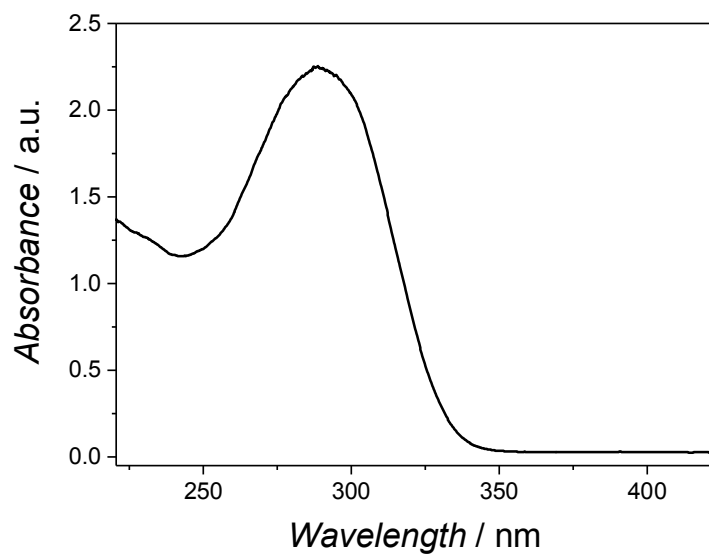
UV/Vis and Fluorescence spectra of the small molecules

Figure 6.1.27: UV/Vis spectra of **6** measured in DMSO with a concentration of 0.016 mol L^{-1} . Adapted with permission from reference [224]. Copyright (2015) American Chemical Society (ACS).²²⁴

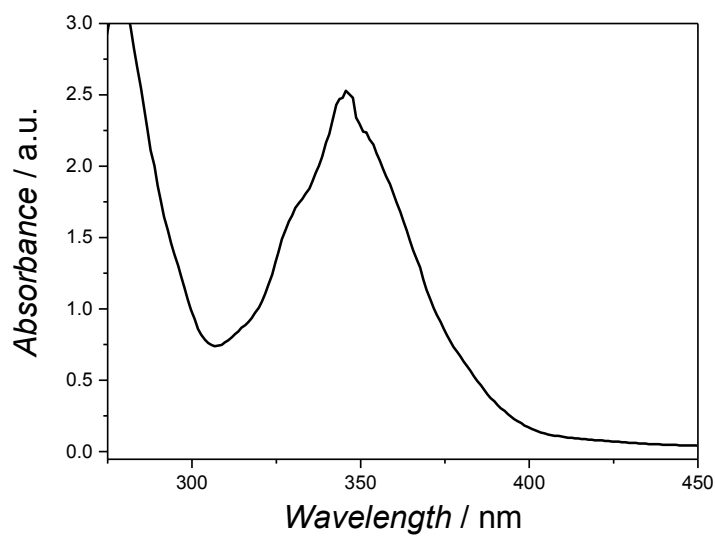


Figure 6.1.28: UV/Vis spectra of **12** measured in DCM with a concentration of 0.2 mg mL^{-1}

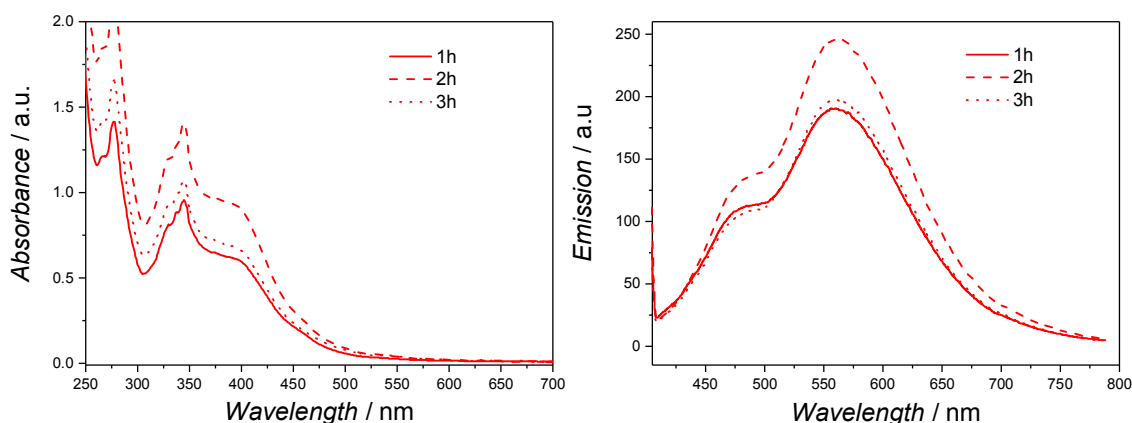


Figure 6.1.29: UV/Vis and fluorescence spectra of the reaction product **13** (reaction of **12** with **4**) measured in DCM with a concentration of 0.2 mg mL⁻¹. Kinetic samples were taken in 1h intervals. Adapted with permission from reference [225] with permission from The Royal Society of Chemistry (RSC).²²⁵

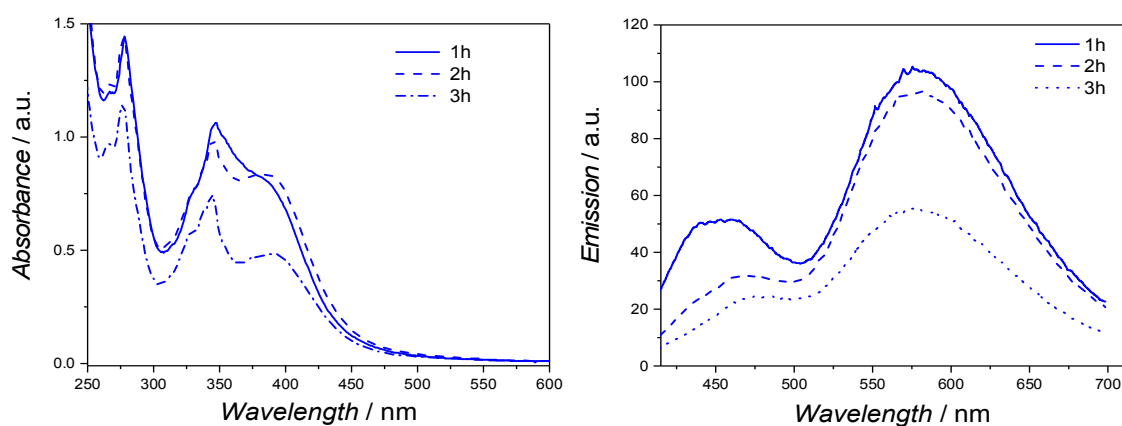


Figure 6.1.30: UV/Vis and fluorescence spectra of the reaction product **15** (reaction of **12** with **14**) measured in DCM with a concentration of 0.2 mg mL⁻¹. Kinetic samples were taken in 1h intervals. Adapted with permission from reference [225] with permission from The Royal Society of Chemistry (RSC).²²⁵

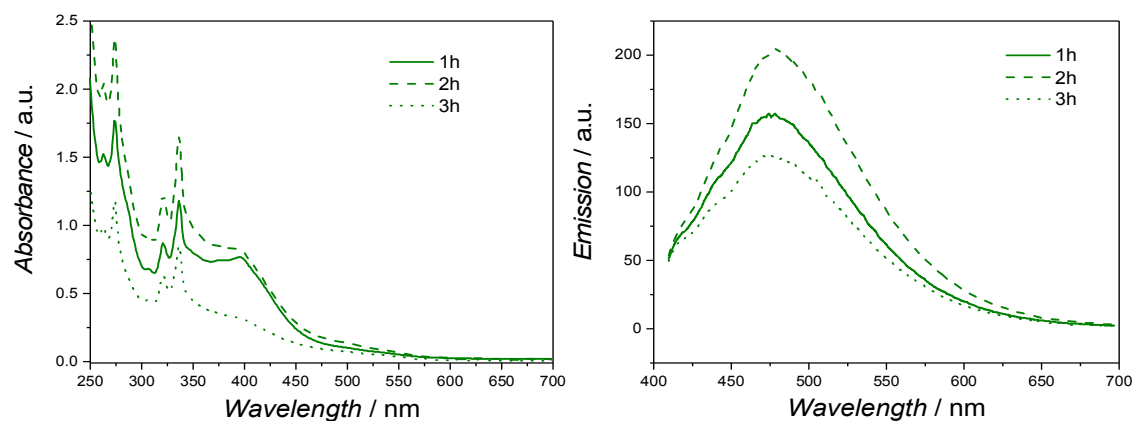


Figure 6.1.31: UV/Vis and fluorescence spectra of the dimerization reaction product **16** (dimerization reaction of **12**) measured in DCM with a concentration of 0.2 mg mL⁻¹. Kinetic samples were taken in 1h intervals. Adapted with permission from reference [225] with permission from The Royal Society of Chemistry (RSC).²²⁵

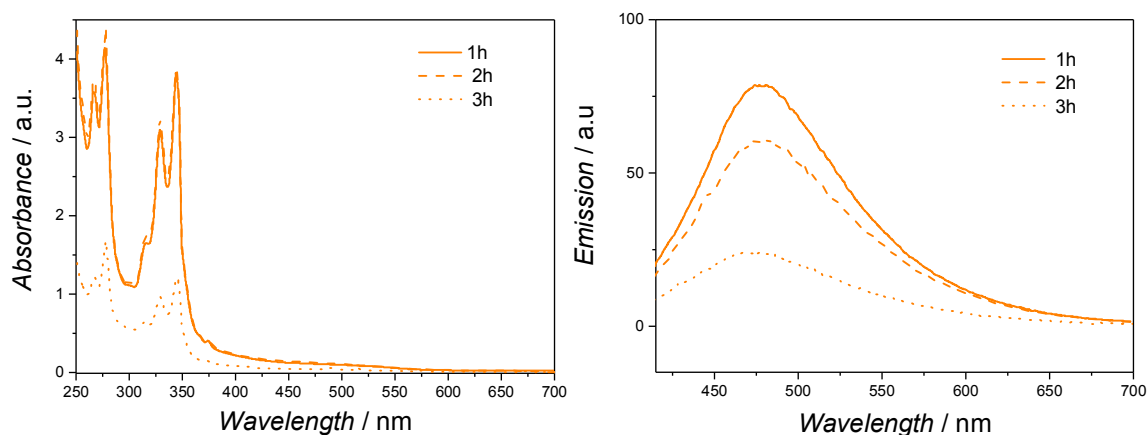


Figure 6.1.32: UV/Vis and fluorescence spectra of the reaction product **17** (reaction of **12** with **9**) measured in DCM with a concentration of 0.2 mg mL⁻¹. Kinetic samples were taken in 1h intervals. Adapted with permission from reference [225] with permission from The Royal Society of Chemistry (RSC).²²⁵

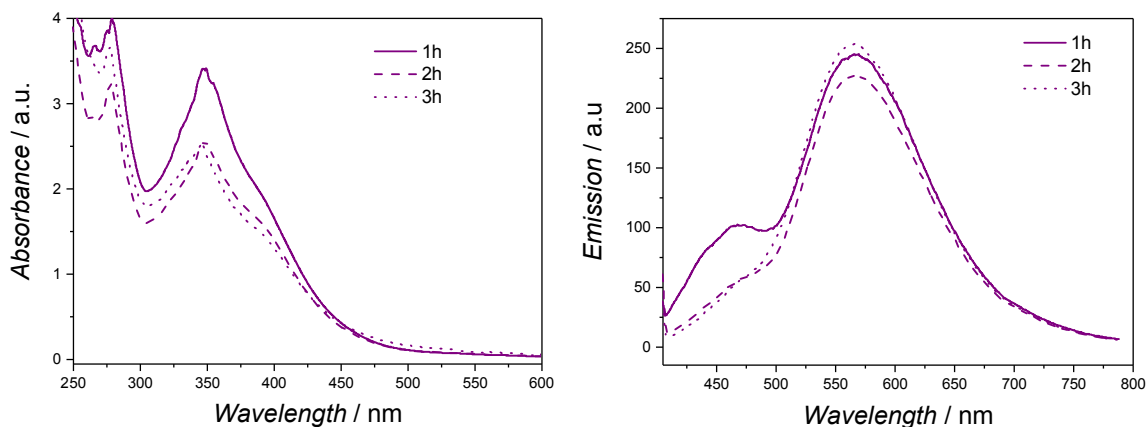


Figure 6.1.33: UV/Vis spectra of the reaction product **19** (reaction of **12** with **18**) measured in DCM with a concentration of 0.2 mg mL⁻¹. Adapted with permission from reference [225] with permission from The Royal Society of Chemistry (RSC).²²⁵

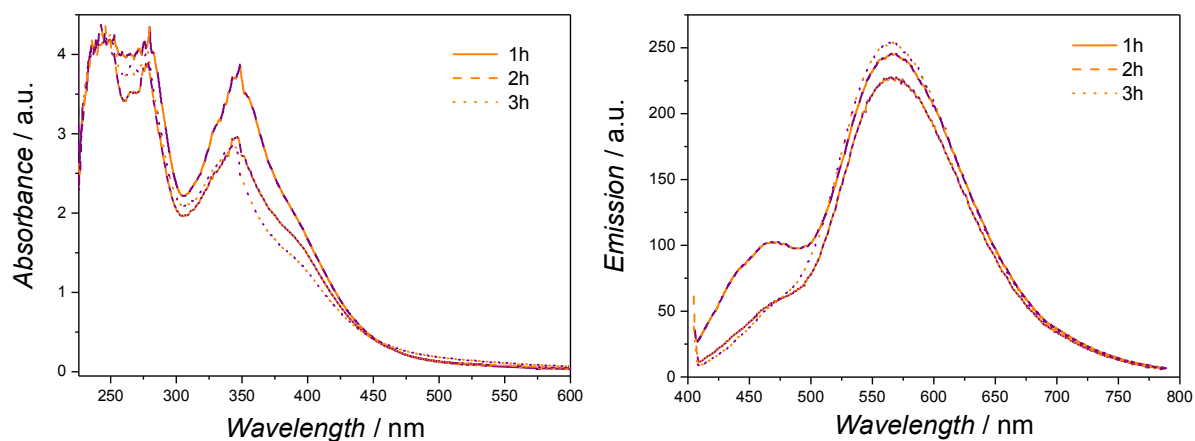


Figure 6.1.34: UV/Vis spectra and fluorescence of the competitive reaction products **17** and **19** (competitive reaction of **12,9** and **18**) measured in DCM with a concentration of 0.2 mg mL^{-1} . Kinetic samples were taken in 1h intervals.

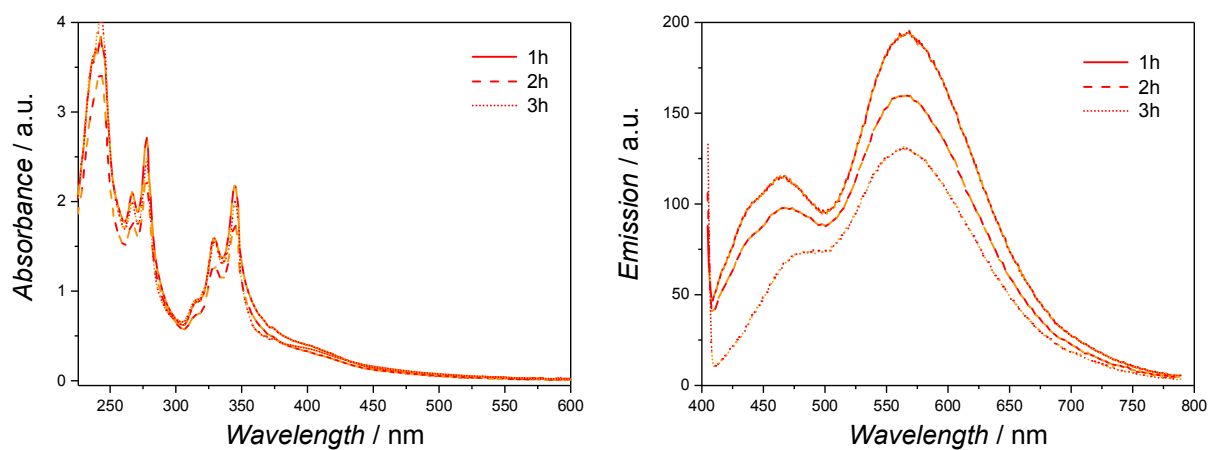


Figure 6.1.35: UV/Vis spectra and fluorescence of the competitive reaction products **13** and **17** (competitive reaction of **12, 9** and **4**) measured in DCM with a concentration of 0.2 mg mL^{-1} . Kinetic samples were taken in 1h intervals.

Characterization of the photoinduced SCNPs

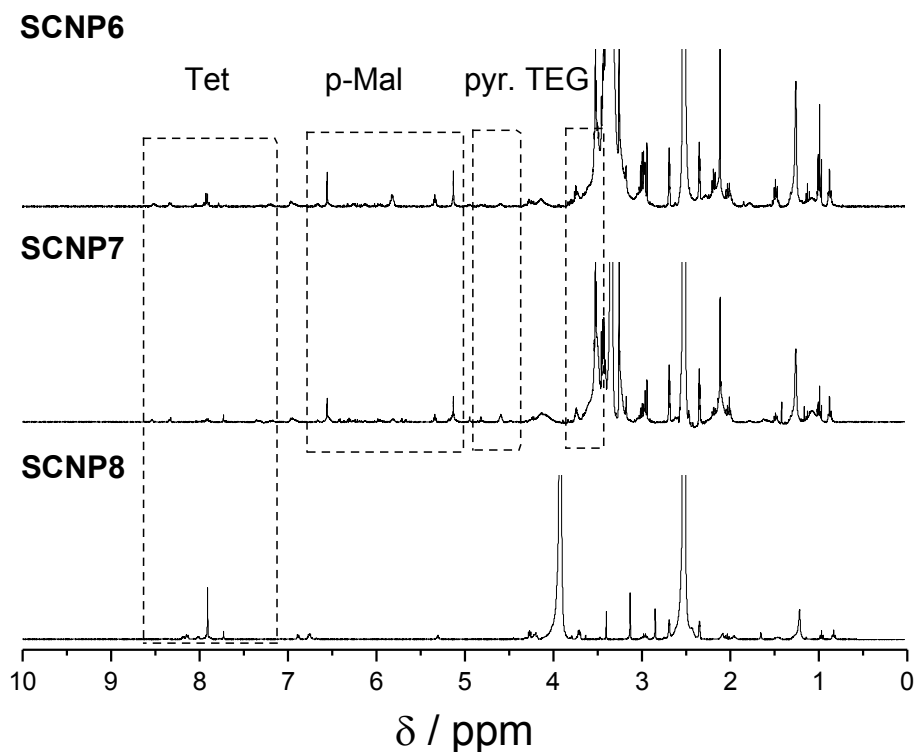


Figure 6.1.36: ^1H NMR spectra of **SCNP6-8** recorded in $\text{DMSO-}d_6$ with 400 MHz. Adapted with permission from reference [224]. Copyright (2015) American Chemical Society (ACS).²²⁴

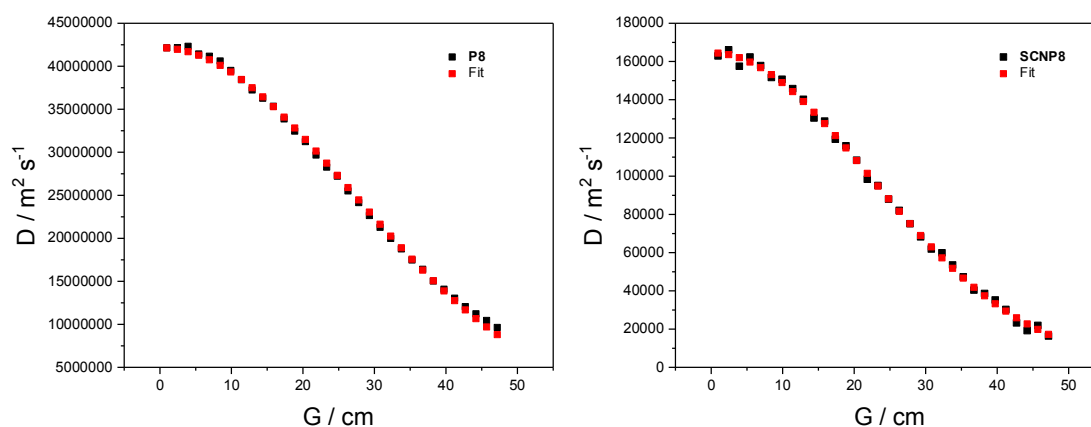


Figure 6.1.37: Exemplarily DOSY data fit for **P8** and **SCNP8** using the tetrazole resonance (8.1 and 7.9 ppm) in NMR spectroscopy. Adapted with permission from reference [224]. Copyright (2015) American Chemical Society (ACS).²²⁴

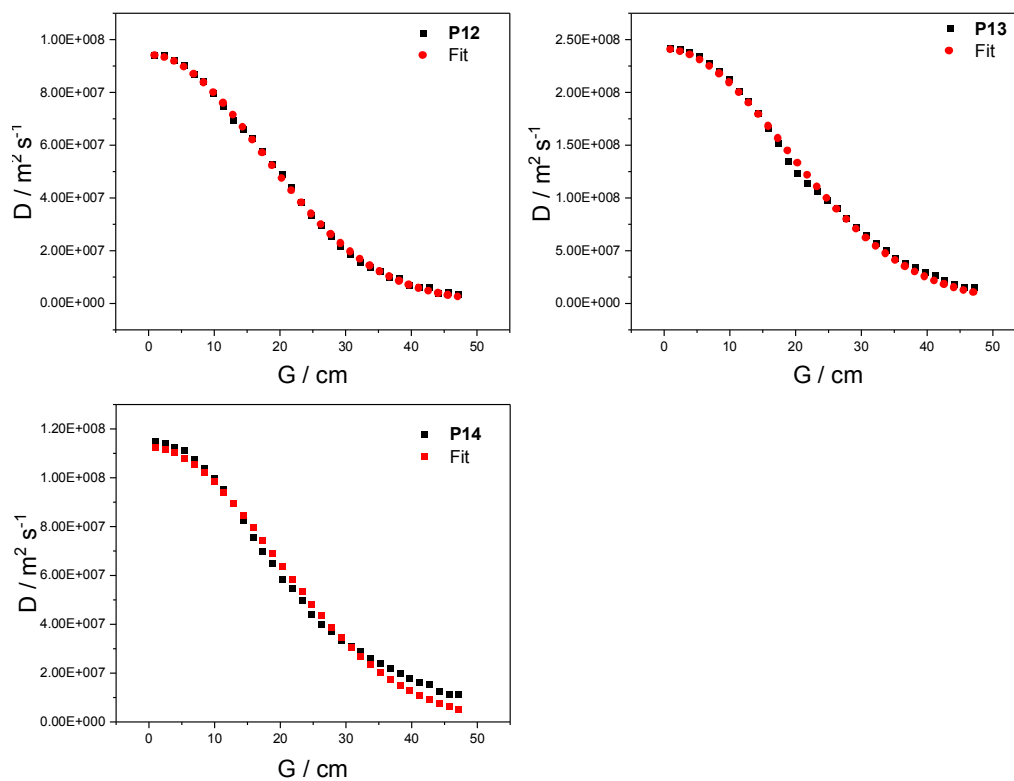


Figure 6.1.38: Exemplarily DOSY data fit for **P12-14** using the poly(styrene) resonance (7.09 ppm) in NMR spectroscopy. Adapted with permission from reference [225] with permission from The Royal Society of Chemistry (RSC).²²⁵

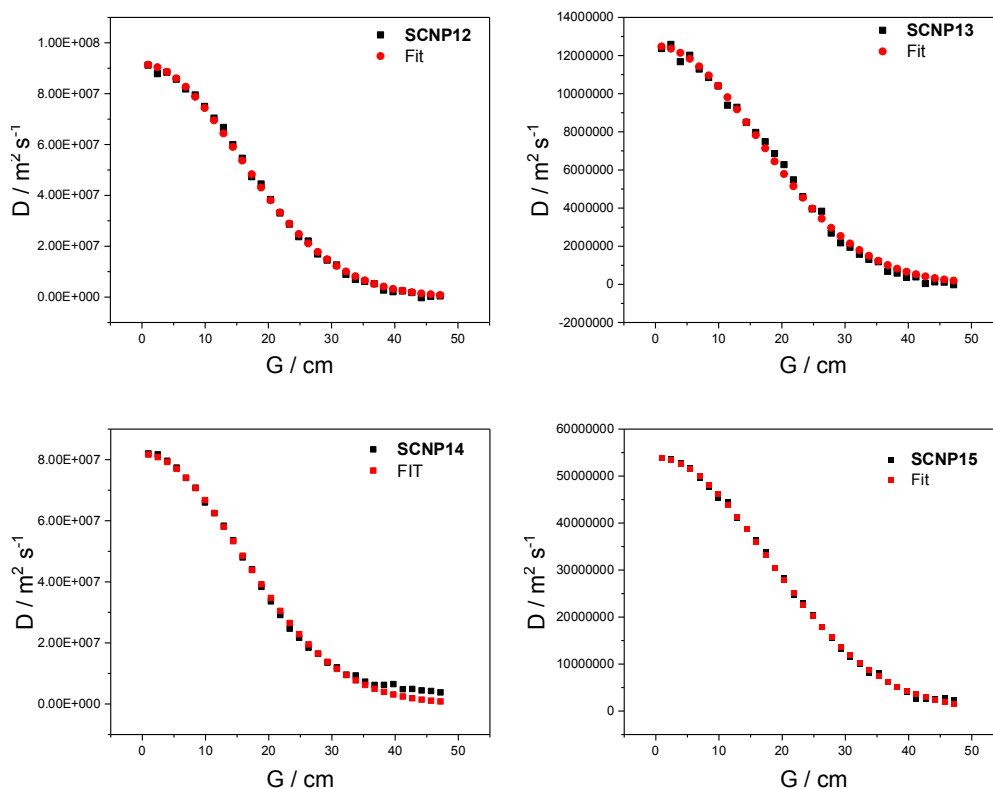


Figure 6.1.39: Exemplarily DOSY data fit for **SCNP12-15** using the poly(styrene) resonance (7.09 ppm) in NMR spectroscopy. Adapted with permission from reference [225] with permission from The Royal Society of Chemistry (RSC).²²⁵

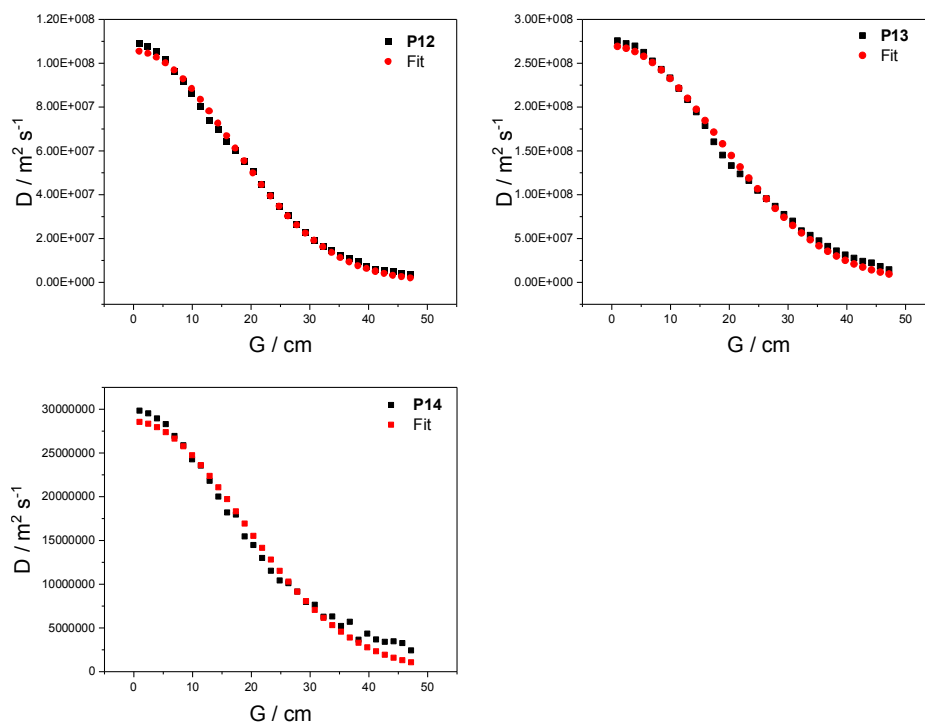


Figure 6.1.40: Exemplarily DOSY data fit for **P12-15** using the tetrazole resonance (8.26 ppm) incorporated in the polymer backbone in NMR spectroscopy. Adapted with permission from reference [225] with permission from The Royal Society of Chemistry (RSC).²²⁵

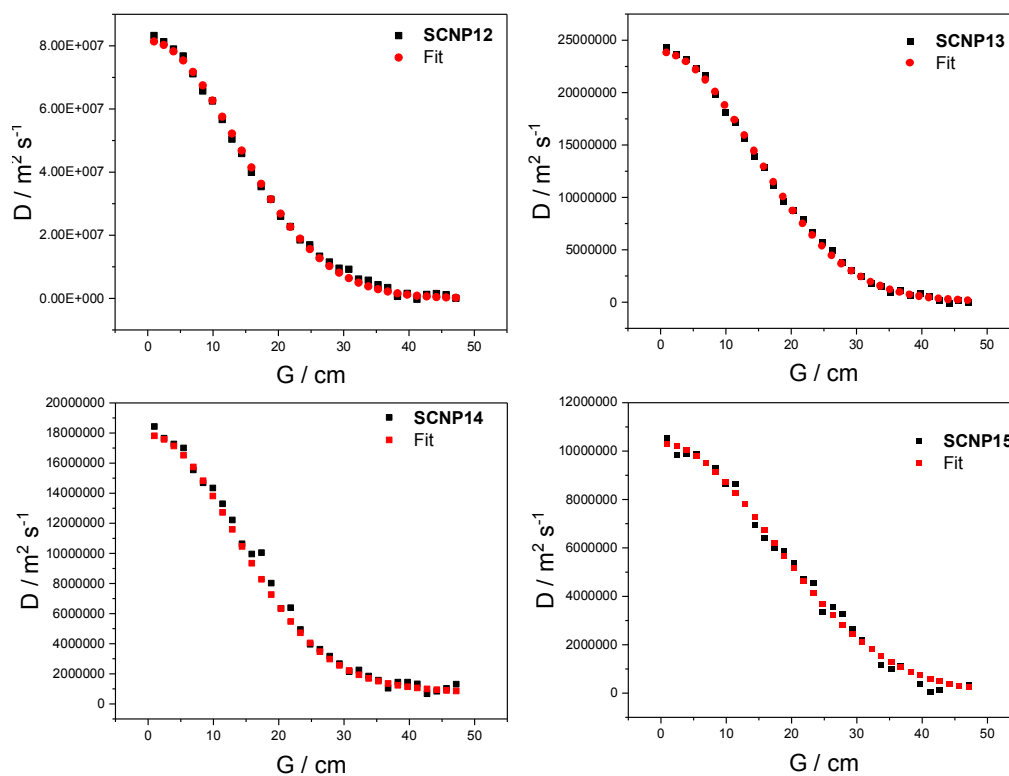


Figure 6.1.41: Exemplarily DOSY data fit for **SCNP12-15** using the tetrazole resonance (8.26 ppm) incorporated in the polymer backbone in NMR spectroscopy. Adapted with permission from reference [225] with permission from The Royal Society of Chemistry (RSC).²²⁵

Table 6.1.1 Diffusion coefficients and their corresponding average hydrodynamic diameters from DOSY NMR spectroscopy of **P12-14** and **SCNP12-15**. Adapted with permission from reference [225] with permission from The Royal Society of Chemistry (RSC).²²⁵

Polymer	Diffusion coefficient	Av. Diameter [nm]
	1.30E-10	
P12	1.35E-10	6.20
	1.29E-10	
	2.77E-10	
SCNP12	2.73E-10	2.9
	2.89E-10	
	1.50E-10	
P13	1.51E-10	5.5
	1.44E-10	
	2.92E-10	
SCNP13	2.93E-10	2.7
	3.11E-10	
	7.66E-11	
P14	7.52E-11	10.6
	7.74E-11	
	1.60E-10	
SCNP14	1.56E-10	5.0
	1.72E-10	
	2.09E-10	
SCNP15	2.12E-10	3.8
	2.18E-10	

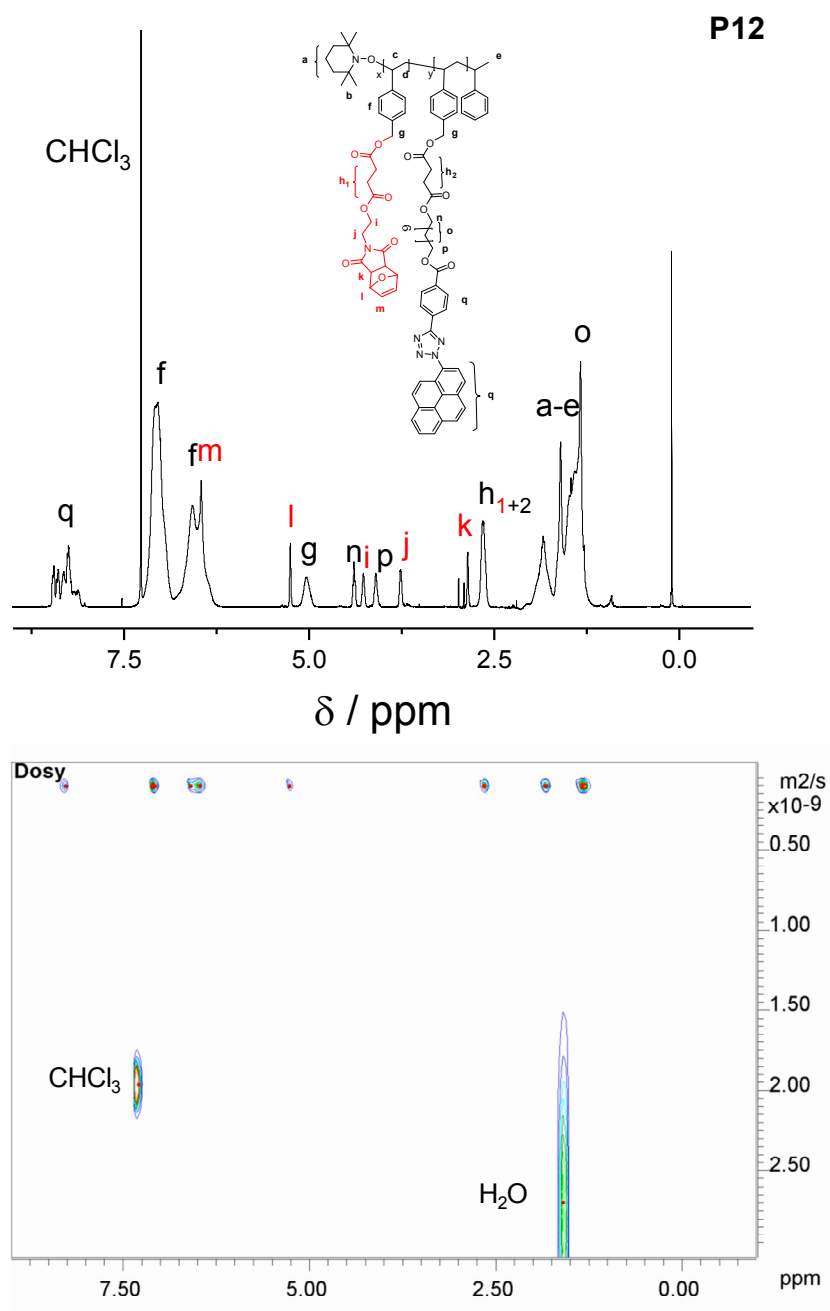


Figure 6.1.42: Combined ¹H NMR and DOSY spectrum of **P12**, showing the diffusion coefficients corresponding to the resonances in the polymer. Adapted with permission from reference [225] with permission from The Royal Society of Chemistry (RSC).²²⁵

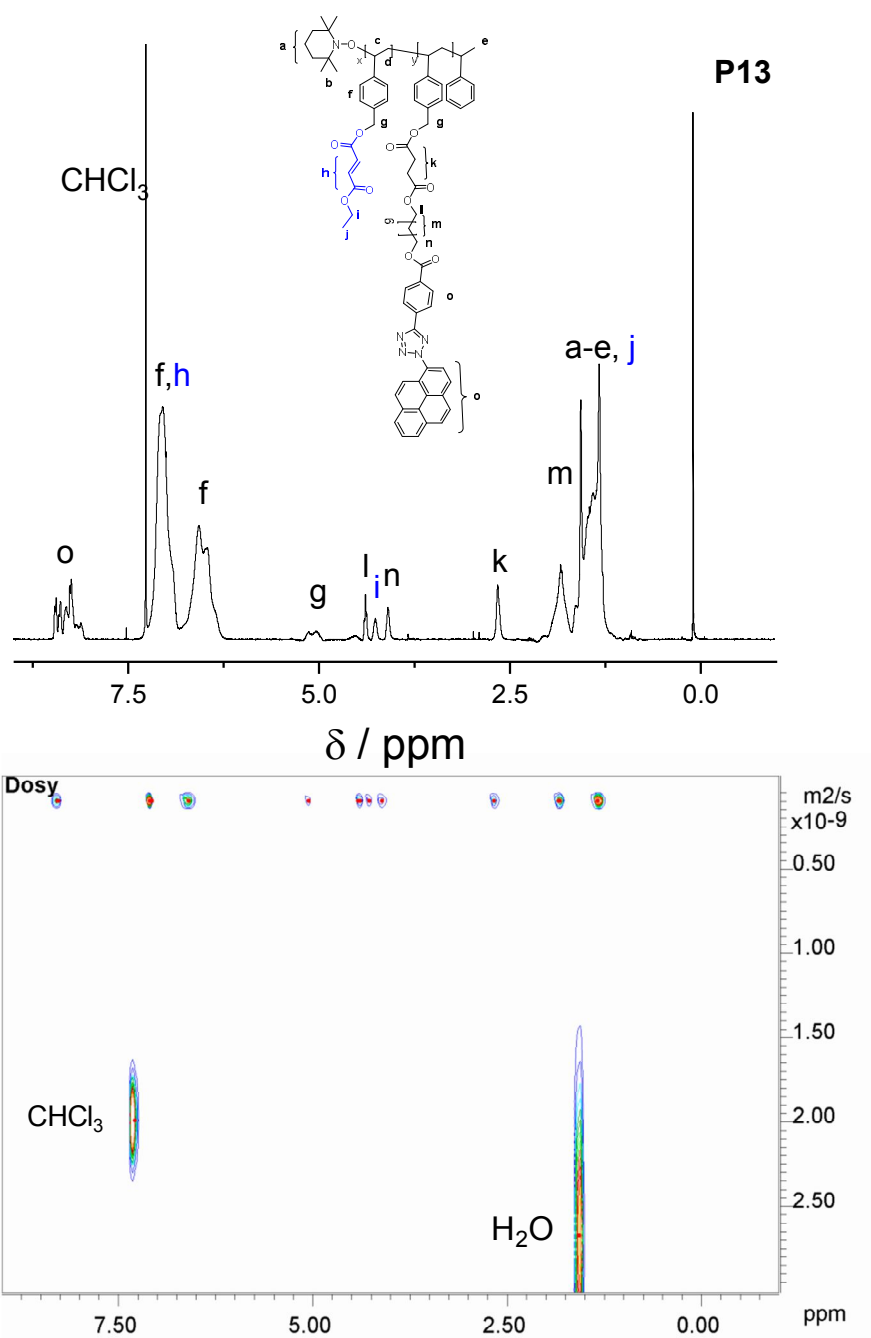


Figure 6.1.43: Combined ^1H NMR and DOSY spectrum of **P13**, showing the diffusion coefficients corresponding to the resonances in the polymer. Adapted with permission from reference [225] with permission from The Royal Society of Chemistry (RSC).²²⁵

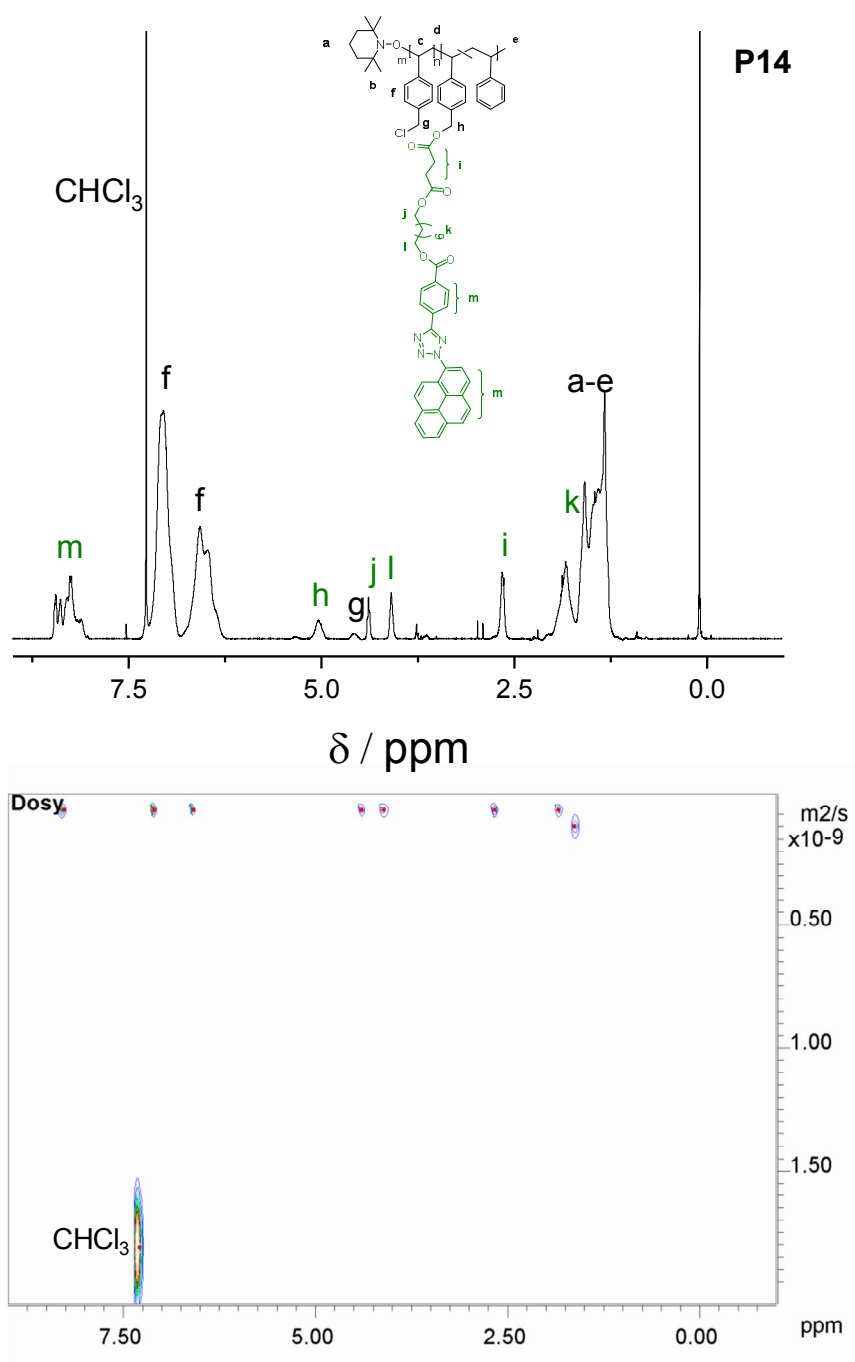


Figure 6.1.44: Combined ^1H NMR and DOSY spectrum of **P14**, showing the diffusion coefficients corresponding to the resonances in the polymer. Adapted with permission from reference [225] with permission from The Royal Society of Chemistry (RSC).²²⁵

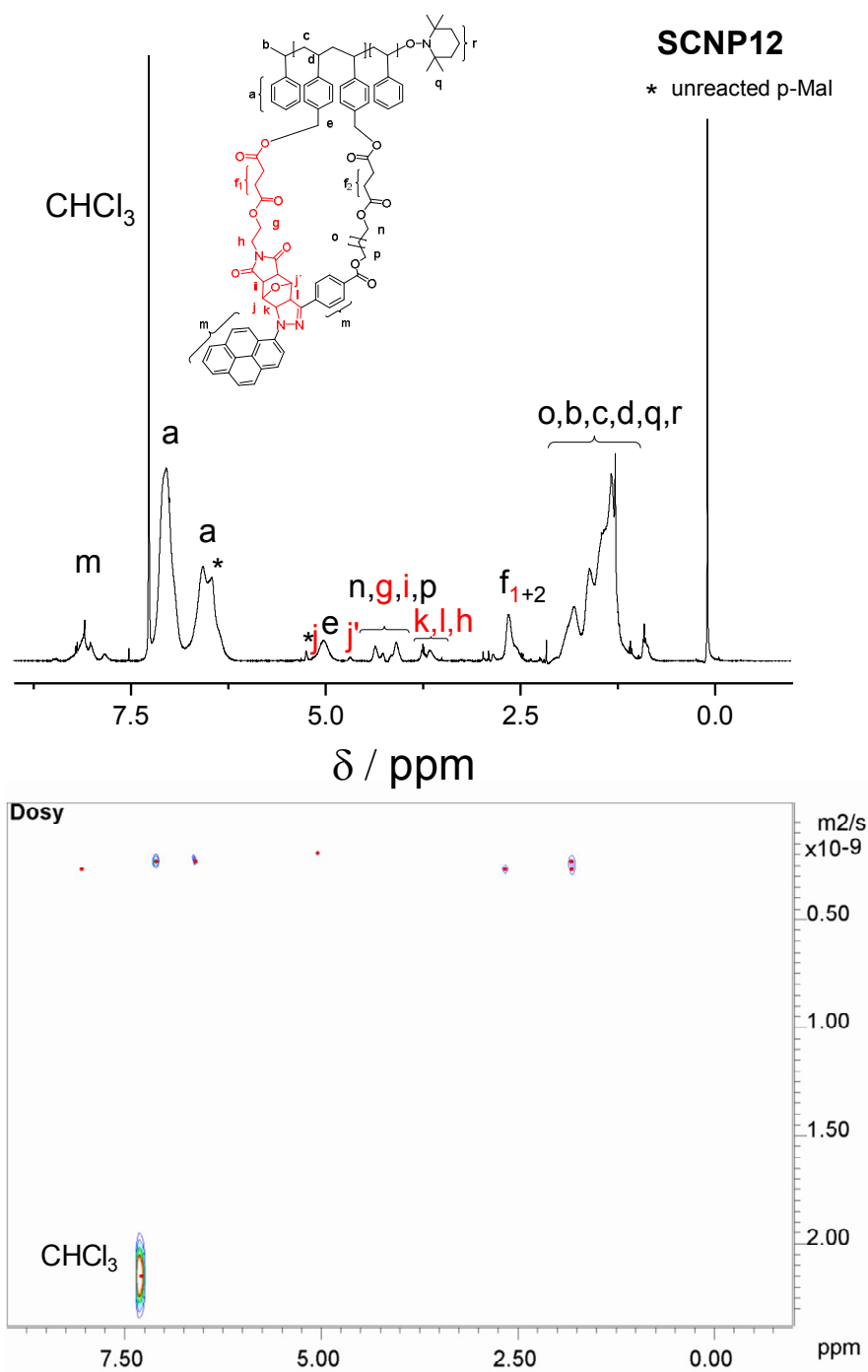


Figure 6.1.45: Combined ^1H NMR and DOSY spectrum of **SCNP12**, showing the diffusion coefficients corresponding to the resonances in the polymer. Adapted with permission from reference [225] with permission from The Royal Society of Chemistry (RSC).²²⁵

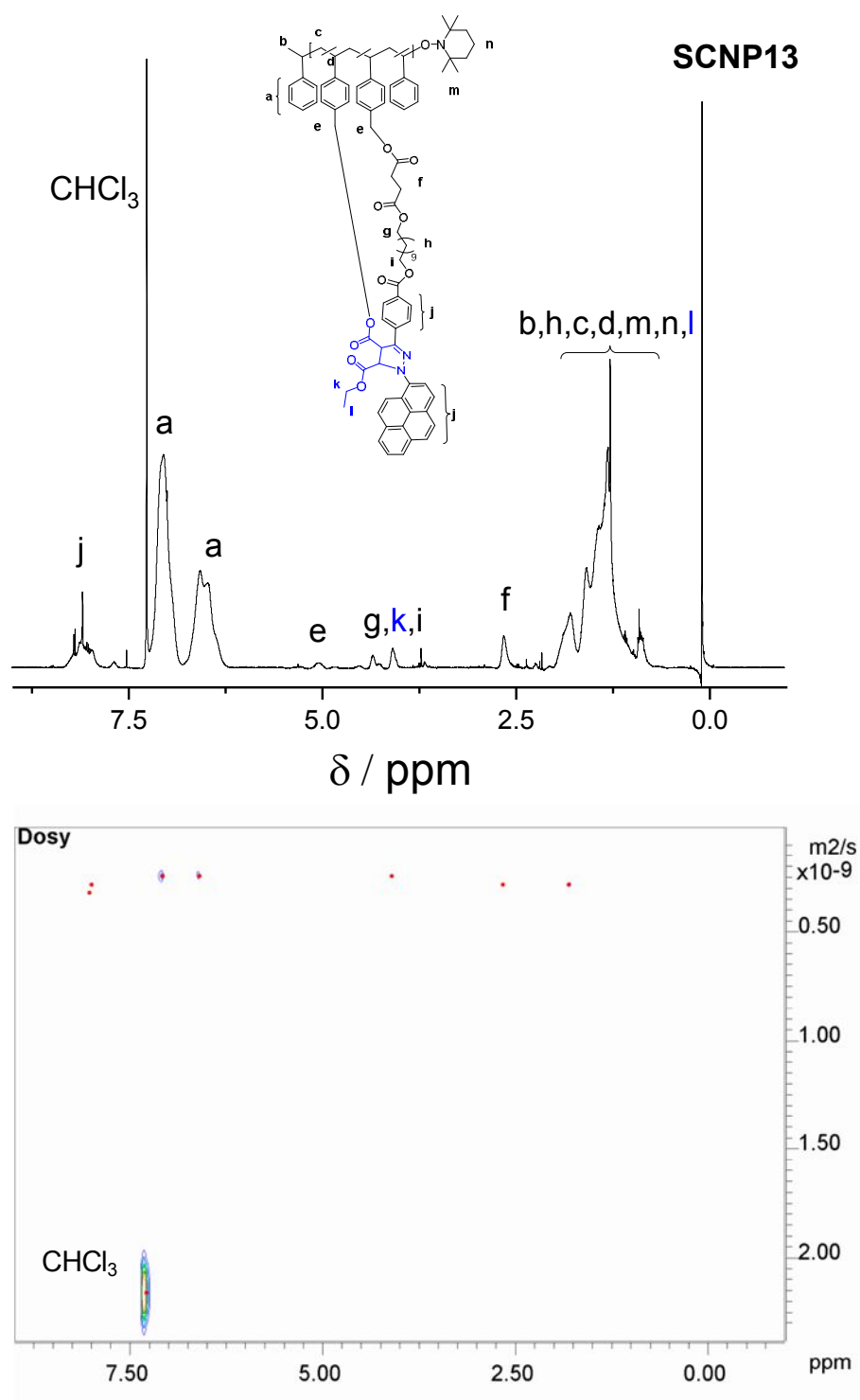


Figure 6.1.46: Combined ^1H NMR and DOSY spectrum of **SCNP13**, showing the diffusion coefficients corresponding to the resonances in the polymer. Adapted with permission from reference [225] with permission from The Royal Society of Chemistry (RSC).²²⁵

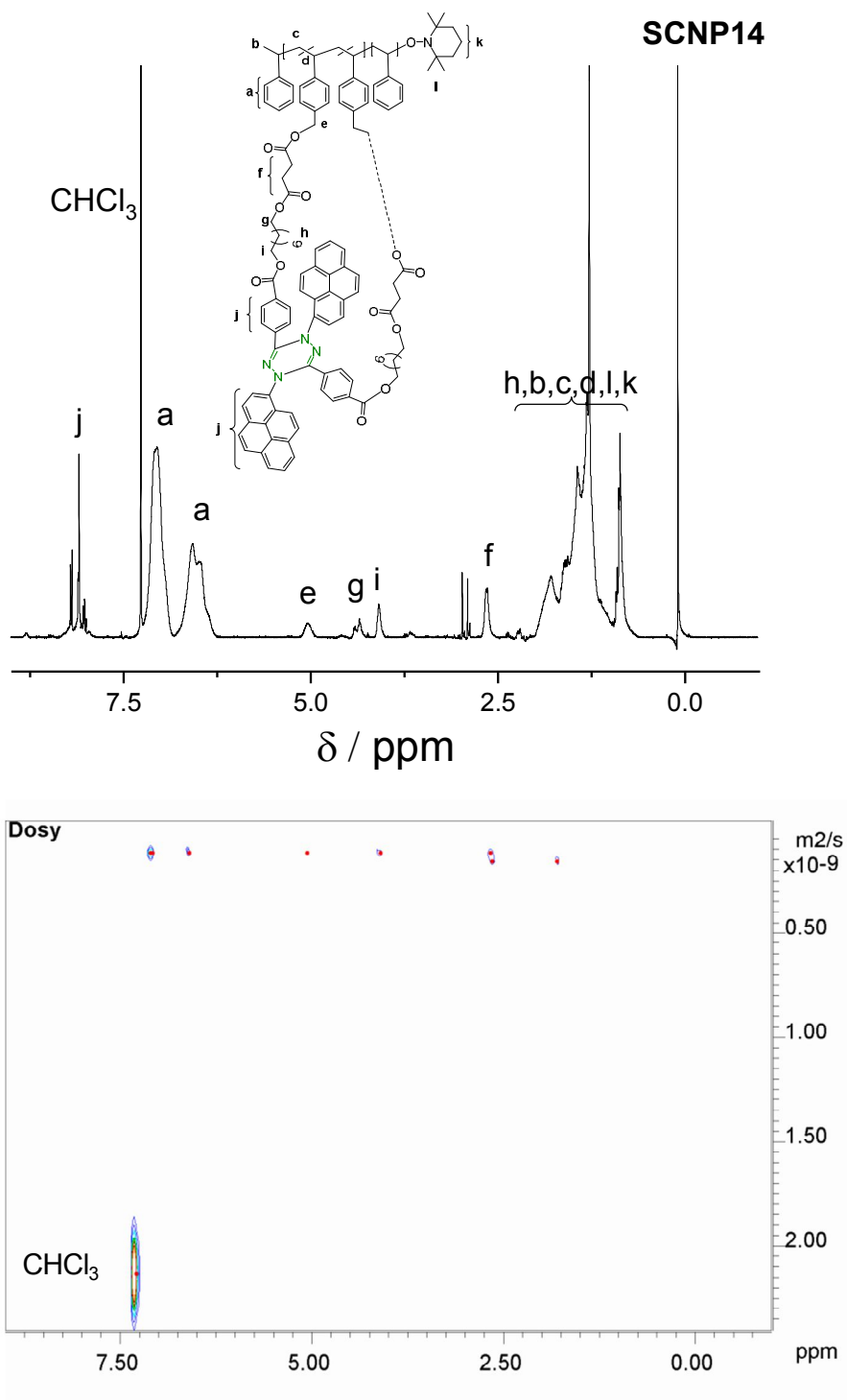


Figure 6.1.47: Combined ^1H NMR and DOSY spectrum of **SCNP14**, showing the diffusion coefficients corresponding to the resonances in the polymer. Adapted with permission from reference [225] with permission from The Royal Society of Chemistry (RSC).²²⁵

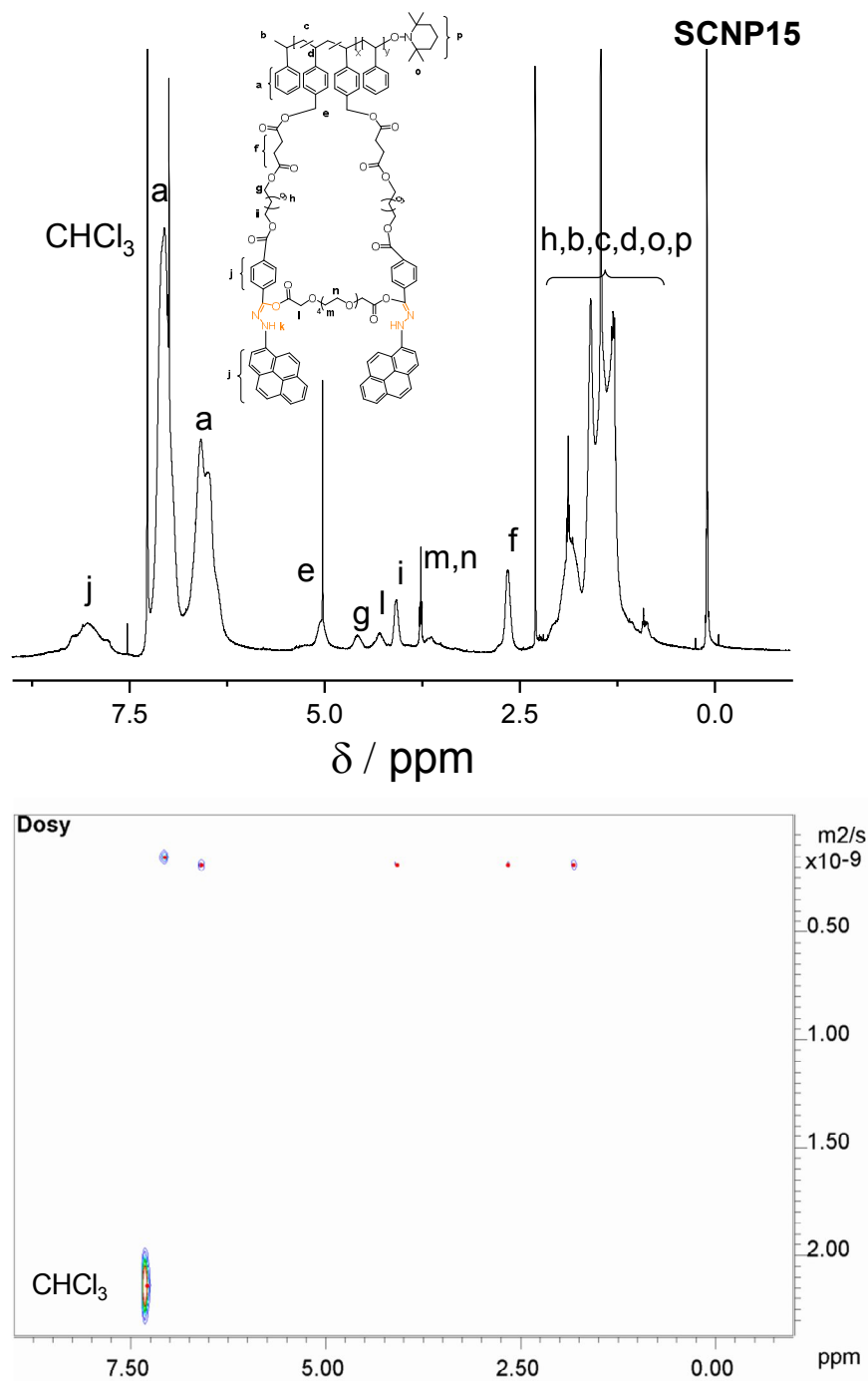


Figure 6.1.48: Combined ^1H NMR and DOSY spectrum of **SCNP15**, showing the diffusion coefficients corresponding to the resonances in the polymer. Adapted with permission from reference [225] with permission from The Royal Society of Chemistry (RSC).²²⁵



Figure 6.1.49: Set-up of the UV-induced formation of the SCNPs employing the Arimed B6 UV-lamp. Adapted with permission from reference [224]. Copyright (2015) American Chemical Society (ACS).²²⁴

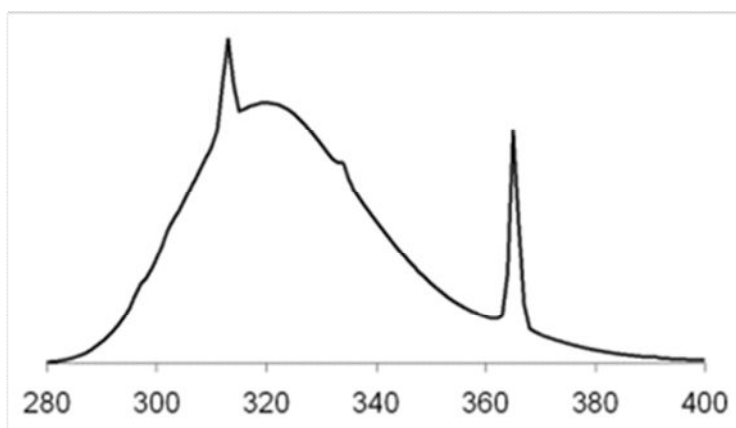


Figure 6.1.50: Emission spectrum of the Arimed B6 UV-lamp with an emission maximum at 320 nm. Adapted with permission from reference [224]. Copyright (2015) American Chemical Society (ACS).²²⁴

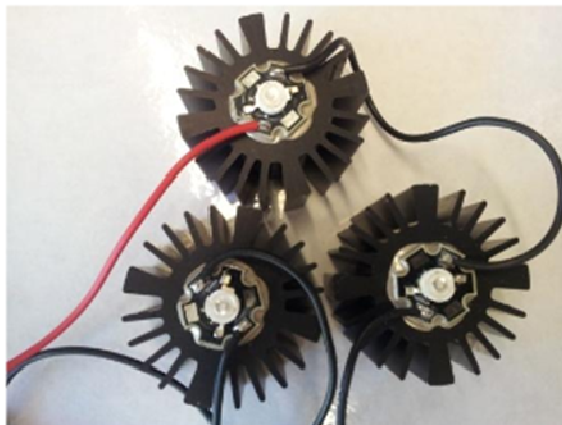


Figure 6.1.51: Avonec LEDs employed for the visible light SCNP formation. Adapted with permission from reference [225] with permission from The Royal Society of Chemistry (RSC).²²⁵

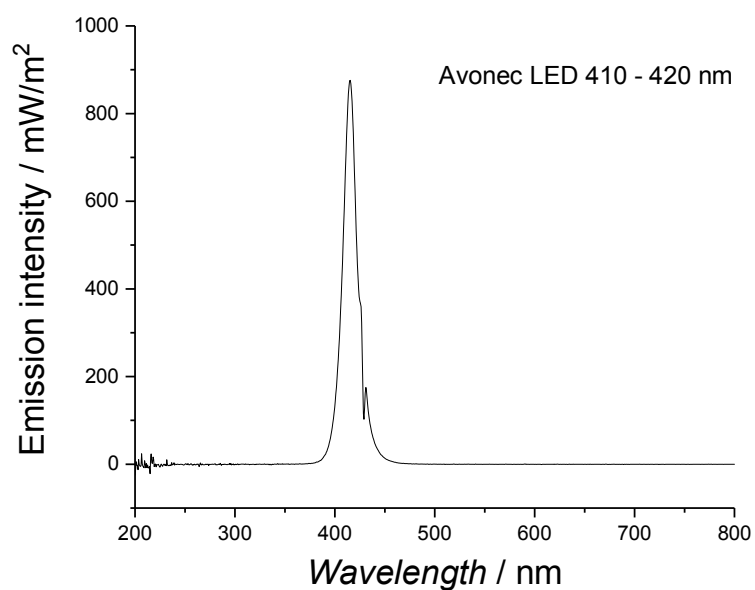


Figure 6.1.52: Emission of the Avonec LED lamps with an emission maximum at 410-420 nm. Adapted with permission from reference [225] with permission from The Royal Society of Chemistry (RSC).²²⁵

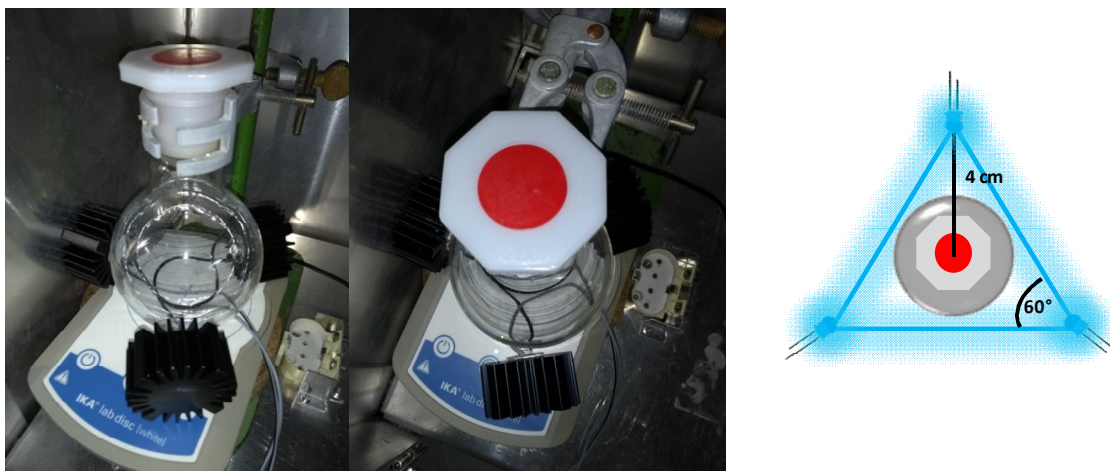


Figure 6.1.53: Arrangement of the LED setup with a frontal and an aerial view. Right: Geometry of the LED setup with the determined angle of 60° for the photochemical reactions. Adapted with permission from reference [225] with permission from The Royal Society of Chemistry (RSC).²²⁵

Abbreviations

ACS	american chemical society
AFM	atomic force microscopy
AIBN	2,2-azoisobutyronitrile
ATRP	atom transfer radical polymerization
bipy	2,2-bipyridine
BPLED	bipolar longitudinal Eddy-current delay
BPO	benzoyl peroxide
BTA	1,3,5-tricarboxamide-based amine
CMS	chloromethylstyrene
CONTIN	constrained regularization
COSY	correlation spectroscopy
CRP	controlled radical polymerization
CSIRO	commonwealth scientific and industrial research organization
CTA	chain transfer agent
CuAAC	copper catalyzed alkyne azide cycloaddition
\bar{D}	polydispersity
DA	Diels-Alder
DCM	dichloromethane
D_h	hydrodynamic diameter
DLS	dynamic light scattering
DMAA	<i>N,N</i> -dimethylacryl amide
DMAc	dimethylacetamide
DMF	dimethylformamide
DNA	deoxyribonucleic acid
DNA	desoxyribonucleic acid
DoPAT	2-(((dodecylthio)carbonothioyl)thio) propanoate
DOSY	diffusion ordered spectroscopy

dpf	days post fertilized
DTT	dithiothreitol
ESI-MS	electrospray ionization mass spectrometry
Et ₃ N	triethylamine
EtOH	ethanol
F	fluorescence
FRP	free radical polymerization
fum	fumarate
HDA	hetero Diels-Alder
HOMO	highest occupied molecule orbital
IC	internal conversion
ISC	intersystem crossing
kDa	kilodalton
LED	longitudinal Eddy-current delay
LUMO	lowest unoccupied molecule orbital
MADIX	macromolecular design <i>via</i> the Interchange of xanthates
MALS	multi angle light scattering
M_{app}	apparent molecular weight
MeCN	acetonitrile
MeOH	methanol
M_n	number average molecular weight
MWD	molecular weight distribution
NICAL	nitrile imine carboxylic acid ligation
NITEC	nitrile imine tetrazole-ene cycloaddition
NMP	nitroxide mediated polymerization
NMR	nuclear magnetic resonance spectroscopy
NNLS	non-negative non-linear least-squares
P	phosphorescence
PAA	poly (acrylic acid)

PAT	pyrene aryl tetrazole
PCSY	photon correlation spectroscopy
PEG	poly (ethylene glycol)
PEGA	poly (ethylene glycol acrylate)
peptoid	pep
PFG	pulsed field gradient
p-Mal	protected maleimide
PS	poly (styrene)
RAFT	reversible addition fragmentation chain transfer
RCM	ring closing metathesis
RDRP	reversible deactivation radical polymerization
ROMP	ring opening polymerization
RSC	royal society of chemistry
SCNP	single chain polymer nanoparticle
SEC	size exclusion chromatography
SG1	4-(diethoxyphosphinyl)-2,2,5,5-tetramethyl-3-azahexane- <i>N</i> -oxy
STE	stimulated echo
TAD	triazolinedione
TEG	tetra ethylene glycol
TEM	transmission electron microscopy
TEMPO	2,2,6,6-tetramethylpiperidinyloxy
Tet	tetrazole
THF	tetrahydrofuran
TIPNO	2,2,5-trimethyl-4-phenyl-3-azahexane- <i>N</i> -oxyl
VR	vibrational relaxation

Acknowledgements

Zu Beginn möchte ich mich bei meinem Doktorvater Prof. Dr. Barner-Kowollik bedanken, der mir die Promotion in seinem Arbeitskreis ermöglichte. Vor allem möchte ich mich für mein spannendes Forschungsthema und für die stetige wissenschaftliche Unterstützung bedanken. Der unermüdliche Enthusiasmus und die positive Einstellung schaffte eine positive Arbeitsatmosphäre, die einen immer wieder aufs Neue motivieren konnte. Vor allem möchte ich mich noch dafür bedanken, dass ich die Gelegenheit hatte 3 Monate in Australien zu verbringen, um dort weiter an meinem Projekt zuarbeiten.

I am very grateful for Dr. Eva Blasco for all your support during my PhD thesis. I want to thank you for all the hours that we spent together in the NMR, sitting together creating new ideas, for research discussions and for the correction of my doctor thesis. I really appreciated to work with you and i wish you all the best for your future.

Außerdem möchte ich meinen großen Dank an Dr. Maria Schneider, Dr. Anja Goldmann, Evelyn Stühling, Vincent Schüler und Katharina Elies aussprechen, die mit ihrer Arbeit die Forschung vieler Doktoranden erleichtern und tatkräftig unterstützen.

Desweiteren möchte ich mich für meine Finanzierung über das Graduiertenprogramm 2039 bedanken, die mir meinen Auslandsaufenthalt ermöglichten. Im Zusammenhang mit dem Graduiertenprogramm möchte ich mich bei meinen Kooperationspartnern Ilona Wehl und Stefan Münch für die gute Zusammenarbeit bedanken.

I want to thank the Westies (Kai, Tanja C., Rouven, Marcel, Tanja R. Christiane L., Alexander S.) for the nice working atmosphere and i want especially thank Paul Lederhose and Markus Zieger for the research discussions and the really great time we had. Many thanks also to the AC team for the really nice working atmosphere, i really appreciated it to work with you!

Furthermore, i want to thank all the current and former group members in the macroarc group for all the doctor waggon sessions, girl's evenings, barbeques, group trips and all other activities we had.

I also want to thank all the people, who corrected my doctor thesis with Hannah Rothfuß, Waldemar Konrad, Dr. Charlotte Petit, Dr. Anja Goldmann, Jan Steinkönig, Matthias Eing, Dr. Eva Blasco, Dr. Paul Lederhose and Andrea Lauer.

Special thanks to Andrea Lauer for the amazing time we had together in Australia and Boulder, driving either a Campervan or a Mustang GT!

Neben der Arbeitsgruppe möchte ich mich auch bei meinen drei Mädels (Andrea Lauer, Franziska Wolff und Bettina Olshausen) für die super Zeit in New York und den vielen anderen Abenteuern, die wir zusammen erleben durften, bedanken.

Vor allem möchte ich mich bei meiner Familie bedanken, die mich immer unterstützt und ermutigt hat diesen Weg zu gehen und immer für mich da war. Leider kann mein Vater meinen akademischen Werdegang nicht mehr erleben, aber er wäre sicher sehr stolz gewesen seine Tochter promovieren zu sehen.

Mein größter Dank gilt Richard Beyle, für deine unermüdliche Geduld, deine motivierenden Worte und noch viel mehr was sich nicht im Rahmen dieser Arbeit ausdrücken könnte. Ich freue mich sehr auf unsere gemeinsame Zukunft!

Bibliography

- (1) Li, Z.; Qian, L.; Li, L.; Bernhammer, J. C.; Huynh, H. V.; Lee, J.-S.; Yao, S. Q. *Angew. Chem. Int. Ed. Engl.* **2016**, *55*, 2002.
- (2) Goethe, W. J. von. *Die Leiden des jungen Werthers*; 1774.
- (3) Darmanin, T.; Guittard, F. *Mater. Today* **2015**, *18*, 273.
- (4) Labeit, S.; Kolmerer, B. *Science (80-.)*. **1995**, *270*, 293.
- (5) Merrifield, R. B. *J. Am. Chem. Soc.* **1963**, *85*, 2149.
- (6) Willenbacher, Johannes, Wuest N.R. Kilian, Mueller O. Jan, K. M.; Wagenknecht, H.; Barner-Kowollik, C. *ACS Macro Lett.* **2014**, *3*, 574.
- (7) Benito, A. B.; Aiertza, M. K.; Marradi, M.; Gil-Iceta, L.; Shekhter Zahavi, T.; Szczupak, B.; Jiménez-González, M.; Reese, T.; Scanziani, E.; Passoni, L.; Matteoli, M.; De Maglie, M.; Orenstein, A.; Oron-Herman, M.; Kostenich, G.; Buzhansky, L.; Gazit, E.; Grande, H.-J.; Gómez-Vallejo, V.; Llop, J.; Loinaz, I. *Biomacromolecules* **2016**, *17*, 3213.
- (8) Cheng, C.-C.; Lee, D.-J.; Liao, Z.-S.; Huang, J.-J. *Polym. Chem.* **2016**, *7*, 6164.
- (9) Perez-Baena, I.; Barroso-Bujans, F.; Gasser, U.; Arbe, A.; Moreno, A. J.; Colmenero, J.; Pomposo, J. A. *ACS Macro Lett.* **2013**, *2*, 775.
- (10) Sanchez-sanchez, A.; Arbe, A.; Kohlbrecher, J.; Colmenero, J.; Pomposo, J. A. *Macromol. Rapid Commun.* **2015**, *36*, 1592.
- (11) Sanchez-Sanchez, A.; Arbe, A.; Colmenero, J.; Pomposo, J. A. *ACS Macro Lett.* **2014**, *3*, 439.
- (12) Rubio-Cervilla, J.; González, E.; Pomposo, J. *Nanomaterials* **2017**, *7*, 341.
- (13) Terashima, T.; Mes, T.; Greef, T. F. A. De; Gillissen, M. A. J.; Besenius, P.; Palmans, A. R. A.; Meijer, E. W. **2011**, *133*, 4742.
- (14) Lim, R. K. V.; Lin, Q. *Chem. Commun. (Camb)*. **2010**, *46*, 1589.
- (15) Roh, J.; Vávrová, K.; Hrabálek, A. *European J. Org. Chem.* **2012**, 6101.
- (16) Nesvadba, P. In *Encyclopedia of Radicals in Chemistry, Biology and Materials*; 2012; pp. 1–36.
- (17) Davis, T. P.; Matyjaszewski, K. *Handbook of Radical Polymerization*; 2002.
- (18) Allen, P.; Patrick, C. *Die Makromol. Chemie* **1961**, *47*, 154.
- (19) Junkers, T.; Schneider-Baumann, M.; Koo, S. S. P.; Castignolles, P.; Barner-Kowollik, C. *Macromolecules* **2010**, *43*, 10427.
- (20) Haehnel, A. P.; Schneider-Baumann, M.; Arens, L.; Misske, A. M.; Fleischhaker, F.; Barner-Kowollik, C. *Macromolecules* **2014**, *47*, 3483.
- (21) Krstina, J.; Moad, G.; Rizzardo, E.; Winzor, C. L.; Berge, C. T.; Fryd, M.

- Macromolecules* **1995**, *28*, 5381.
- (22) Lutz, J. F.; Matyjaszewski, K. *J. Polym. Sci. Part A Polym. Chem.* **2005**, *43*, 897.
- (23) Colombani, D. *Prog. Polym. Sci.* **1997**, *22*, 1649.
- (24) Trommsdorff, E. V.; Kohle, H.; Lagally P. *Macromol. Chem. Phys.* **1947**, *1*, 169.
- (25) Matyjaszewski, K.; Spanswick, J. *Mater. Today* **2005**, *8*, 26.
- (26) Matyjaszewski, K. *ACS Symp. Ser.* **2012**, *1100*, 1.
- (27) Matyjaszewski, K. *Am. Chem. Soc.* **2000**, *768*, 2.
- (28) Barner-Kowollik, C.; Davis, T. P.; Heuts, J. P. A.; Stenzel, M. H.; Vana, P.; Whittaker, M. *highlight* **2003**, *41*, 365.
- (29) Wang, J. S.; Matyjaszewski, K. *J. Am. Chem. Soc.* **1995**, *117*, 5614.
- (30) Kato, M.; Kamigaito, M.; Sawamoto, M.; Higashimura, T. *Macromolecules* **1995**, *28*, 1721.
- (31) Jasinski, N.; Lauer, A.; Stals, P. J. M.; Behrens, S.; Essig, S.; Walther, A.; Goldmann, A. S.; Barner-Kowollik, C. *ACS Macro Lett.* **2015**, *4*, 298.
- (32) Hawker, C. J.; Bosman, A. W.; Harth, E. *Chem. Rev.* **2001**, *101*, 3661.
- (33) Grubbs, R. B. *Polym. Rev.* **2011**, *51*, 104.
- (34) Nicolas, J.; Guillaneuf, Y.; Lefay, C.; Bertin, D.; Gigmes, D.; Charleux, B. *Prog. Polym. Sci.* **2013**, *38*, 63.
- (35) Chiefari, J.; Chong, Y. K. B.; Ercole, F.; Krstina, J.; Jeffery, J.; Le, T. P. T.; Mayadunne, R. T. A.; Meijs, G. F.; Moad, C. L.; Moad, G.; Rizzardo, E.; Thang, S. H.; South, C. **1998**, *9297*, 5559.
- (36) Perrier, S.; Takolpuckdee, P. *J. Polym. Sci. Part A Polym. Chem.* **2005**, *43*, 5347.
- (37) Barner-Kowollik, C.; Blinco, J. P.; Destarac, M.; Thurecht, K. J.; Perrier, S. In *Encyclopedia of Radicals in Chemistry, Biology and Materials*; 2012; pp. 1895–1930.
- (38) Barner-Kowollik, C.; Buback, M.; Charleux, B.; Coote, M. L.; Drache, M.; Fukuda, T.; Goto, A.; Klumperman, B.; Lowe, A. B.; Mccleary, J. B.; Moad, G.; Monteiro, M. J.; Sanderson, R. D.; Tonge, M. P.; Vana, P.; Marie, P. *J. Polym. Sci. Part A Polym. Chem.* **2006**, *44*, 5809.
- (39) Keddie, D. J.; Moad, G.; Rizzardo, E.; Thang, S. H. *Macromolecules* **2012**, *45*, 5321.
- (40) Keddie, D. J. *Chem. Soc. Rev.* **2014**, *43*, 496.
- (41) Destarac, M. *Polym. Rev.* **2011**, *51*, 163.
- (42) Barner-Kowollik, C. *Handbook of RAFT Polymerization*; Barner-Kowollik, C., Ed.; Wiley-VCH Verlag GmbH & Co. KGaA: Weinheim, Germany, 2008.
- (43) Roth, P. J.; Wiss, K. T.; Zentel, R.; Theato, P. *Macromolecules* **2008**, *41*, 8513.

- (44) Gondj, S. R.; Vogt, A. P.; Sumerlin, B. S. *Macromolecules* **2007**, *40*, 474.
- (45) Barner, L.; Zwaneveld, N.; Perera, S.; Pham, Y.; Davis, T. P. *J. Polym. Sci. Part A Polym. Chem.* **2002**, *40*, 4180.
- (46) Barner, L.; Barner-Kowollik, C.; Davis, T. P.; Stenzel, M. H. *Aust. J. Chem.* **2004**, *57*, 19.
- (47) Gaetke, L. M.; Chow-Johnson, H. S.; Chow, C. K. *Arch. Toxicol.* **2014**, *88*, 1929.
- (48) Anderson, N. A.; Shiang, J. J.; Sension, R. J. *J. Phys. Chem. A* **1999**, *103*, 10730.
- (49) Glusac, K. *Nat. Chem.* **2016**, *8*, 734.
- (50) Govindjee. In *Photosynthesis research*; 2006; Vol. 20, pp. 235–239.
- (51) Chatani, S.; Kloxin, C. J.; Bowman, C. N. *Polym. Chem.* **2014**, *5*, 2187.
- (52) Bouguer, P. *Essai d'optique, Sur la gradation la lumière. Claude Jombert, Paris* **1729**, 164.
- (53) Hesse Manfred, Meier Herbert, Z. B. *Spektroskopische Methoden in der org. Chemie*; 2005.
- (54) Beer, A. *Ann. der Phys. und Chemie.* **1852**, *162*, 78.
- (55) Kasha, M. *Discuss. Faraday Soc.* **1950**, *9*, 14.
- (56) Laporte, O.; Meggers, W. F. *J. Opt. Soc. Am.* **1925**, *11*, 459.
- (57) Koziar, J. C.; Cowan, D. O. *Acc. Chem. Res.* **1978**, *11*, 334.
- (58) Wöhrle, D.; Tausch, W. M.; Stohrer, W.-D. *Photochemie*; 1998.
- (59) Michaudel, Q.; Kottisch, V.; Fors, B. P. *Angew. Chemie - Int. Ed.* **2017**, *56*, 9670.
- (60) Posner, T. *Beitrage zur Kenntniss der ungesaettigten Verbindungen. Ueber die Addit. von Mercaptanen an ungesaettigte Kohlenwasserstoffe.* **1905**, *38*, 2649.
- (61) Yagci, Y. *Macromol. Symp.* **2000**, *35*, 19.
- (62) Decker, C. *Polym. Int.* **1998**, *45*, 133.
- (63) Cramer, N. B.; Bowman, C. N. *J. Polym. Sci. Part A Polym. Chem.* **2001**, *39*, 3311.
- (64) Hoyle, C. E.; Lowe, A. B.; Bowman, C. N. *Chem. Soc. Rev.* **2010**, *39*, 1355.
- (65) Lowe, A. B. *Polym. Chem.* **2010**, *1*, 17.
- (66) Stenzel, M. H. *ACS Macro Lett.* **2013**, *2*, 14.
- (67) Kharasch, M., Nudenberg, W., Mantell, G. J. *J. Org. Chem.* **1951**, *16*, 524.
- (68) Cramer, N. B.; Scott, J. P.; Bowman, C. N. *Macromolecules* **2002**, *35*, 5361.
- (69) Blasco, E.; Wegener, M.; Barner-Kowollik, C. *Adv. Mater.* **2017**, *29*, 1604005.
- (70) Justynska, J.; Hordyjewicz, Z.; Schlaad, H. *Polymer (Guildf).* **2005**, *46*, 12057.

- (71) Koňák, Č.; Šubr, V.; Kostka, L.; Štěpánek, P.; Ulbrich, K.; Schlaad, H. *Langmuir* **2008**, *24*, 7092.
- (72) Brummelhuis, N. Ten; Diehl, C.; Schlaad, H. *Macromolecules* **2008**, *41*, 9946.
- (73) Batchelor, R. R.; Blasco, E.; Wuest, K. N. R.; Lu, H.; Wegener, M.; Barner-Kowollik, C.; Stenzel, M. H. *Chem. Commun.* **2018**, *54*, 2436.
- (74) Blasco, E.; Yameen, B.; Quick, A. S.; Krolla-Sidenstein, P.; Welle, A.; Wegener, M.; Barner-Kowollik, C. *Macromolecules* **2015**, *48*, 8718.
- (75) Hagberg, E. C.; Malkoch, M.; Ling, Y.; Hawker, C. J.; Carter, K. R. *Nano Lett.* **2007**, *7*, 233.
- (76) Gong, X.; Wen, W.; Sheng, P. *Langmuir* **2009**, *25*, 7072.
- (77) Lovelady, E.; Kimmins, S. D.; Wu, J.; Cameron, N. R. *Polym. Chem.* **2011**, *2*, 559.
- (78) Hoyle, C. E.; Bowman, C. N. *Angew. Chemie - Int. Ed.* **2010**, *49*, 1540.
- (79) Kade J.M., Burke D., H. J. C. *Polym. Chem.* **2010**, *48*, 511.
- (80) Xi, W.; Peng, H.; Aguirre-Soto, A.; Kloxin, C. J.; Stansbury, J. W.; Bowman, C. N. *Macromolecules* **2014**, *47*, 6159.
- (81) Nakayama, Y.; Matsuda, T. *J. Polym. Sci. Part A Polym. Chem.* **1992**, *30*, 2451.
- (82) He, J.; Tremblay, L.; Zhao, Y. *Soft Matter* **2011**, *7*, 2380.
- (83) Zheng, Y.; Micic, M.; Mello, S. V.; Mabrouki, M.; Andreopoulos, F. M.; Konka, V.; Pham, S. M.; Leblanc, R. M. *Macromolecules* **2002**, *35*, 5228.
- (84) Chujo, Y.; Sada, K.; Saegusa, T. *Macromolecules* **1990**, *23*, 2693.
- (85) Claus, T. K.; Telitel, S.; Welle, A.; Bastmeyer, M.; Vogt, A. P.; Delaittre, G.; Barner-Kowollik, C. *Chem. Commun.* **2017**, *53*, 1599.
- (86) Junkers, T. *Eur. Polym. J.* **2015**, *62*, 273.
- (87) Diels, O.; Alder, K. *Leibigs Ann. Chem.* **1928**, *460*, 98.
- (88) Tasdelen, M. A. *Polym. Chem.* **2011**, *2*, 2133.
- (89) Sun, D.; Hubig, S. M.; Kochi, J. K. *J. Photochem. Photobiol.* **1999**, *122*, 87.
- (90) Pandey, B. ;; Dalvi V. Pramod. *Angew. Chem.* **1993**, *105*, 1724.
- (91) Delaittre, G.; Goldmann, A. S.; Mueller, J. O.; Barner-Kowollik, C. *Angew. Chemie - Int. Ed.* **2015**, *54*, 11388.
- (92) Glassner, M.; Oehlenschlaeger, K. K.; Welle, A.; Bruns, M.; Barner-Kowollik, C. *Chem. Commun.* **2013**, *49*, 633.
- (93) Gruending, T.; Oehlenschlaeger, K. K.; Frick, E.; Glassner, M.; Schmid, C.; Barner-Kowollik, C. *Macromol. Rapid Commun.* **2011**, *32*, 807.
- (94) Konrad, W.; Bloesser, F. R.; Wetzel, K. S.; Boukis, A. C.; Meier, M. A. R.; Barner-Kowollik, C. *Chem. - A Eur. J.* **2018**, *24*, 3413.
- (95) Winkler, M.; Mueller, J. O.; Oehlenschlaeger, K. K.; Montero De Espinosa, L.;

- Meier, M. A. R.; Barner-Kowollik, C. *Macromolecules* **2012**, *45*, 5012.
- (96) Oehlenschlaeger, K. K.; Mueller, J. O.; Heine, N. B.; Glassner, M.; Guimard, N. K.; Delaittre, G.; Schmidt, F. G.; Barner-Kowollik, C. *Angew. Chemie - Int. Ed.* **2013**, *52*, 762.
- (97) Quick, A. S.; Rothfuss, H.; Welle, A.; Richter, B.; Fischer, J.; Wegener, M.; Barner-Kowollik, C. *Adv. Funct. Mater.* **2014**, *24*, 3571.
- (98) Porter, G.; Tchir, M. F. *J. Chem. Soc. D Chem. Commun.* **1970**, *6*, 1372.
- (99) Kerbs, A.; Mueller, P.; Kaupp, M.; Ahmed, I.; Quick, A. S.; Abt, D.; Wegener, M.; Niemeyer, C. M.; Barner-Kowollik, C.; Fruk, L. **2017**, 4990.
- (100) Hirschbiel, A. F.; Konrad, W.; Schulze-Suenninghausen, D.; Luy, B.; Schmidt, B. V. K. J.; Barner-Kowollik, C. **2015**, 5.
- (101) Mueller, P.; Zieger, M. M.; Richter, B.; Quick, A. S.; Fischer, J.; Mueller, J. B.; Zhou, L.; Nienhaus, G. U.; Bastmeyer, M.; Barner-Kowollik, C.; Wegener, M. *ACS Nano* **2017**, *11*, 6396.
- (102) Pauloehrl, T.; Welle, A.; Bruns, M.; Linkert, K.; Börner, H. G.; Bastmeyer, M.; Delaittre, G.; Barner-Kowollik, C. *Angew. Chemie - Int. Ed.* **2013**, *52*, 9714.
- (103) Hildebrandt, K.; Pauloehrl, T.; Blinco, J. P.; Linkert, K.; Boerner, H. G.; Barner-Kowollik, C. *Angew. Chem. Int. Ed. Engl.* **2015**, *54*, 2838.
- (104) Cookson, R. C.; Gilani, S. S. H.; Stevens, I. D. R. *Tetrahedron Lett.* **1962**, *1*, 615.
- (105) Stickler, J. C.; H., P. W. *Chem. Commun.* **1967**, *0*, 760.
- (106) Ban, H.; Gavriluk, J.; Barbas, C. F. *J. Am. Chem. Soc.* **2010**, *132*, 1523.
- (107) Seymour, C. A.; Greene, F. D. *J. Am. Chem. Soc.* **1980**, *102*, 6384.
- (108) De Bruycker, K.; Billiet, S.; Houck, H. A.; Chattopadhyay, S.; Winne, J. M.; Du Prez, F. E. *Chem. Rev.* **2016**, *116*, 3919.
- (109) Houck, A. H.; Prez, F. E. Du; Barner-Kowollik, C. *Nat. Commun.* **2017**, *8*, 1869.
- (110) Bladin, J. A. *Bericht der Dtsch. Chem. Gesellschaft* **1885**, *18*, 1544.
- (111) Song, W.; Wang, Y.; Qu, J.; Madden, M. M.; Lin, Q. *Angew. Chemie - Int. Ed.* **2008**, *47*, 2832.
- (112) Lim, R. K. V.; Lin, Q. *Sci. China Chem.* **2010**, *53*, 61.
- (113) G.I., K.; A.V., O. *Russ. Chem.Rev.* **1994**, *63*, 797.
- (114) Huisgen, R.; Weberndörfer, V. *Chem. Ber.* **1967**, *100*, 71.
- (115) Lesnikovich, A. I.; Levchik, S. V; Balabanovich, A. I.; Ivashkevich, O. A.; Gaponik, P. N. *Thermochim. Acta* **1992**, *200*, 427.
- (116) Blasco, E.; Sugawara, Y.; Lederhose, P.; Blinco, J. P.; Kelterer, A.-M.; Barner-Kowollik, C. *ChemPhotoChem* **2017**, *1*, 159.
- (117) Yu, Z.; Ho, L. Y.; Wang, Z.; Lin, Q. *Bioorganic Med. Chem. Lett.* **2011**, *21*, 5033.

- (118) Wang, Y.; Song, W.; Hu, W. J.; Lin, Q. *Angew. Chemie - Int. Ed.* **2009**, *48*, 5330.
- (119) Ajay Kumar, K.; Govindaraju, M.; Vasanth Kumar, G. *Int. J. Res. Pharm. Chem.* **2013**, *3*, 140.
- (120) Zheng, S. L.; Wang, Y.; Yu, Z.; Lin, Q.; Coppens, P. *J. Am. Chem. Soc.* **2009**, *131*, 18036.
- (121) Du, C. J.; Lederhose, P.; Hlalele, L.; Abt, D.; Kaiser, A.; Brandau, S.; Barner-Kowollik, C. *Macromolecules* **2013**, *46*, 5915.
- (122) Zhang, Y.; Liu, W.; Zhao, Z. K. *Molecules* **2013**, *19*, 306.
- (123) Li, Z.; Qian, L.; Li, L.; Bernhammer, J. C.; Huynh, H. V.; Lee, J.; Yao, S. Q. *Angew. Chemie Int. Ed.* **2016**, *55*, 2002.
- (124) Lederhose, P.; Wüst, K. N. R.; Barner-Kowollik, C.; Blinco, J. P. *Chem. Commun.* **2016**, *52*, 5928.
- (125) Wang, Y.; Hu, W. J.; Song, W.; Lim, R. K. V.; Lin, Q. *Org. Lett.* **2008**, *10*, 3725.
- (126) Mueller, J. O.; Voll, D.; Schmidt, F. G.; Delaittre, G.; Barner-Kowollik, C. *Chem. Commun.* **2014**, *50*, 15681.
- (127) Gegenhuber, T.; Abt, D.; Welle, A.; Özbek, S.; Goldmann, A. S.; Barner-Kowollik, C. *J. Mater. Chem. B* **2017**, *5*, 4993.
- (128) Wilke, P.; Abt, D.; Große, S.; Barner-Kowollik, C.; Börner, H. G. *J. Mater. Chem. A* **2017**, *5*, 16144.
- (129) Dietrich, M.; Delaittre, G.; Blinco, J. P.; Inglis, A. J.; Bruns, M.; Barner-Kowollik, C. *Adv. Funct. Mater.* **2012**, *22*, 304.
- (130) Blasco, E.; Piñol, M.; Oriol, L.; Schmidt, B. V. K. J.; Welle, A.; Trouillet, V.; Bruns, M.; Barner-Kowollik, C. *Adv. Funct. Mater.* **2013**, *23*, 4011.
- (131) Hufendiek, A.; Carlmark, A.; Meier, M. A. R.; Barner-Kowollik, C. *ACS Macro Lett.* **2016**, *5*, 139.
- (132) Offenloch, J. T.; Willenbacher, J.; Tzvetkova, P.; Heiler, C.; Barner-Kowollik, C. *Chem. Commun.* **2016**, *53*, 775.
- (133) Hildebrandt, K.; Kaupp, M.; Molle, E.; Menzel, J. P.; Blinco, J. P.; Barner-Kowollik, C. *Chem. Commun.* **2016**, *52*, 9426.
- (134) Lyon, C. K.; Prasher, A.; Hanlon, A. M.; Tuten, B. T.; Tooley, C. A.; Frank, P. G.; Berda, E. B. *Polym. Chem.* **2015**, *6*, 181.
- (135) Terashima, T.; Mes, T.; De Greef, T. F. A.; Gillissen, M. A. J.; Besenius, P.; Palmans, A. R. A.; Meijer, E. W. *J. Am. Chem. Soc.* **2011**, *133*, 4742.
- (136) Appel, E. A.; Barrio, J. Del; Dyson, J.; Isaacs, L.; Scherman, O. A. *Chem. Sci.* **2012**, *3*, 2278.
- (137) Oria, L.; Aguado, R.; Pomposo, J. a.; Colmenero, J. *Adv. Mater.* **2010**, *22*, 3038.
- (138) Chao, D.; Jia, X.; Tuten, B.; Wang, C.; Berda, E. B. *Chem. Commun. (Camb)*. **2013**, *49*, 4178.

- (139) Murray, B. S.; Fulton, D. A. *Macromolecules* **2011**, *44*, 7242.
- (140) Whitaker, D. E.; Mahon, C. S.; Fulton, D. A. *Angew. Chemie - Int. Ed.* **2013**, *52*, 956.
- (141) Sanchez-Sanchez, A.; Fulton, D. A.; Pomposo, J. A. *Chem. Commun. (Camb)*. **2014**, *50*, 1871.
- (142) Harth, E.; Van Horn, B.; Lee, V. Y.; Germack, D. S.; Gonzales, C. P.; Miller, R. D.; Hawker, C. J. *J. Am. Chem. Soc.* **2002**, *124*, 8653.
- (143) Altintas, O.; Willenbacher, J.; Wuest, K. N. R.; Oehlenschlaeger, K. K.; Krolla-Sidenstein, P.; Gliemann, H.; Barner-Kowollik, C. *Macromolecules* **2013**, *46*, 8092.
- (144) Croce, T. A.; Hamilton, S. K.; Chen, M. L.; Muchalski, H.; Harth, E. *Macromolecules* **2007**, *40*, 6028.
- (145) Sanchez-sanchez, A.; Pérez-baena, I.; Pomposo, J. A. *Molecules* **2013**, *18*, 3339.
- (146) De Luzuriaga, A. R.; Ormategui, N.; Grande, H. J.; Odriozola, I.; Pomposo, J. A.; Loinaz, I. *Macromol. Rapid Commun.* **2008**, *29*, 1156.
- (147) Perez-Baena, I.; Loinaz, I.; Padro, D.; García, I.; Grande, H. J.; Odriozola, I. *J. Mater. Chem.* **2010**, *20*, 6916.
- (148) Cengiz, H.; Aydogan, B.; Ates, S.; Acikalin, E.; Yagci, Y. *Des. Monomers Polym.* **2011**, *14*, 69.
- (149) Sanchez-Sanchez, A.; Asenjo-Sanz, I.; Buruaga, L.; Pomposo, J. A. *Macromol. Rapid Commun.* **2012**, *33*, 1262.
- (150) Bai, Y.; Xing, H.; Vincil, G. A.; Lee, J.; Henderson, E. J.; Lu, Y.; Lemcoff, N. G.; Zimmerman, S. C. *Chem. Sci.* **2014**, *5*, 2862.
- (151) Hanlon, A. M.; Lyon, C. K.; Berda, E. B. *Macromolecules* **2016**, *49*, 2.
- (152) Altintas, O.; Barner-Kowollik, C. *Macromol. Rapid Commun.* **2016**, *37*, 29.
- (153) Mavila, S.; Eivgi, O.; Berkovich, I.; Lemcoff, N. G. *Chem. Rev.* **2016**, *116*, 878.
- (154) Limacher, P. A.; Klopfer, W. *ChemPhysChem* **2017**, *18*, 3352.
- (155) Altintas, O.; Rudolph, T.; Barner-Kowollik, C. *J. Polym. Sci. Part A Polym. Chem.* **2011**, *49*, 2566.
- (156) Seo, M.; Beck, B. J.; Paulusse, J. M. J.; Hawker, C. J.; Kim, S. Y. *Macromolecules* **2008**, *41*, 6413.
- (157) Mes, T.; Van Der Weegen, R.; Palmans, A. R. A.; Meijer, E. W. *Angew. Chemie - Int. Ed.* **2011**, *50*, 5085.
- (158) Artar, M.; Terashima, T.; Sawamoto, M.; Meijer, E. W.; Palmans, A. R. A. *J. Polym. Sci. Part A Polym. Chem.* **2014**, *52*, 12.
- (159) Huerta, E.; Stals, P. J. M.; Meijer, E. W.; Palmans, A. R. A. *Angew. Chemie - Int. Ed.* **2013**, *52*, 2906.
- (160) Willenbacher, J.; Schmidt, B. V. K. J.; Schulze-Suenninghausen, D.; Altintas, O.; Luy, B.; Delaittre, G.; Barner-Kowollik, C. *Chem. Commun.* **2014**, *50*, 7056.

- (161) Appel, E. A.; Dyson, J.; Delbarrio, J.; Walsh, Z.; Scherman, O. A. *Angew. Chemie - Int. Ed.* **2012**, *51*, 4185.
- (162) Inoue, Y.; Kuad, P.; Okumura, Y.; Takashima, Y.; Yamaguchi, H.; Harada, A. *J. Am. Chem. Soc.* **2007**, *129*, 6396.
- (163) Morishima, Y.; Nomura, S.; Ikeda, T.; Seki, M.; Kamachi, M. *Macromolecules* **1995**, *28*, 2874.
- (164) Riddles, C. J.; Zhao, W.; Hu, H. J.; Chen, M.; Van De Mark, M. R. *Polym. (United Kingdom)* **2014**, *55*, 48.
- (165) Chen, M.; Jensen, S. P.; Hill, M. R.; Moore, G.; He, Z.; Sumerlin, B. S. *Chem. Commun.* **2015**, *51*, 9694.
- (166) Gillissen, M. A. J.; Voets, I. K.; Meijer, E. W.; Palmans, A. R. A. *Polym. Chem.* **2012**, *3*, 3166.
- (167) Lu, J.; Ten Brummelhuis, N.; Weck, M. *Chem. Commun.* **2014**, *50*, 6225.
- (168) Knöfel, N. D.; Rothfuss, H.; Willenbacher, J.; Barner-Kowollik, C.; Roesky, P. W. *Angew. Chemie - Int. Ed.* **2017**, *56*, 4950.
- (169) Willenbacher, J.; Altintas, O.; Trouillet, V.; Knöfel, N.; Monteiro, M. J.; Roesky, P. W.; Barner-Kowollik, C. *Polym. Chem.* **2015**, *6*, 4358.
- (170) Willenbacher, Johannes; Altintas, Ozcan; Roesky W. Peter; Barner-Kowollik, C. *Macromol. Rapid Commun.* **2014**, *35*, 45.
- (171) Latorre-Sánchez, A.; Pomposo, J. A. *Polym. Int.* **2016**, *65*, 855.
- (172) Huo, M.; Wang, N.; Fang, T.; Sun, M.; Wei, Y.; Yuan, J. *Polymer (Guildf)*. **2015**, *66*, 1.
- (173) Tuten, B. T.; Chao, D.; Lyon, K.; Berda, E. B. *Polym. Chem.* **2012**, *3*, 3068.
- (174) Shishkan, O.; Zamfir, M.; Gauthier, M. A.; Börner, H. G.; Lutz, J.-F. *Chem. Commun.* **2014**, *50*, 1570.
- (175) Tsarevsky, N. V.; Matyjaszewski, K. *Macromolecules* **2002**, *35*, 9009.
- (176) Song, C.; Li, L.; Dai, L.; Thayumanavan, S. *Polym. Chem.* **2015**, *6*, 4828.
- (177) Buruaga, L.; Pomposo, J. A. *Polymers (Basel)*. **2011**, *3*, 1673.
- (178) Tao, J.; Liu, G. *Macromolecules* **1997**, *30*, 2408.
- (179) Njikang, G.; Liu, G.; Curda, S. A. *Macromolecules* **2008**, *41*, 5697.
- (180) Xie, M. X.; Jiang, L.; Xu, Z. P.; Chen, D. Y. *Chem. Commun.* **2015**, *51*, 1842.
- (181) Zhou, F.; Xie, M.; Chen, D. *Macromolecules* **2014**, *47*, 365.
- (182) Hecht, S.; Khan, A. *Angew. Chemie - Int. Ed.* **2003**, *42*, 6021.
- (183) Fan, W.; Tong, X.; Yan, Q.; Fu, S.; Zhao, Y. *Chem. Commun.* **2014**, *50*, 13492.
- (184) Frank, P. G.; Tuten, B. T.; Prasher, A.; Chao, D.; Berda, E. B. *Macromol. Rapid Commun.* **2014**, *35*, 249.

- (185) Claus, T. K.; Zhang, J.; Martin, L.; Hartlieb, M.; Mutlu, H.; Perrier, S.; Delaittre, G.; Barner-Kowollik, C. *Macromol. Rapid Commun.* **2017**, *38*, 1.
- (186) Fischer, T. S.; Spann, S.; An, Q.; Luy, B.; Tsotsalas, M.; Blinco, J. P.; Barner-Kowollik, C. *Chem. Sci.* **2018**, *9*, 37.
- (187) De-La-Cuesta, J.; González, E.; Pomposo, J. A. *Molecules* **2017**, *22*, 1.
- (188) Wang, P.; Pu, H.; Ge, J.; Jin, M.; Pan, H.; Chang, Z.; Wan, D. *Mater. Lett.* **2014**, *132*, 102.
- (189) Adkins, C. T.; Dobish, J. N.; Brown, S.; Harth, E. *ACS Appl Mater Interfaces* **2013**, *2*, 710.
- (190) Liu, Y.; Pauloehrl, T.; Presolski, S. I.; Albertazzi, L.; Palmans, A. R. A.; Meijer, E. W. *J. Am. Chem. Soc.* **2015**, *3*, 1647.
- (191) Bai, Y.; Feng, X.; Xing, H.; Xu, Y.; Kim, B. K.; Baig, N.; Zhou, T.; Gewirth, A.; Lu, Y.; Oldfield, E.; Zimmerman, S. C. *J. Am. Chem. Soc.* **2016**, *138*, 11077.
- (192) González-Burgos, M.; Alegría, A.; Arbe, A.; Colmenero, J.; Pomposo, J. A. *Polym. Chem.* **2016**, *7*, 6570.
- (193) Zhang, Y.; Zhao, H. *Polym. (United Kingdom)* **2015**, *64*, 277.
- (194) Kröger, A. P. P.; Boonen, R. J. E. A.; Paulusse, J. M. J. *Polym. (United Kingdom)* **2017**, *120*, 119.
- (195) Jiang, J.; Thayumanavan, S. *Macromolecules* **2005**, *38*, 5886.
- (196) Hamilton, S. K.; Harth, E. *ACS Nano* **2009**, *3*, 402.
- (197) Lyon, C. K.; Hill, E. O.; Berda, E. B. *Macromol. Chem. Phys.* **2016**, *217*, 501.
- (198) Ji, X.; Guo, C.; Ke, X.; Sessler, J. L. *Chem. Commun.* **2017**, *53*, 8774.
- (199) Wuest, K. N. R.; Lu, H.; Thomas, D. S.; Goldmann, A. S.; Stenzel, M. H.; Barner-Kowollik, C. *ACS Macro Lett.* **2017**, *6*, 1168.
- (200) Hagnauer, G. L. *Anal. Chem.* **1982**, *54*, 265.
- (201) S.Tayyab., W. Qamar, W. I. *Biochem. Educ.* **1991**, *19*, 149.
- (202) Wu Chi-san. *Handbook of size exclusion chromatography and related techniques*; 2004.
- (203) Barth, H. G.; Mori, S. *Size exclusion chromatography*; 1999.
- (204) Pomposo, J. A.; Perez-Baena, I.; Buruaga, L.; Alegría, A.; Moreno, A. J.; Colmenero, J. *Macromolecules* **2011**, *44*, 8644.
- (205) Bhattacharjee, S. *J. Control. Release* **2016**, *235*, 337.
- (206) Pecora, R. *J. Chem. Phys.* **1964**, *40*, 1604.
- (207) Khintchine, A. *Math. Ann.* **1934**, *109*, 604.
- (208) Stetefeld, J.; McKenna, S. A.; Patel, T. R. *Biophys. Rev.* **2016**, *8*, 409.
- (209) Bro, R.; de Jong, S. *J. Chemom.* **1997**, *11*, 393.

- (210) Provencher, S. W. *Comput. Phys. Commun.* **1982**, *27*, 229.
- (211) Scotti, A.; Liu, W.; Hyatt, J. S.; Herman, E. S.; Choi, H. S.; Kim, J. W.; Lyon, L. A.; Gasser, U.; Fernandez-Nieves, A. *J. Chem. Phys.* **2015**, *142*, 234905.
- (212) Koppel, D. E. *J. Chem. Phys.* **1972**, *57*, 4814.
- (213) Ostrowsky, N.; Sornette, D.; Parker, P.; Pike, E. R. *Opt. Acta (Lond)*. **1981**, *28*, 1059.
- (214) Wu, C.; Unterforsthuber, K.; Lilge, D.; Luddecke, E.; Horn, D. **1994**, *1*, 145.
- (215) Tanner, J. E. *J. Chem. Phys.* **1970**, *52*, 2523.
- (216) Stejskal, E. O.; Tanner, J. E. *J. Chem. Phys.* **1965**, *42*, 288.
- (217) Johnson Jr., C. S. *Prog. Nucl. Magn. Reson. Spectrosc.* **1999**, *34*, 203.
- (218) Hahn, E. L. *Phys. Rev.* **1950**, *80*, 580.
- (219) Cohen, Y.; Avram, L.; Frish, L. *Angew. Chemie - Int. Ed.* **2005**, *44*, 520.
- (220) Gibbs, S. J.; Johnson, C. S. *J. Magn. Reson.* **1991**, *93*, 395.
- (221) Blasco, E.; Tuten, B. T.; Frisch, H.; Lederer, A.; Barner-Kowollik, C. *Polym. Chem.* **2017**, *8*, 5845.
- (222) Hanlon, A. M.; Martin, I.; Bright, E. R.; Chouinard, J.; Rodriguez, K. J.; Patenotte, G. E.; Berda, E. B. *Polym. Chem.* **2017**, *8*, 5120.
- (223) Berkovich, I.; Mavila, S.; Iliashevsky, O.; Kozuch, S.; Lemcoff, N. G. *Chem. Sci.* **2016**, *7*, 1773.
- (224) Heiler, C.; Offenloch, T. J.; Blasco, E.; Barner-Kowollik, C. *ACS Macro Lett.* **2017**, *6*, 56.
- (225) Heiler, C.; Bastion, S.; Lederhose, P.; Blinco, J. P.; Blasco, E.; Barner-Kowollik, C. *Chem. Commun.* **2018**, *54*, 3476.
- (226) Stayton, P. S.; Hoffman, A. S.; Murthy, N.; Lackey, C.; Cheung, C.; Tan, P.; Klumb, L. A.; Chilkoti, A.; Wilbur, F. S.; Press, O. W. *J. Control. Release* **2000**, *65*, 203.
- (227) Duncan, R. *Nat. Rev. Drug Discov.* **2003**, *2*, 347.
- (228) Ji, J.; Jia, L.; Yan, L.; Bangal, P. R. *J. Macromol. Sci. Part A Pure Appl. Chem.* **2010**, *47*, 445.
- (229) Pohlmeier, A.; Haber-Pohlmeier, S. *J. Colloid Interface Sci.* **2004**, *273*, 369.
- (230) Kölmel, D. K.; Hörner, A.; Rönicke, F.; Nieger, M.; Schepers, U.; Bräse, S. *Eur. J. Med. Chem.* **2014**, *79*, 231.
- (231) Zuckermann, R. N.; Kerr, J. M.; Kent, S. B. H.; Moos, W. H. *J. Am. Chem. Soc.* **1992**, *114*, 10646.
- (232) Kölmel, D. K.; Fürniss, D.; Susanto, S.; Lauer, A.; Grabher, C.; Bräse, S.; Schepers, U. *Pharmaceuticals* **2012**, *5*, 1265.

- (233) Lang, C.; Kiefer, C.; Lejeune, E.; Goldmann, A. S.; Breher, F.; Roesky, P. W.; Barner-Kowollik, C. *Polym. Chem.* **2012**, *3*, 2413.
- (234) Brandrup J-, Immergut H. E., E. A. G. *Polymer Handbook, 4th Edition*; 2003.
- (235) Lederhose, P. *From UV to NIR Light, Photo-Triggered 1,3-Dipolar Cycloadditions as a Modern Ligation Method in Solution and on Surface*; Karlsruhe, 2016.